UNIVERSITÀ DEGLI STUDI DI TRIESTE

XXX CICLO DEL DOTTORATO DI RICERCA IN FISICA

Study of Monolithic Active Pixel Sensors for the Upgrade of the ALICE Inner Tracking System

Settore scientifico-disciplinare: FIS/04

Dottorando:
Miljenko Šuljić

Coordinatore:
Prof. Livio Lanceri

Relatore:
Prof. Paolo Camerini

Anno Accademico 2016-2017

Abstract

The upgrade of the ALICE vertex detector, the Inner Tracking System (ITS), is scheduled to be installed during the next long shutdown period (LS2 in 2019-2020) of the CERN Large Hadron Collider (LHC). The current ITS will be replaced by seven concentric layers of Monolithic Active Pixel Sensors (MAPS) with total active surface of $\sim$10 m^2, thus making ALICE the first LHC experiment implementing MAPS detector technology on a large scale.

The scope of this thesis is twofold; to report on the activity on the development and the characterisation of a MAPS for the ITS upgrade and to study the charge collection process using a first-principles Monte Carlo simulation.

The performance of a MAPS depends on a large number of design and operational parameters, such as collection diode geometry, reverse bias voltage, and epitaxial layer thickness. I have studied this dependence by measuring the INVESTIGATOR chip response to X-rays emitted by an ^{55}Fe source and to minimum ionising particles. In particular, I have examined the influence of the parameters considered in the design of the MAPS for the ITS upgrade, on the Q/C ratio, i.e. the ratio of the collected charge in a single pixel and the pixel input capacitance.

The ALPIDE chip, based on TowerJazz 180 nm CMOS Imaging Process, has been developed for the ITS upgrade. I have performed extensive laboratory studies on the full-scale prototypes as well as on the final sensor. I have studied in detail the analogue front-end response in terms of timing characteristics using an infrared laser beam. I have significantly contributed to the measurements of the prototype and final sensors under charged particle beams. The laboratory and test-beam measurements allowed me to verify the compliance of the ALPIDE sensor to the ITS upgrade requirements.

The layers of the new ITS will be azimuthally segmented into the independent units called staves, which integrate the ALPIDE sensors and the mechanical and electrical support elements. The NA61/SHINE collaborations offered the opportunity to test an ITS stave in the Pb–Pb collision environment of their experiment. I have integrated a stave consisting of nine ALPIDE sensors in the NA61 experiment and tested its performance in terms of detection efficiency and spatial resolution at the multiplicities comparable to those expected in the ITS after the LS2.

While the successful operation of the sensors for the ITS upgrade has been confirmed, a great deal still remains to be understood about the charge collection process of MAPS. The exact response of MAPS is challenging to model due to contributions from both epitaxial layer and substrate, a typically only partially depleted active volume, and complex well structures. Transient TCAD simulations provide a good description but are not sufficiently fast to be used in the experiments simulations. Therefore, I have developed a *fast tool* to model the response of ALICE ITS MAPS. The basic concept is a first principles MC simulation, using electric fields extracted from a TCAD simulation to model the charge carrier drift. That is, the more complex part is handled by a TCAD simulation while preserving the speed of a MC simulation with only one free parameter. The tool is versatile, any MAPS architecture can be simulated once the proper external electric field is provided. So far, I have simulated the response of the INVESTIGATOR (analogue output) and ALPIDE (digital output) chips. An excellent agreement between data and simulation has been achieved, both for ^{55}Fe X-rays and minimum ionising particles.

Contents

1

Introduction

A Large Ion Collider Experiment (ALICE) [1] is designed to address the physics of strongly interacting nuclear matter, and in particular the properties of the Quark-Gluon Plasma (QGP), using proton–proton, proton–nucleus and nucleus–nucleus collisions at the CERN LHC. For the second long shutdown (LS2) of the LHC, the ALICE Collaboration is preparing a major upgrade of its apparatus targeting both an improvement of the measurement precision, and an increase of the event readout rate. A key element of the upgrade is a new, ultra-light, high resolution Inner Tracking System (ITS), equipped with Monolithic Active Pixel Sensors (MAPS).

This thesis is oriented towards a deeper understanding of the charge collection process in MAPS in relation to the development of the new pixel chip for the ITS upgrade In this chapter an overview of ALICE and its detectors, focusing on the ITS upgrade, will be given. In chapter 2, the properties of silicon as detector material and the principles of operation of MAPS will be discussed. The influence of the collection diode geometry and the reverse substrate bias on the charge collection properties is studied in chapter 3 using the INVESTIGATOR chip. ALPIDE, the final chip for the ITS upgrade, is presented in chapter 4 and it is verified that it fully complies with the ITS upgrade requirements. In chapter 5 the ALPIDE performance in the Pb–Pb collision environment of the NA61/SHINE experiment is studied, showing that the required performance is maintained in the experimental situation similar to that expected in ALICE. Chapter 6 is dedicated to the *fast tool* for the MAPS simulation that has been developed to study the charge collection process in MAPS. The simulation concept is discussed, and comparison of simulation results and measurements is presented. The summary of this work can be found in chapter 7.

1.1 Quark-gluon plasma

Strongly interacting matter is described at the fundamental level by the interaction of quarks through the exchange of gluons. This theory, called Quantum Chromodynamics (QCD), features a coupling constant $\alpha_s(q^2)$ which decreases logarithmically at short distances or large momenta q, while it becomes strong at large distances or small momenta, resulting in the phenomena of quark confinement and chiral symmetry breaking. As the temperature increases, the interactions among quanta occur at ever shorter distances, governed by weak coupling, whereas the long range interactions become dynamically screened. As a consequence, nuclear matter at very high temperature exhibits neither confinement nor chiral symmetry breaking. This new phase of QCD is called the quark-gluon plasma (QGP). It is assumed that QGP lasted for about 10 µs after the Big-Bang [2]. In the laboratory, ultra-relativistic heavy ion collisions are used to study the QGP.

The LHC allows to accelerate and collide protons and nuclei to unprecedented center-of-mass energies, of so far up to $\sqrt{s} = 13$ TeV for protons, and up to $\sqrt{s_{NN}} = 5.02$ TeV per nucleon pair for Pb-nuclei, thus offering a unique opportunity to carefully study the properties of the QGP.

QGP signatures

Since the size and lifetime of the quark-gluon plasma are expected to be small, at most a few fm in diameter and 5–10 fm/c in duration [2], it is necessary to identify the appropriate experimental tools for observing its formation and to study its properties. Furthermore, signals of the quark-gluon plasma compete with backgrounds emitted from the hot hadronic gas phase that follows the hadronization of the plasma and are modified by final state interactions in the hadronic phase.

The basic concept behind kinematic probes is the determination of the energy density ε and entropy density s of hadronic matter as a function of the temperature T and the baryochemical potential μ_B of the plasma. Observables related to the variables T, s, and ε are customarily identified with the average transverse momentum $\langle p_{\mathrm{T}} \rangle$, the hadron rapidity distribution dN/dy, and the transverse energy dE_{T}/dy, respectively [3].

The enhancement of strangeness production in collisions of heavy ions with respect to the p–p collisions was one of the first proposed signatures of the transition to the quark-gluon plasma [4]. The reason is that the energy threshold for the production of strange

quarks is smaller in the QGP compared to the hadron gas. Moreover, the strangeness content can be decreased only through weak decays for which the time scale is much longer compared with the lifetime of the QGP fireball. Hence, strange quarks may survive hadronisation to become constituents of the strange hadrons. In fact, experimental data reveal an enhancement of the hyperon produced in nucleus–nucleus collisions when compared with p–p collisions. Such enhancement is proportional to the strange content of the hyperons [5].

The suppression of J/ψ production in a quark-gluon plasma occurs because a $c\bar{c}$ pair formed by fusion of two gluons from the colliding nuclei cannot bind inside the quark-gluon plasma because of the screening of neighbouring quarks. Lattice simulations of SU(3) gauge theory show that this condition should be satisfied already slightly above the deconfinement temperature [6, 7].

Photons and lepton pairs provide probes of the interior of the quark-gluon plasma during the earliest and hottest phase of the evolution of the fireball because they are not affected by final state interactions [8].

The color structure of QCD matter can be probed by its effects on the propagation of a fast parton. The mechanisms are similar to those responsible for the electromagnetic energy loss of a fast charged particle in matter; energy may be lost either by excitation of the penetrated medium or by radiation [9, 10]. The nuclear modification factor i.e. the transverse momentum spectra of charged particles produced in nucleus-nucleus collisions and normalized to proton-proton collision spectra at the same energy, is a fundamental observable in high energy heavy ion experiments and can be expressed as

$$R_{AA}(p_{\mathrm{T}}) = \frac{1}{N_{coll}^{AA}} \frac{d^2N^{AA}/dydp_{\mathrm{T}}}{d^2N^{pp}/dydp_{\mathrm{T}}} \tag{1.1}$$

where N_{coll} denotes the number of binary collisions, y the rapidity, and N^{AA} and N^{pp} the multiplicities of particles produced in nucleus–nucleus and proton–proton collisions, respectively. If one assumes that nucleus-nucleus collision is a superposition of N_{coll} nucleon–nucleon collisions, then the $R_{AA} = 1$. The scaling with N_{coll} is expected for hard processes (with large momentum transfer). Therefore, the R_{AA} should be less than unity. In fact, suppression of high-p_{T} particles which is attributed to strong parton energy loss and large medium density in ultra-relativistic heavy ion collisions was found [11, 12].

Most of the heavy ion collisions are non-central, therefore the initial overlap region has an ellipsoidal shape in the transverse plane. The density gradient emerging in the

collision transforms into a pressure gradient due to particle interactions. The pressure gradients are larger along the shorter axis of the ellipse, thus the created acceleration is larger in this direction (in-plane). Such phenomenon of spatial asymmetry generates an azimuthal anisotropy of the momentum distributions is called "elliptic flow", which is usually described by a Fourier coefficient v_2. The momentum anisotropy emerges at the beginning of the evolution of the fireball, thus v_2 is sensitive to the early phase of the collision [13, 14].

Identical particle correlations, e.g. $\pi\pi$, KK, or pp, yield information on the reaction geometry and provides important information about the dynamics of nuclear collisions. By studying the two-particle correlation function along various directions in phase space, it is possible to obtain measurements of the transverse and longitudinal size, of the lifetime, and of flow patterns of the hadronic fireball at the moment when it breaks up into separate hadrons [15].

1.2 A Large Ion Collider Experiment

The ALICE apparatus allows for a comprehensive study of hadrons, electrons, muons, photons and jets produced in heavy ion collisions. The heavy ion programme is complemented by precision measurements from p–p and p–Pb collisions to provide a quantitative base for comparison with results from Pb–Pb collisions.

Prior to the start-up of the LHC heavy ion programme, the nature of the QGP as an almost perfect liquid emerged from the experimental investigations [16]. ALICE has confirmed this basic picture, observing the creation of hot hadronic matter at unprecedented values of temperatures and energy densities, and exceeding the precision and kinematic reach of all significant probes of the QGP that had been measured over past decades (see sec. 1.1). These physics results have been achieved by ALICE after only three years of Pb–Pb running and two p–Pb runs, demonstrating its excellent capabilities to measure high-energy nuclear collisions at the LHC.

The ALICE apparatus (see fig. 1.1) consists of a central barrel, which measures hadrons, electrons and photons, and a forward muon arm. The central barrel covers polar angles from 45° to 135° and is embedded in a large solenoid magnet. Moving from centre to periphery, it consists of several detectors: the already mentioned Inner Tracking System

(ITS), which will be described in the next section, a cylindrical Time-Projection Chamber (TPC), three particle identification arrays of Time-of-Flight (TOF), Ring Imaging Cherenkov (HMPID) and Transition Radiation (TRD) detectors, and two electromagnetic calorimeters (PHOS and EMCAL). All detectors except HMPID, PHOS, and EMCAL cover the full azimuth. The forward muon arm (2° - 9°) consists of a complex arrangement of absorbers, a large dipole magnet, and fourteen planes of tracking and triggering chambers. Several smaller detectors (ZDC, PMD, FMD, T0, V0) for global event characterization and triggering are located at very small angles. An array of scintillators (ACORDE) on top of the L3 magnet is used to trigger on cosmic rays.

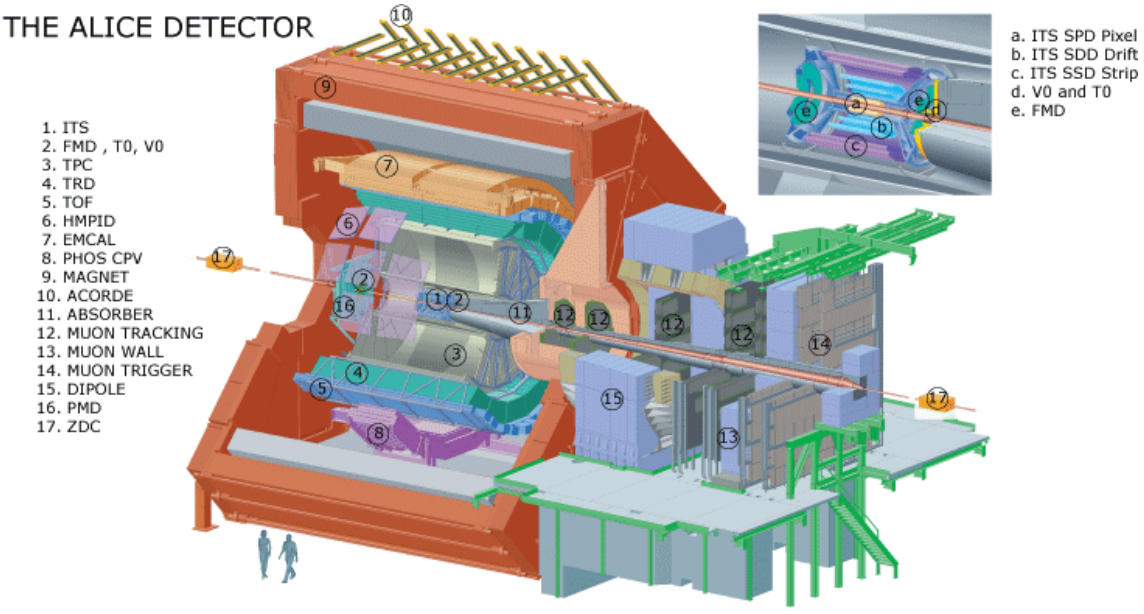

Figure 1.1: ALICE detectors - The ALICE apparatus consists of a central barrel, which measures hadrons, electrons, and photons, and a forward muon arm.

Despite this success there are several frontiers, including high precision measurements of rare probes over a broad range of transverse momenta, for which the current experimental setup is not yet fully optimised. The detector upgrade, combined with a increase of LHC luminosity [17], will significantly enhance the physics capabilities of ALICE, which is therefore preparing a major upgrade of its apparatus [18, 19, 20], planned for installation in the second long LHC shutdown (LS2) in the years 2019–2020.

The main physics topics addressed require the measurement of heavy flavour hadrons

(see tab. 1.1), quarkonia, and low mass dileptons at low transverse momenta, together with novel measurements of jets and their constituents [18]. To make all of this possible a significant improvement in vertexing and tracking efficiency at low transverse momentum is needed.

Part.	Yield m.b., 0-10%	$dN/d\eta\|_{\eta=0}$ m.b., 0-10%	$c\tau$ [μm]	decay channel	branching ratios
D^0	23, 100	2.3, 11	≈ 120	$K^-\pi^+$	3.8%
D^{*+}	9, 44	0.9, 4.4	≈ 0	$D^0\pi^+$	67.7%
D_s^+	4.3, 20	0.4, 2.0	≈ 150	$\Phi(\rightarrow K^+K^-)\pi^+$	4.4%(×49%)
Λ_c^+	2.9, 14	0.29, 1.4	≈ 60	$pK^-\pi^+$	5.0%
				$p\overline{K}^0(K_s^0 \rightarrow \pi^+\pi^-)$	1.15% (×69.2%)
				$\Lambda\pi^+(\rightarrow \mathrm{p}\pi^-)$	1.1%(×63.9%)
B	1.3, 6.2	0.2, 0.9	≈ 500	$J/\psi(\rightarrow e^+e^-) + X$	1.2%(×6%)
				$D^0(\rightarrow K^-\pi^+) + X$	60%(×3.8%)
				$e^+ + X$	10.9%
B^+	0.6, 2.7	0.1, 0.4	≈ 500	$\overline{D}^0(\rightarrow K^+\pi^-)\pi^+$	0.5%(×3.8%)
B^0	0.6, 2.7	0.1, 0.4	≈ 500	$D^{*-}(\rightarrow K^+\pi^-\pi^-)\pi^+$	0.3%(×2.6%)
Λ_b^0	0.1, 0.5	0.015, 0.07	≈ 400	$\Lambda_c^+(\rightarrow pK^-\pi^+) + e^- + X$	9.9%(×5%)
				$\Lambda_c^+(\rightarrow pk^-\pi^+) + \pi^-$	0.6%(×5%)

Table 1.1: Expected production yields (total and per unit of rapidity at mid-rapidity) for charm and beauty particles (+ anti-particles) in minimum-bias and 0% to 10% events for central Pb–Pb collisions at 5.5 TeV, mean proper decay length and branching ratios to the relevant decay channels [18, 21].

1.2.1 ALICE upgrade plans

The upgrade strategy is based on the LHC plans to increase the luminosity of Pb–Pb collisions progressively after LS2, eventually reaching an interaction rate of about 50 kHz, i.e. instantaneous luminosity of $\mathcal{L} = 6 \times 10^{27}$ cm^{-2}s^{-1}. In the proposed plan, the ALICE detector will be upgraded to enable the read-out of all interactions and accumulate more than 10 nb^{-1} of Pb–Pb collisions following LS2, corresponding to about 10^{11} interactions [18]. The upgrades include:

- A new beampipe with smaller diameter;
- A new, high resolution, low material budget Inner Tracking System (see sec. 1.3);

- Upgrade of the Time Projection Chamber [19];
- Upgrade of the forward trigger detectors [22];
- Upgrade of the online systems and offline reconstruction [23].

A new detector, the Muon Forward Telescope (MFT), was recently proposed to add vertexing capabilities to the current Muon Spectrometer [20]. The MFT consists of five planes of silicon pixel detectors placed in front of the hadronic absorber (see fig. 1.1), covering the acceptance of the Muon Spectrometer. The detector technology foreseen for the MFT is the same as that proposed for the ITS, and strong synergy exists between the two projects.

1.3 ALICE Inner Tracking System upgrade

Heavy flavour measurements are the primary scope of a new ITS with largely improved tracking and readout rate capabilities. The two main open questions concerning heavy flavour interactions with the QGP medium, along with the corresponding experimental handles, are [18]:

- Thermalisation of charm and beauty in the QGP. This is possible by measuring the baryon/meson ratio for charm (Λ_c/D) and for beauty (Λ_b/B) and the azimuthal anisotropy coefficient v_2 for charm mesons and baryons; in fact, at low momentum the study of the elliptic flow provides the most direct evidence of collective hydrodynamical behaviour of the medium.
- Heavy quark in-medium energy loss and its mass dependence. It can be addressed by measuring the nuclear modification factors $R_{AA}(p_{\mathrm{T}})$ distributions of D and B mesons separately in a wide momentum range, and heavy flavour production associated with jets.

In addition, the reduced material thickness and the improved tracking precision and efficiency of the new ITS provide an essential contribution for a detailed measurement of low mass dielectrons. This measurement gives access to:

- Thermal radiation from the QGP, via real and virtual photons detected as dielectrons.
- In-medium modifications of hadronic spectral functions related to chiral symmetry restoration, in particular for the ρ meson in its $\mathrm{e}^+\mathrm{e}^-$ decay mode.

1.3.1 Present ITS and its limitations

The present ALICE ITS (fig. 1.2) consists of six cylindrical layers of silicon detectors placed coaxially around the beam pipe. The layers are located at radii between 39 mm and 430 mm and cover the pseudo-rapidity range $|\eta| < 0.9$ for vertices located within $z = \pm 60$ mm with respect to the nominal interaction point. The number, position and segmentation of the layers were optimised to achieve both high precision in the determination of the charged particle distance of closest approach to the primary vertex and efficient track finding in combination with the TPC (within the boundaries set by technological limitations and available funds). While the inner radius is the minimum allowed by the radius of the beam pipe, the outer radius is determined by the necessity to match tracks with those from the TPC.

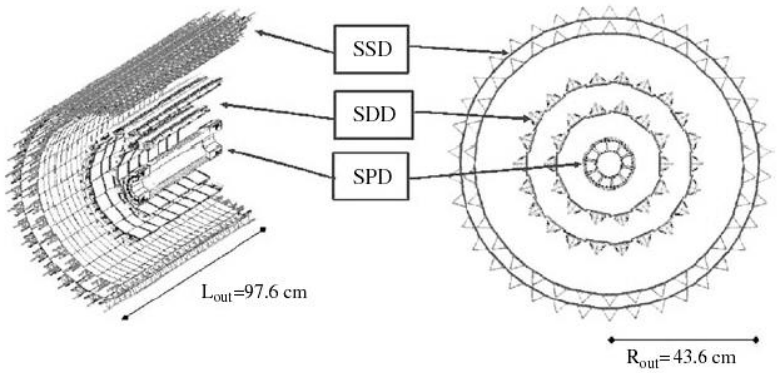

Figure 1.2: Present ITS layout - The present ITS consists of six cylindrical layers of silicon detectors placed coaxially around the beam pipe.

In view of the high particle density (the current system is designed for up to 100 particles per cm^2 for Pb–Pb collisions at $\sqrt{s_{NN}} = 5.5$ TeV), and in order to achieve the required accuracy in the measurement of the track distance of closest approach, the first two layers of the ITS are made of Silicon Pixel Detectors (SPD), while the two middle layers are made of Silicon Drift Detectors (SDD). The two outer layers, where the track density falls to one particle per cm^2, are equipped with double-sided Silicon micro-Strip Detectors (SSD). Also, the information from SDD and SSD was used for particle identification (PID) via dE/dx measurement in the non-relativistic region. All detector components were carefully optimised to minimise their radiation length, achieving 1.1% X_0 per layer, the lowest value among all the current LHC experiments [24].

The precision of the present ITS in the determination of the impact parameter (75 µm at values of transverse momentum above 1 GeV/c [25]) is adequate to study the production of charm mesons in exclusive decay channels (e.g. $D^0 \to K\pi$ and $D^+ \to K\pi\pi$ with decay lengths $c\tau$ of 123 µm and 312 µm, respectively). The challenge is even greater for charm baryons; the most abundantly produced charm baryon (Λ_c) has a decay length $c\tau$ of only 60 µm [21]. This is lower than the impact parameter resolution of the present ITS in the transverse momentum range of the majority of Λ_c daughter particles. Therefore, charm baryons are presently not measurable by ALICE in central Pb–Pb collisions. For the same reasons as outlined above, the study of beauty mesons, beauty baryons, and of hadrons with more than one heavy quark are also beyond the capability of the current detector.

A crucial limitation of the present ITS detector is given by its limited readout rate capabilities. The ITS can run at a maximum rate of 1 kHz (with dead time close to 100%), irrespective of the detector occupancy. For all the physics channels that cannot be selected by a trigger, this rate limitation restricts ALICE to use only a small fraction of the full Pb–Pb collision rate of 8 kHz that the LHC presently can deliver [18].

1.3.2 ITS upgrade concept

The objectives for the ITS upgrade are to record Pb–Pb collisions at up to 100 kHz and p–p collisions at 400 kHz, while improving the pointing resolution by a factor of 3 in $r\varphi$ and a factor of 5 in z at $p_{\mathrm{T}} = 500$ MeV/c with respect to the present ITS (see fig. 1.3a).

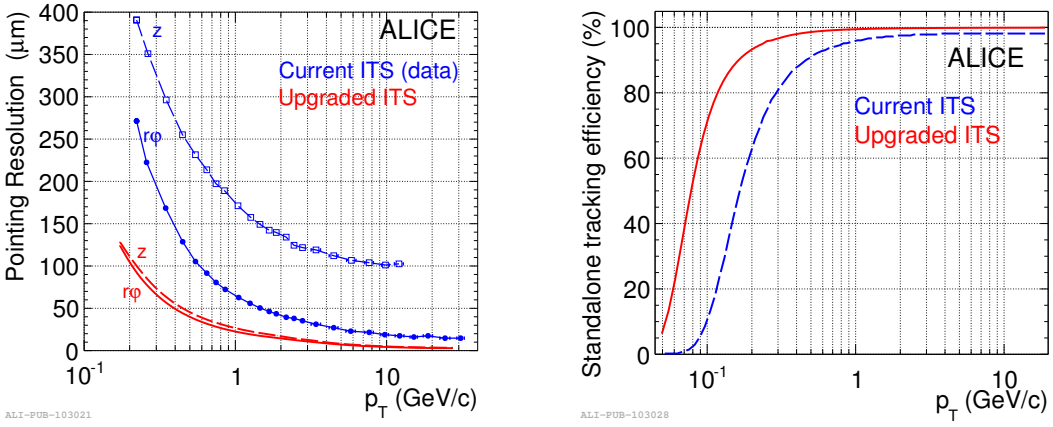

(a) Pointing resolution as a function of p_{T}

(b) Tracking efficiency as a function of p_{T}

Figure 1.3: Upgraded ITS performance - Performance (for primary charged pions) of the current ITS compared to the expected performance of the upgraded ITS [18].

The pointing resolution σ_p is mainly determined by two aspects:

- The error σ_p^{sp} of the geometrical extrapolation from measured points along the particle track to the interaction point (IP). This contribution is given by the intrinsic spatial resolution σ_i and the position r_i of the detector elements i.

- Uncertainty σ_p^{ms} introduced by multiple Coulomb scattering occurring in the beam pipe and the detector layers themselves, especially the one closest to the IP. The distribution of the angular deflection due to scattering can roughly be described by a Gaussian with RMS width θ_{RMS} [21]:

$$\theta_{RMS} = \frac{13.6[\text{MeV}]}{\beta cp} z\sqrt{x/X_0}\,[1 + 0.038\ln(x/X_0)]\,, \tag{1.2}$$

  where p, βc, and z are the momentum, velocity and charge of the incident particle, and x/X_0 is the thickness of the material in terms of radiation length X_0.

In order to assess the influence of these parameters on the pointing resolution of a tracking system, already the simple example of a two-layer detector (see fig. 1.4) provides valuable insights [26].

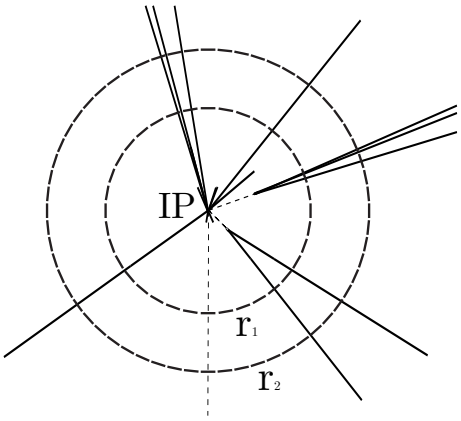

Figure 1.4: Example of two-layers detector - Concentric arrays of position-sensitive detectors, shown schematically and not to scale, provide track coordinates at two radii. [26]

Considering a configuration with the inner layer at radius r_1 and the outer layer at r_2, featuring a spatial resolution of σ_1 and σ_2, respectively, the contributing σ_p^{sp} yields

$$\sigma_p^{sp} = \sqrt{\left(\frac{r_2}{r_2 - r_1}\sigma_1\right)^2 + \left(\frac{r_1}{r_2 - r_1}\sigma_2\right)^2}. \tag{1.3}$$

The multiple scattering causes a deviation from zero pointing resolution due to θ_{RMS} over the lever arm r_1 (or the beam pipe radius), which is $\sigma_p^{ms} \approx r_1 \theta_{RMS}$. For a particle with unit charge and neglecting the logarithmic term in eq. 1.2, the contribution of multiple scattering to σ_p can be written as

$$\sigma_p^{ms} \approx r_1 \frac{13.6[\text{MeV}]}{\beta cp} \sqrt{x/X_0}. \tag{1.4}$$

The pointing resolution σ_p is then obtained by summing the two contributions in quadrature

$$\sigma_p \approx \sigma_p^{sp} \oplus \sigma_p^{ms}. \tag{1.5}$$

This simple treatment indicates that a better pointing resolution is mainly achieved by small inner radii (r_1) and low material budget (x/X_0), especially for the innermost layer and the beam pipe. The position resolution at the inner radius is weighted by the outer radius, so precision at the inner layer is paramount.

Detailed simulations have been performed to determine the optimum design parameters for the ITS upgrade. In summary, the following design objectives were defined [18]:

- Reducing the distance between the first layer and the interaction point from 39 mm to 22 mm;
- Reducing the material budget from 1.14% to 0.3% x/X_0 per layer for the innermost layers;
- Reducing the pixel size from 50 µm × 425 µm to about 30 µm × 30 µm;
- Increasing the number of layers from currently six to seven; this will also improve the standalone tracking efficiency (see fig. 1.3b) and p_{T}-resolution at low transverse momenta.

1.3.3 Layout of the upgraded ITS

To achieve the design objectives, the present ITS will be fully replaced by a new detector consisting of seven layers equipped with monolithic silicon pixel detectors (see fig. 1.5). The layers are grouped into two separate barrels. The Inner Barrel (IB) consists of the three innermost layers, while the Outer Barrel (OB) contains the two middle and two outer layers.

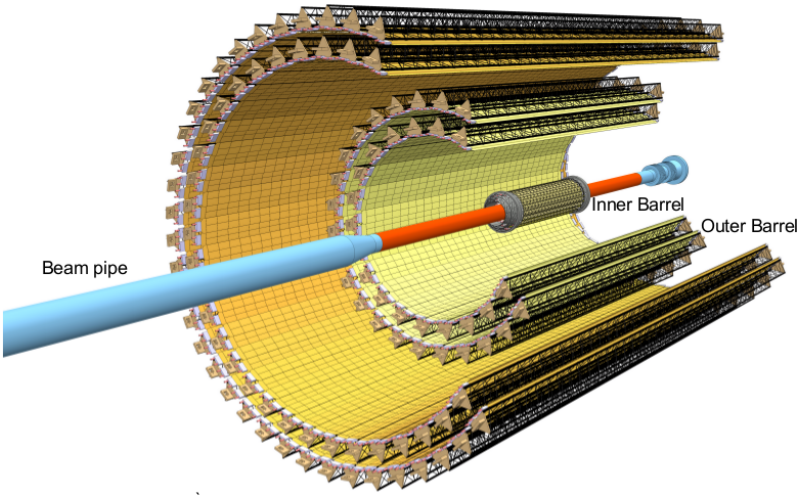

Figure 1.5: New ITS conceptual layouts - The Inner Barrel (IB) consists of the three innermost layers, while the Outer Barrel (OB) contains the two middle and two outer layers.

The layers are azimuthally segmented in mechanically independent elements named staves. Even though the inner and outer barrel staves have different geometries, they have the same basic structure consisting of the following elements (see tab. 1.2):

- **Space Frame:** truss-like lightweight mechanical support structure for the single stave based on composite material (carbon fiber).
- **Cold Plate:** carbon ply that embeds the cooling pipes.
- **Hybrid Integrated Circuit:** assembly consisting of a polyimide flexible printed circuit (FPC) which interconnects several pixel chips and contains additional passive components. The interconnection is established via wire-bonding.

	Inner Barrel			Outer Barrel			
	Layer 0	Layer 1	Layer 2	Layer 3	Layer 4	Layer 5	Layer 6
Length [cm]		27.1		84.3		147.5	
Radial position [cm]	2.3	3.1	3.9	19.4	24.7	35.3	40.5
N. staves	12	16	20	24	30	42	48
N. HICs	12	16	20	384	480	1176	1344
N. pixel chips	108	114	180	2688	3360	8232	9408

Table 1.2: Layout parameters of the new ITS [18].

The inner barrel stave hosts a single HIC containing nine pixel chips. On the other hand, the outer barrel staves are further segmented in azimuth into two halves extending over the full stave length, called half-staves (see fig. 1.6). Each half-stave is subdivided in longitudinal direction into a number of HICs[1], each integrating two rows of seven pixel chips. An additional power bus, soldered to the FPC, is added to improve power distribution over the full length of the staves.

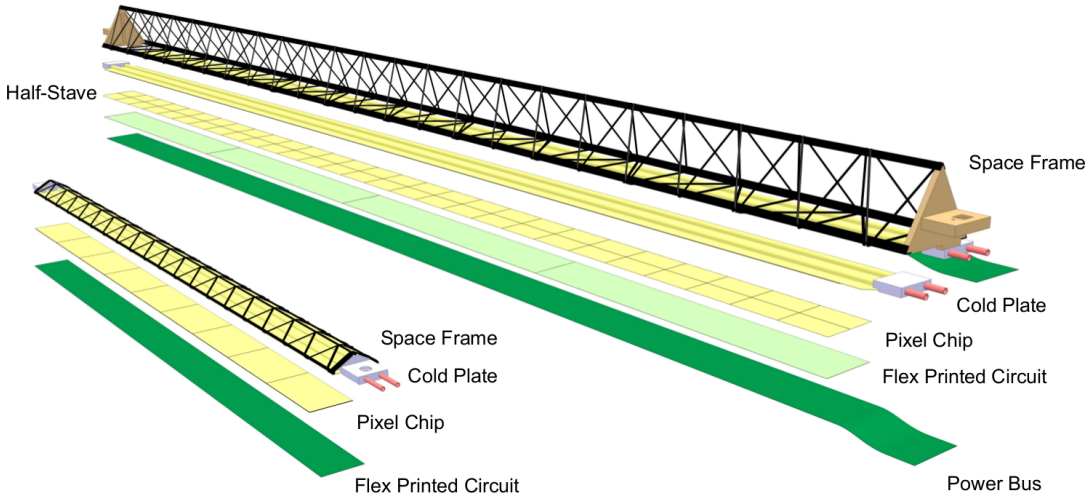

Figure 1.6: ITS upgrade staves - Schematic drawing of the Inner Barrel (left) and Outer Barrel (right) Staves [18].

1.3.4 Pixel chip

The design objectives together with the operation environment of the upgraded ITS led to the requirements on the pixel chip as presented in table 1.3. By accommodating detection volume and readout circuitry on the same die, Monolithic Active Pixel Sensor (MAPS) allow for very thin sensors and make an interconnection of readout and sensor chip obsolete. MAPS can be implemented cost effectively using a commercial CMOS process without the need for an expensive interconnection. In the last years, there has been significant progress on the development of MAPS. Today, MAPS are used in high-energy physics experiments, such as the STAR experiment [27].

The stringent requirements of the ITS upgrade compared to previous applications, as e.g. the STAR PXL detector, which features integration time of ≈ 200 µs, power consump-

[1]Four and seven HICs in case of two middle and two outer layers of the outer barrel, respectively.

tion of ≈ 170 mW/cm^2, and radiation hardness of ≤ 90 krad TID and $\leq 10^{12}$ 1 MeV n_{eq}/cm^2 NIEL, both per year of operation [28], necessitate further R&D.

Parameter	Inner Barrel	Outer Barrel
Max. silicon thickness[a]	50 µm	100 µm
Intrinsic spatial resolution	5 µm	10 µm
Chip size	15×30 mm^2	
Max. power density	300 mW/cm^2	100 mW/cm^2
Max. integration time	30 µs	
Max. dead time	10% at 50 kHz Pb-Pb	
Min. detection efficiency	99%	
Max. fake hit rate[a]	10^{-6}	
TID[1,a] radiation hardness	2.7 Mrad	100 krad
NIEL[2,a] radiation hardness	1.7×10^{13} 1 MeV n_{eq}/cm^2	3×10^{10} 1 MeV n_{eq}/cm^2

[a] Updated with respect to the reference.
[1] Total Ionising Dose (includes a safety factor of ten).
[2] Non Ionising Energy Loss (includes a safety factor of ten).

Table 1.3: ALICE pixel chip general requirements [18].

2

Monolithic Active Pixel Sensors

Particle sensors and their associated readout electronics, used for vertexing and tracking detection systems in particle physics experiments, have very demanding requirements in terms of granularity, material thickness, read-out speed, power consumption and radiation hardness (see table 1.3 and [18]). The development of sensors based on semiconductor technology and of readout electronics based on CMOS technology in the 1980s revolutionised the implementation of such detection systems. This technology can be used to match the majority of the above requirements. Nowadays Si pixel sensors are at the heart of the vast majority of particle tracking systems used in particle physics experiments. Compromises exist in the implementation of this technology. Perhaps the most significant is the interface between the sensor and the readout electronics, i.e. they are typically separate components. For example, the present Si pixel detectors used in the innermost layers of the LHC experiments ATLAS, CMS, LHCb and ALICE all consist of Si pixel sensors bump-bonded to CMOS read-out electronics (see fig. 2.1a). This technology can be optimised by thinning both sensor and read-out chip, as well as by reducing the bump-bonding pitch as much as possible. Nevertheless there are technical limitations and these are being reached with the present detectors. To go beyond these limitations and build detection systems with, for example, higher granularity and less material thickness, requires the development of a new technology. One way to achieve this goal is to merge both sensor and read-out electronics into a single piece of Silicon. This is the approach taken with Monolithic Active Pixels Sensors (MAPS) (see fig. 2.1b).

Over the last 15 years, extensive R&D has been carried out on MAPS. This has brought the technology to the level where it is now, a viable option for vertexing and tracking systems in particle and nuclear physics. The technology can meet the majority of

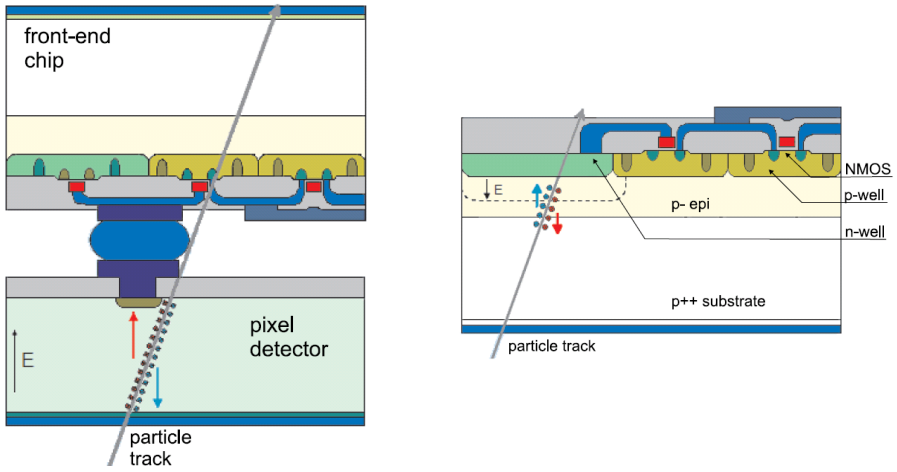

(a) Hybrid pixel **(b)** MAPS pixel

Figure 2.1: Cross section scheme of a hybrid and a MAPS pixel. - Hybrid pixel (a) consist of Si sensor bump-bonded to CMOS read-out electronics while MAPS (b) combines the two in a single volume. Not to scale.

the requirements of such systems, with some problems at the moment: a limited radiation tolerance and a moderate readout time. It is, however, a very promising technology for heavy-ion experiments such as ALICE, which have less stringent radiation tolerance and readout time requirements (see table 1.3). It is also in such experiments, where measurements at low transverse momentum are crucial, that the advantages of MAPS technology are readily seen [18].

In this chapter the properties of silicon detectors will be reviewed, the principle of operation of MAPS will be described and common techniques and observables encountered in MAPS characterisation will be introduced.

2.1 Silicon properties

In silicon, electron-hole (e-h) pairs are constantly being thermally excited. At the same time, some of them recombine (see sec. 2.1.3). Under stable conditions, an equilibrium between the two processes is established and the e-h pairs concentration n_i is proportional to $T^{3/2}\exp(-E_g/2kT)$. $E_g = 3.6$ eV is the energy required to excite an electron from valence to conduction band [29], k is the Boltzmann constant and T is the absolute temperature. At room temperature $n_i \cong 1.5 \times 10^{10}$ cm^{-3} [30]. The resistivity of a semiconductor is

given by:

$$\rho = \frac{1}{e(n\mu_e + p\mu_h)} \tag{2.1}$$

where e is the elementary charge, μ_e and μ_h are electron and hole mobilities, and n and p are negative and positive charge carrier concentrations. In intrinsic silicon $n = p = n_i$, therefore

$$\rho = \frac{1}{en_i(\mu_e + \mu_h)} \tag{2.2}$$

Knowing electron and hole mobilities (1350 and 480 $\mathrm{cm^2V^{-1}s^{-1}}$ respectively), intrinsic silicon resistivity can be calculated as $\rho \approx 230$ kΩcm at 300 K [30].

2.1.1 Doping and junctions

Adding pentavalent atoms to the silicon crystal, an n-type silicon is obtained, while adding trivalent atoms results in a p-type silicon. This process is called doping, and the pentavalent and trivalent atoms are called donors and acceptors because they introduce an additional electron or a hole, which accepts an electron, to the lattice. This excess of charge carriers introduced by doping can significantly change the properties of silicon. For example in a p-type silicon, the resistivity is reduced as it can be seen from eq. 2.1 which can be approximated as $\rho \approx \frac{1}{eN_A\mu_h}$, since $p \gg n$ and $p \approx N_A$. Furthermore, the mobility is affected by scattering due to ionised impurities [29], whose concentration is increased after doping (see fig. 2.2).

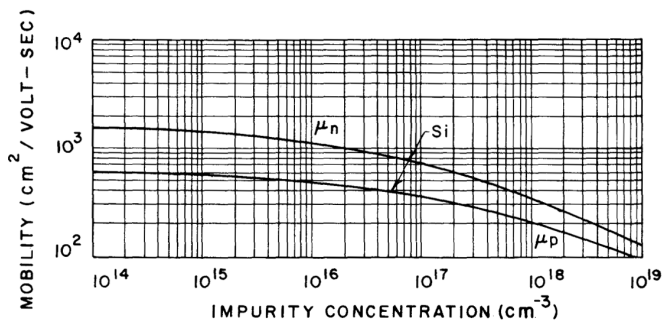

Figure 2.2: Mobility as a function of impurity concentration - Mobility is affected by scattering due to ionised impurities introduced by doping [29].

Structures with particular characteristics can be obtained by combining silicon regions with different doping type and concentration. The contact area between two silicon regions with different doping type (p or n) is called anisotype junction and that between different doping concentrations is called isotype junction.

2.1.1.1 Anisotype Junction (p–n)

The concentration difference of electrons and holes in the two differently doped silicon regions causes diffusion of electrons towards p-type silicon and holes towards n-type silicon. Electrons fill-up holes and holes capture electrons, creating a potential difference (built-in potential) between the two initially neutral regions (p-type becomes negative while n-type becomes positive). When equilibrium is established, the contact region is devoid of charge carriers and therefore is called *the depleted region* (see fig. 2.3). Any charge carrier entering or created in this region is accelerated by the electric field (electrons towards n-type and holes towards p-type).

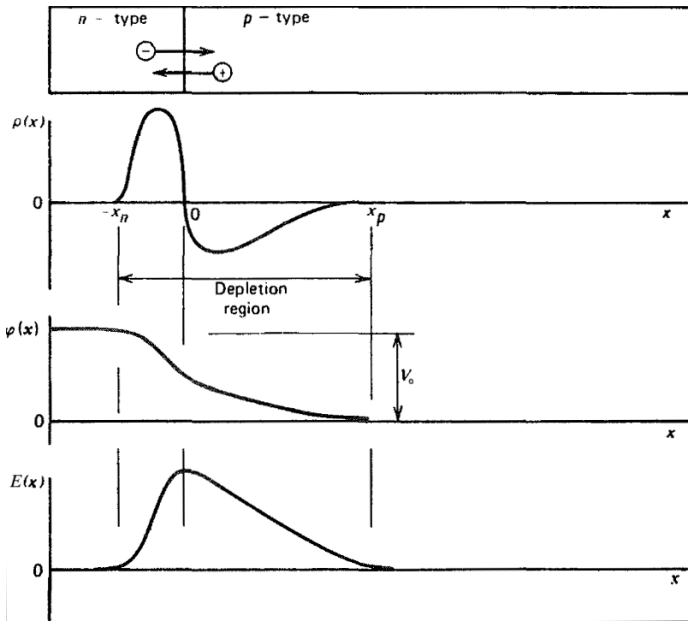

Figure 2.3: P–n junction - The carrier diffusion across the junction gives rise to the illustrated profiles for space charge $\rho(x)$, electric potential $\varphi(x)$ and electric field $E(x)$ [31].

For simplicity, properties of the p–n junction can be studied on an idealised planar junction i.e. by representing the space charge $\rho(x)$ sketched in figure 2.3 by a uniform distribution:

$$\rho(x) = \begin{cases} eN_D & -x_n < x < 0 \\ -eN_A & 0 < x < x_p \end{cases} \tag{2.3}$$

where N_D and N_A are donor and acceptor impurity concentrations. Conservation of charge implies that:

$$N_A x_p = N_D x_n \tag{2.4}$$

Potential value can be determined from Poisson's equation:

$$\frac{d^2\varphi}{dx^2} = -\frac{\rho(x)}{\varepsilon} \tag{2.5}$$

where ε is the dielectric constant. By integrating eq. 2.5:

$$-E(x) = \frac{d\varphi(x)}{dx} = \begin{cases} -\dfrac{eN_D}{\varepsilon}(x - x_n) & -x_n < x < 0 \\ \dfrac{eN_A}{\varepsilon}(x + x_p) & 0 < x < x_p \end{cases} \tag{2.6}$$

with boundary conditions $E(x_p) = E(x_n) = 0$. Integrating one more time and setting $\varphi(-x_n) = V_0$ (built-in potential) expression for the potential is obtained:

$$\varphi(x) = \begin{cases} -\dfrac{eN_D}{2\varepsilon}(x - x_n)^2 + V_0 & -x_n < x < 0 \\ \dfrac{eN_A}{2\varepsilon}(x + x_p)^2 & 0 < x < x_p \end{cases} \tag{2.7}$$

The two solutions join at $x = 0$ so V_0 can be calculated:

$$V_0 = \frac{e}{2\varepsilon}(N_D x_n^2 + N_A x_p^2) \tag{2.8}$$

Using 2.4 x_n and x_p can be calculated and so the thickness d of the depleted region:

$$d = x_n + x_p = \sqrt{\frac{2\varepsilon V_0}{e}\frac{N_D + N_A}{N_D N_A}} \tag{2.9}$$

The depleted region can be further increased by applying an external potential difference V, so that $\varphi(-x_n) = V_0 + V$:

$$d = x_n + x_p = \sqrt{\frac{2\varepsilon}{e}\frac{N_D + N_A}{N_D N_A}(V_0 + V)}. \tag{2.10}$$

V_0 can also be expressed as [32]:

$$V_0 = \frac{kT}{q}\ln\left(\frac{N_D N_A}{n_i^2}\right) \tag{2.11}$$

The junction capacitance can be easily calculated starting from $C = \varepsilon\frac{A}{d}$ and eq. 2.9

$$C_j = A\sqrt{\frac{\varepsilon e}{2(V_0 + V)}\frac{N_D N_A}{N_D + N_A}} \tag{2.12}$$

where A is the junction area. In the most applications, including MAPS, $N_D \gg N_A$ (or vice-versa) so the above equation can be simplified to

$$C_j = A\sqrt{\frac{\varepsilon e N_A}{2(V_0 + V)}}. \tag{2.13}$$

2.1.1.2 Isotype Junction (n–n$^+$ or p–p$^+$)

Isotype junctions can be treated in a similar way. Consider for instance p–p$^+$ junctions[1]; p and p$^+$ types in isotype junctions can be treated as n and p type in anisotype junctions, respectively. This treatment isn't entirely correct as there are no intermediate band levels corresponding to the acceptor atoms. Nevertheless, majority charge carriers (in this example holes) diffuse from the highly doped region (p$^+$) to the region with lower doping level (p). Analogue to a p–n junction, two initially neutral regions become charged creating a potential difference. Holes excited in the p-region, in the proximity of the junction, will be attracted toward the p$^+$ region while electrons will be reflected back into the p-region. The situation is opposite in case of the n–n$^+$ junction; electrons are attracted by the n$^+$ region while holes are reflected by it [33]. The built-in voltage is given by

$$V_0 = \frac{kT}{q} \ln\left(\frac{N_{A,p^+}}{N_{A,p^-}}\right) \tag{2.14}$$

where N_{A,p^+} and N_{A,p^-} are the acceptor concentrations in the high and low doping regions, respectively.

2.1.2 Charge carrier migration

The key equations that describe charge carrier behaviour are the current density equations and the continuity equations [29]. The current density equations for electrons and holes are

$$\vec{J_n} = q\mu_n n\vec{E} + qD_n\vec{\nabla}n \tag{2.15}$$

$$\vec{J_p} = q\mu_p p\vec{E} - qD_p\vec{\nabla}p \tag{2.16}$$

and the continuity equations are given by

$$\frac{\partial n}{\partial t} = G_n - U_n + \frac{1}{q}\nabla\cdot\vec{J_n} \tag{2.17}$$

$$\frac{\partial p}{\partial t} = G_p - U_p + \frac{1}{q}\nabla\cdot\vec{J_p} \tag{2.18}$$

where G_n and G_p are the electron and hole generation rate respectively, and U_n and U_p the recombination rates. D_n and D_p are diffusion coefficients which, in a non-degenerate semiconductor such as silicon used in MAPS, are related to the mobility via Einstein's

[1] The + sign indicates higher doping level.

relation $D_{n/p} = \frac{kT}{q}\mu_{n/p}$. From these equations the basic equations describing carrier motion can be derived. For simplicity, only the cases where $G_n = G_p = 0$ and $U_n = U_p = 0$ will be considered, i.e. the cases where there is no generation of carriers and where recombination rate is negligible w.r.t. the charge carrier motion time scale.

Combining equations 2.15 and 2.17 in a case without an electric field applied, the diffusion equation is obtained

$$\frac{\partial n}{\partial t} = D_n \nabla^2 n. \tag{2.19}$$

The well known solution is obtained with boundary conditios $n(\vec{r}, t) \to 0$ as $|\vec{r}| \to \pm\infty$ and initial condition $n(\vec{r}, 0) = \delta(\vec{r})$

$$n(\vec{r}, t) = \frac{1}{\sqrt{2\pi}\sigma(t)} \exp\left(-\frac{|\vec{r}|^2}{2\sigma(t)^2}\right), \quad \text{with } \sigma(t) = \sqrt{6D_n t}. \tag{2.20}$$

In case with a static electric field applied, the combination of equations 2.15 and 2.17 yields the drift-diffusion equation

$$\frac{\partial n}{\partial t} = D_n \nabla^2 n + \mu_n E \nabla n. \tag{2.21}$$

The solution is in the form of 2.20 but with $\vec{r}$ replaced by $(\vec{r} - \mu_n \vec{E} t)$, thus adding drift component. The drift velocity is given by

$$\vec{v_d} = \mu_n \vec{E}. \tag{2.22}$$

Carrier mobilities μ_n and μ_p depend on the magnitude of the electric field and temperature. For electric fields up to 10^3 V/cm mobilities of both electron and holes are constant [31].

2.1.3 Carrier lifetime, recombination and trapping

Electron-hole recombination is a process opposite to the e-h creation; the electron drops from the conduction band into the valence band with the emission of a photon. Since electrons and holes are required to have the exact energies in order for this to occur, this process is rare. In fact, theoretical calculations show that if this was the only recombination process, the charge carriers would have lifetimes in the order of a second which is in disagreement with experimental values (up to miliseconds) [30].

Impurities in Si crystal produce the so-called *recombination centres* which introduce additional energy levels between the valence and conduction bands. Then, an electron from the conduction band can be captured by a recombination centre and subsequently either

recombined with a captured hole or released after a certain time delay. Some impurities are capable of capturing only one charge carrier type. Therefore, a charge carrier is *trapped* and held before being released after a characteristic time.

The most common source of impurities is doping. The following empirical expression describes the relationship between doping concentration N_d and the carrier lifetime

$$\tau(N_d) = \frac{\tau_0}{1 + \frac{N_d}{N_{0d}}} \tag{2.23}$$

where τ_0 and N_{0d} are reference carrier lifetime and doping concentration [34].

2.1.4 Radiation damage

Two radiation damage mechanisms affect semiconductor detectors [26]:

- Non-ionising damage: Incident radiation displaces silicon atoms from their lattice sites. The resulting defects alter the electrical characteristics of the crystal.
- Ionising damage: Energy absorbed by ionization in insulating layers, usually SiO_2, liberates charge carriers, which diffuse or drift to other locations where they are trapped. This leads to unintended concentrations of charge and, as a consequence, parasitic electric fields.

2.1.4.1 Non-ionising radiation damage

Non-ionising radiation damage is linked to Non-Ionising Energy Loss (NIEL) which depends on the particle type and energy. NIEL is usually expressed as equivalent fluence of 1 MeV neutrons per square centimetre (1 MeV n_{eq} cm^{-2}).

Carrier lifetime Under neutron irradiation, the reciprocal of carrier lifetime in silicon increases proportionally to the fluence (Φ) up to neutron levels in the order of at least 10^{15} cm^{-2}. To account for bulk damage effects, the lifetime can be expressed as [35]:

$$\tau(N_d, \Phi) = \left[\frac{1}{\tau_0(N_d)} + \frac{\Phi}{K(N_d)}\right]^{-1} \tag{2.24}$$

where N_d is doping level, τ_0 is the carrier lifetime before irradiation and K is the silicon damage constant[1].

[1] $K \approx 2 \cdot 10^6$ s/cm^2 [36].

Doping characteristics Four processes are responsible for effective doping changes [33]: (1) removal of donors due to the formation of defect complexes containing donors, (2) removal of acceptors due to the formation of defect complexes containing acceptors, (3) creation of defect complexes assuming positive charge states in the space-charge region and (4) creation of defect complexes assuming negative charge states in the space-charge region. The following fluence dependence of the effective doping concentration is expected from an independent occurrence of these processes:

$$N_{eff} = N_{a0}e^{-c_a\Phi} - N_{d0}e^{-c_d\Phi} + b_a\Phi - b_d\Phi \tag{2.25}$$

where N_{a0} and N_{d0} are donor and acceptor concentrations before irradiation and c_a, c_d, b_a and b_d empirical constants. Effective doping concentration in a p-type silicon as a function of neutron fluence is shown in fig. 2.4.

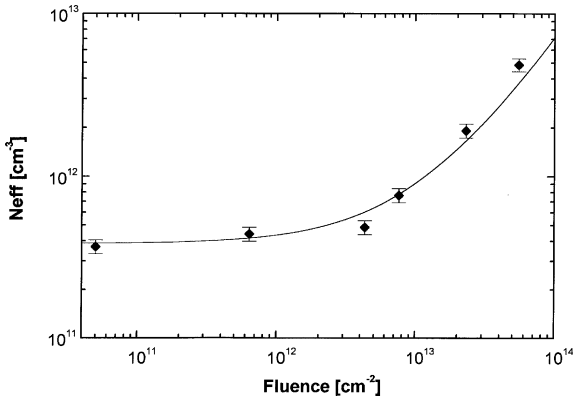

Figure 2.4: Effective doping concentration vs neutron fluence - Effective doping concentration in a p-type silicon as a function of neutron fluence[37]

Leakage current in p–n junctions Leakage current increase is proportional to the fluence Φ and is given by the following equation [38]:

$$\Delta I = \alpha A z \Phi \tag{2.26}$$

where α is a current damage factor, z is the thickness of the depleted region at the junction and A is the junction area.

2.1.4.2 Ionising radiation damage

The basic detector is insensitive to ionization effects. In the bulk, ionizing radiation creates electrons and holes that are swept from the sensitive volume; charge can flow freely through the external circuitry to restore equilibrium. A potential problem in case of MAPS lies in the integrated circuitry in particular MOS transistors; positive charge build-up due to hole trapping in the oxide and at the interface shifts the gate voltage required for a given operating point [26].

2.2 Energy deposit and charge generation in silicon

In this section, a brief, non exhaustive, overview of charge deposit mechanisms in silicon, relevant for this work, will be provided.

2.2.1 Energy loss of charged particles

Moderately relativistic charged particles other than electrons lose energy in matter primarily by ionization and atomic excitation. The mean rate of energy loss (or stopping power) is given by the Bethe-Bloch equation

$$-\frac{dE}{dx} = 4\pi N_A r_e^2 m_e c^2 z^2 \frac{Z}{A}\frac{1}{\beta^2}\left[\frac{1}{2}\ln\frac{2m_e c^2\beta^2\gamma^2 T_{\max}}{I^2} - \beta^2 - \frac{\delta}{2}\right] \tag{2.27}$$

with $T_{\max}$ the maximum kinetic energy which can be imparted to a free electron in a single collision, δ density effect correction and z particle charge.

The probability density function (PDF) describing the fluctuations in energy loss (energy straggling function) depends on the absorber thickness. For very thick absorbers, where the energy loss exceeds one half of the original energy, the straggling PDF begins to approximate a Gaussian. For thin silicon absorbers ($x > 300$ µm) energy straggling is well described by the Landau distribution. The Landau model fails to describe energy loss in ultra-thin silicon absorbers ($x < 160$ µm); the MPV is underestimated while the distribution's FWHM is overestimated [39].

A much better description of energy straggling in ultra-thin absorbers is given by "Bichsel functions" [40] (see fig. 2.5a). Bichsel's calculations indicate that the most probable energy loss increases, in first approximations, as $x(a + \ln x)$ and the ratio of FWHM and MPV decreases as absorber thickness x increases, shown in fig. 2.5b. An important point to note is that the most probable energy loss is significantly lower than the usually

quoted [26, 30] value of 80 eV/µm. In fact, for sensitive layer thickness of 20-30 µm, as in MAPS, the most probable energy loss is around 60 eV/µm.

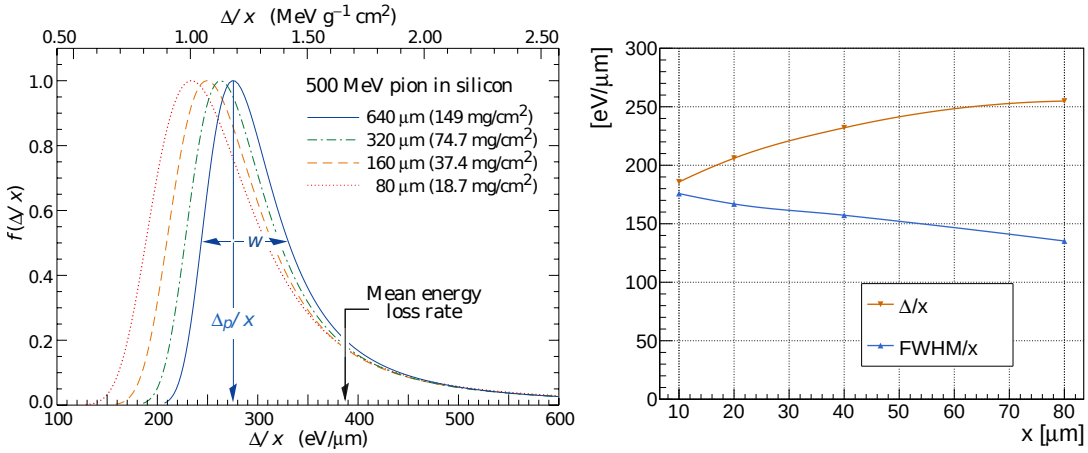

(a) Straggling functions in silicon [39]. **(b)** MPV and FWHM vs. x [40]

Figure 2.5: Energy straggling in ultra-thin absorbers - **(a)** Straggling functions in silicon for 500 MeV pions, normalized to unity at the most probable value Δ_p/x. The width w is the FWHM. **(b)** Most probable energy loss and FWHM as a function of absorber thickness for all particles with $\beta\gamma > 100$.

2.2.2 Energy loss of electromagnetic radiation

The most important processes photons undergo when interacting with matter are the photoelectric effect, Compton (incoherent) scattering, and pair production [30]. The cross sections for theses three interaction processes are shown in figure 2.6.

Photoelectric effect involves the absorption of a photon by an atomic electron with the subsequent ejection of the electron from the atom. The energy of the outgoing electron is then $E = h\nu - E_0$ where E_0 is the binding energy of the electron. An incident photon beam undergoing photoelectric absorption in material is attenuated according to

$$I(x) = I_0 e^{-\mu x} \tag{2.28}$$

where I_0 is the intensity before traversing the material with absorption coefficient μ and thickness x.

Compton scattering is the inelastic scattering of photons on free electrons. In matter, of course, the electrons are bound; however, if the photon energy is high with respect

to the binding energy, the binding energy can be ignored and the electrons can be considered as essentially free.

Pair production involves the transformation of a photon into an electron-positron pair. In order to conserve momentum, this can only occur in the presence of a third body, usually a nucleus. Moreover, to create the pair, the photon must have at least an energy of $2m_e c^2$.

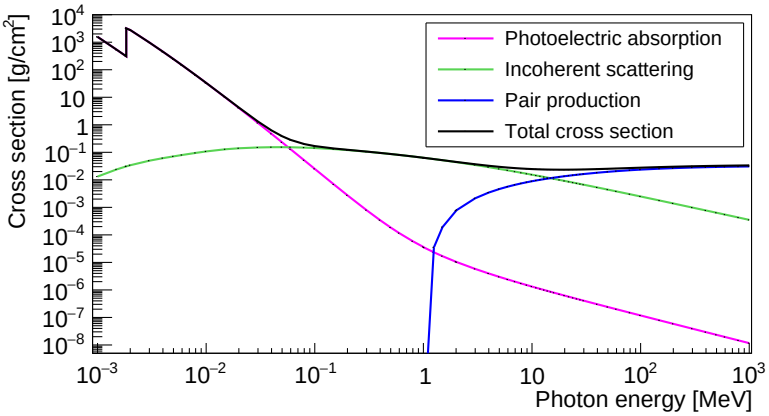

Figure 2.6: Photon cross section in silicon - Total photon cross section in silicon [41].

2.2.2.1 ^{55}Fe X-ray source

In characterisation of MAPS, a ^{55}Fe source is commonly used since the emitted X-rays deposit an amount of charge similar to that of an minimum ionising particle orthogonally incident to the MAPS sensitive volume. Hence, a description of the ^{55}Fe source follows.

$^{55}_{26}\mathrm{Fe}_{29}$ disintegrates by electron capture with half life of $T_{1/2} = 2.747$ y. Particles produced by its decay[1], along with their energies and rates normalized to 100 disintegrations are reported in table 2.1.

A 5-6 keV electron has a range of ~ 2.9 g/cm^2 [43] in air, that is 2.4 mm which is smaller than the distance between the ^{55}Fe source and the detector (≈ 2 cm in this work). The emission probability of a 126 keV γ-ray is eight orders of magnitude lower than the emissions of X-rays, therefore its contribution to the measured spectrum is negligible.

Attenuation coefficients in air for 1.0, 5.9 and 6.5 keV X-rays are 3.6×10^3, 23.7 and 17.7 cm^2/g respectively [41]. For distances between the source and detector of about few

[1]The X-rays and Auger electrons are produced by outer electrons replacing the captured inner electron.

	Energy (keV)	Emissions per 100 disint.
Auger electrons	0.47 - 0.67	140.2 (8)
	4.95 - 6.53	60.1 (5)
X-rays	0.56 - 0.72	0.524 (21)
	5.888	8.45 (14)
	5.899	16.57 (27)
	6.490	3.40 (7)
	6.535	
γ	125.959	1.3 (1) $\times 10^{-7}$

Table 2.1: ^{55}Fe emissions [42]. Numbers in parenthesis are errors on the last digit(s) of the preceding value.

centimetres, all emitted X-rays can reach the detector, but the flux of the X-rays with the lowest energies (< 1 keV) is negligible.

The main interaction process for soft X-rays is the photoelectric absorption; its cross-section is four orders of magnitude higher than that of the incoherent scattering [41]. The electron emitted by the photoelectric absorption event generates electron-hole (e-h) pairs along its path (the range of a 6 keV electron in silicon is $\lesssim 1$ µm [44]). An average energy of 3.6 eV is required to produce an e-h pair. Therefore 5.9 and 6.5 keV photoelectrons create on the average ≈ 1640 and ≈ 1800 e-h pairs, respectively. The intrinsic energy resolution is given by $R = 2.35\sqrt{\frac{Fw}{E}}$ where F is the Fano factor in silicon ($F \approx 0.116$ for 5.895 keV [45]), w the energy required to excite an e-h pair and E the energy deposited by a photoelectron. Thus $R \approx 2\%$ (≈ 120 eV) for energies between 5.9 and 6.5 keV and therefore 5.888 and 5.899 keV (6.490 and 6.535 keV) X-rays can't be resolved.

In conclusion, it is expected to observe only two peaks from the photoelectric absorption of 5.9 and 6.5 keV photons in silicon.

2.3 Principles of operation of MAPS

A typical monolithic active pixel sensor developed for use in high energy physics experiments consists of three layers (see fig. 2.7): a highly p-doped (p^{++}) substrate which acts as mechanical support, a thin (few tens of µm) p^- epitaxial layer that is used as sensitive volume, and n-type and p-type implants on top of the epitaxial layer called *wells*. N-type implants act as collecting diodes for electrons (see sec. 2.1.1.1) while p-wells host

the circuitry. On top of the implants (see fig. 2.8), there are metal layers forming the in-pixel circuitry, and propagating the signal and bias from the chip periphery. Most of the modern MAPS are produced on high-resistivity ($\rho > 1$ kΩcm) epitaxial layer[1].

A small voltage[2] is applied to the diode resulting in an increased depleted region, however most of the epitaxial layer remains undepleted. It is possible to further increase the depleted region by applying a negative (reverse) bias voltage (see eq. 2.10) to the diode via the substrate, indicated by V_{BB}[3] in fig. 2.7.

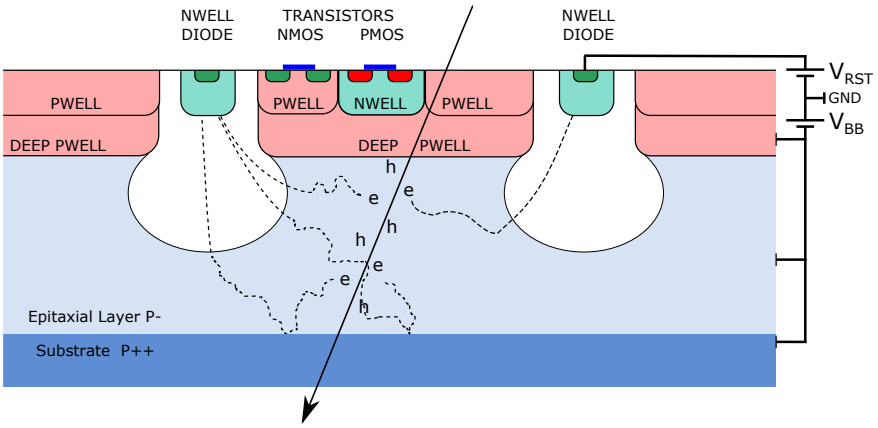

Figure 2.7: MAPS cross section - The arrow represents a charged particle passing trough the detector and wobbling lines represent excited electrons. Not to scale. [48]

Figure 2.9 shows a schematic cross section of a single pixel cell. In the middle there is a collection diode surrounded by readout circuitry. This structure is repeated in both dimensions creating a pixel matrix. Some circuits that operate only on n-type silicon bulk (e.g. PMOS transistors) must be isolated from the epitaxial layer since n-wells containing them can also collect electrons. This is done by implementing a deep p-well[4] underneath an n-well (see fig. 2.7).

A charged particle passing trough the silicon detector loses energy due to ionisation, creating e-h pairs along its path. In first approximation, electrons created in the epitaxial

[1]Roughly, doping levels of MAPS for the ALICE ITS upgrade are $N_{A,sub} \approx 10^{18}$ cm^{-3}, $N_{A,epi} \approx 10^{13}$ cm^{-3} and $N_{A,pwell} \approx 10^{18}$ cm^{-3} for the substrate, epitaxial and p-wells respectively, and $N_{D,nwell} \approx 10^{18}$ cm^{-3} for the n-wells.

[2]In case of MAPS for the ALICE ITS upgrade the applied voltage is up to 1.8 V [46].

[3]For ALICE ITS upgrade MAPS, the maximum applicable V_{BB} is -8 V. Above this voltage, breakdowns of reversely biased p–n junctions occur. To ensure a safe operation, measurements have only been performed to a V_{BB} up to -6 V [47].

[4]A feature of TowerJazz 180 nm CMOS process [49].

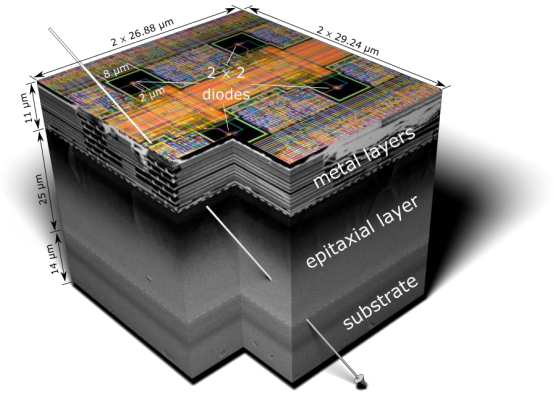

Figure 2.8: MAPS 3D cross section - A matrix of 2 × 2 pixels belonging to the ALPIDE chip.

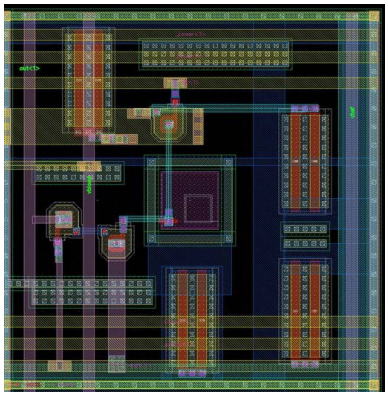

Figure 2.9: MAPS pixel cell layout - Collection diode in the centre surrounded by basic readout circuitry.

layer are trapped there since the p^-–p^{++} and p^-–p-well junctions act as reflective barriers (see sec. 2.1.1.2). Therefore, electrons diffuse thermally in the epitaxial layer until they reach a depleted region (where they are collected) or until they are recombined (negligible in non-irradiated sensor). Electrons created in the p-wells or in the substrate, which thermally diffuse into the epitaxial layer (electrons can pass through p–p^+ junction in one direction) are also collected. Electrons lifetime depends on doping concentration (see sec. 2.1.3) and is $\sim$ 50 ns[1] and $>$ 100 µs[2] in the substrate and epitaxial layer respectively. This description will be addressed in detail in ch. 6, where it will be argued that not all electrons generated in region defined as epitaxial layer are trapped there but can also migrate to the substrate.

MAPS can provide excellent spatial resolution even at high occupancies due to a small pixel size ($\sim 30 \times 30$ µm^2). About 1500 e-h pairs are generated by a traversing MIP in 25 µm epitaxial layer, which is an order magnitude lower than in a common $\sim$ 300 µm thick silicon detector. This means that the energy resolution is lower and consequently particle identification capabilities are limited.

2.3.1 Signal formation

Signal formation in MAPS depends on the pixel input capacitance C_p formed by the junction capacitance of the collection diode C_j and the parasitic capacitance of the in-

[1]Given the doping concentration of $\sim 10^{18}$ cm^{-3}. See sections 2.1.3 and 6.1.2.
[2]Given the doping concentration of $\sim 10^{13}$ cm^{-3} [50].

pixel readout circuit C_r. A reset potential is applied to charge the input capacitance to operational level. A charge collection discharges the capacitance thus causing a voltage drop

$$\Delta V = \frac{Q_{coll}}{C_p} \tag{2.29}$$

where Q_{coll} is the amount of collected charge. In order to maximise the signal ΔV, the input capacitance has to be as low as possible. This can be achieved by optimising the readout circuit to minimise C_r. The C_j can be reduced by applying a reverse bias to the collection diode (see eq. 2.13) and by selecting an appropriate geometry of the diode.

2.3.2 Design parameters

When designing a monolithic pixel sensor, there is a number of parameters that influence the charge collection properties and overall detection performance. The most obvious is the **pixel pitch** which ideally should be as small as possible. However, this is limited by the size of the in-pixel circuitry and the readout rate.

The collection diode geometry (see fig. 2.10) i.e. **n-well size (diameter)** and **spacing** from the surrounding p-well have impact on the diode capacitance. In fact, the eq. 2.13 for the planar junction shows that the capacitance increases with the junction (diode) area. On the other hand, larger n-well size provides a larger depletion region and thus more collected charge. This is the simplest example of the entire design effort, which aims to optimise the Q/C ratio i.e. the ratio of collected charge and diode capacitance (see sec. 2.3.1). Thus, smaller n-well size will yield a smaller capacitance but also smaller collected charge, so the optimal value will has to be empirically determined (see ch. 3).

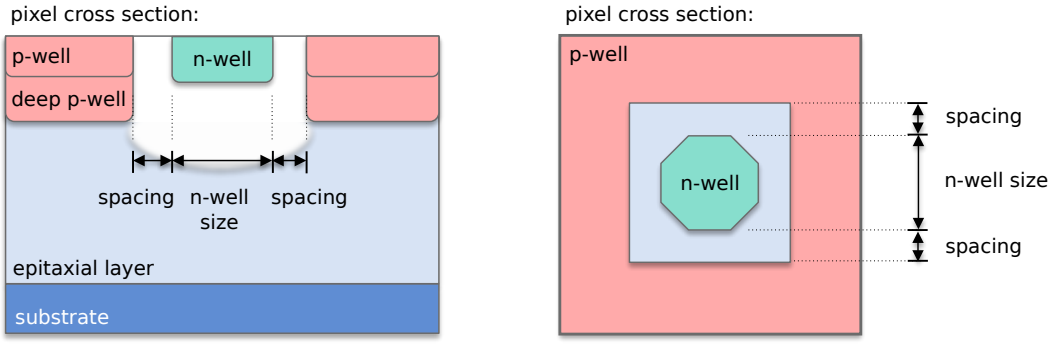

Figure 2.10: Collection diode geometry - Cross section and top view. The collection n-well in ITS upgrade MAPS has an octagonal shape. Not to scale.

Increasing the **epitaxial layer thickness** increases the amount of charge deposited by an ionising particle, but if most of the epitaxial layer is undepleted, the charge is collected primarily by diffusion which can lead to lower charge collection efficiency and reduced radiation hardness. To further increase the depletion the **doping concentration** of the epitaxial layer should be kept as low as possible (see eq. 2.9).

The doping profiles of ITS upgrade wafers (used for the prototypes production) with different epitaxial layer thicknesses are shown in fig. 2.11. It can be observed that the doping concentration between the epitaxial layer and the substrate changes gradually. This affects the epitaxial layer thickness, which is lower than nominal. The effect of this doping profile will be discussed in detail in section 6.2.2.

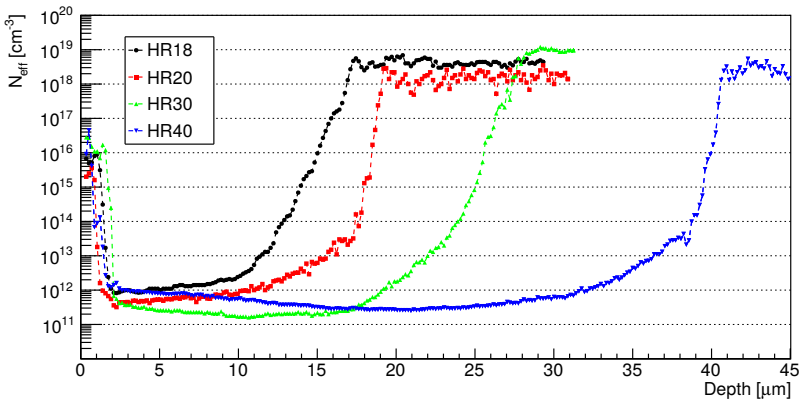

Figure 2.11: Doping profile of ALICE ITS upgrade sensors epitaxial layer - Effective doping concentration profiles as estimated from a Spreading Resistance Profiling (SRP) measurement of the resistivity [47]. Data are presented for various wafers types used within the ITS upgrade pixel chip R&D. The nominal epitaxial layer thicknesses are 18 µm (HR18), 20 µm (HR20), 30 µm (HR30) and 40 µm (HR40). Data points for $N_{\text{eff}} < 10^{13}$ cm^{-3} not calibrated.

2.4 Observables in MAPS data analysis

MAPS can be classified as analogue and binary. The former are sensors in which the information on the amount of the collected charge by each pixel is read-out, while in case of the latter only whether the collected charge is higher than a previously set threshold (1) or not (0) is registered. In the following, the common observables and methods used in the following chapters for the analysis of MAPS response are summarised.

Cluster is a set of adjacent pixels which collected an amount of charge higher than a certain **threshold**. In case of analogue sensors the threshold is set during the data analysis, and is the same for all pixels (in this work 100 e^- unless stated otherwise). In case of binary sensors the threshold is active online, during the data taking (comparator is on-chip or in-pixel), and is characterised by pixel-to-pixel variations[1].

Cluster size or **multiplicity** is the number of pixels in a cluster.

Cluster shape ID is a numerical identifier associated to a unique cluster shape. Cluster shapes for ID ranging from 0 to 15 are shown in figure 2.12.

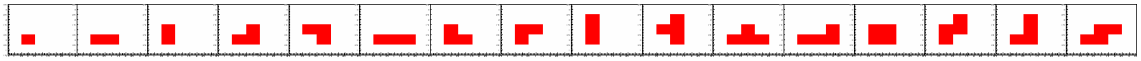

Figure 2.12: Cluster shape ID - First 16 cluster shaped IDs.

Cluster centre of mass is defined as

$$(x_{CM}, y_{CM}) = \frac{\sum_i s_i \cdot (x_i, y_i)}{\sum_i s_i} \tag{2.30}$$

where x_i and y_i are position of i-th pixel in the cluster and s_i is the i-th pixel signal (in case of binary sensor $s_i = 1$).

The following observables are exclusive to the analysis of the analogue sensors response:

Seed pixel is a pixel with the largest collected charge in a cluster.

Seed signal is the charge collected by the seed pixel.

Cluster signal is the sum of charge collected by all pixels in a cluster.

Matrix signal is the sum of charge collected by all pixel in a $N \times N$ matrix[2] centred on the seed signal. Difference w.r.t. the cluster signal is that matrix signal also contains charge collected by pixels with signal below threshold. On the downside, it also contains noise of all $N \times N$ pixels.

[1] These variations are often referred to as fixed pattern noise (FPN). See sec. 4.2.1.
[2] Typically 3×3 in this work, unless stated otherwise.

2.4.1 Plots and observables in ^{55}Fe analysis

The observed signal distribution of the ^{55}Fe source (see sec. 2.2.2.1) depends on the geometry of the detector. Three primary regions for the photoelectric conversion can be identified[1] (numbered accordingly in figure 2.13):

1) **Depleted region** (high electric field region) - since the range of the photoelectron is $\lesssim 1$ µm, it is possible that all the e-h pairs are created inside the depleted region and therefore collected by a single pixel.

2) **Undepleted epitaxial layer** (low or no electric field region) - electrons remain trapped in the epitaxial layer and diffuse thermally until they reach a depleted region (or until they recombine) and are collected by the n-well diodes. Therefore the deposited charge is shared between several pixels.

3) **Substrate** - electrons diffuse thermally in the substrate. Because of the potential difference between p^{++} and p^{-} type silicon (see sec. 2.1.1.2), those electrons which reach the epitaxial layer are trapped there and eventually collected.

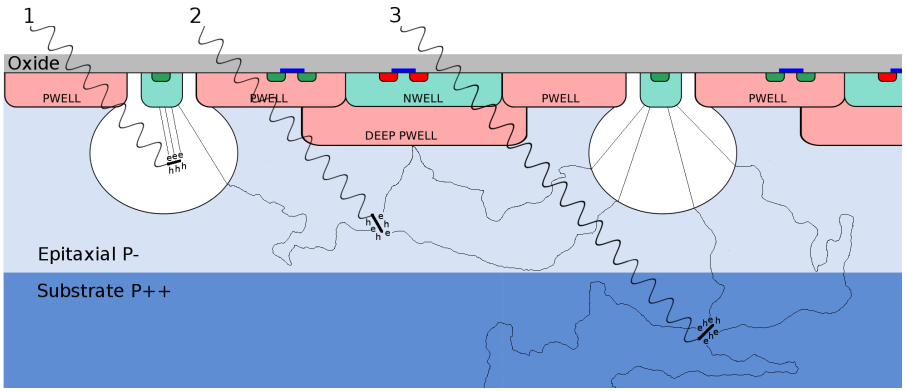

Figure 2.13: Photoelectric absorption in MAPS - The three main regions for the photoelectric conversion. Waves represent photons, straight lines photoelectrons, and wobbling lines motion of excited electrons. Not to scale.

In the first two cases, the entire charge deposited by the photoelectron is expected to be collected. In the third case the amount of collected charge depends on the depth of the photoelectric conversion and the carrier lifetime in the substrate, and is generally smaller than the deposited charge. The resulting spectrum is a continuous distribution up to the

[1] For a detailed study of MAPS response to ^{55}Fe X-rays see ch. 6 and [51].

6.5 keV peak. Photoelectric conversions in other regions, e.g. circuitry, also contribute to this spectrum.

Detector geometry and charge collection characteristics are reflected in seed and matrix signal distributions in figure 2.14. In the seed signal spectrum three peaks can be observed; the peaks at 1640 e^- and 1800 e^- correspond to the conversions of 5.9 and 6.5 keV X-rays in the depleted region (region #1) while the peak around 800 e^- matches the photoelectric conversions in region #2. The peak at 1640 e^- is often referred as **calibration peak** since it is clearly distinguished and its position can be used to calibrate the sensor response in electrons (see sec. 3.1.3). The "peak" at 800 e^- will be referred to as **charge sharing peak** since the number of events and position of this peak depend and the charge sharing characteristics of the pixel matrix. The relative number of events in the calibration peak w.r.t. the charge sharing peak indicates the fraction of the depleted volume and therefore the strength and the spatial extension of the electric field; more prominent is the calibration peak, more spatially extended is the electric field.

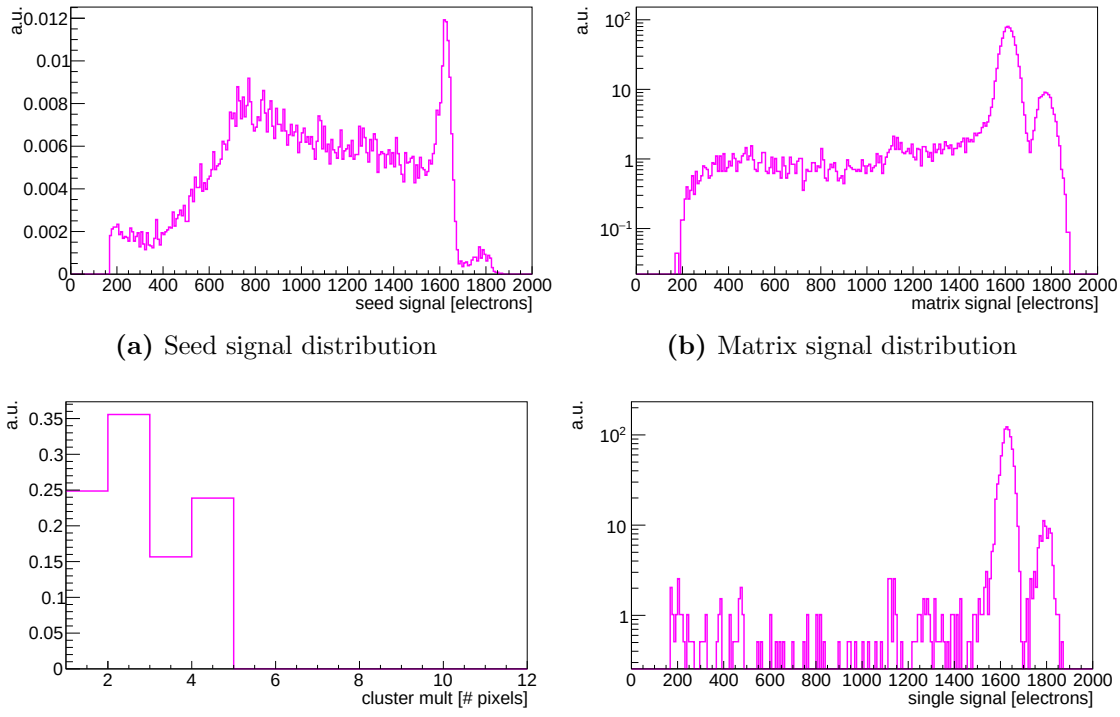

(a) Seed signal distribution

(b) Matrix signal distribution

(c) Cluster size distribution

(d) Single pixel cluster signal distribution

Figure 2.14: Typical plots in ^{55}Fe analysis - Seed signal (the spectrum ends at $\sim$ 300 e^- due to triggering threshold), matrix signal, cluster size and single pixel cluster signal.

The matrix signal is characterised by two peaks and a long tail. The peaks correspond to photoelectric conversion in the epitaxial layer (regions #1 and #2) while the tail corresponds to the conversions in the substrate (region #3).

The other two plots in figure 2.14 show the cluster size distribution and the seed signal distribution of single pixel clusters (clusters with only seed pixel collecting charge)[1]. The latter is a subset of seed signal distribution, corresponding to photons converted in the high electric field region.

Another instructive plot, the seed signal distribution with separated contributions of clusters with different sizes, is shown in figure 2.15. Besides the clearly distinctive peaks corresponding to conversions in regions #1 and #2, which are equally visible in the standard seed signal distribution, the contribution from the substrate (region #3) is also evident as seed signal for cluster size ≤ 2 in range from ~ 300 to ~ 700 e^- (black and red in the figure). In fact, the minimum possible seed signal for a certain cluster size, assuming all charge is collected, can be roughly modelled as[2]

$$s_{\min}(cs) = \frac{Q - T \cdot (cs_{\max} - cs)}{cs} \tag{2.31}$$

where cs is the cluster size, $cs_{\max}$ the maximum cluster size (in this case 4, see fig. 2.14), T the threshold (100 e^-), and Q the deposited charge (1640 e^-). This gives minimum seed signals of approximately 1300, 700, 500, and 400 e^- for cluster with size 1, 2, 3, and 4, respectively[3]. Therefore, the seed signal from ~ 300 to ~ 700 e^- with cluster size 1 and 2 cannot be associated with conversions in the epitaxial but matches those in the substrate.

2.4.2 Observables in test-beam analysis

A typical test-beam setup consists of a DUT sandwiched by tracking planes and positioned orthogonally to the beam of ionising particles, as shown in figure 2.16. The number and position of tracking planes can vary, but are optimised in order to achieve the best tracking resolution. Tracking planes can be omitted if the goal is to measure only energy deposit of the ionising particles. However, the main reason for a test beam measurement is to determine the detection efficiency and the spatial resolution of a sensor.

[1] A hard cut of having signal < 0 is imposed on neighbouring pixels to select single pixel clusters.

[2] Certainly, this is a very empirical and qualitative approach but the goal here is not a precise method for calculating the minimum seed signal, and this coarse approach doesn't change the conclusions.

[3] The implicit assumption here is that all charge generated in the epitaxial layer is eventually collected.

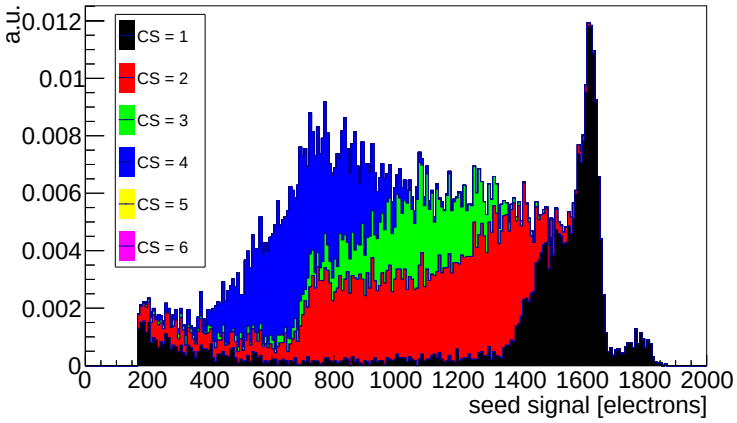

Figure 2.15: Typical plot in ^{55}Fe analysis - Seed signal distribution as a function of cluster size (indicated by different colours).

The test-beam data acquisition and analysis, described in this work, were based on `EUDAQ` and `EUTelescope` frameworks, respectively [48, 52, 53]. The tracks through the tracking planes were reconstructed using a broken-line fit that considers multiple-scattering effects in all the planes.

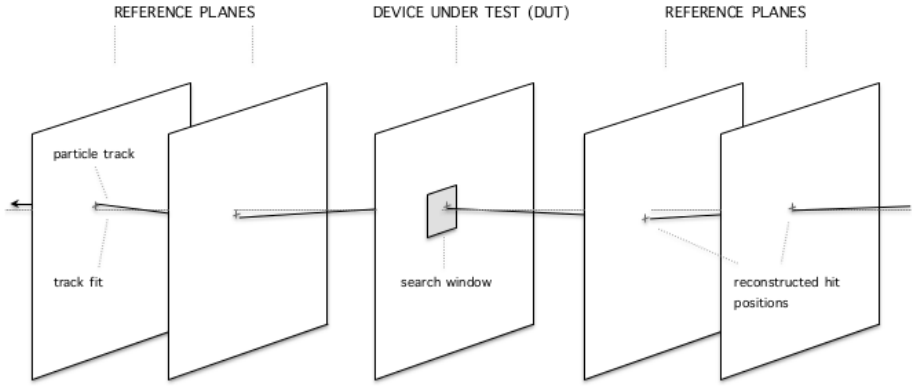

Figure 2.16: Example of a test-beam setup - DUT and four tracking planes; two downstream and two upstream.

To calculate the **detection efficiency**, a search window (see fig. 2.16) around the intersection point between the DUT and the reconstructed track is considered; if a hit is found within the search window the track is counted as efficient. The detection efficiency is defined as

$$\varepsilon = \frac{k}{n} \tag{2.32}$$

where k is the number of efficient tracks and n is total number of tracks. The variance is

determined from[1]

$$\sigma_{\bar{\varepsilon}}^2 = \frac{(k+1)(k+2)}{(n+2)(n+3)} - \frac{(k+1)^2}{(n+2)^2} \tag{2.33}$$

The choice of the search window size is based on the experimental setup and particle beam energy and type; in a situation with higher multiple scattering, the search window size is increased.

The **spatial resolution** is determined by calculating the variance σ_{res}^2 of the residual distribution, i.e. the differences between the reconstructed hit position and the extrapolated track intersection point at the DUT. The spatial resolution is then estimated as

$$\sigma_{sp}^2 = \sigma_{res}^2 - \sigma_{track}^2, \tag{2.34}$$

Where the track resolution σ_{track} depends on the intrinsic resolution of the tracking planes and physical uncertainties such as multiple scattering and therefore it is experimental setup specific.

Typically, the detection efficiency and spatial resolution are plotted as a function of charge threshold, as shown in fig. 2.17. The 99% efficiency and 5 µm resolution are marked with dashed lines to indicate the ITS upgrade requirements (see table 1.3). The main purpose of these two plots is determining the operational margins of a sensor.

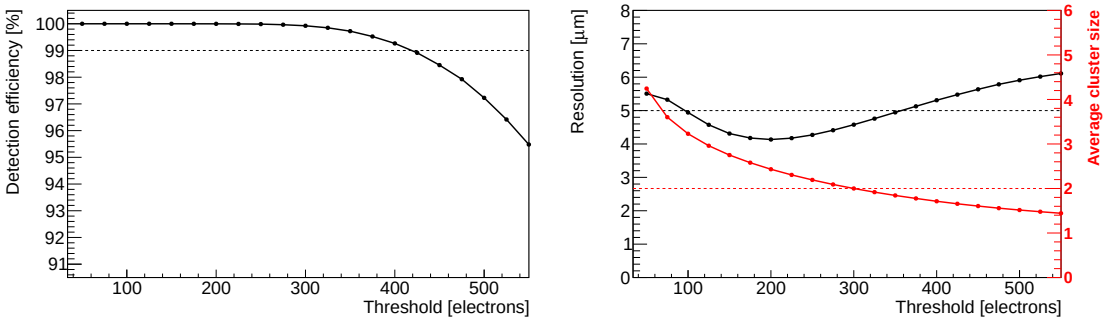

(a) Detection efficiency **(b)** Spatial resolution and average cluster size

Figure 2.17: Examples of detection efficiency and spatial resolution as a function of charge threshold - Simulated detection efficiency, spatial resolution and average cluster size plotted as a function of threshold. The ITS upgrade requires sensors to operate with 99% efficiency and spatial resolution better than 5 (10) µm (see table 1.3), therefore these plots are crucial in determining the operational range of a sensor.

[1] Actually, if the efficiency distribution is considered, eq. 2.32 is the mode. while $\bar{\varepsilon} = (k+1)/(n+2)$ is the mean. Thus uncertainty interval is $\langle \bar{\varepsilon} - \sigma, \bar{\varepsilon} + \sigma \rangle$, yielding asymmetrical error bars on the efficiency estimate $\varepsilon^{+\sigma+\bar{\varepsilon}-\varepsilon}_{-\sigma+\bar{\varepsilon}-\varepsilon}$. For more details see [54].

3

INVESTIGATOR – A MAPS for the study of design parameters

The performance of a monolithic active pixel sensor (MAPS) depends on a large number of design parameters, such as pixel size, collection diode geometry, epitaxial layer thickness and doping concentration, etc (see sec. 2.3.2). The choice of the parameter values is driven by the maximisation of the ratio of the collected charge and the pixel input capacitance, i.e. Q_{coll}/C_p ratio (see sec. 2.3.1).

In order to determine the optimal parameter values for the MAPS for the ALICE ITS upgrade, the INVESTIGATOR chip was developed [47, 55]. It contains 134 pixel matrices with different pixel pitches ranging from 20 µm to 50 µm, collection diode geometries, reset mechanisms, deep p-well coverages and input transistor configurations. The sensor was produced on wafers with different epitaxial layer thicknesses (18, 25 and 30 µm). A reverse bias up to −6 V can be applied to the collection diode via the substrate. In total, there are over 1600 design and operational parameter combinations, considering four typically tested reverse bias voltages (0 V, −1 V, −3 V and −6 V).

In this chapter, only a part of the parameter phase space, most relevant for the MAPS for the ITS upgrade (see ch. 4) and for the simulation (see ch. 6), will be explored. Therefore, only matrices with 28×28 µm^2 pixel size with active (PMOS) reset and maximum p-well coverage will be tested. The unconstrained parameters studied in this chapter are the spacing and the n-well size (see sec. 3.2.3), as well as the epitaxial layer thickness (see sec. 3.2.2) and the reverse bias voltage (see sec. 3.2.1).

MM identifier	Pixel pitch (µm)	# of MM (per pitch)
0-35	20	36
36-57	22	22
58-67	25	10
68-103	28	36
104-111	30	8
112-123	40	12
124-133	50	10

Table 3.1: Mini-matrix identifier numbers and quantity sorted by pixel pitch.

3.1 Chip overview

INVESTIGATOR is a prototype chip produced using TowerJazz 0.18 µm CMOS process [49] on wafers with a high-resistivity epitaxial layer with thicknesses of 18 µm, 25 µm, and 30 µm. The chip consists of 134 *mini-matrices* (MM) with the pixel pitch ranging from 20 µm to 50 µm (see fig. 3.1 and tab. 3.1). Each of the mini-matrices contains 10×10 pixels, of which only the central 8×8 are read out, while those in the outermost crowns are implemented to reduce edge effects in the mini-matrix. The results presented in this chapter are obtained using MMs with 28 µm pitch, which is the pixel size most similar to the one present in the ALPIDE (see ch. 4).

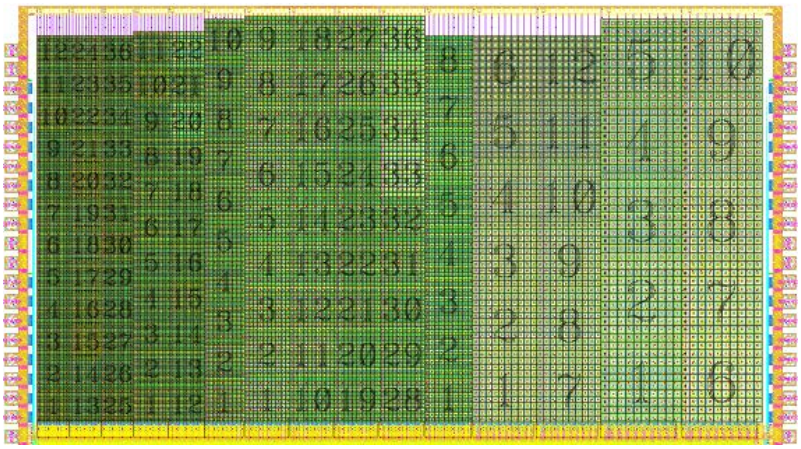

Figure 3.1: INVESTIGATOR layout - There are 134 mini-matrices of 10×10 pixels organised according to the pixel pitch, ranging from 20 µm to 50 µm (see tab. 3.1).

INVESTIGATOR is equipped with 64 channel analogue parallel readout, allowing to read out one entire MM at a time. A simplified schematic in fig. 3.2 shows the pixel circuit

with active (PMOS) reset, the column circuit and the output buffer circuit. There are four other variants of the pixel circuit, including a diode reset and different implementations of the source follower (`M1`). Principle of operation of the pixel circuit is discussed in the next section.

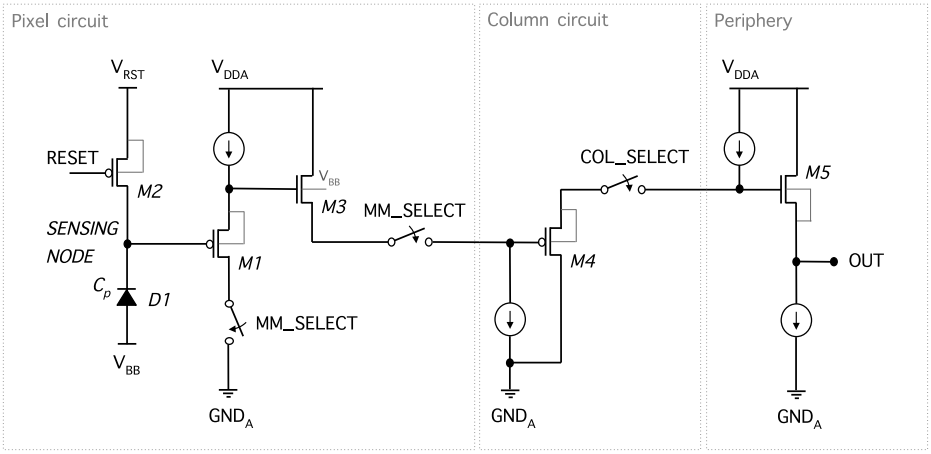

Figure 3.2: Simplified schematic of the INVESTIGATOR chip - Pixel circuit with active (PMOS) reset, column circuit and output buffer circuit. [47]

The TowerJazz process features the possibility to implant n-wells on top of deep p-wells (see fig. 2.7) and thus separate all n-wells, except for the collection n-wells, from the active volume i.e. the epitaxial layer. Therefore, it is possible to implement PMOS reset (`M2`) and source follower (`M1`) transistors inside the pixels. There are three MM variants considering the pixel area covered by deep p-wells; pixels with minimum coverage have only strictly necessary surface covered by deep p-wells, those with maximum coverage have the entire surface covered, except for the collection diode and the spacing, and last pixel variant is in-between the two. All mini-matrices used in this work have maximum deep p-well coverage[1].

A reverse substrate bias voltage (V_{BB}) can be applied to the collection diodes via the substrate (see sec. 3.2.1). The maximum applicable reverse bias voltage is -8 V. To ensure a safe operation, the largest V_{BB} applied was -6 V. The measurements were also performed at -3 V, -1 V and 0 V revere bias.

[1]This choice is motivated by the deep p-well coverage in the ALPIDE (see ch. 4), which is also maximal to allow for the extensive and complex in-pixel circuitry.

3.1.1 Principle of operation

The source follower (SF) transistor (`M1`) in fig. 3.2 acts as a buffer which isolates the sensing diode from the readout circuit. The SF gain g_S is $\lesssim 1$ and the output voltage is proportional to the input voltage ($V_{out} = g_s V_{in}$).

Initially, the collection diode is set to a potential V_1. Thus, the input capacitance C_p (see sec. 2.3.1) is charged to $Q_1 = C_p V_1$. A particle passing through the sensor deposits charge in the epitaxial layer and the diode collects a certain amount Q_{coll}. This charge is subtracted from the input capacitance which is discharged to $Q_2 = Q_1 - Q_{coll}$, resulting in the potential drop on the SF gate $V_2 = Q_2/C_p$. The pixel output voltage before and after the charge collection is $V_{out_1} = g_S V_1$ and $V_{out_2} = g_S V_2$, where g_S is the SF gain, and the potential drop is:

$$\Delta V_{out} = g_S V_1 - g_S V_2 = g_S \frac{(Q_1 - Q_2)}{C_p} = g_S \frac{Q_{coll}}{C_p}. \tag{3.1}$$

The output voltage difference is therefore ideally also proportional to the collected charge.

Two processes are responsible for the discharge of the sensing diode: leakage current and collection of charge (deposited by a particle). The former is a small effect that can be considered constant per unit of time while the latter is a short pulse, large respect to the leakage current. Since both mechanisms discharge the collection diode, at times a potential must be applied to the sensing node to restore the original conditions. This is done by switching the reset transistor (`M3`), so the collection diode gets in contact with the reset potential V_{RST}. This is called *reset phase*. If the reset phase is long enough to fully charge of the input capacitance, the input node will have potential $V(t_0) = V_{RST}$, where t_0 is the time at which `M3` is switched off. Otherwise, the input node will have potential $V(t_0) < V_{RST}$. Figure 3.3 shows $V(t)$, the variation in time of the potential at the gate of `M1` transistor. After the reset phase, $V(t_0) = V_{RST}$ and discharges slowly due to leakage current until the next reset phase when the potential is again brought to V_{RST}. The collection of charge deposited by an ionising particle is observed as a fast potential drop.

3.1.2 Signal sampling and calculation

The measurements with the INVESTIGATOR were performed using the INVROS readout system [47]. It features 64 14-bit ADCs with 65 MHz sampling rate, allowing to read out

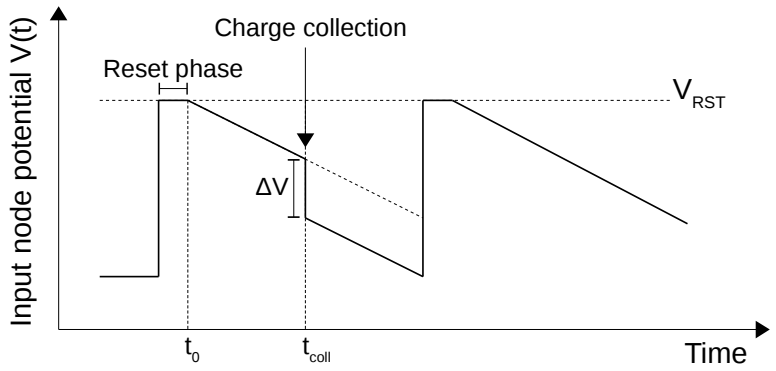

Figure 3.3: Input node potential as a function of time - During the reset phase the input node potential is brought to V_{RST}. A charge collection discharges the input capacitance which is observed as a potential drop ΔV.

all pixels in a MM in parallel. The pixel output is continuously sampled; a potential drop between two samples in any of the 64 channels, higher than defined trigger threshold, starts a readout of N samples for all of the 64 channels, with M samples before the triggering sample and $N - M$ samples after (see fig. 3.4). Triggering is disabled during and immediately after the reset phase to avoid potential reset related distortions. In fact, the trigger acceptance window is selected so that the N recorded samples do not contain any samples from the reset phase.

The signal of a pixel ΔV (see fig. 3.4) is calculated as the difference between the pixel baseline before (V_B) and after (V_A) the triggering sample. V_B is defined as the average over N_B samples d_B samples before the triggering sample, while V_A is defined as the average over N_A samples d_A samples after the triggering sample. Consequently, pixel signals are clusterised (see sec. 2.4) for further analysis.

3.1.3 Output voltage to charge calibration

The pixel signal is measured in volts[1], however it often useful to represent pixel signal in collected charge i.e. electrons. The main advantage of the charge calibration is that measured signal is decoupled from the input capacitance (see sec. 2.3.1) which varies with the collection diode geometry and the reverse bias.

To calibrate the output voltage to the collected charge, an ^{55}Fe source is used. ^{55}Fe emits two X-rays with energies of 5.9 keV and 6.5 keV which, by photoelectric conversion,

[1]More precisely, pixel signal is measured in ADC counts. Calibration of the INVROS provides the conversion to volts.

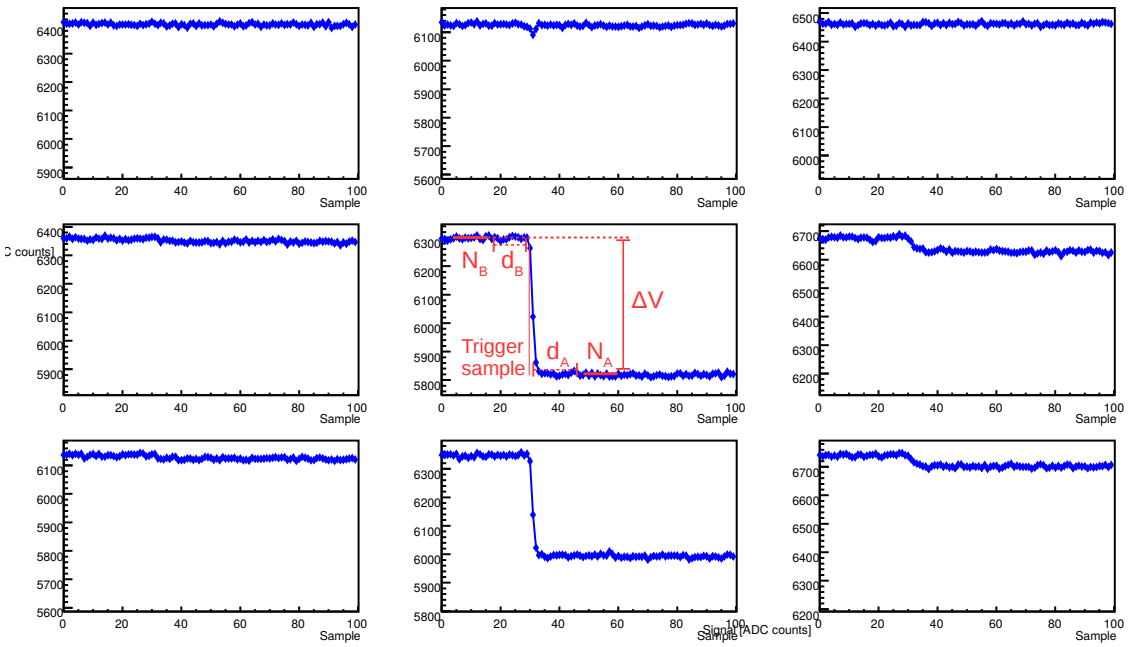

Figure 3.4: Example of an INVESTIGATOR event - Sampled output of a 3×3 sub-matrix.

deposit 1640 and 1800 electrons in silicon, respectively (see sec. 2.2.2.1). It is assumed that photoelectric conversions in the high electric field (depleted) region directly below collection diodes will result in clusters where only the seed pixel collects charge. Consequently, the seed pixel signal of these events corresponds to a known charge deposit.

The seed signal distribution of single pixel clusters (see sec. 2.4) is shown in fig. 3.5. The two peaks visible in the distribution correspond to the two ^{55}Fe X-rays converted in the depleted part of the epitaxial layer while the tail corresponds to conversions in the substrate (see sections 2.4.1 and 6.2). The peak corresponding to 5.9 keV X-ray is fitted with a Gaussian distribution $\mathcal{N}(\mu, \sigma)$. The fit interval corresponds to $\langle \mu - 2\sigma, \mu + 2\sigma \rangle$. The signal to charge conversion factor is calculated as

$$f_e = \frac{1640 \text{ e}^-}{\mu}. \tag{3.2}$$

Finally, the signal is converted to electrons by multiplying it by f_e.

This procedure assumes linearity of the pixel output signal w.r.t. the collected charge (see eq. 3.1). The calibration precision depends on the uncertainty of the fitting parameter μ, pixel gain, and the implicit assumption that all of the charge deposited in the high-field

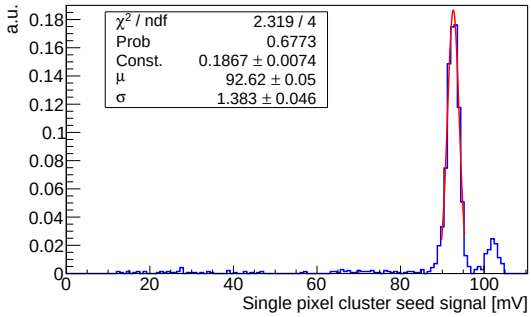

Figure 3.5: Seed signal distribution of single pixel clusters - The red curve is the result of a fit with a Gaussian pdf.

region is collected by a single pixel. The relative uncertainty on the charge conversion factor was estimated to $\Delta_{f_e}/f_e \approx 1\%$.

3.2 Influence of design and operational parameters on sensor performance

3.2.1 Sensor response at different reverse bias voltages

Figure 3.6 shows the seed signal distribution for different reverse bias voltages in the ^{55}Fe measurement of the MM75[1] on a chip with a 25 µm epitaxial layer.

Figure 3.6a shows the pixel signal measured in mV. The trigger threshold (see sec. 3.1.2) was set to $\sim$ 10 mV, thus the measured distributions start at $\sim$ 10 mV for all reverse bias voltages. The position of the calibration peak[2] shifts towards higher values as the reverse bias voltage is increased. This is consistent with the expected junction capacitance decrease (see sections 2.1.1.1 and 2.3.1).

Figure 3.6b shows the pixel signal calibrated in electrons (see sec. 3.1.3); this representation disentangles the gain (capacitance change) from other reverse bias effects. Therefore, it allows to directly compare the charge collection properties at different reverse bias voltages. Since the charge threshold decreases with increasing gain, the measured distributions start at different charge values. In particular, a significant portion of the seed signal distribution at $V_{BB} = 0$ V is cut, concealing the exact position of the charge sharing peak[3]. However, it can be observed that the position of the charge sharing peak shifts

[1] MM75 features 2 µm n-well size and 3 µm spacing.
[2] Defined in sec. 2.4.1.
[3] Defined in sec. 2.4.1.

towards higher values with the increasing reverse bias. That is, the number of events with higher seed pixel signal increases with the reverse bias voltage, indicating less charge sharing. These observations are consistent with the increasing strength and spatial extension of the electric field in the epitaxial layer.

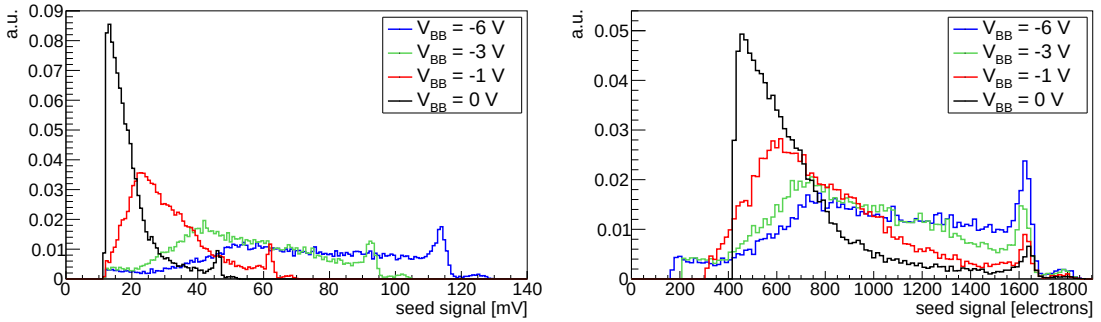

(a) Signal in mV **(b)** Signal in e^-

Figure 3.6: Seed signal distributions at different revere bias voltages - (a) The position of the calibration peak shifts towards higher values as the reverse bias voltage increases. (b) The number of events with higher seed pixel signal increases with the reverse bias voltage, indicating a stronger electric field. MM75, $d_{epi} = 25$ µm.

Figure 3.7a shows the 3×3 matrix signal[1] distributions in electron units, at different reverse bias voltages. It can be observed that the position of the peaks shifts towards lower values as the reverse bias voltage decreases. Figure 3.7b shows the 5×5 matrix signal distributions, where the shift is not visible. Therefore, it can be concluded that the shift is caused by the notably larger charge sharing at lower reverse bias voltages i.e. the spatial extension and the strength of the electric field are reduced.

3.2.2 Epitaxial layer thickness

The influence of the epitaxial layer thickness on the sensor performance was studied at the CERN SPS using a 120 GeV/c proton beam. The charge deposited by the traversing particles is approximately proportional to the epitaxial layer thickness (see sec. 2.2.1), thus a sensor with a thicker epitaxial layer is expected to collect more charge. On the other hand, the diffusion volume is enlarged when increasing the epitaxial layer thickness, thus resulting in less efficient charge collection and more charge sharing (see sec. 6.2).

[1]Defined in sec. 2.4.

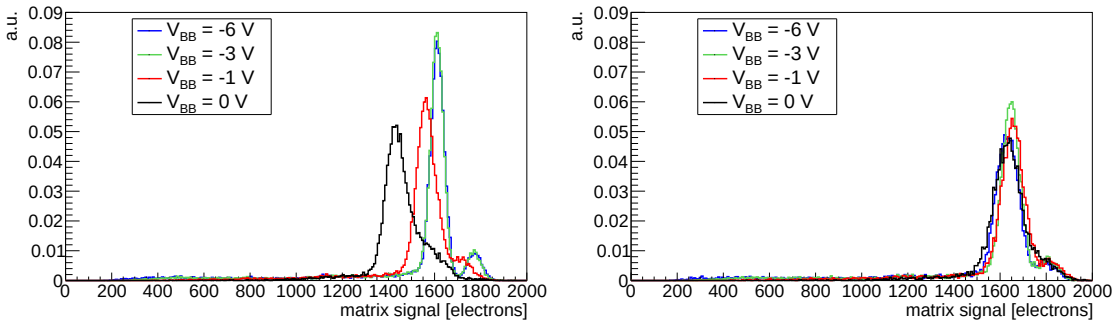

(a) 3×3 matrix **(b)** 5×5 matrix

Figure 3.7: Matrix signal distributions at different reverse bias voltages - (a) The position of the peaks shifts towards lower values as the reverse bias voltage decreases. (b) The deposited charge is contained within a larger pixel matrix. MM75, $d_{epi} = 25$ µm.

The matrix signal[1] distributions for different epitaxial layer thicknesses are shown in fig. 3.8a. The distributions are fitted with a convolution of a Landau and a Gaussian distribution[2] and the MPVs are reported in the plot. The amount of collected charge increases with the epitaxial layer thickness, but it is systematically larger than expected, considering the nominal epitaxial layer thicknesses and the theoretical value for a MIP charge deposit of about 60 $e^-/\mu m$. This excess can be explained by the contributions from the substrate (see sec. 6.3.1).

For practical purposes, the seed signal distribution is more important as it is strongly correlated with the detection efficiency. Although more charge is deposited in a sensor with a thicker epitaxial layer, this is not necessarily seen in the seed signal distribution. This can be observed in fig. 3.8b; when increasing the epitaxial layer thickness from 18 µm to 25 µm the improvement is evident, less so for the additional 5 µm increase from 25 µm to 30 µm.

Figure 3.9a shows the cluster size distribution (see sec. 2.4) for different epitaxial layer thicknesses. Increasing cluster size (larger charge sharing) is consistent with the increased diffusion volume.

A conclusive benchmark of a sensor performance is the detection efficiency. Unfortunately, in the test-beam setup where the INVESTIGATOR was tested, tracking information was not available, so it was not possible to calculate the detection efficiency using the

[1] MM75 was used, featuring 2 µm n-well size and 3 µm spacing. $V_{BB} = -6$ V.

[2] The energy straggling of MIP in ultra-thin absorbers is described by Bichsel's functions (see sec. 2.2.1) which can be approximated by a convolution of a Landau and a Gaussian distribution (see sec. 6.1.5.3.

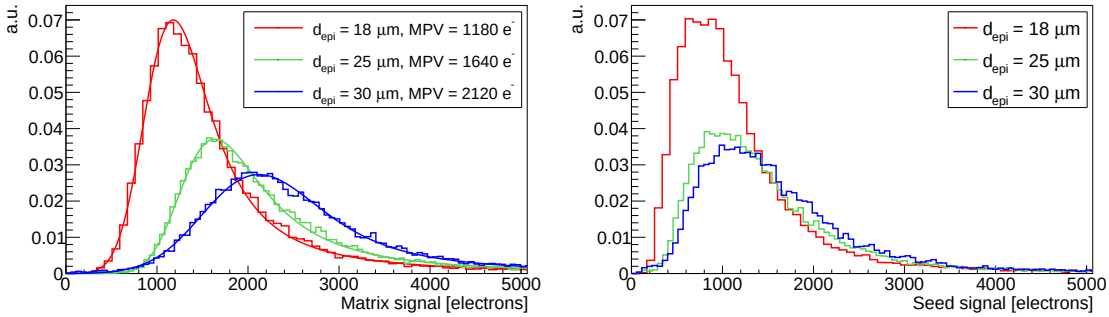

(a) Matrix signal **(b)** Seed signal

Figure 3.8: Matrix and seed signal distributions for different epitaxial layer thicknesses - (a) The matrix distributions are fitted with a Langaus distribution and the MPVs are reported. (b) The increase of the epitaxial layer thickness from 18 µm to 25 µm is evident, while the additional 5 µm increase is negligible. MM75, $V_{BB} = -6$ V.

standard approach (see sec. 2.4.2), but rather the following formula was adopted

$$\text{Detection efficiency} = \frac{\text{Number of events with seed signal above threshold}}{\text{Total number of triggered events}}. \tag{3.3}$$

The detection efficiency as a function of charge threshold is shown in fig. 3.9b. There is a significant improvement from 18 µm to 25 µm epitaxial layer, however, the further increase in epitaxial layer thickness has a negligible effect on the detection efficiency, which is in agreement with the observations on the seed signal distribution (see fig. 3.8b). This, of course, is valid for this particular MM, while a sensor employing a stronger and more spatially extent electric field would be expected to benefit from even thicker epitaxial layer.

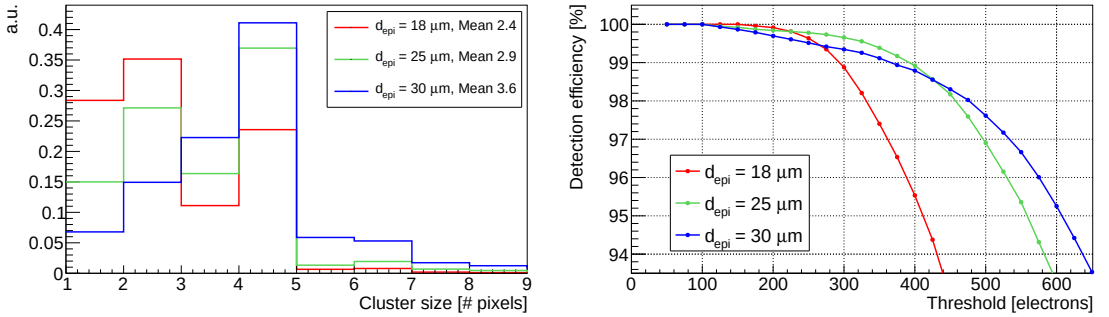

(a) Cluster size **(b)** "Detection efficiency"

Figure 3.9: Cluster size and detection efficiency for different epitaxial layer thicknesses - Detection efficiency is significantly improved increasing epitaxial layer thickness from 18 µm to 25 µm, however, the further increase has a negligible effect on the detection efficiency. MM75, $V_{BB} = -6$ V.

3.2.3 Collection diode geometry

All mini-matrices feature an octagonal collection diode in the centre of a square deep p-well opening (see fig. 2.10). The collection diode geometry differs between mini-matrices only in spacing and n-well size. For the 28 µm pixel pitch, there are 25 different diode geometries, with spacing ranging from 1 µm to 5 µm and n-well size from 1.17 µm to 5 µm [55]. Due to a high number of parameters, comparing cluster signal and size distributions is not practical. Therefore the following quantities are defined on the basis of the observables in ^{55}Fe measurements (see sec. 2.4.1):

Calibration peak signal - position of the calibration peak in seed signal distribution is correlated to the input capacitance (e.g. see fig. 3.6a).

Fraction of single pixel clusters - number of clusters with size equal to one divided by the total number of clusters. The number of clusters with a single pixel collecting charge is correlated with the spatial extension of the electric field i.e. the depleted volume (see fig. 2.13).

Charge collection efficiency (CCE) - the ratio of the MPV of the matrix signal distribution and the MPV of the single pixel cluster signal distribution[1]. The CCE is an estimate of the ratio of the collected charge and the deposited charge. The deposited charge, which is not measurable, is estimated from the single pixel cluster signal distribution, assuming that when the X-ray conversion occurs inside or near the depleted volume, most or all charge is collected by a single pixel. The collected charge is given by the matrix signal.

Average cluster size - the average of a cluster size distribution. A higher average cluster size is an indication of a higher charge sharing between pixels. It provides information on the spatial resolution; in case of sensors with binary readout the average cluster size[2] of two is minimum to achieve spatial resolution better than 5 µm (see sec. 4.4.1).

[1] N.B. This variable is not mathematically an efficiency as its definition does not assure it is ≤ 1.

[2] The cluster size, and therefore also the average, depends on the clusterisation threshold (see sec. 2.4), which was set to 100 e^-.

3.2.3.1 N-well size

Figure 3.10 shows a summary of ^{55}Fe measurements for different n-well sizes and two values of spacing between the n-well and surrounding p-well.

The calibration peak signal (see fig. 3.10a) is decreasing as the n-well size is increasing, which is expected since the junction capacitance, formed by the n-well and the epitaxial layer scales with the junction area (see eq. 2.13). Different spacing has negligible influence on the calibration peak signal.

The fraction of single pixel clusters (see fig. 3.10b) is proportional to the n-well size, indicating a more spatially extended and stronger electric field. The larger spacing provides a further increase of the fraction of single pixel clusters.

The charge collection efficiency (see fig. 3.10c) saturates for an n-well size larger than 3–4 µm i.e. all the charge deposited in the epitaxial layer is collected. The larger spacing provides a significantly higher CCE in case of a very small n-well size.

The average cluster size (see fig. 3.10d) decreases with increasing n-well size, which is consistent with the observations made for the fraction of single pixel clusters. For the largest n-well sizes (> 4 µm for 3 µm spacing and > 5 µm for 2 µm spacing), the average cluster size drops below 2, which could results in a spatial resolution worse than the ITS requirement of 5 µm (see tab. 1.3) for the sensors with ~ 28 µm pitch and binary readout[1].

Finally, it can be observed that the performance of the collection diode with 2 µm n-well size and 3 µm spacing (MM75) is similar to that of 3 µm n-well size and 2 µm spacing in terms of CCE, fraction of single pixel cluster and average cluster size. However, the calibration peak signal is $\sim 25\%$ higher in case of 2 µm n-well size and 3 µm spacing. Therefore, in case of this measurement i.e. $d_{epi} = 25$ µm and $V_{BB} = -6$ V, it offers the highest Q/C ratio.

[1]The relationship between cluster size of 2 and spatial resolution of ~ 5 µm can be also be proven mathematically. The spatial resolution of a pixel sensor with 28 µm pitch and binary readout, assuming only one pixel fires per particle crossing, is $\frac{p}{\sqrt{12}} \approx 8$ µm [32]. However, assuming that a particle crossing near the pixel border activates also the neighbouring pixel, e.g. at maximum $\frac{p}{4}$ from the border, then 3 different sensor responses can be identified: pixel center with 1 firing pixel, pixel corners with 3 or 4 firing pixels, and the rest of pixel borders with 2 firing pixels. Considering the equivalent areas for these three responses, the average response i.e. cluster size equals 2 and the equivalent pitch is reduced by half thus the expected spatial resolution is $\frac{p}{2\sqrt{12}} \approx 4$ µm.

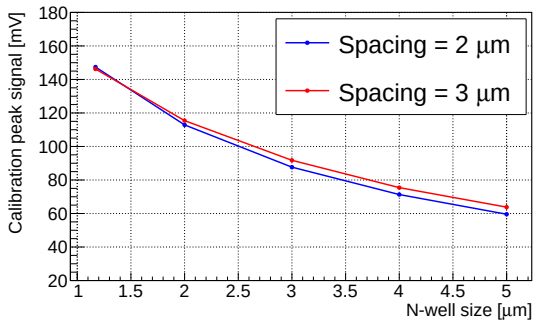

(a) Calibration peak signal

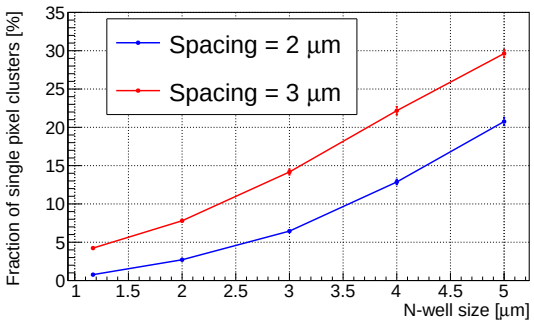

(b) Fraction of single pixel clusters

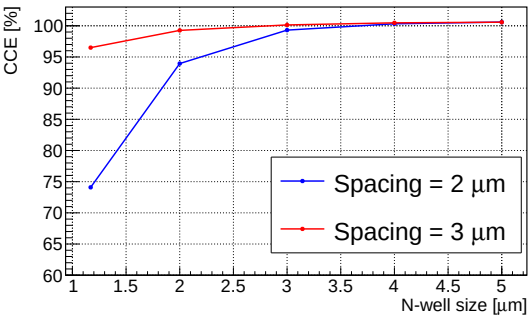

(c) Charge collection efficiency

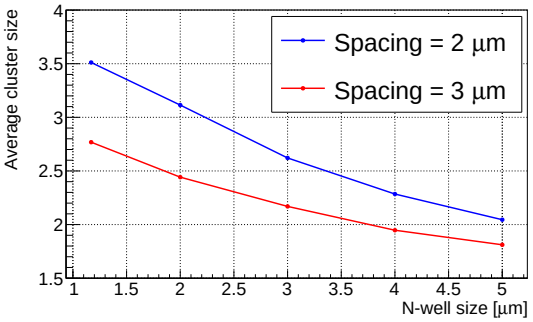

(d) Average cluster size

Figure 3.10: ^{55}Fe measurement results for different n-well sizes - Increasing the n-well size decrease the junction capacitance and enlarges the depleted volume. $d_{epi} = 25$ µm, $V_{BB} = -6$ V.

3.2.3.2 Spacing

Figure 3.11 shows a summary of ^{55}Fe measurements for different spacing between the n-well and the surrounding p-well, at a fixed n-well size (2 µm).

Unlike the previous case in which the n-well size was varied, the calibration peak signal as a function of spacing (see fig. 3.11a) exhibits a non-monotonous behaviour, indicating that there are at least two competing effects contributing to the measured spectrum. The spacing affects the junction capacitance formed by the n-well and surrounding p-well; for a small spacing, the p-well and n-well are practically in contact, while for a large spacing, there is low-doped p-type epitaxial layer in between.

The fraction of single pixel clusters (see fig. 3.11b) is increasing with the spacing, indicating a more spatially extended and stronger electric field.

The charge collection efficiency (see fig. 3.11c) saturates for a spacing larger than 3 µm i.e. all the charge deposited in the epitaxial layer is collected.

The average cluster size (see fig. 3.11d) increases from 1 µm to 2 µm spacing and then steadily decreases with the increasing spacing. The drop at 1 µm spacing is consistent with a very low CCE; the average cluster size drops because not all charge is collected.

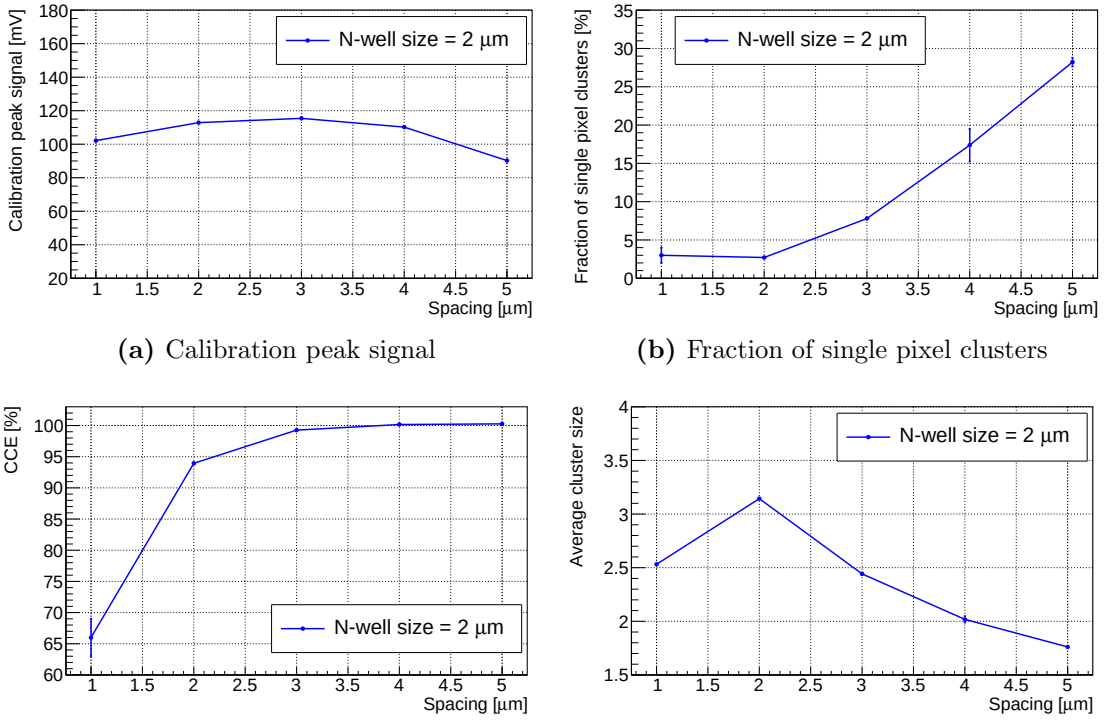

(a) Calibration peak signal

(b) Fraction of single pixel clusters

(c) Charge collection efficiency

(d) Average cluster size

Figure 3.11: ^{55}Fe measurement results for different spacings - Increasing the spacing between the n-well and surrounding p-well increases the spatial extension and strength of the electric field. $d_{epi} = 25$ µm, $V_{BB} = -6$ V.

3.3 Summary

The design of the INVESTIGATOR1 chip was motivated by the observation that the pixel performance is influenced by several parameters, namely by the collection diode size and distance to the surrounding p-well, pixel pitch, different reset mechanisms (diode or PMOS), deep p-well coverage and different source follower implementations. In this chapter, only a part of the parameter phase space, most relevant for the MAPS for the ITS upgrade (see ch. 4) and for the simulation (see ch. 6), was studied. The unconstrained parameters in this study were the spacing and the n-well size. Sensors produced on wafers

with different epitaxial layer thicknesses were also studied, as well as the influence of the reverse bias voltage on the pixel response.

It was shown that applying a reverse bias to the collection diode via the substrate significantly improves the Q/C ratio. The epitaxial layer thickness was discussed for a fixed pixel geometry and reverse bias voltage. It was seen that a higher thickness results in a better performance, but after a certain thickness is reached, the improvement is negligible (for the studied MM). The optimal thickness finally depends on the strength of the electric field (reverse bias voltage an pixel geometry). It has been shown that a small n-well results in a low-capacitance, while a large n-well provides better charge collection properties. Therefore, the optimal n-well size for the 25 µm epitaxial layer thickness and 28 µm pixel pitch is in the range from 2 µm to 4 µm, depending on the spacing from surrounding p-well. The influence of the spacing on the charge collection is similar to that of the n-well size; increasing the spacing strengthens the electric field and enlarges the depleted volume, but it has a small effect on the input capacitance compared to the effect of the n-well size.

4

ALPIDE – The MAPS for the ALICE ITS upgrade

The development of the monolithic active pixel sensor (MAPS) for the ALICE Inner Tracking System upgrade started in 2012 with a study of the charge collection properties and optimisation of the collection diode using small-scale prototypes with analogue readout (MIMOSA [51, 56], Explorer [47, 48], and CHERWELL [57]). Almost in parallel, in 2013, the ALPIDE architecture (in-pixel amplification and discrimination, and in-matrix zero suppression) was verified and optimised through small-scale prototypes (pALPIDEss [48]). In 2014, the first full-scale ALPIDE prototype pALPIDE-1 was produced and tested [47, 56, 58], followed by the pALPIDE-2 [48, 59] and the pALPIDE-3 [60] in 2015, and the final chip ALPIDE in 2016. All the sensors in the ALPIDE family and their key specifications are summarised in table 4.1.

In this chapter, the ALPIDE design and its operational features will be introduced (sec. 4.1 and 4.2), optimisations of the front-end circuit from pALPIDE-1 to ALPIDE will be discussed (sec. 4.3), and the performance of final sensor will be presented (sec. 4.4).

4.1 ALPIDE architecture

The ALPIDE sensor (see fig. 4.1) is based on TowerJazz 180 nm CMOS imaging sensor process [49]. It features the possibility to implant an n-well on top of a deep p-well (see fig. 2.7) and thus separate all n-wells, except for the collection diodes, from the active volume i.e. the epitaxial layer. Therefore, it is possible to implement PMOS transistors inside the pixels, without deteriorating the charge collection efficiency. This allows for a

Test start	Chip	Specification & purpose
2012	Explorer	- 20×20 and 30×30 μm^2 pixels, analogue readout - testing pixel and collection diode geometry, epitaxial layer properties (thickness and resistivity) reverse substrate bias and radiation hardness
2013	pALPIDE-ss	- 64×512 pixels of 22×22 μm^2 - first prototype with in-pixel discrimination and buffering - zero suppression within pixel matrix
2014/May	pALPIDE-1	- 1024×512 pixels of 28×28 μm^2 - in-pixel masking, on-chip bias DACs - bonding pads over matrix, no final interface
2015/May	pALPIDE-2	- 1024×512 pixels of 28×28 μm^2 - optimisations of several circuit blocks - final interface, but no high speed link
2015/Oct	pALPIDE-3	- 1024×512 pixels of 29.24×26.88 μm^2 - analogue front-end optimisations - high speed link
2016/Aug	ALPIDE	- final chip

Table 4.1: The ALPIDE family sensors.

more complex in-pixel circuitry, hence ALPIDE is not limited to the traditional rolling shutter readout[1].

All the prototypes, as well as the final ALPIDE chip, are produced on wafers with a high resistivity (> 1 kΩ cm) p-type epitaxial layer on a p-type substrate. Sensors with different epitaxial layer thicknesses, ranging from 18 µm to 40 µm, were produced and tested, settling to 25 µm for the final sensor. The TowerJazz process allows the application of a negative bias to the substrate (see sec. 2.3). Such bias further depletes the high resistivity epitaxial layer and increases the strength and the spatial extension of the electric field (see sec. 2.1.1). Therefore, the charge is collected faster and the fraction of charge collected by the seed pixels is increased. Furthermore, the detector capacitance is reduced, and consequently Q/C ratio is improved (see ch. 3).

Each ALPIDE pixel contains an amplifier, a discriminator and a multi-event buffer. Pixels are organised in double-columns (see fig. 4.2) each one having 1024 pixels. There are 512 double-columns in an ALPIDE chip thus forming a matrix of 1024 columns and 512 rows. The central part of each double-column is occupied by priority encoding circuits

[1]Rolling shutter readout is the standard for MAPS based on processes limited to NMOS transistors inside the pixels [61].

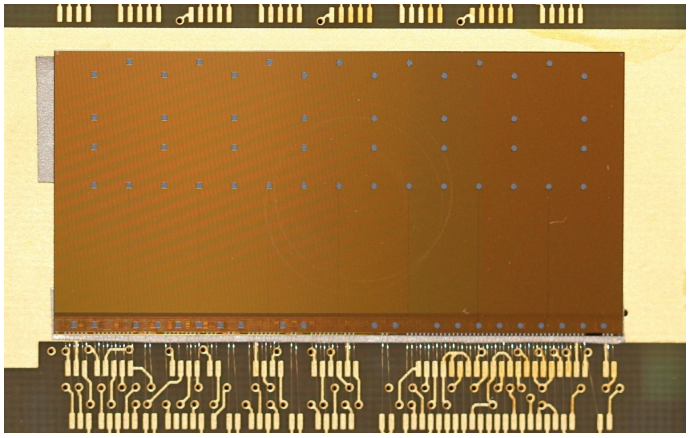

Figure 4.1: ALPIDE chip - wire bonded on a carrier card for laboratory testing. The die size is 30×15 mm^2 and thickness is 50 µm.

which propagate the addresses of the hit pixels to the periphery [62]. There is not any clock distributed over the matrix and the pixels which are not hit do not cause activity in the readout circuitry. The entire design is oriented towards very low power consumption; a single pixel uses about 40 nW, and the power density measured with the latest full-scale prototype is < 40 mW/cm^2 [60].

4.1.1 Principle of operation of in-pixel circuitry

A simplified layout of the in-pixel circuitry i.e. the input stage, the analogue front-end (amplifier/shaper and discriminator) and the digital logic (event buffering and masking), are shown in figure 4.3.

The input stage consists of a collection diode[1], a continuous reset of the input node and a pulse injection capacitance (C_{inj}) which is used to inject test charges into the analogue front-end. When the charge is collected, there is a fast potential drop at the input node of the amplifying circuit (see fig. 4.4a). The reset then slowly restores the potential to its nominal value. In ALPIDE prototypes two different reset mechanisms, PMOS and diode[2], were tested and the latter is implemented in the final chip.

The potential drop at the amplifier input node is shaped to a signal with a duration up to 10 µs and peaking time of ~ 2 µs (see fig. 4.4b). The peaking time and pulse length

[1]The ALPIDE prototypes implemented multiple collection diode geometries on the same chip (4 in case of pALPIDE-1 and pALPIDE-2, and 8 in case of pALPIDE-3). The final sensor features a collection diode with 2 µm n-well size and 3 µm spacing (see fig. 2.10).

[2]For more details on the two reset mechanisms see [47] and [51].

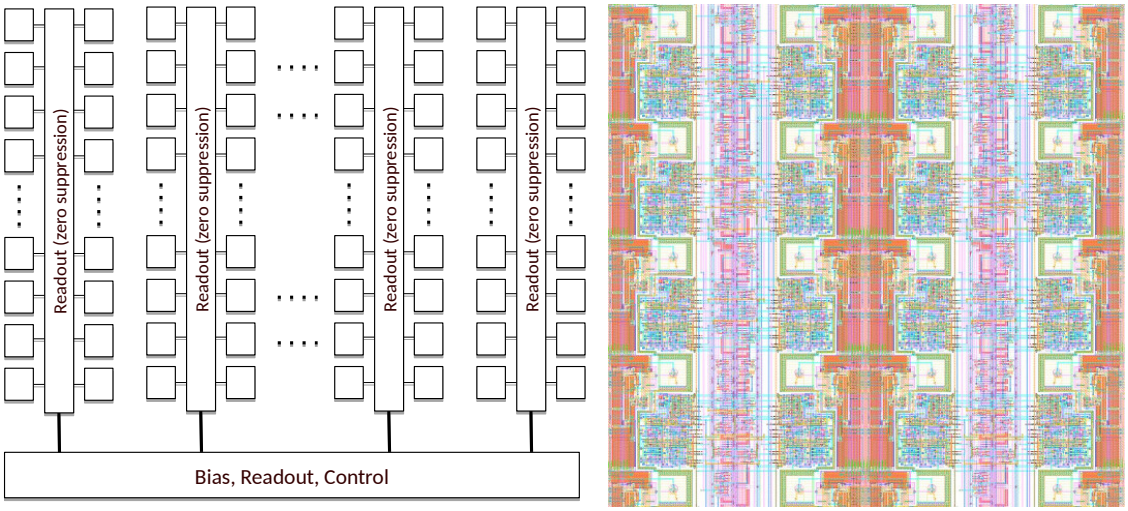

(a) ALPIDE architecture **(b)** Double-column layout

Figure 4.2: ALPIDE architecture - ALPIDE pixels are organised in double-columns of 1024 pixels. The central part of each double-column is occupied by priority encoding circuits which propagate the addresses of hit pixels to the periphery. Each pixel contains an amplifier, a discriminator and a multi-event buffer. Collection diodes are visible in (b) as octagons in the centres of green squares.

are chosen such that the power consumption is optimised while maintaining the required physics performance [18]. There are several bias voltages and currents, adjustable via on-chip 8-bit digital-to-analogue converters (DAC), that allow fine tuning of signal shaping and discrimination i.e. the charge threshold (see sec. 4.1.2).

As long as the amplitude of the signal exceeds the threshold, the discriminator output stays asserted. If the strobe signal, given by the trigger (common to all pixels), is asserted at the same time (see fig. 4.4c), the discriminator output state is stored into a register. Each pixel contains three registers which act as a multi-event buffer. A latch in the in-pixel digital logic allows to mask malfunctioning or noisy pixels individually (see sec. 4.1.3).

4.1.2 Analogue front-end

A detailed scheme of the ALPIDE analogue (in-pixel) front-end is shown in fig. 4.5. Diode `D1` is the collection n-well do p-type epitaxial layer junction (see sec. 2.1.1). The input node is continuously reset by diode `D0`. `VRESETD` establishes the reset voltage of the input node (`pix_in`).

A particle hit will lower the potential at the pixel input `pix_in` by a few tens of mV

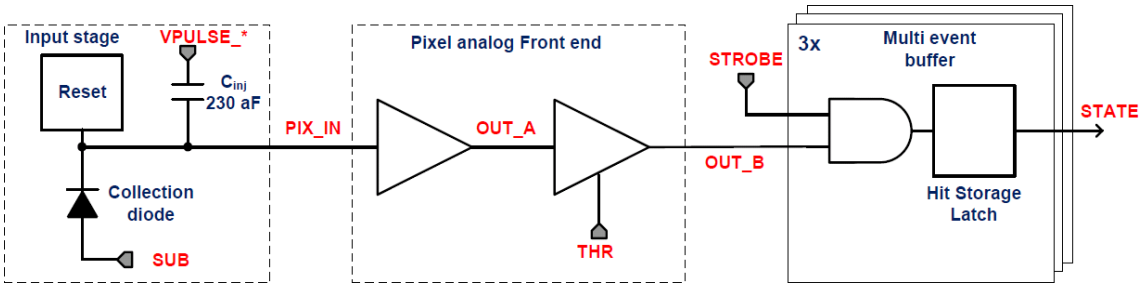

Figure 4.3: ALPIDE in-pixel scheme - Schematic representation of the in-pixel circuitry implemented in ALPIDE sensor.

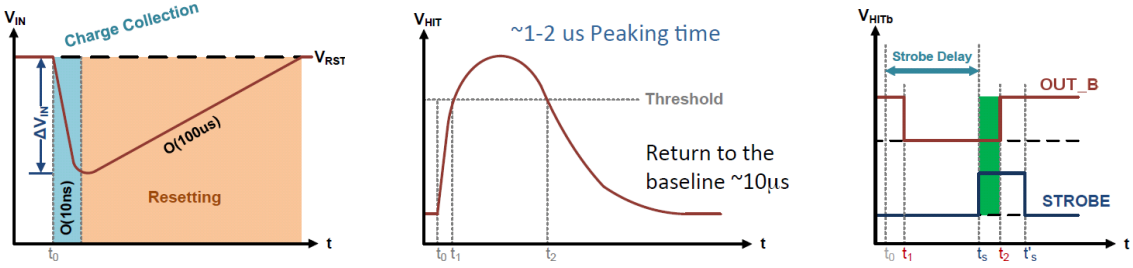

(a) Signal at the input node of analogue front-end.

(b) Signal after shaping; at discriminator input.

(c) Discriminator output and trigger signal.

Figure 4.4: ALPIDE pixel response - Graphical illustration of the in-pixel circuitry response to charge collection [48].

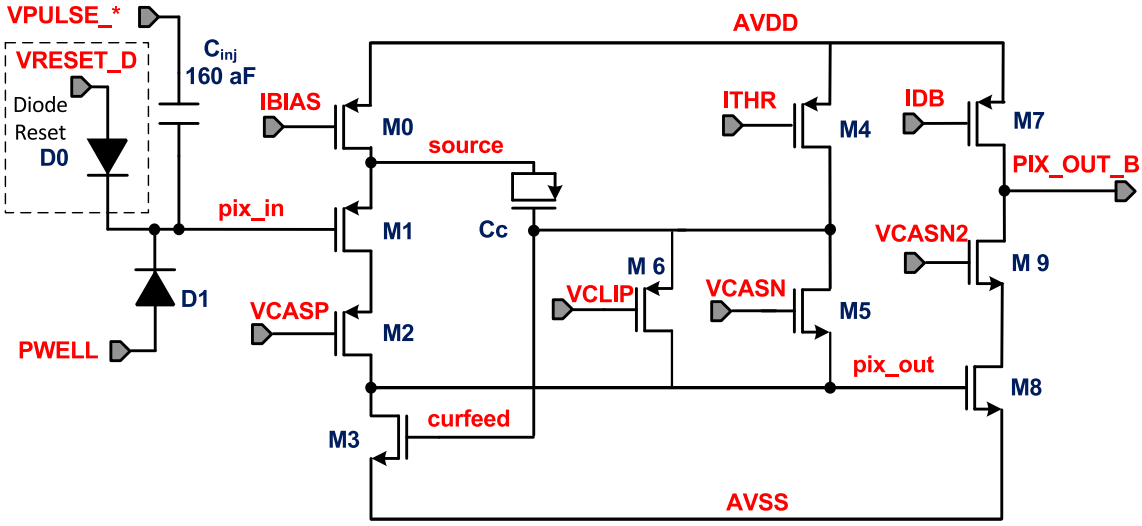

Figure 4.5: ALPIDE analogue front-end scheme - Simplified layout of ALPIDE reset, shaper and discriminator circuitry. There are minor differences w.r.t. first full-scale prototypes such as introduction of `VCLIP` and `VCASN2`.

[63]. This will increase the current through the source follower M1 and make the source node follow the input. Consequently charged stored at the source node is dumped on the analogue output node `pix_out` (see fig. 4.6a). In addition, the coupling of the source node to the `curfeed` node by `Cc` will reduce the current through `M3`. Both effects add and cause the potential on the output node `pix_out` to swing upwards by several hundreds of mV (according to simulations, see fig. 4.6a). This forces `M8` into conduction and if the charge deposit from the particle hit is sufficiently large to overcome the current setting `IDB` on `M7`, `M8` will drive the `PIX_OUT_B` node to zero (see fig. 4.6b).

The charge threshold of the pixel is defined by `ITHR`, `VCASN` and `IDB`. The effective charge threshold is increased by increasing `ITHR` or `IDB`. It is decreased by augmenting `VCASN`. Voltage bias `VCLIP` controls the gate of the clipping transistor `M6`. The lower `VCLIP`, the sooner the clipping will set in (see fig. 4.6a). The active-low `PIX_OUT_B` signal is applied to the digital section of the pixel where it is used to set the hit status register.

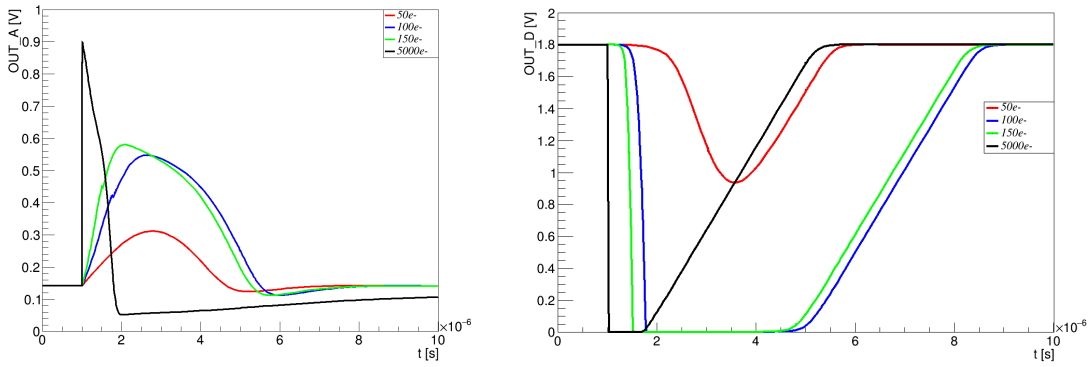

(a) Signal at `pix_out` node. **(b)** Signal at `PIX_OUT_B` node.

Figure 4.6: Pixel front end transient simulation plots - Analogue front-end simulated signals at `pix_out` and `PIX_OUT_B` nodes for different injected charges [64].

It is possible to electrically inject a test charge into the input node. This is achieved by applying a voltage pulse of controllable amplitude to the `VPULSE` pin of the C_{inj} capacitor. The design value of C_{inj} is 230 aF. The pulse generation is controlled by the digital section of the pixel and the periphery.

4.1.3 Digital in-pixel circuitry

The digital section of a pixel is illustrated in fig. 4.7. The pixel features three registers. Each register is a set-reset latch that can keep the hit information. The register is normally

set by the front-end discriminated output PIX_OUT_B if the STROBE_B signal is asserted simultaneously. It can also be set by the DPULSE signal as a test of digital in-pixel circuitry. A register can be selected for read/reset by asserting the corresponding MEMSEL_B signal. A register is reset either by a PIX_RESET pulse generated by the Priority Encoder during the readout, either by a global FLUSH_B signal. The logic provides two programmable functions: masking and pulsing. When control bit MASK_EN is set high, the STATE output is forced to 0, effectively masking the pixel output to the priority encoder. The analogue pulsing consists in the injection of a test charge in the input node through C_{inj} (see fig. 4.5). The amplitude of the applied voltage pulse is defined by the difference between VPLSE_HIGH and VPLSE_LOW (see fig. 4.7).

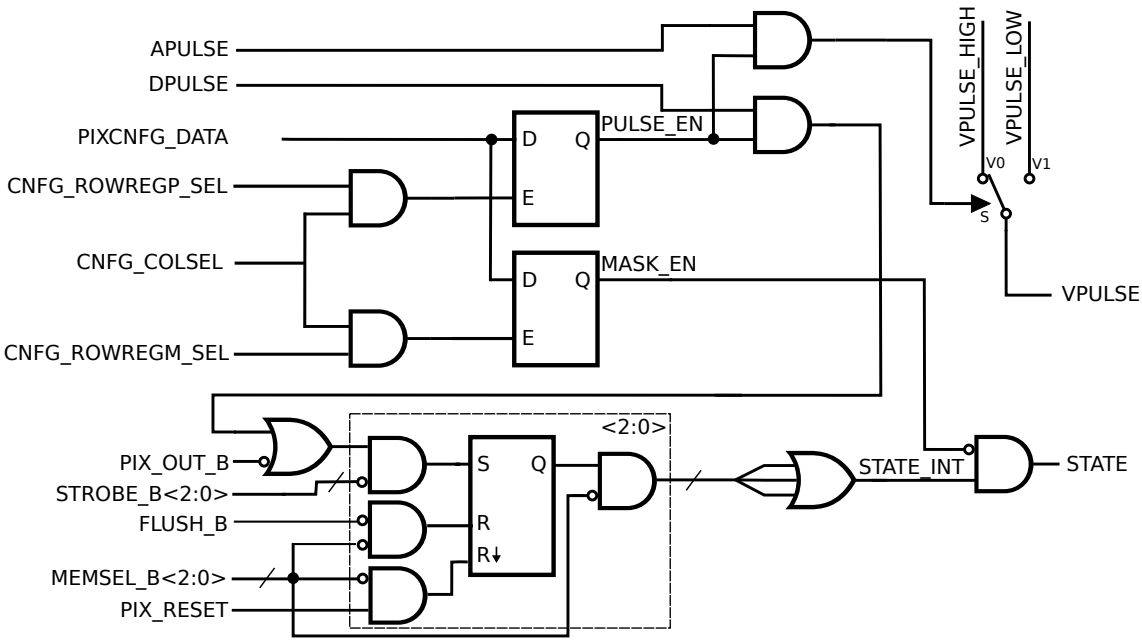

Figure 4.7: ALPIDE digital in-pixel circuitry - Digital circuitry inside ALPIDE pixel features three registers (event buffers), masking, and digital and analogue pulsing.

4.2 Basic chip tests

4.2.1 Threshold and noise

The key parameter steering the chip performance is the charge threshold. As discussed in sec. 4.1.2, the in-pixel discriminator charge threshold is defined by three front-end

biasing parameters (`ITHR`, `VCASN`, and `IDB`, common to all pixels). For a given set of these parameters, pixel charge threshold can be determined using the analogue pulsing (see sec. 4.1.3). The measurement consists in injecting N_{inj} times a range of test charges Q_{inj} via pulsing capacitance C_{inj} such that

$$Q_{\text{inj}} = C_{\text{inj}} \left(\texttt{VPLSE\_HIGH} - \texttt{VPLSE\_LOW}\right). \tag{4.1}$$

`VPLSE_HIGH` and `VPLSE_LOW` maximum value is 1.8 V and are set via on-board 8-bit DACs. The minimum voltage step equivalent to 1 DAC unit is 7 mV. Consequently, the minimum charge step is 10 e^-, considering the nominal value of the pulsing capacitance (230 aF). For each test charge Q^i_{inj}, out of N_{inj} injections, N^i_{hit} pass the threshold i.e. result in pixel hits. The plot of $N^i_{\text{hit}}/N_{\text{inj}}$ as a function of Q^i_{inj} is shown in figure 4.8. It is often referred to as *s-curve* measurement as its shape resembles the letter *S*. The threshold is defined as charge at which pixel fires in 50% of cases (injections). Since the electronic noise is expected to be Gaussian, the data is fitted with an error function

$$f(x) = \frac{1}{2}\left[1 + \text{erf}\left(\frac{x-\mu}{\sqrt{2}\sigma}\right)\right] \tag{4.2}$$

where μ is the threshold and σ is the temporal noise of a pixel.

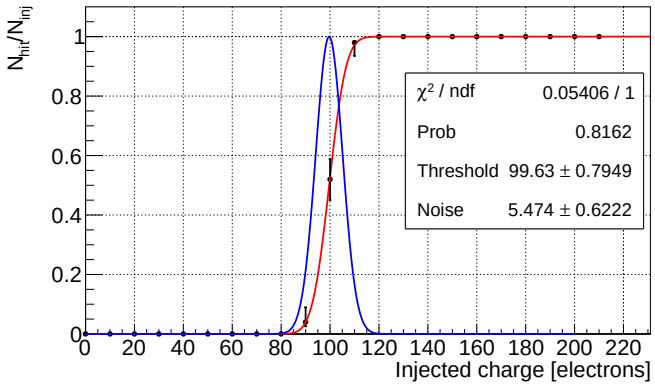

Figure 4.8: S-curve measurement - $N^i_{\text{hit}}/N_{\text{inj}}$ as a function of Q^i_{inj} for an ALPIDE pixel. The red line is the error function fit and the blue line is its derivative representing electronic noise of the pixel.

S-curve measurement is performed on all pixels in a sensor; the distribution of thresholds and noise are shown in figure 4.9. It can be observed that the threshold RMS is larger than the average pixel noise i.e. the fixed-pattern noise (FPN) is larger than the

temporal noise. The FPN originates from transistor mismatches in the in-pixel circuitry, thus causing pixel to pixel variations with a stable pattern.

The average of the threshold distribution is defined as the chip threshold. This value is used in standard plots introduced in section 2.4.2 and presented later in this chapter. The calibration of the chip threshold depends on the injection capacitance C_{inj}.

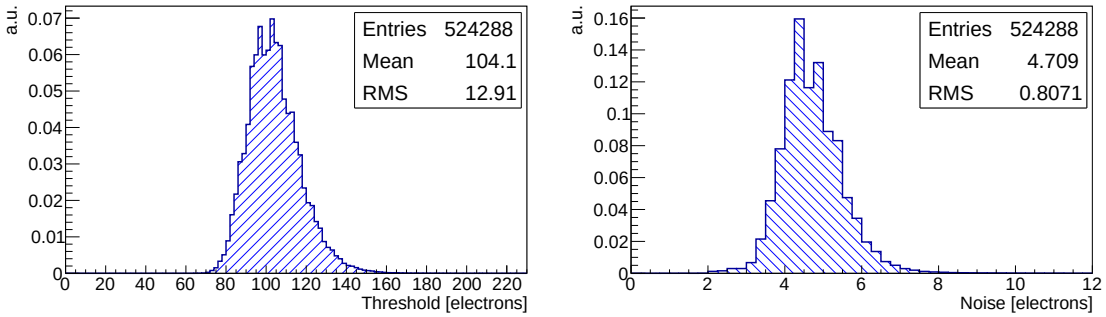

(a) Threshold distribution **(b)** Noise distribution

Figure 4.9: Threshold and noise distributions - The threshold RMS is larger than the average pixel noise.

As discussed in section 4.1.2, the threshold can be varied by adjusting the biasing parameters `ITHR`, `VCASN` and `IDB`. In figure 4.10, threshold RMS and noise are plotted as a function of threshold, where the threshold was varied by changing the `ITHR` parameter. It can be observed that both noise and threshold RMS increase as the threshold increases.

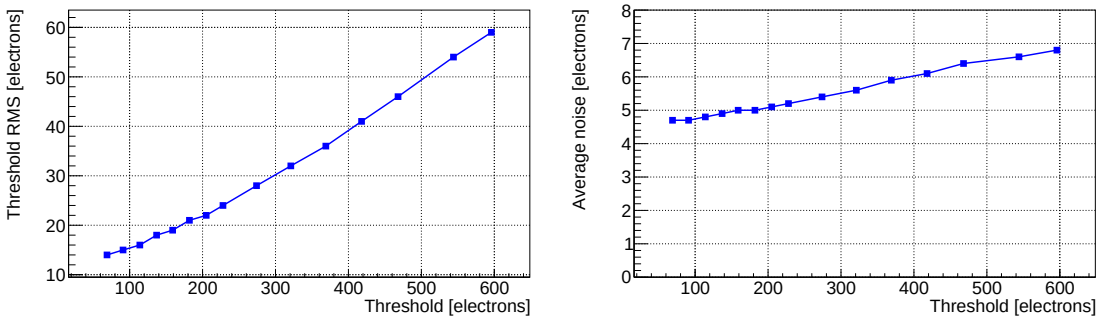

(a) Threshold RMS as a function of threshold. **(b)** Average noise as a function of threshold.

Figure 4.10: Threshold RMS and average noise as a function of threshold - Threshold in this measurement was varied by changing `ITHR`.

4.2.2 Fake-hit rate

The fake-hit rate of a sensor is defined as the number of hits per pixel per event in absence of any external stimulus. There are two sources of fake-hits; thermal/shot noise and random telegraph noise (RTN). The former can be modelled as follows. The probability that a pixel fires in absence of charge collection is given by

$$f(t_p, n_p) = \int_{t_p}^{\infty} \mathcal{N}(x|t_p, n_p) = \text{erfc}\left(\frac{t_p}{\sqrt{2}n_p}\right) \tag{4.3}$$

where $\mathcal{G}(x|t_p, n_p)$ is a normal distribution with mean t_p and standard deviation n_p with t_p and n_p threshold and noise of a pixel, determined from an s-curve measurement (see sec. 4.2.1). As it can be clearly seen, increasing the threshold or decreasing the noise lowers the fake-hit probability. Since threshold and noise change from pixel to pixel, the average fake-hit rate of a sensor can be calculated as the expectation value of the $f(t, n)$

$$\overline{\text{FHR}} = E[f(t, n)] = \iint f(t, n)\text{pdf}(t)\text{pdf}(n)\, dt\, dn \tag{4.4}$$

where pdf(t) and pdf(n) are probability density function of threshold and noise distribution, respectively. These distributions are shown in fig. 4.9, and, for simplicity, both can be approximated with Gaussians. Therefore

$$\overline{\text{FHR}} = \int_{-\infty}^{+\infty} dt \int_{0}^{+\infty} dn\ \text{erfc}\left(\frac{t}{\sqrt{2}n}\right) \mathcal{N}(t|\mu_t, \sigma_t)\mathcal{N}(n|\mu_n, \sigma_n) \tag{4.5}$$

where μ_t and σ_t are average chip threshold and threshold RMS, and μ_n and σ_n are average noise and noise RMS. This equation can be partially integrated, yielding

$$\overline{\text{FHR}}(\mu_t|\sigma_t, \mu_n, \sigma_n) = \int_{0}^{+\infty} \text{erfc}\left(\frac{\mu_t}{\sqrt{2}\sqrt{n^2 + \sigma_t^2}}\right) \mathcal{N}(n|\mu_n, \sigma_n)\, dn. \tag{4.6}$$

The remaining integral has to be computed numerically.

There is no simple underlying model describing the RTN contribution, and therefore it is not included in the FHR model. RTN manifests itself as discrete changes of the pixel output between two or more levels, and while amplitudes are typically well defined, the period is random and may reach from µs up to minutes [65]. RTN depends on various parameters, including the transistor size and type, the applied gate voltage, the oxide thickness and the temperature [47, 66, 67].

The fake-hit rate is measured by sending a number of triggers (N_{trg}) to the chip without providing any external stimulus, and recording the number of hits N_{hit}

$$\text{FHR}_{\text{meas}} = \frac{N_{\text{hit}}}{N_{\text{pix}} \cdot N_{\text{trg}}} \tag{4.7}$$

where N_{pix} is the number of pixels in the sensor. The number of triggers limits the sensitivity of a measurement, therefore, this limit will be indicated in the FHR plots.

The measured fake-hit rate of an irradiated[1] ALPIDE sensor as a function of charge threshold is shown in figure 4.11. The 20 noisiest pixels were masked in this measurement. The squares connected with lines are measured points calculated using eq. 4.7 while the dotted line represents FHR model given by eq. 4.6. The model closely follows the data points up to the threshold of about 100 e^-, after which it predicts a FHR below the sensitivity limit, while the measured FHR is above the said limit even at the highest measured thresholds. This could be explained by random telegraph noise.

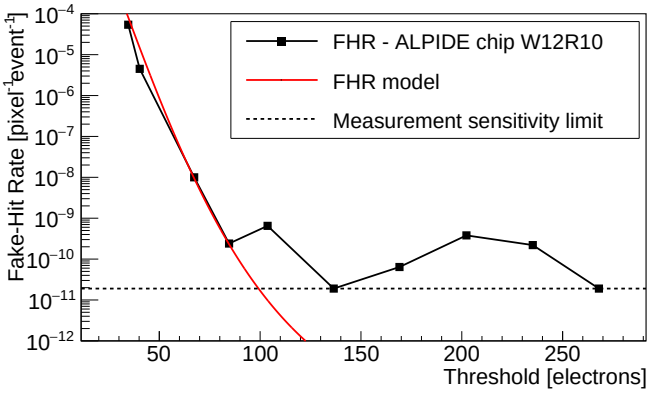

Figure 4.11: ALPIDE fake-hit rate - Fake-hit rate as a function of threshold. The black squares represent the measured points while the red curve represents the FHR model.

4.3 Optimisations of full-scale prototypes

Each digital sensor prototype in the ALPIDE family (see tab. 4.1) included optimisations of various design parameters (see sec. 2.3.2), the front-end circuitry and the periphery logic. A number of these optimisations have already been covered in [47], [48] and [64], therefore in this section only the complementary developments will be discussed.

[1] TID of 108 krad and NIEL of $1.16 \cdot 10^{12}$ 1 MeV $n_{\text{eq}}\,\text{cm}^{-2}$.

4.3.1 Pulse length and uniformity

The shape of a pulse produced by the analogue front-end after a charge collection (see sec. 4.1.2), i.e. its rise time, fall time and length, has a central role in defining the sensor performance as it influences the optimal triggering time and the maximum trigger rate (pile-up), and consequently the detection efficiency. One way to study the pulse shape is using the pulsing capacitance, as was done in [47] and [48], however this method is limited by a low maximum charge that can be injected, which is about 1700 e^- considering nominal capacitance value of 230 aF. Taking into account that an MIP deposits $\sim$ 1500 e^- in 25 µm thick epitaxial layer (see sec. 2.2.1) and that particles which deposit significantly higher energy are present in the ALICE vertex (see ch. 1), it is necessary to study the pulse shape for a larger range of injected charges.

Since the pulse shape measurement requires adjustable timing, variable energy, and precise positioning of the charge deposit, it was decided to use a focused 1060 nm laser beam for the charge generation in the individual pixels. Infrared light of 1060 nm wavelength is very weakly absorbed by silicon (absorption coefficient $\alpha \approx 30$ cm^{-1} [68]). A beam of this light passing through a silicon device will generate charge carrier pairs in its path. The detector circuitry on the top of the epitaxial layer contains six metal layers (see fig. 2.8) which almost completely reflect the infrared light, and the transmitted fraction is absorbed in the first nanometres[1]. Therefore, it is expected to observe a variation in the detector response depending on the laser beam position, with minima corresponding to the position of the metallisations and amplitudes depending on their width. Moreover, the maximum charge deposit is expected when the laser beam is centred over a pixel diode as it is not completely covered by the metal layers (see fig. 4.2b).

The pulse shape measurement setup scheme is shown in figure 4.12. The chip is fixed on a X-Y micro-positioning stage while the laser beam focuser is fixed perpendicularly to the chip surface, on the Z stage[2]. The setup is enclosed in a light-tight box. The laser beam focuser is connected to the laser driver outside the box via an optical fibre. The laser driver requires a positive input signal (between 1 and 2.5 V) in order to produce a laser

[1] For example, aluminium has normal incidence reflectance of ≈ 0.95 and penetration depth of ≈ 10 nm for 1060 nm wavelength [69], hence the fraction of the laser beam hitting the metal doesn't reach the epitaxial layer (assuming a few µm thick metal layers). The light is also partially reflected by the air-oxide and oxide-Si boundaries; normal incidence reflectances for the relevant wavelength are respectively ≈ 0.04 and ≈ 0.17 [70].

[2] Zaber T-LSM200A (X and Y stages) and T-LSM100A (Z stage).

beam with a proportional optical power (up to 2 mW). The pulse, generated by an external pulse generator and sent to the laser driver, was a 10 ns long trapezoidal signal with 4 ns rise and fall edges. The resulting beam had a diameter of 15 µm on the chip surface and a duration of 5 ns. The shortcoming of this setup is that the amount of deposited charge is not calibrated. Nevertheless, the linear correspondence of pulse amplitude and energy deposit was verified. For more details see appendix C.

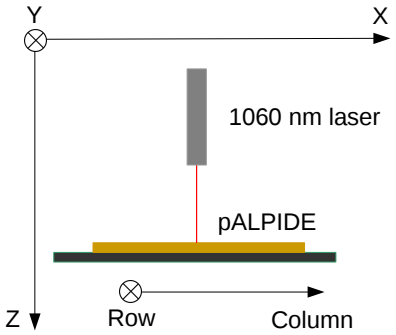

Figure 4.12: Laser setup scheme - The sensor is fixed on a X-Y micro-positioning stage while the laser beam focuser is fixed perpendicularly to the chip surface, on the Z stage.

The triggering and timing scheme is shown in figure 4.13. The laser was triggered with a delay of 250 ns w.r.t. the chip[1]. Triggering the chip asserts internally the `STROBE_B` signal (see sec. 4.1.3) of which the duration was set to 100 ns. All the pixels which fire during this period are read out and registered as hit. The delay between the trigger signal and assertion of a `STROBE_B` is adjustable and was varied from 0 to 15 µs in 250 ns steps. For each step 100 triggers were recorded[2]. The measurement was repeated at different laser powers, thus providing a "scan" of the front-end pulses for different amounts of injected charge.

4.3.1.1 Pulse shape of pALPIDE-1

The response of a part of the pALPIDE-1 matrix[3] where the laser beam was positioned is shown in figure 4.14 at different `STROBE_B` delays. The beam was focused[4] on the pixel that can be observed to stop firing the first. The zero delay corresponds to the moment of laser triggering i.e. charge deposit. A high laser power (deposited charge) was used in

[1] The laser beam driver emits the beam within 10 ns of the trigger signal.
[2] Triggering period was $\geq$ 10 ms to ensure that input node was reset to the baseline (see sec. 4.1.1).
[3] Pulse shape measurements of pALPIDE-1 were carried out on pixels in columns $\langle 512, 767 \rangle$, i.e. sector 2.
[4] For the positioning and focusing procedure see appendix C.

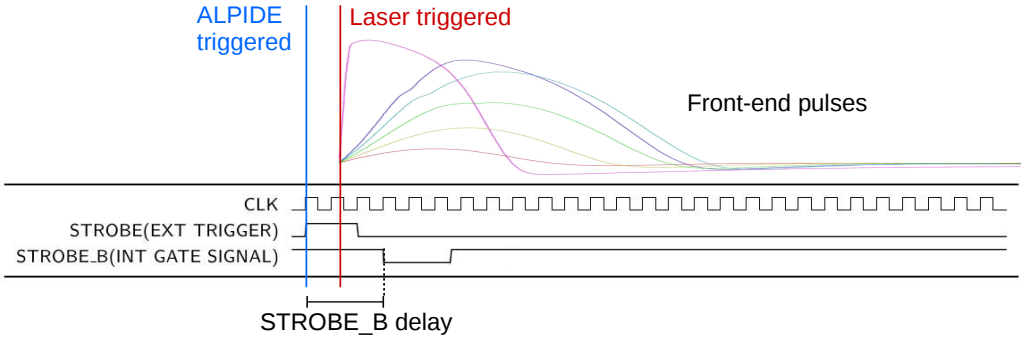

Figure 4.13: Laser triggering and timing scheme - Both laser and ALPIDE are triggered by an externally generated signal, with an adjustable trigger delay between the two.

this figure to illustrate how the pulses of pixels that collect different amount of charge develop after the charge deposit. The pixels that collected the largest amount of charge (closest to the pixel on which the laser beam was focused) fire immediately but are also the first to stop firing. Their neighbours start firing with a delay of about 1 µs but their pulse duration is longer. Finally, there are pixels at the edge of the cluster which collected the least amount of charge and fire only for a short time, with pulse rise time delayed up to 4 µs. These observations correspond to the pulse shape trend expected from the simulation shown in fig. 4.6a. The large cluster size can be explained by the diffusion of charge carriers[1].

Figure 4.14 also points out the effect of a potential misaligned trigger timing w.r.t. a measured physical event; if the chip is triggered too soon, the information on the pixels on the cluster border is lost, while in the opposite case, the pixels in the centre of the cluster are not read-out as hit[2]. The former, leads to potentially reduced spatial resolution, while the latter can lead to loss of detection efficiency and bad reconstruction of a cluster (e.g. as multiple clusters).

Another, more comprehensive, way to plot pixel response at different `STROBE_B` delays in the case of a low cluster size[3] (low deposited energy) is presented in figure 4.15. It shows

[1]This explanation is supported by measurements with low energy α-particles emitted by an ^{241}Am source in which similarly large clusters have been observed [71]. In fact, both considered laser beam and α-particles deposit charge in few tens of µm [43] while the charge is collected by pixels which are more than 150 µm apart.

[2]The non-uniformity of front-end pulses was already known from the pulse shape measurements with the pulsing capacitance, see [47] and [48].

[3]In case of large cluster size the plot becomes overcrowded and incomprehensible. Therefore, the fig. 4.15 represents a pALPIDE-1 response at lower laser power w.r.t. fig. 4.14.

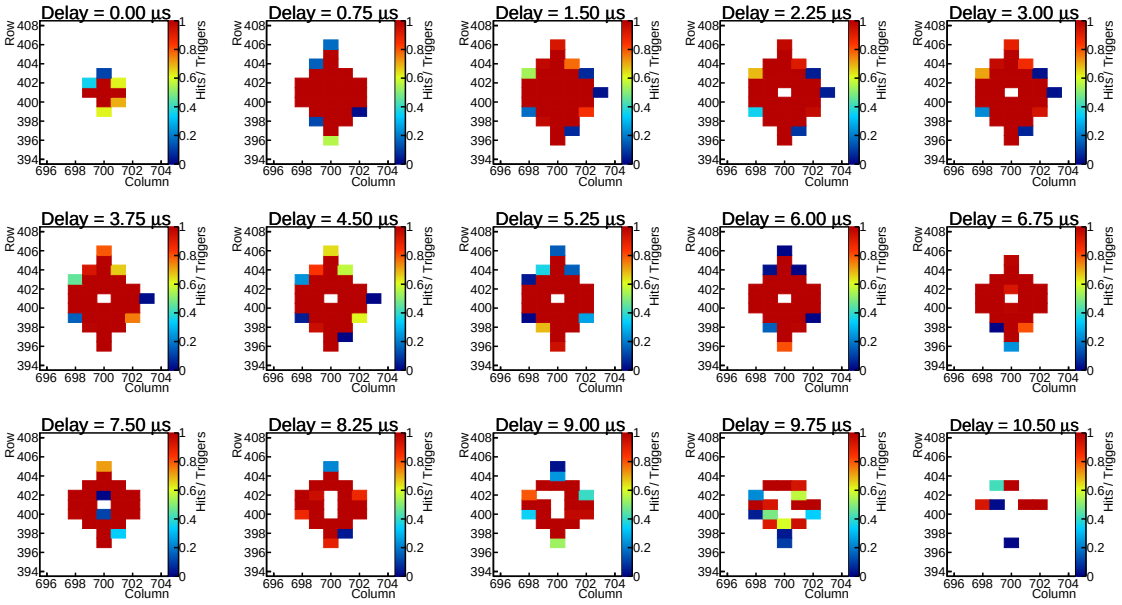

Figure 4.14: Laser spot vs `STROBE_B` delay - pALPIDE-1 response to the laser beam at increasing `STROBE_B` delay. The color scale indicates pixel firing frequency within 100 events.

number of triggers recorded as hits as a function of `STROBE_B` delay for several pixels in a cluster. It can be observed that there is a quite high non-uniformity in the pixel responses (at least some left-right/top-bottom symmetry is expected). Furthermore, pulse length ($\sim$ 10 µs) is longer than what was nominally expected from the design simulations ($\sim$ 4 µs).

A couple of definitions are required in order to quantify how the pulse shape scales with the laser power. The rising edge t_1 shall be defined as the time (delay) at which the pixel starts firing for every trigger. The falling edge t_2 shall be defined as the last instance at which the pixel is firing for every trigger. Time over threshold (TOT) or pulse length is defined as $t_2 - t_1$. For example, the pixel indicated with red colour in fig. 4.15, $t_1 = 1.25$ µs, $t_2 = 3.5$ µs and TOT $= 2.25$ µs.

Time over threshold as a function of laser power for pALPIDE-1 pixels in a 3×3 matrix is shown in figure 4.16. The laser spot was positioned over the central pixel's collection diode. The central pixel has apparently different behaviour, but this is because it collects more charge w.r.t. the pixels in the crown. In fact, the TOT is plotted as a function of laser power, but since the laser is positioned over the central pixel, the injected charge is not the same in all of the pixels. However, due to the symmetry, the charge collected by

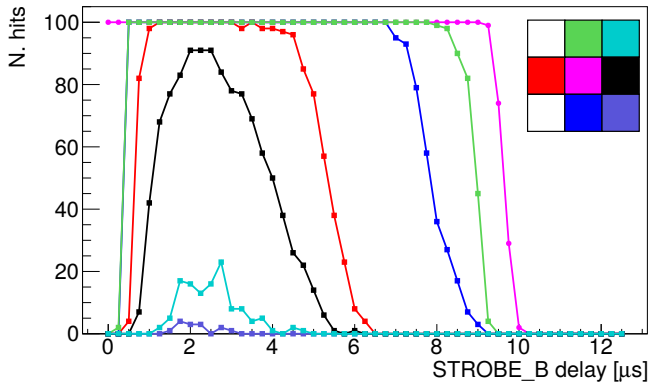

Figure 4.15: Measured pulses with pALPIDE-1 - Number of hit as a function of `STROBE_B` delay. Different pixels in the cluster are indicated with colors indicated in the scheme in the top right corner.

the four corner pixels should be approximately the same, as well as the charge collected by four first neighbours of the central pixel, which is not observed.
There are three important things to note about pALPIDE-1 pulse shape from fig. 4.16:

1. The time over threshold (pulse length) saturates to ~ 2 µs for high injected charges[1].
2. The maximum pulse length can be higher than 10 µs.
3. The maximum pulse length varies up to $\sim 40\%$ from pixel to pixel.

The high maximum pulse length can lead to pile-up, while the non-uniformity of the pulse shape makes it difficult to optimise triggering of the sensor. Therefore, an additional design effort was put into optimising the analogue front-end to achieve shorter pulses and a more uniform response from pixels, as a function of collected charge. The sensors in which those optimisations were implemented is pALPIDE-3.

4.3.1.2 Pulse shape of pALPIDE-3

Figure 4.17 shows the number of triggers recorded as hits as a function of `STROBE_B` delay, for several pixels in a pALPIDE-3[2] cluster (analogue to pALPIDE-1 cluster in

[1] It is difficult to evaluate the exact amount of injected charge at which the pulse length saturates as it is not possible to calibrate the laser energy deposit. However, the order of magnitude can be very roughly estimated as charge deposit equivalent to 10-100 MIP (50-500 keV), by confronting figure C.6 (see appendix C) and results from [71].

[2] Pulse shape measurements of pALPIDE-3 were carried out on pixels in columns $\langle 896, 1023 \rangle$, i.e. sector 7.

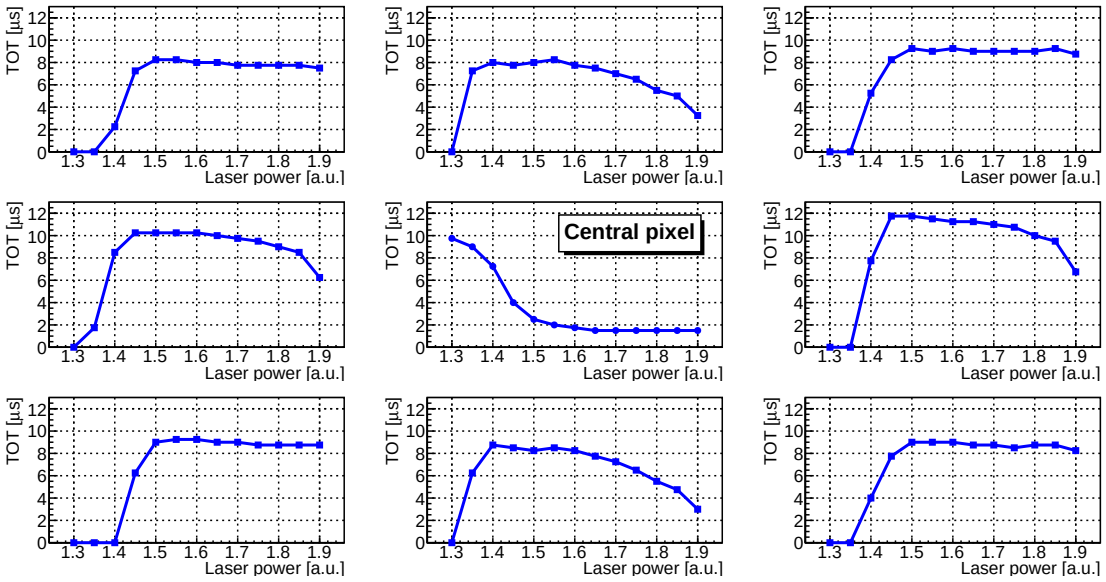

Figure 4.16: Pulse length vs laser power (pALPIDE-1) - Time over threshold as a function of laser power for pALPIDE-1 pixels in a 3×3 matrix. Laser beam is positioned over the diode of the central pixel.

figure 4.15). It can be observed that pixel response is much more uniform than the response of pALPIDE-1 pixels. Furthermore, the pulse length is notably shorter.

The time over threshold as a function of laser power for pALPIDE-3 pixels in a 3×3 matrix is shown in figure 4.18. The laser spot was positioned over the central pixel's collection diode. As was the case with pALPIDE-1 (see fig. 4.16), the central pixel has a behaviour, but it is because it collects more charge w.r.t. the pixels in the crown. It can be observed that, unlike in case of pALPIDE-1 case, the pulse shape of the four corner pixels is symmetric, as well as the pulse shape of four first neighbours of the central pixel. The improvement w.r.t. pALPIDE-1 pulse shape can be summarised in the following:

1. The maximum pulse length is reduced by about 50% and notably shorter than 10 µs.

2. The maximum pulse length is more uniform.

4.3.2 Fake-hit rate reduction

As discussed in sec. 4.2.2, it was assumed that the main source of fake-hits is the random telegraph noise (RTN). The input transistor of the analogue front-end was suspected to

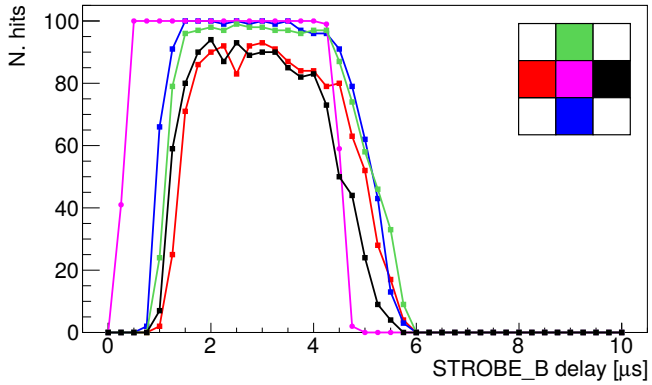

Figure 4.17: Measured pulses with pALPIDE-3 - Number of hit as a function of `STROBE_B` delay. Different pixels in the cluster are indicated with colors indicated in the scheme in the top right corner.

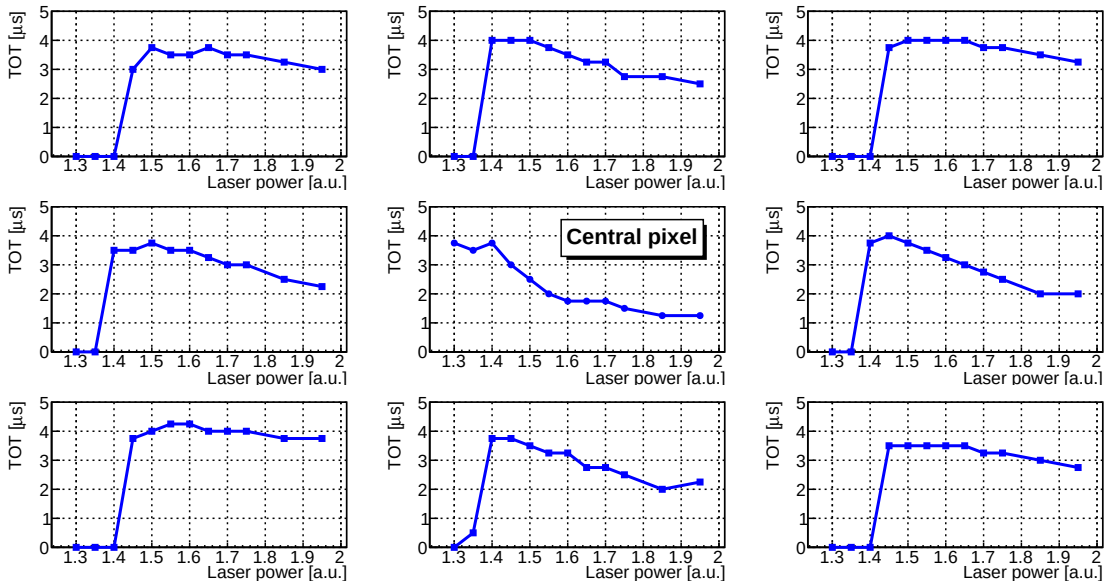

Figure 4.18: Pulse length vs laser power (pALPIDE-3) - Time over threshold as a function of laser power for pALPIDE-3 pixels in a 3×3 matrix. Laser beam is positioned over the diode of the central pixel.

be the origin as the RTN generated there would have the largest impact on the front-end operation [72]. It was expected that by increasing the transistor size, the effect of the RTN would be reduced (see sec. 4.2.2) [67]. Therefore pALPIDE-3 was produced in two versions featuring different size of the input transistor; pALPIDE-3a features a 0.22/0.18 µm (W/L) transistor (as the previous full-scale prototypes), while pALPIDE-3b a 0.92/0.18 µm (W/L) transistor.

Figure 4.19 shows the measured[1] detection efficiency and fake-hit rate of pALPIDE-3a and pALPIDE-3b as a function of the analogue front-end bias parameter `ITHR` (see sec. 4.1.2). Both versions satisfy the ITS upgrade requirements (see table 1.3) with regard to both detection efficiency and fake-hit rate. However, the difference in the fake-hit rate is evident; as expected from the larger input transistor, pALPIDE-3b exhibits orders of magnitude lower fake-hit rate and therefore this version is selected for the final ALPIDE design.

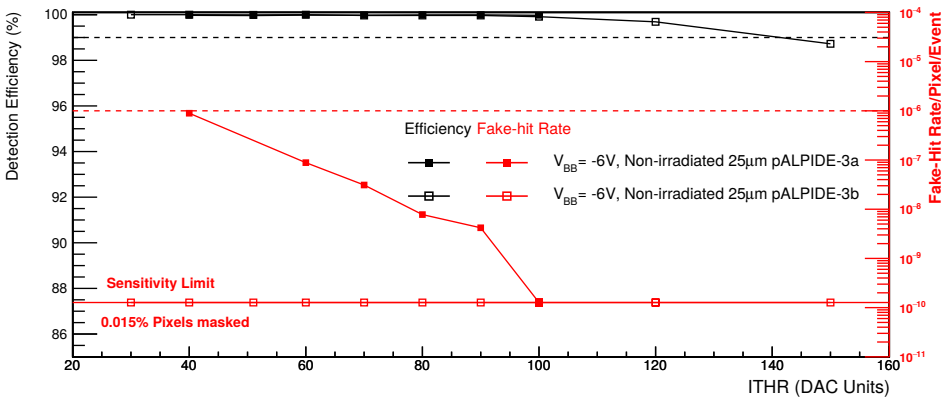

Figure 4.19: pALPIDE-3a and pALPIDE-3b comparison - Detection efficiency and fake-hit rate as a function of `ITHR`.

4.4 Performance of the final chip

In addition to laboratory measurements, the ALPIDE design has been validated in an extensive test-beam campaign by measuring the detection efficiency, the spatial resolution and the radiation hardness of the chip. The campaign was carried out using telescopes (see sec. 2.4.2) made entirely of the ALPIDE prototypes. The results of this campaign, supplemented with the laboratory measurements of fake-hit rate and analogue front-end

[1] Combined test-beam and laboratory measurements. See sections 2.4.2 and 4.3.2, respectively.

pulse shape, presented in this section demonstrate the compliance of the ALPIDE sensor with the ITS upgrade requirements (see tab. 1.3).

The results are discussed in two groups by the applied reverse substrate bias. In section 4.4.1, it is shown that ALPIDE can comply with both Inner and Outer Barrel requirements if the reverse substrate bias is applied. The performance without reverse substrate bias is presented in section 4.4.2, showing that Outer Barrel design and assembly could be simplified by not supplying reverse bias to the chips, while maintaining the required detection efficiency, fake-hit rate and spatial resolution.

4.4.1 Performance with reverse substrate bias

The impact of irradiating the ALPIDE with protons and neutrons on the detection efficiency and the fake-hit rate as a function of charge threshold is shown in figure 4.20. The NIEL fluence of 1.7×10^{13} 1 MeV n_{eq} cm^{-2} has no effect on the fake-hit rate while the detection efficiency is reduced. Nevertheless, it is still possible to operate the sensor with a detection efficiency higher than 99% for a wide range of threshold settings. The TID of 509 krad[1] on the other hand has no significant effect on the detection efficiency while the fake-hit rate is increased. However, it is still lower than the maximum allowed 10^{-6} $pixel^{-1}event^{-1}$, even at the lowest threshold.

The spatial resolution and the cluster size, before and after irradiation are shown in figure 4.21. It can be observed that the effect of the full non-ionising radiation dose expected during the detector lifetime in ALICE, including a safety factor of ten, and the full ionising radiation dose, is on the order of chip-to-chip fluctuations. In any case, the detector can be operated with a spatial resolution better than 5 µm.

The pulse shape characteristics of a sample of unirradiated ALPIDE chips i.e. the maximum pulse length and the maximum time walk (rising edge)[2] are shown in figure 4.22 as a function of the bias parameter `ITHR`[3]. The measured pulse length and time walk are in the agreement with the ITS upgrade timing requirements (see tab. 1.3).

[1] N.B. The TID of 509 krad is above the ionising radiation dose expected during the detector lifetime in ALICE (which is 270 krad). Irradiation to higher doses is ongoing in order to study the safety margin in terms of radiation dose.

[2] Maximum time walk is the rising edge t_1 defined in sec. 4.3.1. The naming change here is to draw attention to the effect of the increased t_1 which is the time walk.

[3] The threshold corresponding to different `ITHR` settings was not measured for the chips in the figure. Roughly, `ITHR` of 50 and 90 DAC units correspond to thresholds of 100 and 230 e^-, respectively.

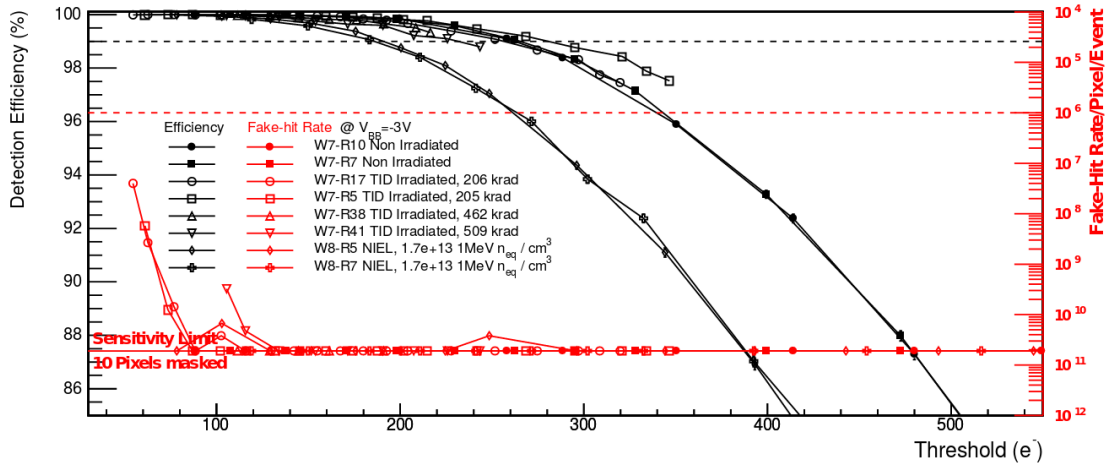

Figure 4.20: ALPIDE efficiency and fake-hit rate at $V_{BB} = -3$ V - Detection efficiency and fake-hit rate as a function of threshold of multiple sensors; comparison of performance before and after ionising and non-ionising radiation.

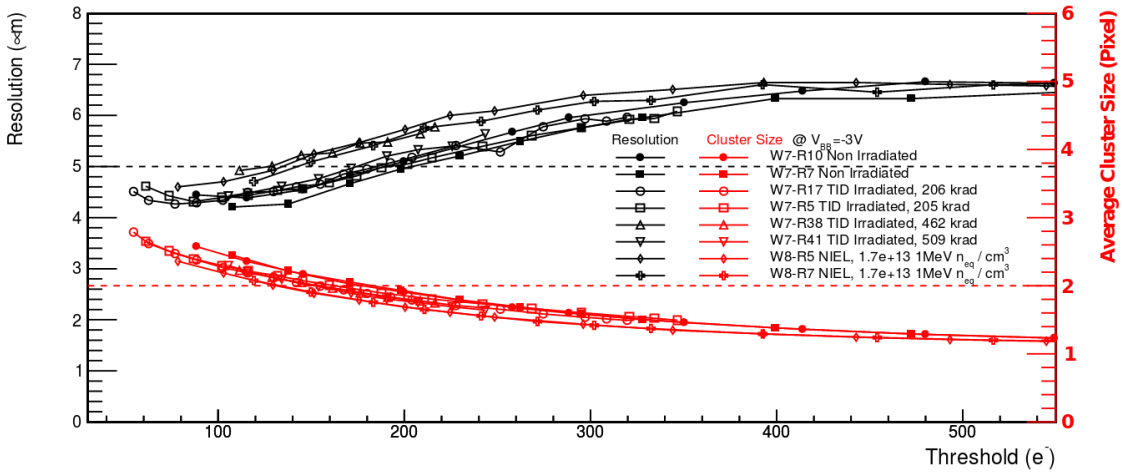

Figure 4.21: ALPIDE spatial resolution at $V_{BB} = -3$ V - Spatial resolution and average cluster size as a function of threshold of multiple sensors; comparison of performance before and after ionising and non-ionising radiation.

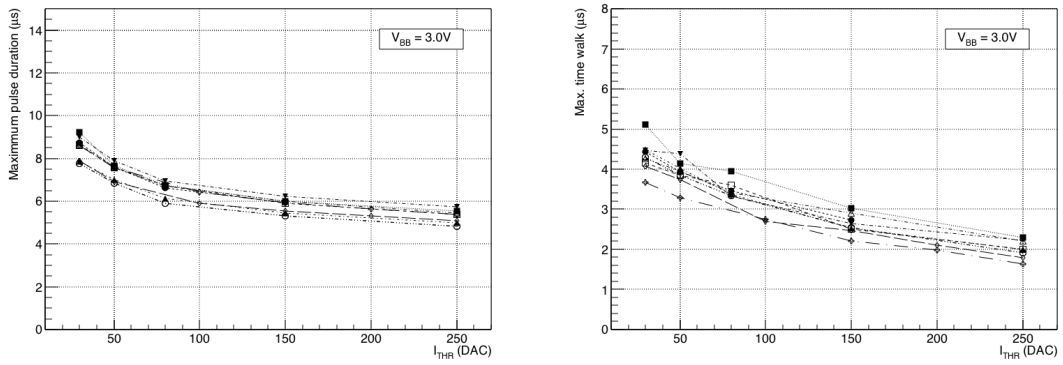

(a) Maximum pulse length vs ITHR. **(b)** Maximum time walk vs ITHR.

Figure 4.22: ALPIDE pulse shape at $V_{BB} = -3$ V - Maximum pulse length and maximum time walk (rising edge t_1) as a function of ITHR for a sample of tested chips.

4.4.2 Performance without reverse substrate bias

The detection efficiency and the fake-hit rate as a function of threshold for the ALPIDE chips with no reverse bias applied are shown in figure 4.23. Closed symbols represent the non-irradiated sensors while the open symbols represent the sensors that have received the full radiation dose expected during the detector lifetime in ITS OB, including a safety factor of ten (TID of 100 krad and NIEL of 10^{12} 1 MeV n_{eq} cm^{-2}). There is not any visible impact of the irradiation on the detection efficiency. The fake-hit rate is increased but still within the ITS upgrade tolerance. Confronting the fake-hit rate with the one measured at $V_{BB} = -3$ V (see fig. 4.20), it can be observed that, although still within the requirements, it is notably higher.

The residuals and the cluster size, before and after irradiation are shown in figure 4.24. The residuals are plotted instead of the spatial resolution as the telescope resolution was not evaluated for the telescope used in this measurement[1]. Furthermore, the outliers correspond to the datasets where some problems in the alignment were encountered, resulting in higher residuals. However, this doesn't change the fact that even after receiving the full radiation dose expected in Outer Barrel during the detector lifetime in ITS OB (see tab. 1.3), including a safety factor of ten, the detector can be operated without revere bias at a spatial resolution better than 10 µm.

[1]The residuals are actually spatial resolution and telescope resolutions summed in quadrature (see sec. 2.4.2), i.e. the spatial resolution is always lower than the measured residuals.

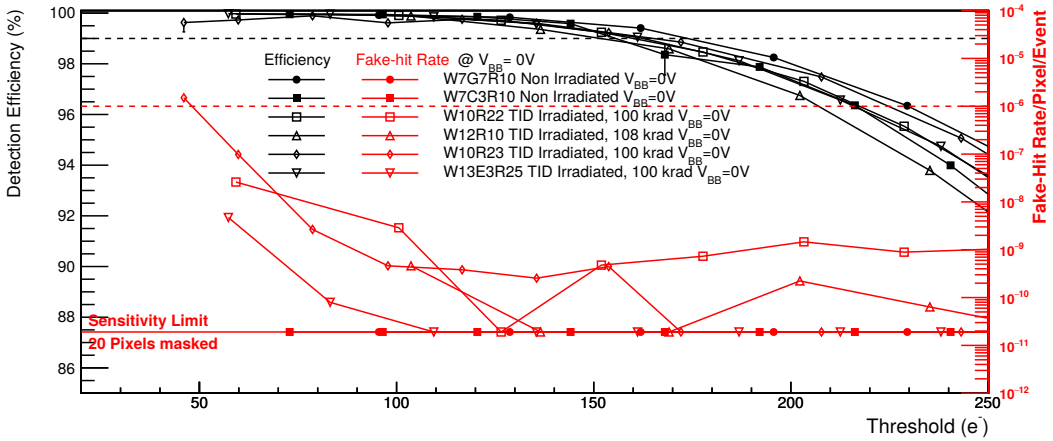

Figure 4.23: ALPIDE efficiency and fake-hit rate at $V_{BB} = 0$ V - Detection efficiency and fake-hit rate as a function of threshold of multiple sensors; comparison of performance before (open symbols) and after (closed symbols) ionising and non-ionising radiation (irradiated sensors have been exposed to a TID of 100 krad and NIEL of 10^{12} 1 MeV n_{eq} cm^{-2}).

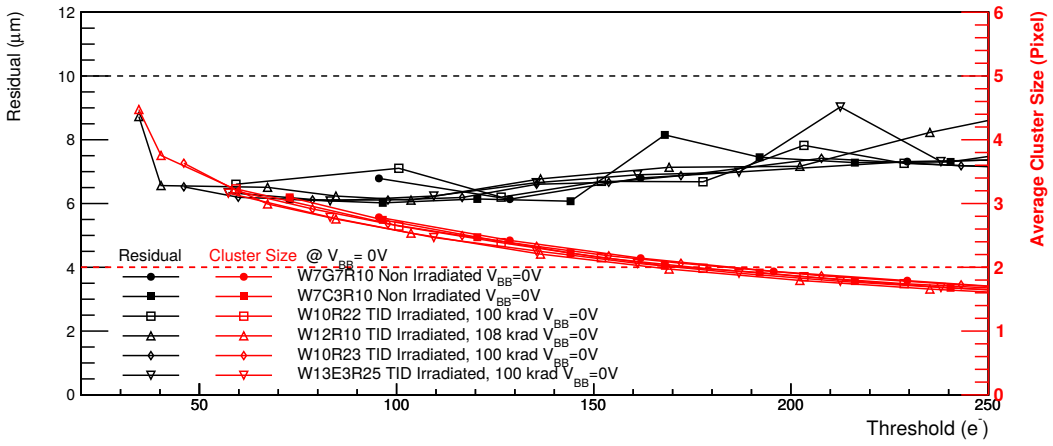

Figure 4.24: ALPIDE spatial resolution at $V_{BB} = 0$ V - Residuals and average cluster size as a function of threshold of multiple sensors; comparison of performance before (open symbols) and after (closed symbols) ionising and non-ionising radiation (irradiated sensors have been exposed to a TID of 100 krad and NIEL of 10^{12} 1 MeV n_{eq} cm^{-2}).

The maximum pulse length and the maximum time walk (rise edge) as a function of threshold and ITHR[1] are shown in figure 4.22 for a sample of irradiated and non-irradiated ALPIDE chips. The impact of the irradiation on the pulse shape is not significant compared to the chip to chip fluctuations. Also, the reverse bias has no apparent effect on the maximum pulse length and time walk.

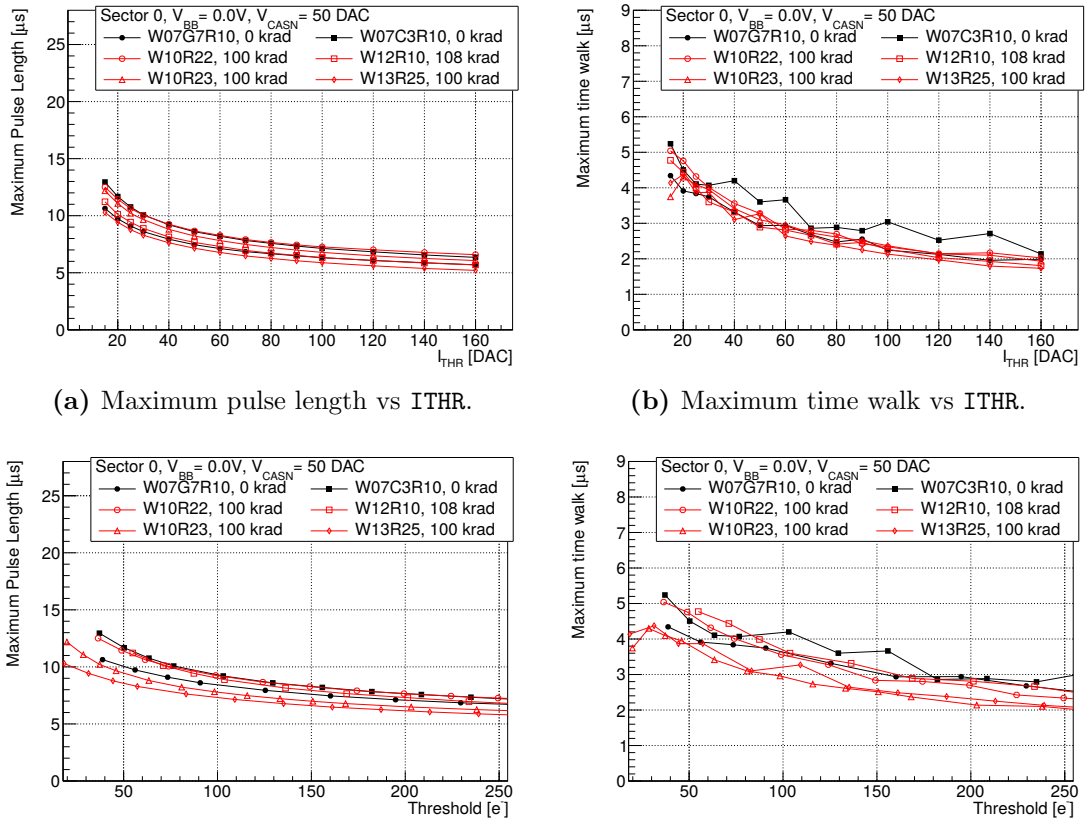

(a) Maximum pulse length vs ITHR.

(b) Maximum time walk vs ITHR.

(c) Maximum pulse length vs threshold.

(d) Maximum time walk vs threshold.

Figure 4.25: ALPIDE pulse shape at $V_{BB} = 0$ V - Maximum pulse length and maximum time walk (rising edge t_1) as a function of ITHR and threshold for a sample of tested chips. Irradiated sensors (open symbols) have been exposed to a TID of 100 krad and NIEL of 10^{12} 1 MeV n_{eq} cm^{-2}.

The presented results indicate that ALPIDE chip operated without reverse substrate bias is suitable for equipping the Outer Barrel of the ITS but in order to cope with the increased radiation in Inner Barrel it is desirable to have the additional operation margin provided by the reverse substrate bias.

[1]The data is plotted as a function of ITHR for easier comparison with figure 4.25.

4.5 Summary

The ALPIDE chip, based on the TowerJazz 180 nm CMOS Imaging Process, has been developed for the ALICE ITS upgrade. A particular process feature, the deep p-well, is exploited so the full CMOS logic can be implemented over the active sensor area without impinging on the deposited charge collection. ALPIDE is implemented on silicon wafers with a high resistivity epitaxial layer. A single chip measures 15 mm by 30 mm and contains half a million pixels distributed in 512 rows and 1024 columns. The in-pixel circuitry features amplification, shaping, discrimination and multi-event buffering. The readout is hit driven i.e. only addresses of hit pixels are sent to the periphery.

Three full-scale prototype generations have been produced in the context of the ALPIDE development. The in-pixel front-end pulse length has been measured with pALPIDE-1 and pALPIDE-3, showing improvements in case of the latter in terms of shorter pulse length and better uniformity of the pixel response. Two versions of pALPIDE-3, featuring different input transistor sizes. have been tested. The version with the larger input transistor presented orders of magnitude better performance in terms of fake-hit rate.

The upgrade of the ITS presents two different sets of requirements for sensors of the Inner and of the Outer Barrel due to the significantly different track density, radiation level and active detector surface. The ALPIDE chip fulfils the stringent requirements in both cases. The detection efficiency is higher than 99%, fake hit probability is orders of magnitude lower than the required 10^{-6} and spatial resolution within required 5 µm. This performance is maintained even after an irradiation up to 500 krad and few 10^{13} 1 MeV n_{eq}/cm^2, which is above what is expected during the detector lifetime.

5

Test of an ITS upgrade stave in the NA61/SHINE experiment

The ALPIDE chip was extensively characterised in the laboratory and has been shown to fulfil the requirements of ITS upgrade (see ch. 4). Furthermore, it is desirable to confirm its performance under operation in a heavy-ion physics experiment[1]. The opportunity to test an ALPIDE stave in an experiment, before the installation in ALICE, was granted by the NA61/SHINE collaboration. The NA61/SHINE experiment has similar physics goals as ALICE, among which the study of the physics of strong interactions by investigating fixed-target Pb-Pb collisions [73]. Therefore, implementing an ALPIDE stave in the NA61 recently developed Vertex Detector [74], provides a similar environment to the one ITS detectors will face in ALICE in terms of particle multiplicities and the studied physics.

In this chapter, the NA61/SHINE experiment, with a particular focus on its Vertex Detector, will be presented and the performance of an ALPIDE Inner Barrel stave in the NA61 experiment will be discussed.

5.1 NA61/SHINE experiment

NA61/SHINE (SPS Heavy Ion and Neutrino Experiment) is a particle physics experiment at the CERN SPS. The experiment studies the hadronic final states produced in interactions of various beam particles (pions, protons and beryllium, argon, and xenon nuclei) with a variety of fixed nuclear targets at the SPS energies. The NA61 physics goals include measurements of physics of strong interactions, in particular, the study of the onset

[1] In an experiment, the operational environment contains additional (more realistic) noise sources as, for example, other detectors and the corresponding readout electronics.

of deconfinement and search for the critical point of strongly interacting matter which is pursued by investigating fixed target p-p, p-nucleus and nucleus-nucleus collisions [73].

The layout of the NA61/SHINE detector is sketched in fig. 5.1. It consists of a large acceptance hadron spectrometer with excellent capabilities in charged particle momentum measurements and identification by a set of six Time Projection Chambers (TPC) as well as Time-of-Flight (TOF) detectors. The high resolution forward calorimeter, the Projectile Spectator Detector (PSD), measures energy flow around the beam direction, which in nucleus-nucleus reactions is primarily a measure of the number of spectator nucleons and thus related to the centrality of the collision. An array of beam detectors identifies beam particles, secondary hadrons and ions as well as primary ions, and measures precisely their trajectories.

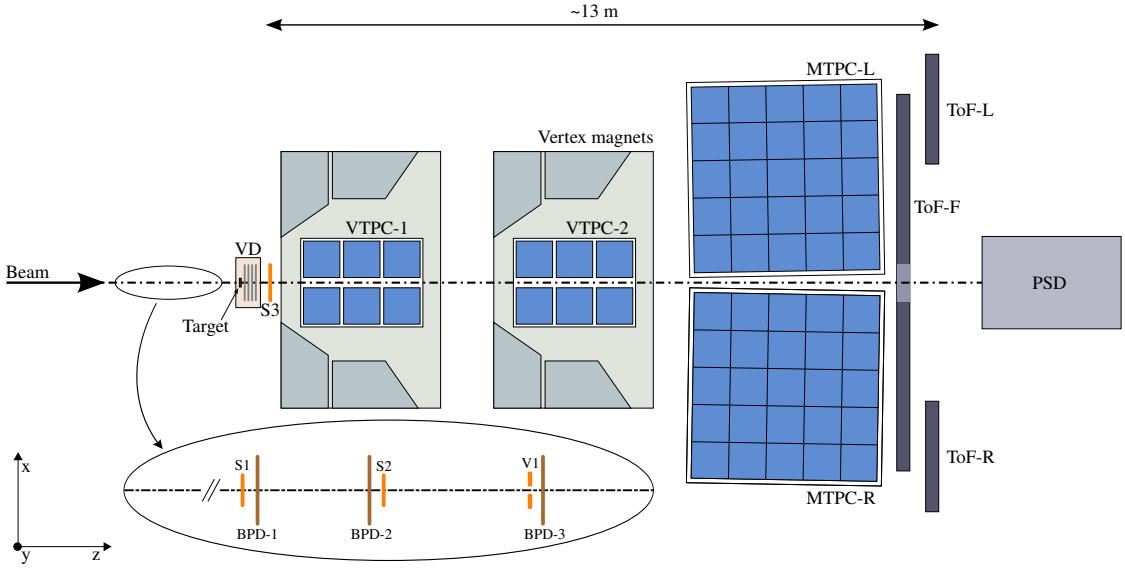

Figure 5.1: Schematic layout of NA61/SHINE experiment - The chosen right-handed coordinate system is shown on the plot. The incoming beam direction is along the z axis. The magnetic field bends charged particle trajectories in the x-z (horizontal) plane. Not to scale.

5.1.1 Vertex Detector

The recently installed Vertex Detector (VD) is positioned between the primary vertex (target) and the first VTPC of the NA61/SHINE apparatus (see fig. 5.1). The VD sensors and the relevant supporting elements form stations, called VDS1-VDS4, located at 5, 10, 15

and 20 cm distance from the target (see fig. 5.2a). The design includes four VD stations i.e. four planes of monolithic active pixels sensors MIMOSA-26 mounted on lightweight vertical carbon fibre panels. These carbon fibre panels are actually the identical structures to those used as the cold plates of the Inner Barrel (IB) stave of the ALICE ITS upgrade (see ch. 1), thus allowing straightforward installation of the IB staves in the VD. The lightweight support, cooling and precise positioning carbon fibre structures with MIMOSA-26 chips are mounted on the C-shape support frames depicted in figure 5.2b. The number of MIMOSA-26 chips, forming each sensitive plane, vary depending on the distance to the target; for each side of the beam[1], there is a single sensor in the first two VD stations, two sensors in the third station and four sensors in the last station (see fig. 5.2a). All VD components and the target are housed inside a hermetic box structure filled with helium (at atmospheric pressure). The He gas inside the box helps to further minimise the multiple scattering and hence improves the tracking performance for low-momentum charged particles within the VD. The design of the NA61/SHINE VD ensures $X/X_0 \leq 0.2\%$ per sensitive layer of Si-detectors (including the chip and the services) [75].

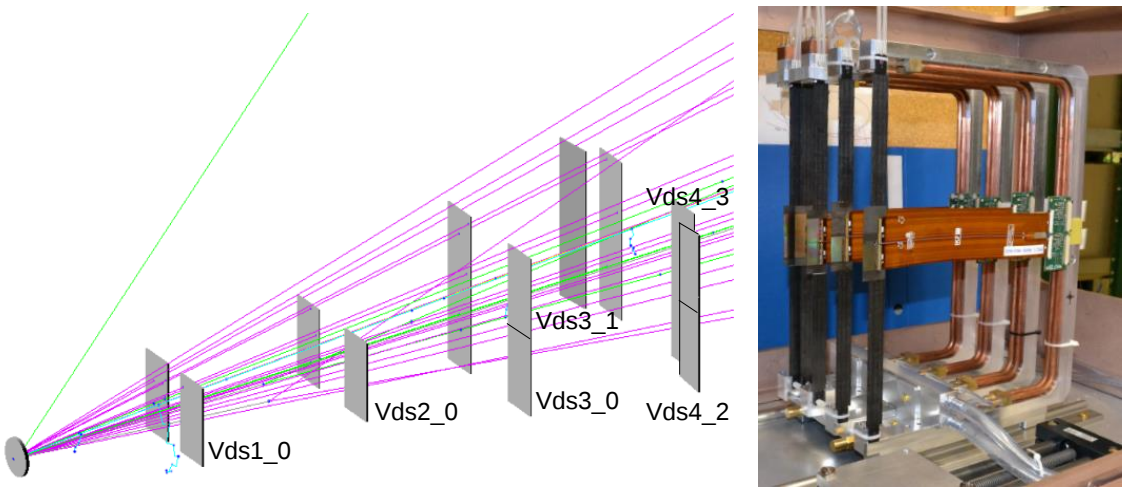

(a) 3-D scheme **(b)** C-shape support

Figure 5.2: NA61 Vertex Detector - Detectors and the relevant supporting elements form stations, located at 5, 10, 15 and 20 cm distance from the target. The stations are mounted on the C-shape support.

[1]The beam sides are named by the mountains they are facing i.e. Salève and Jura.

5.2 Integration of an Inner Barrel stave in the NA61 Vertex Detector

An Inner Barrel (IB) stave (see ch. 1), composed of 9 fully operational ALPIDE chips, was installed in the NA61 Vertex Detector before the Pb-Pb data taking from 8th to 12th December 2016 [76, 77]. The stave was positioned in the third VD station on the Salève side (see fig. 5.3), slightly in front of the respective MIMOSA-26 sensors (see fig. 5.4). This position has the advantage that the IB stave is sandwiched between the VD layers allowing for a detection efficiency measurement (see sections 2.4.2 and 5.3). The resulting geometrical overlap of the IB stave with the all four VD stations is very limited (indicated by thick red and blue lines in fig. 5.4), while the overlap with the first, second and fourth VD station (indicated by thick red lines) is sufficient for the analysis performed in the following section.

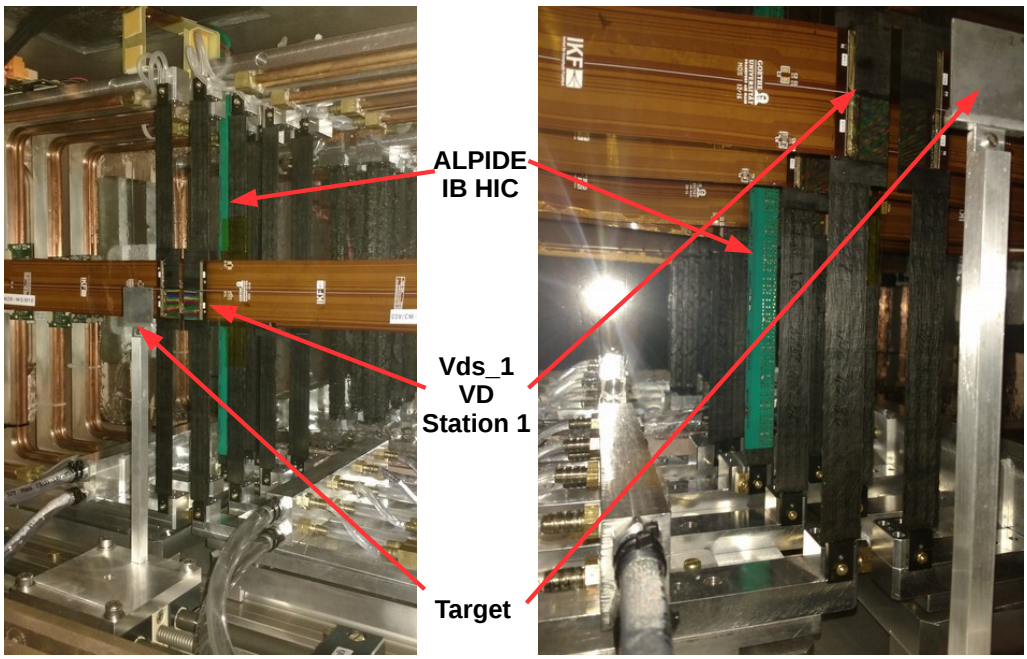

Figure 5.3: Inner Barrel stave inside VD - The IB stave is installed in the third VD station. The Pb target and the first VD station sensors are also visible in the picture.

The mechanical constraints did not allow to attach the cooling pipes to the cold plate and therefore the ALPIDE sensors temperature was not regulated. Furthermore, due to an issue with the reverse bias connection caused during the stave assembly, it was not possible to apply reverse substrate bias and hence all IB sensors were operated at $V_{BB} = 0$ V.

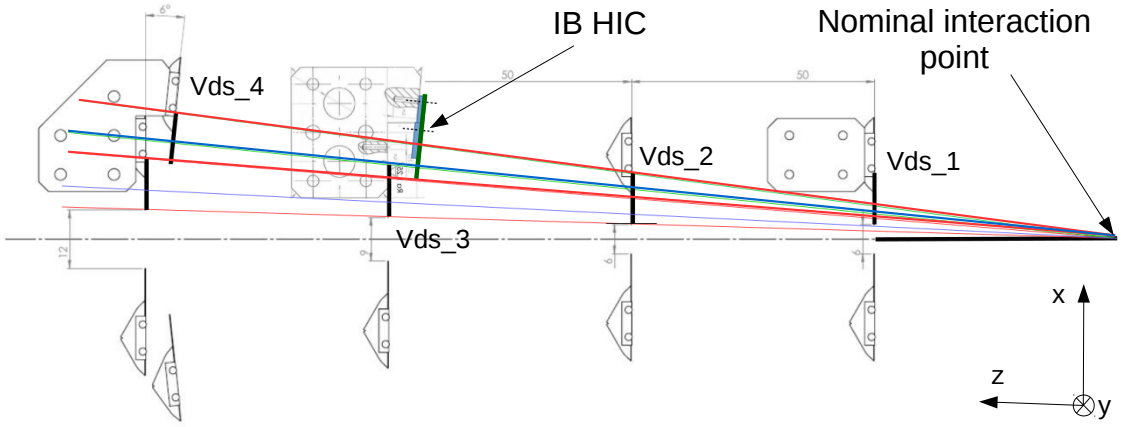

Figure 5.4: Schematic (top) view of the VD including the IB stave - The IB stave is installed in the third VD station, 15 cm from the Pb target. and at an angle of 6 deg w.r.t. the beam-line. The coloured lines indicate the VD acceptance. Thick red lines show overlap of the IB stave with the 1st, 2nd and 4th VD station. ADD MIMOSA-26 label

The IB stave was read out using the MOSAIC board [78] which is also used for the laboratory tests of staves. The readout software was written specifically for this purpose based on the existing laboratory testing software. The stave readout and control was standalone i.e. not integrated in the NA61 DAQ, and the data was merged offline. The offline merging was done in the reconstruction phase using the trigger counter, since the trigger signal used by the IB was the same one sent to the VD. The maximum NA61 trigger rate is 83 Hz [79] which is orders of magnitude lower than what the ALPIDE and MOSAIC readout system can handle. Furthermore, the NA61 trigger employs ± 25 µs past/future protection (against off-time particles) [80], which is significantly longer than the ALPIDE front-end pulse length (see sections 4.1.2 and 4.4). Therefore no trigger related issues such as high busy or pileup were expected (nor encountered). In total 645k physics triggers were recorded, of which 125k were acquired without the magnetic field and were used for the alignment and analysis in section 5.3.

The IB sensors 0, 1 and 2 were not read out due to a loose connection of the high speed data transmission cable connecting the stave and the MOSAIC board. The issue was discovered only after the data taking had already started and the connector was not accessible without interfering with the NA61 operations. However, since the three sensors were in any case out of the beam i.e. outside the VD acceptance, this was not a problem.

5.3 Analysis and results

A hit map measured with the IB stave in a Pb-Pb run is shown in figure 5.5. The first three ALPIDE sensors show no hits since they were disconnected from the readout (see sec. 5.2). Predictably, most of the hits involve ALPIDE chip 4 as it is closest to the beam axis. Therefore, all the following plots in this section will refer to that sensor[1], unless stated otherwise.

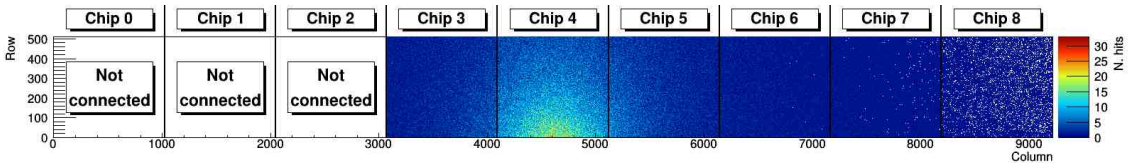

Figure 5.5: IB stave hit map in Pb–Pb run - The beam is centred near chip 4.

The distribution of hit pixels per event is shown in fig. 5.6a, which after the clusterisation (see sec. 2.4) results in the distribution of hit clusters per event shown in fig. 5.6b. The distribution of hit pixels per event indicates that the number of pixels 3 per event varied from few to up to more than 300, yet the readout of this variable data-stream was handled without issues. In fact, ALPIDE is designed to handle the particle densities of 30 hit/cm^2 [18], which is also the maximum hit density measured in NA61 (considering chip active area of 4.1 cm^2 and maximum number of hit clusters in fig. 5.6b.

The cluster size distribution in figure 5.7a shows that clusters containing more than 100 pixels have been observed. An example of such a cluster, containing 869 pixels is shown in figure 5.7b. It is most likely a product of a δ-ray emitted parallel to the sensor surface. Indeed, these events are rare, but it was important to verify that they can be reconstructed i.e. do not cause any problems in the stave readout.

5.3.1 Fake-hit rate

A period without beam, while the NA61 experiment was fully operational and prepared for the data taking[2], was exploited to measure the fake-hit rate (see sec. 4.2.2) in the experi-

[1] There would be no difference if the entire stave was considered in the analysis, however the choice of analysing only chip 4 greatly simplifies the plotting and speeds up the code by reducing the combinatorial background (see sec. 5.3.2) with no information loss. Furthermore, the results are more directly comparable with the single chip results (see ch. 4) and division of IB stave into 9 chips is anyhow natural.

[2] All detectors and the corresponding electronics were operational thus acting as potential noise sources.

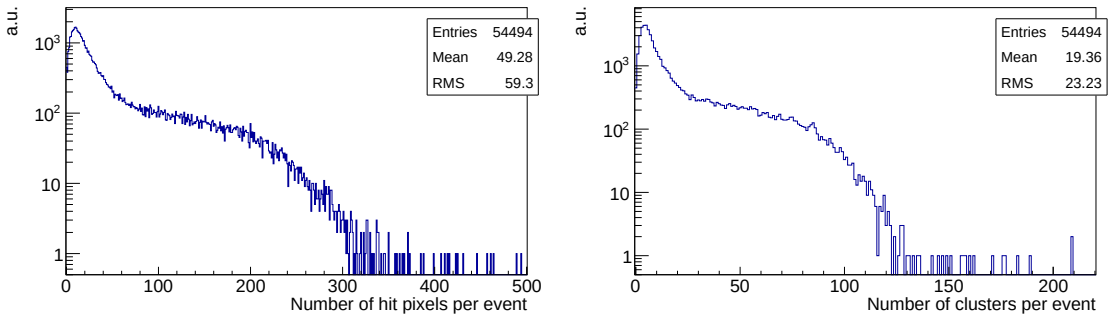

(a) Number of hit pixels per event **(b)** Number of clusters per event

Figure 5.6: Distributions of hit pixels and clusters per event - The distribution of hit pixels per event (a) indicates that number of pixels was as high as 300 per event. The distribution of clusters per event (b) gives the maximum hit density of 30 hit/cm^2 (chip 4).

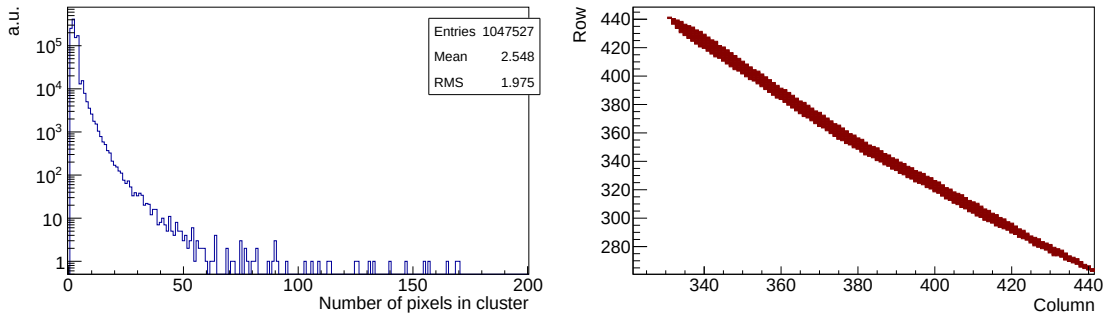

(a) Cluster size distribution **(b)** Example of a large cluster

Figure 5.7: Measured cluster size in Pb-Pb collisions - Cluster size distribution (a) and an example of cluster containing 868 pixels (b).

ment. A total of 2.8×10^6 random triggers were issued to the IB stave and the number and position of hits is reported in figure 5.8. 22 pixels showed a total of 121,440 hits, concentrated to a single noisy pixel in chip 5. The resulting fake-hit rate is $\approx 10^{-8}$ pixel^{-1}event^{-1} without masking, and lower than the sensitivity limit i.e. $< 10^{-11}$ pixel^{-1}event^{-1} with 10 noisiest pixels masked. This result is compatible with the single chip results (see sec. 4.4.2).

5.3.2 Alignment and residuals

In order to determine the spatial resolution and the detection efficiency, the sensor had to be aligned w.r.t. the VD. Since the IB stave DAQ was standalone (see sec. 5.2), the data were not integrated into the VD reconstruction and analysis framework. Therefore, the alignment procedure was done with a dedicated procedure, as described here.

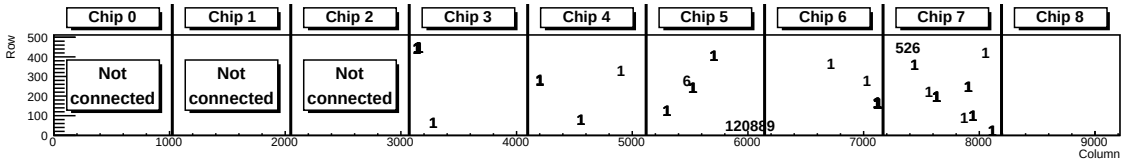

Figure 5.8: Fake-hit rate of the IB stave installed in NA61 VB - The numbers indicate the approximate position and the number of times a pixel fired in 2.8×10^6 recorded events.

Starting from the IB stave nominal position[1], the differences between the all combinations of the IB stave reconstructed cluster positions[2] and the VD track hits on the IB stave plane were calculated. Only the VD tracks[3] involving all four VD stations were used in this procedure as they provide better tracking resolution (w.r.t. the VD tracks involving three VD stations). The resulting distributions are plotted in figure 5.9. The alignment peak (around 0 mm), corresponding to the correctly matched clusters and tracks, is dominated by the combinatorial background.

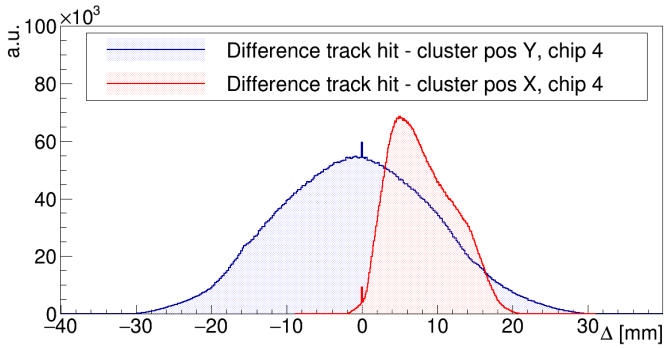

Figure 5.9: Reconstructed cluster position and track hit difference - The alignment peak (around 0 mm) is dominated by the combinatorial background.

The very different shape of the X and Y combinatorial backgrounds is given by the position of the IB stave (see fig. 5.4). That is, the IB stave is centred w.r.t. the beam in the Y-direction while it is shifted in the X-direction. This is best visible in figure 5.10 which shows impinging points of all the VD reconstructed tracks (which include all 4 stations) on the IB stave plane. The tracks hitting the IB stave are plotted in the color-scale, while all other tracks in the grey-scale. The impinging point distribution shape is given by the

[1]Nominal position was determined from metrology performed after positioning VD into place.
[2]For reconstructing cluster position centre of mass method is used, see sec 2.4.
[3]VD track were reconstructed via dedicated VD simulation and reconstruction framework [76, 81].

spatial arrangement of the VD sensors. In particular, lower statistics in the bottom half of the IB stave chip 4 is due to `VDS4_2` sensor (see fig. 5.2a and 5.4) not being operational.

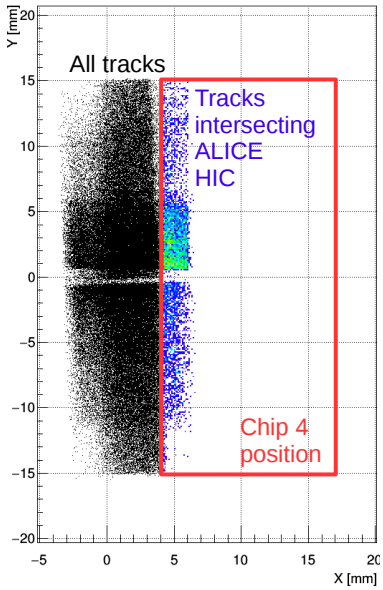

Figure 5.10: Impinging points of VD tracks on the IB stave - The VD reconstructed tracks (which include all 4 stations) hitting the IB stave are plotted in the color-scale, while other tracks in the grey-scale. The approximate position of chip 4 is indicated by the red square.

In order to reduce the combinatorial background (see fig. 5.9), the following cut was applied. Taking into account all the cluster-track pairs, and the corresponding position differences $\Delta x = x_{\text{cluster}} - x_{\text{track}}$ and $\Delta y = y_{\text{cluster}} - y_{\text{track}}$, only those Δx and Δy are considered for which $|\Delta y| < 0.25$ mm and $|\Delta x| < 0.25$ mm, respectively. The resulting distributions are plotted in figure 5.11, where it can be seen that the combinatorial background has been significantly reduced. In fact, the signal (events in the alignment peak) now dominates the combinatorial background.

The same distributions are shown in figure 5.12 with a smaller x-axis range, around the alignment peak. At this scale, the combinatorial background can be approximated as constant. Therefore, the data is fitted with a sum of Gaussian and uniform distributions. The fit results are shown in the figure; there is a small offset in both dimensions (the distributions are expected to be centred at 0 mm).

To correct for this offset i.e. to achieve the final alignment, it was decided to use a numerical procedure to minimise the residuals. First of all, the track-cluster pairs in the

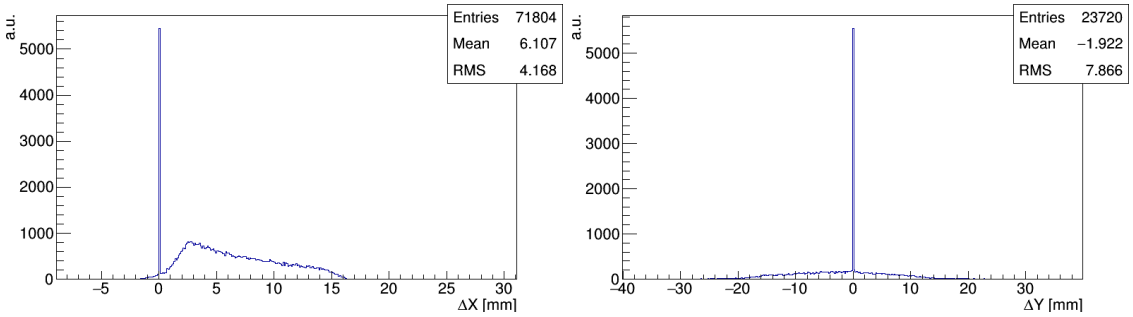

(a) X-direction **(b)** Y-direction

Figure 5.11: Cluster position and track hit difference with cuts - The combinatorial background has been significantly reduced.

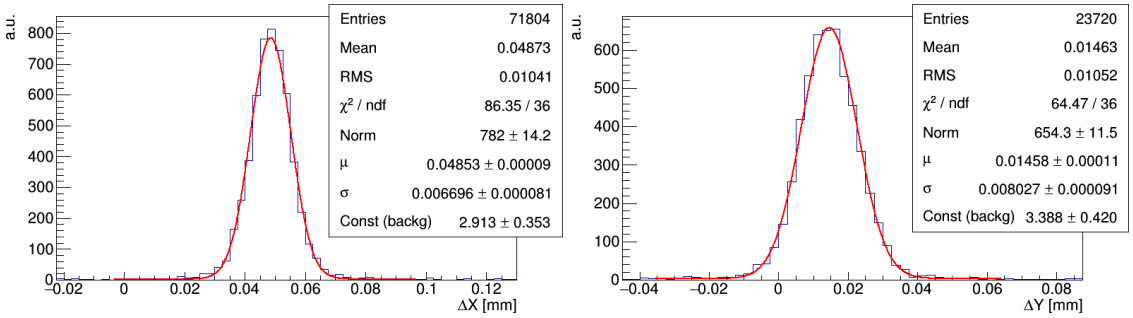

(a) X-direction **(b)** Y-direction

Figure 5.12: Cluster position and track hit difference with cuts zoomed - The same distribution as in figure 5.11 but with different x-axis range. The red curve is a result of a fit with sum of a Gaussian and a uniform distribution.

alignment peak were selected such that $|\Delta x - \mu_x| < 4\sigma_x$ and $|\Delta y - \mu_y| < 4\sigma_y$ with values for μ and σ reported in figure 5.12. For the selected track-cluster pairs, the sum of residuals is defined as

$$R(x_s, y_s, z_s, \theta_s, \varphi_s, \psi_s) = \sum_i \left[(x_{\text{cluster},i} - x_{\text{track},i})^2 + (y_{\text{cluster},i} - y_{\text{track},i})^2 \right]$$

where x_s, y_s, z_s and $\theta_s, \varphi_s, \psi_s$ are coordinates and rotations defining the IB stave position in the NA61 reference frame[1]. $R(x_s, y_s, z_s, \theta_s, \varphi_s, \psi_s)$ is minimised w.r.t. all six variables using the MINUIT package [82]. The residual distributions after alignment are shown in figure 5.13. The distributions are now centred at 0 mm and RMS values (residuals) are

[1] It is not explicitly stated in the equation but the quantities depending on these variables are $x_{\text{cluster},i}$ and $y_{\text{cluster},i}$.

reduced. A slightly wider distribution in Y-direction is consistent with the rectangular pixels (see sec. 4.1).

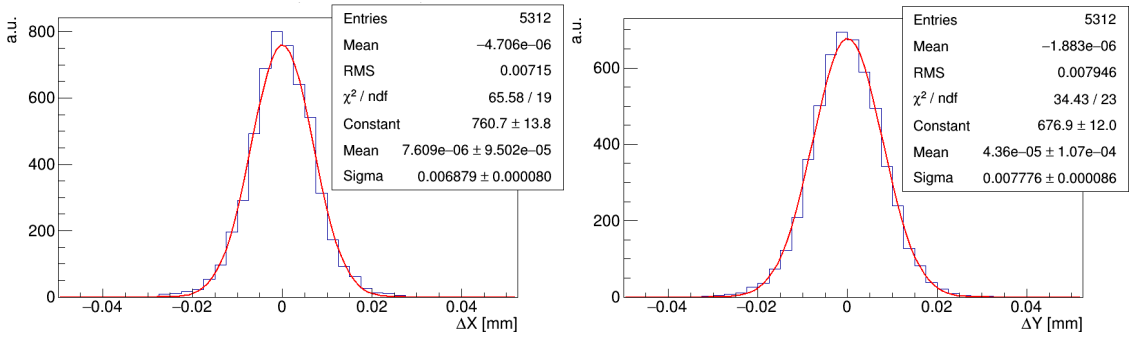

(a) X-direction **(b)** Y-direction

Figure 5.13: Residual distributions - Cluster position and track hit difference after alignment. Better resolution X-dimension is consistent with rectangular pixel pitch.

In order to calculate the spatial resolution, the tracking resolution would have to be subtracted (see sec. 2.4). However, to evaluate the tracking resolution, a full physics simulation is required as the particle used as tracks originate from the Pb-Pb collisions and therefore their species and momentum have to be modelled and are not known as in a test-beam. Alternatively, the particle species and momentum range could be selected using particle identification information from the TPCs, but the TPC reconstructed data were not available at the time of writing of this thesis.

Anyhow, the measured residuals of 7-8 µm are consistent with the results obtained with single chips operated at $V_{BB} = 0$ V (see sec. 4.4.2).

5.3.3 Detection efficiency

The detection efficiency calculated using the method discussed in section 2.4.2 results to be $\approx 75\%$. This result is unexpectedly low; previous measurements have shown (see fig. 4.23) that even for high threshold values, the ALPIDE detection efficiency remains higher than 90%. Furthermore, 7 µm residuals are not consistent with a low efficiency caused by a high threshold (see fig. 4.24). Also, the IB stave was operated at nominal settings and the measured threshold was ~ 90 e$^-$ (with chip to chip variations within ± 20 e$^-$).

After a thorough investigation, only one hypothesis capable of explaining these results remained. The VD sensors, MIMOSA-26 feature integration time of $\sim$ 100 µs, while ALPIDE $<$ 10 µs, determined by the pulse length or the `STROBE_B` length, whichever

is longer (see sec. 4.1.1). Furthermore, the NA61 past/future protection is ±25 µs (see sec. 5.2). Therefore, it is possible that an off-time particle is detected by the MIMOSA-26 sensors but not by the ALPIDE chips. In order to verify this hypothesis, two cuts were introduced.

The first cut requires that all tracks used in the efficiency calculation originate from the primary vertex. Therefore a well defined primary vertex is required i.e. at least 10 contributors to the primary vertex are imposed with the RMS of the distance of closest approach of all contributing tracks to each other < 100 µm in both x and y dimensions[1]. The detection efficiency after implementing this cut increased to 96%.

The second cut discarded from the efficiency calculation all events that did not contain any efficient tracks at all. Although it might appear that this cut introduces a strong bias, it actually separates two classes of events. Figure 5.14a shows the IB stave hit multiplicity distribution for the discarded events and the events considered in the efficiency calculation. The discarded events exhibit significantly lower hit multiplicity in the IB stave while for the same events the number of VD reconstructed tracks (see fig. 5.14b) follows the same distribution as in case of the accepted events. This behaviour is consistent with the off-time events hypothesis. This hypothesis can be further verified once the full NA61 TPC reconstructed tracks become available.

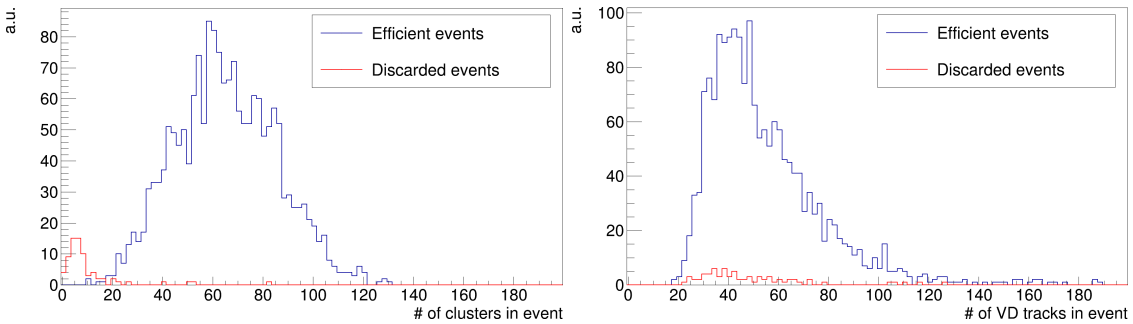

(a) IB stave hit multiplicity **(b)** VD reconstructed track multiplicity

Figure 5.14: IB stave hit and VD track multiplicity - The number of IB stave clusters (left) and the VD tracks (right) per event for discarded and accepted (efficient) events.

After implementing both cuts the detection efficiency results $99.85^{+0.06}_{-0.34}$ (stat) %. This result is achieved by using only the tracks involving all 4 VD stations i.e. the same that were

[1] VD vertex reconstruction precision in z dimension is an order of magnitude lower than in x and y [75] and was omitted in this cut.

used for the alignment (see sec. 5.3.2). However, the geometrical overlap of the IB stave and the 3rd VD stations is very limited (see fig. 5.4), resulting in limited statistics as shown in fig. 5.15a. Therefore, it was decided to also use the tracks reconstructed using 3 VD stations (1st, 2nd and 4th) since the tracking resolution performance is not crucial in this analysis. The impinging points of these tracks on the IB stave are shown in figure 5.15b. An order of magnitude was obtained in statistics and the measured detection efficiency is $99.79^{+0.04}_{-0.07}$ (stat) %. This result is compatible with single chip test-beam measurements within the statistical uncertainties (see sec. 4.4.2).

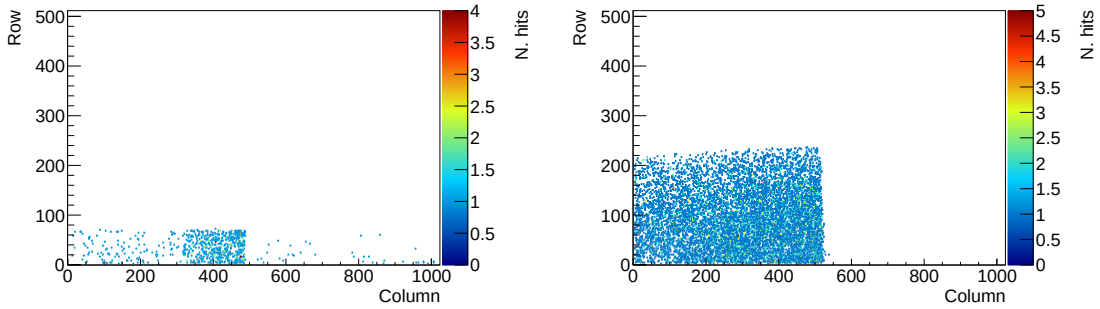

(a) Tracks involving 4 VD stations **(b)** Tracks involving 3 VD stations

Figure 5.15: Impinging points of tracks used in efficiency calculation on the IB stave - Tracks impinging points extrapolated to ALPIDE chip 4. There are almost no hits on the right half of the sensor due to an inefficient VD sensor (`VDS4_2`, see sec. 5.3.2 and fig. 5.10).

5.4 Summary

An ALICE ITS Inner Barrel stave, composed of 9 ALPIDE chips was tested in the Pb-Pb collision environment of the NA61/SHINE experiment. The integration was successful and no issues with the readout or chips were encountered. Hit multiplicities up to 30 hit/cm^2 were measured which is the expected maximum hit density at the first layer of the upgraded ITS. The chip performance in a stave is comparable with the performance of chips in the laboratory and test-beam; the detection efficiency is higher than 99% and fake-hit rate is lower than 10^{-10} pixel^{-1}event^{-1}. The spatial resolution was not calculated but the residuals of 7-8 µm are comparable to single-chip results.

6

Monte Carlo simulation of charge collection process in MAPS

Low-level simulations of the sensor are important for providing in-depth understanding of the detector response, which subsequently plays a key part in the simulation and analysis chain in HEP experiments. The exact response of MAPS is challenging to model due to contributions from both epitaxial layer and substrate, a typically only partially depleted active volume, and complex well structures. Transient TCAD simulations provide a good description but are not sufficiently fast to be used in the experiments simulations.

A *fast tool* developed to model the response of ALICE ITS MAPS, will be presented in this chapter. The basic concept is a first principles Monte Carlo simulation, using electric fields extracted from a TCAD simulation to model the charge carrier drift. That is, the more complex part is handled by a TCAD simulation while preserving the speed of a MC simulation with only one free parameter. The tool is versatile, any MAPS architecture can be simulated once the proper external electric field is provided. So far, INVESTIGATOR (analogue output) and ALPIDE (digital output) chips, developed for the ALICE ITS upgrade, have been simulated. It will be shown that an excellent agreement between data and simulation has been achieved, both for ^{55}Fe X-rays and minimum ionizing particles.

6.1 Simulation concept

The simulation design is based on three requirements - the simulation had to be versatile, simple and fast. Therefore, it was decided to implement it without using any of the pre-existing simulation frameworks such as GEANT4 or TCAD but rather to write it from

scratch. The main code is written in C++ and optimised to be run as parallel batch processes.

The essential task of the simulation is carrier transport in a sensitive volume with and without the presence of an electric field. In fast Monte Carlo simulations[1], the electric field can be approximated as uniform or negligible, therefore allowing to reduce carrier transport to either drift or diffusion. With high-resistivity epitaxial layer MAPS this is not the case, so an alternative approach had to be devised. Diffusion is simulated as random walk of each individual electron. A random walk step corresponds to an elapsed time which can be calculated[2] from the diffusion equation (see sec. 6.1.1). If there is an electric field present a drift step is calculated (knowing the elapsed time) and added to the diffusion step.

Response of various MAPS types is obtained by setting the geometrical parameters such as pixel pitch, epitaxial and substrate layer thicknesses (see sec. 6.1.3) and using a different electric field (see sec. 6.1.4). Carrier lifetime is also taken into account as it depends on the doping level (which is orders of magnitude higher in the substrate w.r.t. the epitaxial layer) and can also be used to simulate non-ionising radiation damage (see sec. 6.1.2).

6.1.1 Stepping

While the diffusion equation describes collective behaviour of deposited charge cloud, single charge carrier motion can be represented as random walk [84]. An electron diffusion step $\vec{l_i}$ is therefore a movement in a random direction uniformly distributed over the full solid angle. The step length is $|\vec{l_i}| = \Delta l$ and corresponds to the time interval Δt. After N steps, and an elapsed time $t = N\Delta t$, the electron will move a distance along its own path

$$L_{rw} = \left| \sum_{i=1}^{N} \vec{l_i} \right| \tag{6.1}$$

with mean distance from the starting point

$$\langle L_{rw} \rangle = \sum_{i=1}^{N} \vec{l_i} = 0 \tag{6.2}$$

[1] E.g. simulations described in [47] and [83].

[2] The motivation to execute simulation in diffusion steps and then convert them to time steps is purely historical, there is no reason why one couldn't do it the other way around. This simulation started out as an approximation without an electric field [47], that is, the only carrier transport mechanism was diffusion, while electric field was approximated as depletion regions where electrons were collected immediately.

and mean square value of

$$\langle L_{rw}^2 \rangle = \left(\sum_{i=1}^{N} \vec{l}_i \right)^2 = \sum_{i=1}^{N} \vec{l}_i \cdot \vec{l}_i + \sum_{i \neq j}^{N} \vec{l}_i \cdot \vec{l}_j = \sum_{i=1}^{N} |\vec{l}_i|^2 = N \Delta l^2 \tag{6.3}$$

These moments can also be calculated starting from the diffusion equation[1]

$$\frac{\partial n(\vec{r}, t)}{\partial t} = D \nabla^2 n(\vec{r}, t) \tag{6.4}$$

where D is the diffusion coefficient and $n(\vec{r}, t)$ is the carrier concentration normalised as

$$\int_{\mathbb{R}^3} n(\vec{r}, t) d\vec{r} = N_{tot} \tag{6.5}$$

with N_{tot} the total number of electrons. Now the equation for the mean charge displacement is

$$\langle L_d \rangle = \int_{\mathbb{R}^3} \vec{r} n(\vec{r}, t) d\vec{r} = 0 \tag{6.6}$$

and for its mean square value

$$\langle L_d^2 \rangle = \int_{\mathbb{R}^3} |\vec{r}|^2 n(\vec{r}, t) d\vec{r} = 6Dt \tag{6.7}$$

Equations 6.6 and 6.7 can be demonstrated to be valid in the general case, however this result is obvious if we consider the well know solution of the diffusion equation (eq. 2.20):

$$n(\vec{r}, t) = \frac{1}{\sqrt{2\pi}\sigma(t)} \exp\left(-\frac{|\vec{r}|^2}{2\sigma(t)^2} \right), \quad \text{with } \sigma(t) = \sqrt{6Dt}. \tag{6.8}$$

Equating eq. 6.3 and 6.7 and taking into account that $t = N\Delta t$ yields

$$\Delta t = \frac{\Delta l^2}{6D} \tag{6.9}$$

which is a crucial results since it provides the timescale of an electron random walk.

Until now only diffusion was considered as transport mechanism, however, in presence of an electric field a drift term has to be added to the diffusion equation (see sec. 2.1.2)

$$\frac{\partial n(\vec{r}, t)}{\partial t} = D \nabla^2 n(\vec{r}, t) - \vec{v}_d \cdot \nabla n(\vec{r}, t) \tag{6.10}$$

where $\vec{v}_d$ is the drift velocity. In case of a constant static electric field, the solution to this equation is known

$$n(\vec{r}, t) = \frac{1}{\sqrt{2\pi}\sigma(t)} \exp\left(-\frac{|\vec{r} - \vec{v}_d t|^2}{2\sigma(t)^2} \right) \tag{6.11}$$

[1] See sec. 2.1.2.

and the first two moments are

$$\langle S_d \rangle = \int_{\mathbb{R}^3} \vec{r} n(\vec{r}, t) d\vec{r} = \vec{v}_d t \tag{6.12}$$

and

$$\langle S_d^2 \rangle - \langle S_d \rangle^2 = \int_{\mathbb{R}^3} |\vec{r}|^2 n(\vec{r}, t) d\vec{r} = 6Dt. \tag{6.13}$$

Obviously, in case of MAPS the field is not constant but this result provides a hint on how to modify the simulated random walk. If a drift component is added to the diffusion step $\vec{l_i}$, the total step becomes

$$\vec{s_i} = \vec{l_i} + \vec{v}_d \Delta t. \tag{6.14}$$

After $t = N\Delta t$ steps, the electron will travel a distance of

$$|S_{rw}| = \left| \sum_{i=1}^{N} \vec{s_i} \right| = \left| \sum_{i=1}^{N} \vec{l_i} + N\vec{v}_d \Delta t \right| = \left| \sum_{i=1}^{N} \vec{l_i} + \vec{v}_d t \right| \tag{6.15}$$

with mean

$$\langle S_{rw} \rangle = \sum_{i=1}^{N} \vec{s_i} = \langle L_{rw} \rangle + \vec{v}_d t = \vec{v}_d t \tag{6.16}$$

and mean square value of

$$\langle S_{rw}^2 \rangle = \left(\sum_{i=1}^{N} \vec{s_i} \right)^2 = \left(\sum_{i=1}^{N} \vec{l_i} + \vec{v}_d t \right)^2 = \langle L_{rw}^2 \rangle + |\vec{v}_d|^2 t^2 = N\Delta l^2 + |\vec{v}_d|^2 t^2 \tag{6.17}$$

therefore

$$\langle S_{rw}^2 \rangle - \langle S_{rw} \rangle^2 = N\Delta l^2 \tag{6.18}$$

Again, equating eq. 6.13 and 6.18 and taking into account that $t = N\Delta t$, the same results as in previous case (diffusion only) is obtained (eq. 6.9).

In this calculation, electron velocity $\vec{v}_d$ was considered constant while actually $\vec{v}_d = \vec{v}_d(\vec{r}) = \vec{v}_{d,i}$, which would have made impossible to solve the drift-diffusion equation (eq. 6.10) analytically. Also, eq. 6.11 is valid for certain boundary conditions and assumptions which definitely do not represent the sensor geometry. Nevertheless, on a particular case, this derivation has shown how to modify the random walk in order to simulate both diffusion and drift. That is, the simulated electron step is

$$\vec{s_i} = \vec{l_i} + \vec{v}_{d,i} \Delta t = \vec{l_i} + \frac{|\vec{l_i}|^2}{6D} \vec{v}_{d,i}(\mu, \vec{E}(\vec{r})). \tag{6.19}$$

Obviously, the step size should be kept as small as possible but that leads to very high computation time. It is therefore necessary to determine the maximum allowed step size, as one of the aims of this simulation is low execution time. Considering eq. 6.19 and $|\vec{l_i}| = \Delta l$, $\vec{l_i} \,||\, \vec{v}_{d,i}$, the maximum step size for a given Δl (Δt) is

$$s_{max} = \Delta l + |\vec{v}_{d,max}|\frac{\Delta l^2}{6D} = \sqrt{6D\Delta t} + |\vec{v}_{d,max}|\Delta t. \tag{6.20}$$

This equation consists of two terms depending on the chosen step size, one having linear while the other quadratic dependence. Large Δl (Δt) provides a rougher description of the regions where the drift velocity rapidly changes. On the other hand, low Δl (Δt) means high computation time in the regions where the only transport mechanism is diffusion. After studying the electric field (see sec. 6.1.4), it was decided to set the $\Delta l = 1$ µm ($\Delta t \approx 50$ ps)[1]. This yields a maximum step size up to 3 µm, but only in the region closest to the collection diode i.e. where the electrons are collected anyhow[2].

Drift velocity is calculated using the following empirical formula:

$$\vec{v}_d = \mu\frac{\vec{E}}{[1 + (E/E_c)^\beta]^{1/\beta}} \tag{6.21}$$

where μ is the carrier mobility, and $E_c = 7240$ V/cm and $\beta = 1.3$ are measured fitting parameters [85]. The reason not to use the commonly known formula $v = \mu E$ is its validity only for low values of electric field, while in the simulated MAPS, in the vicinity of the collection diode the field can reach a magnitude of a few tens of kV/cm (see sec. 6.1.4).

6.1.2 Carrier lifetime

Taking into account the carrier lifetime is crucial to simulate the contribution from the substrate properly. It also provides the opportunity to study the non-ionising radiation effects. As discussed in sec. 2.1.3, doping concentration has a significant effect on the carrier lifetime; it can vary from > 100 µs for nominal epitaxial layer doping ($\sim 10^{13}$ cm^{-3}) to ~ 10 ns[3] for the typical doping in the substrate ($\sim 10^{18}$ cm^{-3}). Since the carrier lifetime in the epitaxial layer is orders of magnitude higher than the collection time[4], its impact

[1] No difference in results was observed trying $\Delta l = 0.5$ or 1 µm

[2] The average step size was 1.2 µm in case of the configuration with the highest electric field i.e. $d_{epi} = 18$ µm, $V_{BB} = -6$ V and $\Delta l = 1$ µm.

[3] Numbers quoted here are calculated for doping concentrations of MAPS developed for the ITS upgrade. See sections 2.1.3 and 2.3.

[4] Collection time will be further discussed in sec. 6.5. For now, a reference value of ∼100 ns collection time can be considered [47, 86]. N.B. This value was obtained for low electric field MAPS i.e. where main carrier transport mechanism is diffusion.

on the simulation results is negligible. Therefore, to optimise the computation time, the lifetime in the epitaxial layer was set to infinite. This, of course, is an approximation since the epitaxial layer doping concentration is not uniform (see fig. 2.11).

The effects of the non-ionising radiation (see sec. 2.1.4) can be simulated by reducing the carrier lifetime reciprocally to the neutron equivalent fluence i.e. the lifetime can be expressed as [35]

$$\tau(\Phi) = \left(\frac{1}{\tau_0} + \frac{\Phi}{K}\right)^{-1} \tag{6.22}$$

where Φ is the fluence, K is the silicon damage constant and τ_0 is the carrier lifetime before irradiation.

6.1.3 Geometry and boundary conditions

The total simulated volume consist of a matrix of $N \times N$ pixels[1] (see fig. 6.1). Each pixel consists of three logical volumes - substrate layer, epitaxial layer and collection region.

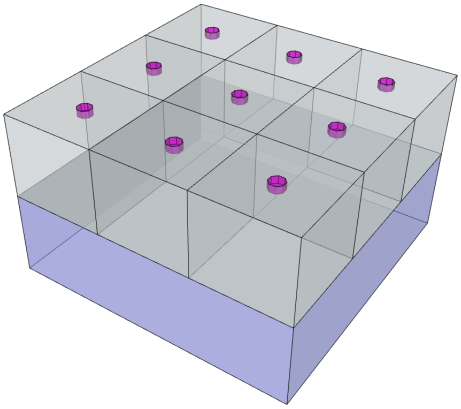

Figure 6.1: Simulated volume of 3×3 pixels - Substrate (blue), epitaxial layer (grey) and collection diodes (green).

The coordinate system used in the simulation is defined in fig. 6.2. The origin is set at the center of the central pixel of the $N \times N$ matrix, at the bottom of the epitaxial layer (at the interface to the substrate). The x and y-axes are parallel to the sensor surface (plane containing the collection diodes). The z-axis is positive in the epitaxial layer and negative in the substrate.

[1] Given the charge collection properties of the simulated MAPS, a 5×5 matrix proved to be sufficient. N is always an odd number.

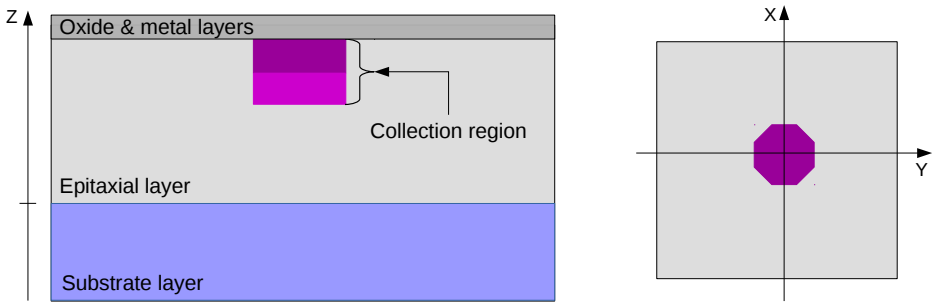

Figure 6.2: Simulated pixel - Cross-section (left) and top view (right) of a simulated pixel. The coordinate system origin is set at the center of the pixel, at the bottom of the epitaxial layer. Not to scale.

Collection region is defined as the volume occupied by the collection diode plus a 2 µm thick volume directly underneath. Electrons in this region are considered collected and are not transported any further. The additional 2 µm region is included to avoid carrier transport calculations in the highly non-uniform and intense electric field (electrons entering this volume will be anyhow collected in the next few steps).

Epitaxial and substrate are two functionally identical volumes but with different thickness and charge carrier properties. The latter arises from the different doping levels of the two layers and in practice means higher mobility, diffusion coefficient and carrier lifetime in the epitaxial layer (see sec. 2.1). Also, since the substrate is devoid of an electric field, is considerably larger than the epitaxial layer, and doesn't contain fine structures[1], a larger step size (2 µm) is used to optimise the computation time (carrier transport mechanism is diffusion which is computationally slow).

Interfaces between the various sensor volumes have different behaviour and have to be considered individually.

Epitaxial – collection region interface is an absorbing barrier. Any electron crossing it is considered collected.

Epitaxial – substrate interface is defined as a surface between the epitaxial and the substrate volumes. This is, obviously, an approximation since the doping profile is not a step function but shows a transition from the high-resistivity epitaxial layer

[1]The substrate is uniform and common for all pixels; there is no effect of pixel segmentation on carrier transport in the substrate.

to the highly-doped substrate across a few μm (see fig. 2.11). Initially, based on consideration on isotype junctions in sec. 2.1.1.2, this interface was implemented as a one-way reflecting barrier (from epitaxial to substrate) and one-way transparent (from substrate to epitaxial). After the first simulations this concept was revised (see sec. 6.2.2.1) and the reflecting barrier was removed i.e. the interface is set as transparent both ways.

Epitaxial – oxide interface ("the top surface" of the epitaxial layer) is set as a totally reflecting barrier. This is consistent with a strong electric field pushing electrons from this interface towards epitaxial layer (see sec. 6.1.4).

Substrate – air interface ("the bottom surface" of the substrate) is set to be totally absorbing. This choice was made to optimise the computation time, since anyhow the probability of an electron starting at the bottom of the substrate to reach the epitaxial layer is negligible[1].

Edge of the simulated matrix ("lateral borders") is defined as an absorbing barrier. The fraction of charge reaching this edge is monitored and the matrix size is set so only less than 0.1% electrons can reach this interface.

It can be noticed that a relevant structure, the implants i.e. p-wells and n-wells, is not being simulated. This is considered an acceptable approximation because:

1. The difference in doping between the p-wells and the epitaxial layer creates a potential difference that pushes electrons into the epitaxial layer (see sec. 2.1.1.2). This is taken into account implicitly via the electric field (see sec. 6.1.4 and the above description of the epitaxial – oxide interface).

2. The higher doping concentration of the p-wells reduces the carrier lifetime. This effect is limited since the implant thickness is <2 μm.

3. N-wells other than the collection diode, such as those present for the implementation of the PMOS transistors, can collect a small fraction of charge and therefore cause a charge collection efficiency lower than 100%. The magnitude of this effect obviously depends on the fraction of pixel surface covered by the n-wells. In case of the

[1] Considering a typically simulated substrate thickness of 20 μm, $\sim$ 50 ns electron lifetime, and transport only by diffusion.

INVESTIGATOR chip (see ch. 3 and sec. 6.2) this fraction is lower than 10% while for the ALPIDE (see ch. 4 and sec. 6.4) it is significantly larger but its response is binary so this effect is not directly observable. Therefore this effect was not accounted for in the simulation.

Therefore, as long as the electric field accounts for the potential difference, the approximation of not simulating the implants in detail should still yield satisfactory results.

6.1.4 Electric field – extraction from TCAD and implementation

Since the analytical expression for the electric fields inside MAPS is unknown due to their complex layout, the electric field used for the simulation of the INVESTIGATOR (see ch. 3) and the ALPIDE (see ch. 4) chips was obtained using Synopsys TCAD [87]. The doping profile used as input for the TCAD simulation was based on the SRP measurement of the wafers used for construction of the ITS upgrade prototypes (see fig. 2.11) and on approximate values[1] for the CMOS processes (implants) [87]. It is worth noting that SRP measurements are known to be operator-dependant and their reproducibility not good [88, 89, 90]. Furthermore, the doping profiles of the CMOS processes might be quite different w.r.t. those implemented by TowerJazz[2]. The impact of both of these uncertainties is complex to quantify, but has to be kept in mind while interpreting the simulation results.

Another key aspect of this particular TCAD simulation is that it is two dimensional i.e. only a sensor cross-section through pixel centre, orthogonal to the sensor surface, like the one shown in fig. 6.3, is simulated. That is, instead of an $N \times N$ pixel matrix, an N pixel array is simulated, with $N = 5$ and periodic boundary conditions. Therefore, in order to implement the electric field extracted from TCAD into the fast simulation it had to be converted from 2-D to 3-D. This conversion introduces additional inaccuracy which will be discussed later in this section.

Since the electric field depends on the pixel pitch, epitaxial layer thickness, reverse bias voltage, collection diode characteristics, doping profile, etc, if any of those is modified a new electric field has to be simulated/extracted. However, the simulated sensors, INVESTIGATOR and ALPIDE, share the wafer and collection diode characteristics so only the

[1] The actual doping profile of p-wells and n-wells are foundry's confidential information.
[2] Manufacturing company of ITS upgrade MAPS [49].

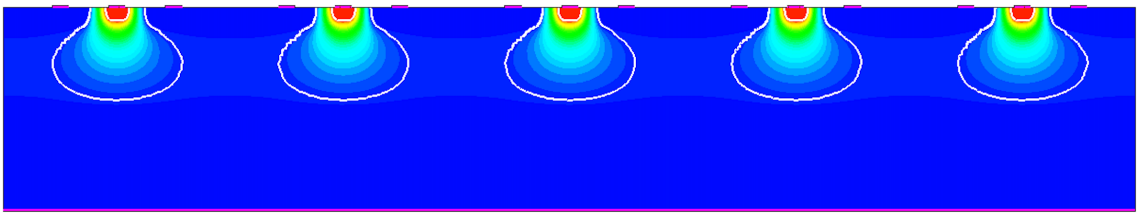

Figure 6.3: 2-D TCAD simulation - Pixel array simulated in TCAD. Colour scale represents the electrostatic potential. [87]

electric field in different epitaxial layer thicknesses and reverse bias voltage configurations had to be extracted (a total of 8 configurations, 2 epitaxial thicknesses $\times$ 4 bias voltages).

Figure 6.4 shows the electric field for an INVESTIGATOR matrix[1] with 28×28 μm^2 pixel size, 25 µm epitaxial layer and -3 V reverse bias. The field is in *fast tool* coordinates therefore the diode centre is at position $(0, 0, 25)$. Field symmetry w.r.t. the diode centre is exploited so only half of the pixel is shown. Figures 6.4a and 6.4b show x (parallel to epitaxial layer) and z (orthogonal to epitaxial layer) components of the field in linear scale and 6.4c and 6.4d in logarithmic scale. There are three things to note; (1) that the electric field gets as high as 25 kV/cm in the immediate proximity of the collection diode, (2) that it is present in most of the epitaxial layer with a lower magnitude of few hundreds V/cm, and (3) that it vanishes in the substrate layer. There is a strong negative orthogonal component of the field at the top of the epitaxial layer (see fig. 6.4b), pushing the electrons from the p-wells towards the epitaxial layer.

The observations made so far are not revealing anything unexpected; what is more interesting is the "$\sim$1 kV/cm line" at $z = 5$ µm, visible in figures 6.4b and 6.4d. A high field, preventing the electrons to migrate from the epitaxial layer to the substrate, is expected at the epitaxial-substrate interface (around $z = 0$ µm), but not at $z = 5$ µm. The origin of this shift might be found in the doping profile which is gradual between the epitaxial layer and the substrate (see fig. 2.11), rather than a step function. Additional cross-checks were carried out but no other explanation was found.

Since the TCAD simulation and the extracted field are 2-dimensional, before implementing it in the fast simulation it was necessary to convert it to three dimensions. The adopted approach consists of rotating the field around the pixel center (z-axis) and then extrapolating the field to the pixel corners (see fig. 6.5). Since the field is almost constant

[1] MM75. See chapter 3 for further details.

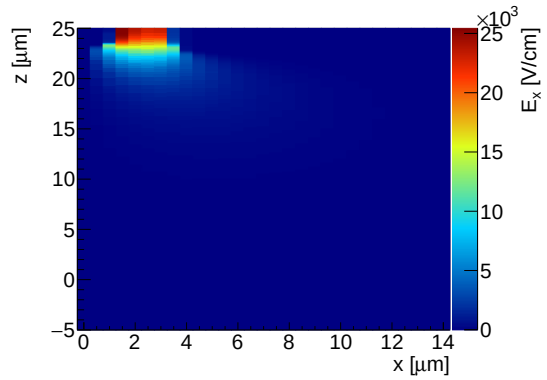

(a) E_x as a function of x and z

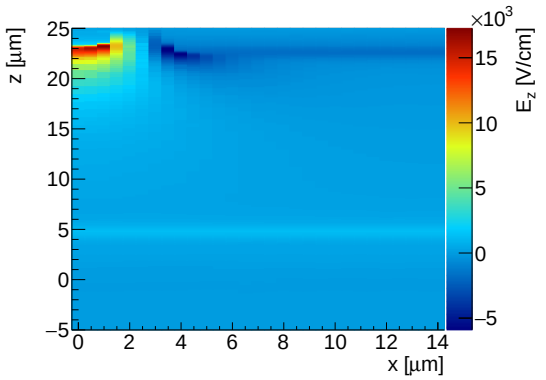

(b) E_z as a function of x and z

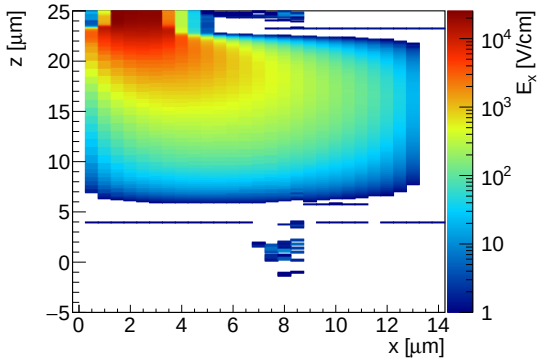

(c) E_x as a function of x and z, log scale

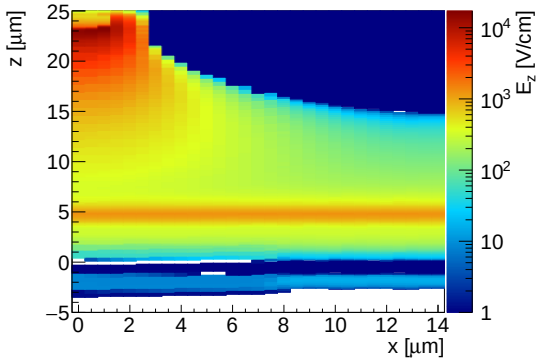

(d) E_z as a function of x and z, log scale

Figure 6.4: TCAD electric field (2-D) - Electric field resulting from a TCAD simulation of the INVESTIGATOR matrix with 28 µm × 28 µm pixel size, 25 µm epitaxial layer and −3 V reverse bias. [87]

towards the pixel border (see fig. 6.4d) it was decided to simply extend the last known field value until the pixel edge. Rephrasing it mathematically

$$\vec{E}(x,y,z) = (E_x, E_y, E_z) = \begin{cases} \left(\frac{x}{r}E_x^{2D}(r,z), \frac{y}{r}E_x^{2D}(r,z), E_z^{2D}(r,z)\right) & \text{for } r < \frac{p}{2} \\ \left(\frac{x}{r}E_x^{2D}(\frac{p}{2},z), \frac{y}{r}E_x^{2D}(\frac{p}{2},z), E_z^{2D}(\frac{p}{2},z)\right) & \text{for } r \geq \frac{p}{2} \end{cases} \tag{6.23}$$

with $r = \sqrt{x^2+y^2}$ and p the pixel pitch.

The resulting 3-D field is shown in fig. 6.6 as sections along z-axis. Figures 6.6a, 6.6b and 6.6c show E_x, E_y and E_z at $z = 15$ µm i.e. 10 µm from the collection diode, while 6.6d shows E_z at $z = 22$ µm i.e. 3 µm from the diode. This 3-D extrapolation looks reasonable but certain discrepancies between data and simulation are expected to emerge. First of all, the field should not have perfect radial symmetry since the diode is octagonal and the

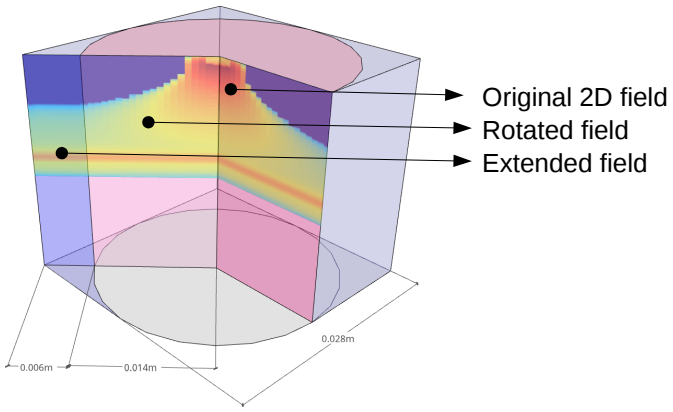

Figure 6.5: Expanding electric field from 2-D to 3-D - Rotation of the field doesn't cover pixel corners, so the field is extrapolated from the last known value.

surrounding p-well has a square opening (see fig. 2.10). Therefore, this approximation is expected to cause discrepancy in the description of events close to the collection diode. Furthermore, setting the field constant towards the pixel corner means that there will be similar response at the pixel edge (at distance $\frac{p}{2}$ from the nearest diode) and at the pixel corner (at distance $\frac{p\sqrt{2}}{2}$ from the nearest diode). This is not expected to cause major discrepancies (following the previous line of assumption; electric field at the pixel edge is small and constant), but can result in slightly skewed ratio of clusters with size of 2, 3 and 4 pixels

6.1.5 Implementation

6.1.5.1 Electron transport

The simulation procedures discussed in this chapter can be summarised in the block diagram shown in figure 6.7. After an energy deposit, a corresponding number of electrons is individually transported. The algorithm starts with an electron at a certain starting position. Then, depending on which volume it is in (see sec. 6.1.3), a step is calculated (see sec. 6.1.1). To determine if the electron is still alive (see sec. 6.1.2), a uniformly distributed random number $0 \leq r \leq 1$ is generated and compared with the survival probability $\Delta t/\tau$, where τ is the electron lifetime. If $r < \Delta t/\tau$ the electron is considered dead. The block "Step allowed?" refers to the behaviour at the interfaces, e.g. if a step would bring the electron out of the volume through the epitaxial-oxide interface, the step is recalculated

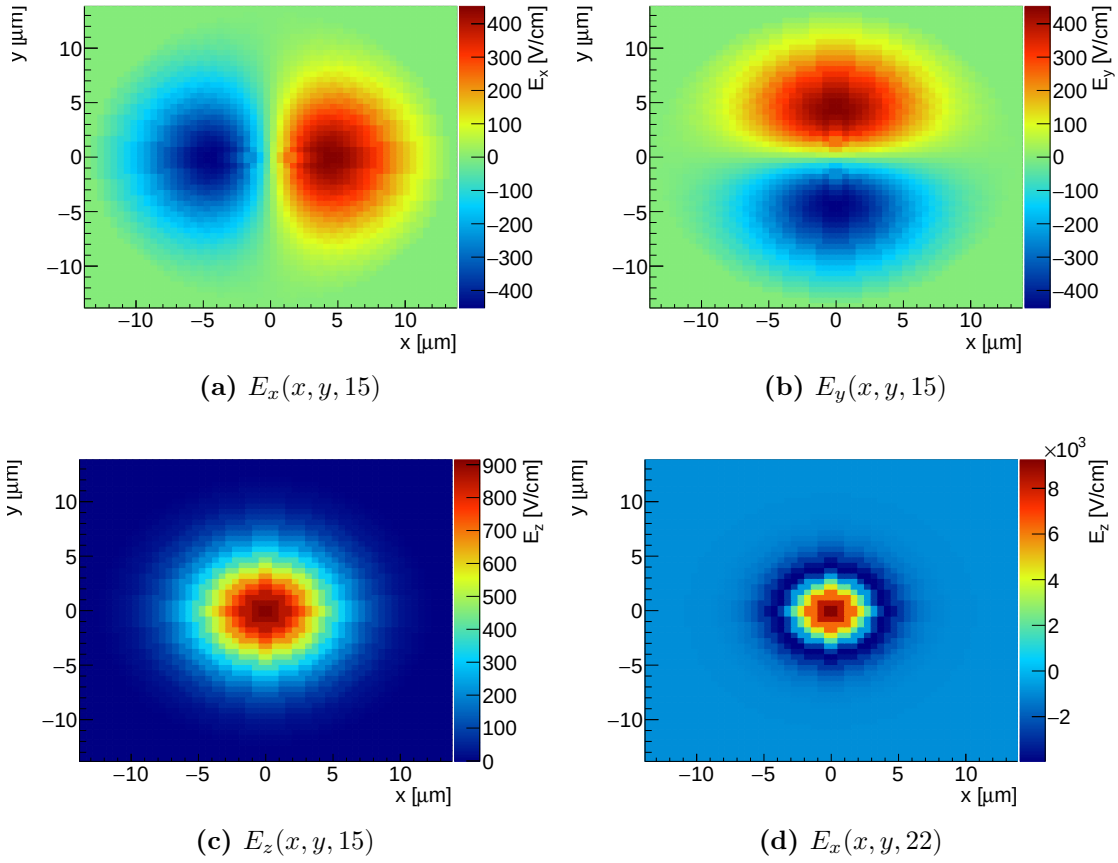

(a) $E_x(x, y, 15)$ **(b)** $E_y(x, y, 15)$

(c) $E_z(x, y, 15)$ **(d)** $E_x(x, y, 22)$

Figure 6.6: TCAD electric field (3-D) - TCAD field from fig. 6.4 extended in 3-D. [87]

so it is reflected back into the epitaxial layer. The algorithm is repeated until the electron arrives to the collection region, dies or reaches maximum number of steps[1].

Multiple scoring modes are possible; typically the number of collected electrons by each of the pixels in $N \times N$ matrix is saved but the same information can also be saved every step or every k steps, if interested in temporal analysis.

This algorithm is the simulation core, but to simulate the detector response to a particular ionising radiation, additional steps are required. In the next sections, the full procedures for simulation of detector response are presented.

[1]Maximum number of steps was set to 10^4 or approximately 500 ns. Less than 0.1% electrons reached this limit in a case with the lowest electrical field and the largest epitaxial layer thickness.

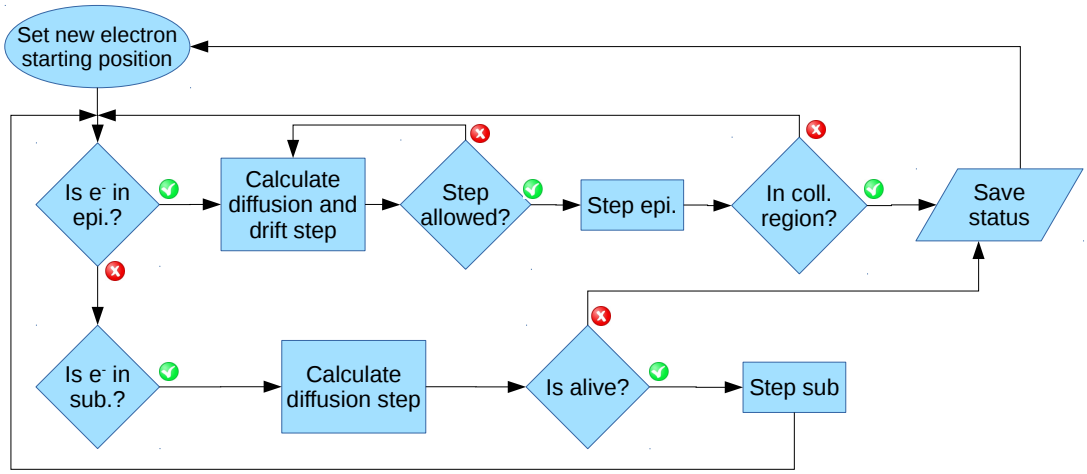

Figure 6.7: Electron transport algorithm - Represented with a block diagram.

6.1.5.2 Simulation of the sensor response to the ^{55}Fe X-rays

^{55}Fe source is an important tool in MAPS characterisation thanks to energy range of the emitted photons (see sec. 2.2.2.1). The simulation of detector response to ^{55}Fe X-rays is implemented in the following procedure:

1. Select randomly the photon energy (5.9 or 6.5 keV) according to the branching ratio.
2. Determine the conversion point (x_0, y_0, z_0); x_0 and y_0 are picked from a uniform distribution over the central pixel surface while z_0 is chosen from the exponential distribution with p.d.f. $p(z) = \mu(E) \exp[-\mu(E)z]$, with $\mu(E)$ attenuation coefficient for a photon with energy E (see sec. 2.2.2).
3. Generate the number of electrons n_e from the normal distribution $\mathcal{N}\left(\frac{E}{w}, \sqrt{\frac{FE}{w}}\right)$, where w is the energy required to generate an e-h pair and F is Fano factor.
4. Following the electron transport algorithm (see fig. 6.7), propagate n_e electrons through the sensor, starting from the conversion point (x_0, y_0, z_0). Store the number of electrons collected by each of the pixels in the $N \times N$ matrix.
5. Add noise (based on the experimental data) to each of the pixels in the $N \times N$ matrix.
6. Run the same analysis as for the data (see sec. 2.4).

6.1.5.3 Simulation of the sensor response to minimum ionising particles

Before entering into details of the procedure for simulating the detector response to MIPs, there are a few comments to be made on the energy straggling in ultra-thin detectors. The distribution describing the energy straggling is based on calculations by Bichsel (see sec. 2.2.1). This distribution doesn't have a simple analytical form but can be quite well described by the convolution of Landau and Gaussian distributions (*Langaus distribution*). Therefore the straggling function is described by Landau and Gaussian parameters but those are not provided in the literature. Furthermore, the energy loss depends on the detector thickness, but in case of MAPS it is rather difficult to precisely quantify the effective thickness; while all of the charge generated in the epitaxial layer is collected, only a fraction of charge generated in the substrate reaches the collection diodes (see sec. 6.3.1). In order to overcome these issues, it was decided to extract the Langaus parameters from data by fitting the straggling distribution obtained from the INVESTIGATOR test-beam measurement (see sec. 3.2.2).

Once the energy straggling is known, the rest of the procedure is straightforward:

1. Determine the incident point (x_0, y_0), uniformly distributed over the central pixel surface.

2. Get a random energy deposit from the energy straggling distribution (obtained from data) and convert it to number of e-h pairs n_e.

3. Following the electron transport algorithm (see fig. 6.7), n_e electrons are propagated through the simulated volume. Each electron starts at a different position (x_0, y_0, z_i), $i = 1..n_e$ such that electrons are equidistant along the particle track. The first point of the track (z_0) is at the top of the epitaxial layer, while the last point (z_{n_p})[1] is in the substrate. At the end, the number of electrons collected by each of the pixels in the $N \times N$ matrix is stored.

4. Add noise (based on experimental data) to each of the pixels in $N \times N$ matrix

5. Run the same analysis as for the experimental data (see sec. 2.4).

[1] z_{n_p} is determined as the point at which less than 1% of total deposited charge reach epitaxial layer i.e. is collected. In this work z_{n_p} was set to 5 µm deep in the substrate. See sec. 6.3.1 for more details.

6.2 Simulation of response of analogue sensors to X-rays

The ^{55}Fe source is an excellent tool for characterising MAPS; the two emitted X-rays, at 5.9 and 6.5 keV, deposit energy locally via the photoelectric effect (see sec. 2.2.2.1), which allows to study the contribution from specific sensor regions (see sec. 2.4.1). In the simulation context, reproducing the ^{55}Fe spectra is an excellent benchmark test since the spectra are sensitive to the slightest changes in charge collection properties. It also provides an environment for fine tuning of simulation parameters (e.g. carrier lifetime).

The analogue MAPS chosen as the reference for this simulation is the INVESTIGATOR (see ch. 3). This choice is motivated by the INVESTIGATOR being produced on different epitaxial layer thicknesses, containing sub-matrices with various design parameters (among which, one similar to the ALPIDE), and also providing timing information (see sec. 6.5).

The ^{55}Fe source was also used to calibrate the reference sensor response in electrons. The calibration procedure is discussed in section 3.1.3.

6.2.1 Preliminary results and discussion

Figure 6.8 shows the seed signal and cluster size distributions[1] resulting from the very first simulation[2], which did not include any parameter tuning, compared to the data. In the cluster size distribution, clusters with size one and two are overestimated, while those with size three and four are underestimated, which indicates smaller charge sharing i.e. a potentially overestimated electric field strength. The simulated cluster sizes are within $\pm 5\%$ of data, which is a good result considering that there was no experimental result used as input to the simulation[3].

The seed signal distribution supports the premise of an overestimated electric field; there is an excess of events in the calibration peak (1640 e^-) and a lack of events in the charge sharing peak (around 800 e^-). Furthermore, another excess of events can be observed, at around 300 e^-, that can be associated to the contribution from the substrate. An alternative explanation could be that this surplus at the lower edge of the spectrum is generated by not modelling properly the trigger in the simulation, but this hypothesis is dismissed by considering the seed signal as a function of cluster size (see fig. 6.9). It can be observed that the surplus is not limited to the spectrum lower edge but extends

[1] Distributions and observables in this analysis are introduced and discussed in section 2.4.1.
[2] Epitaxial layer thickness 18 µm, -3 V reverse bias voltage and 28×28 µm^2 pixel size
[3] Except for the noise, which was measured beforehand and has a very limited effect on cluster size.

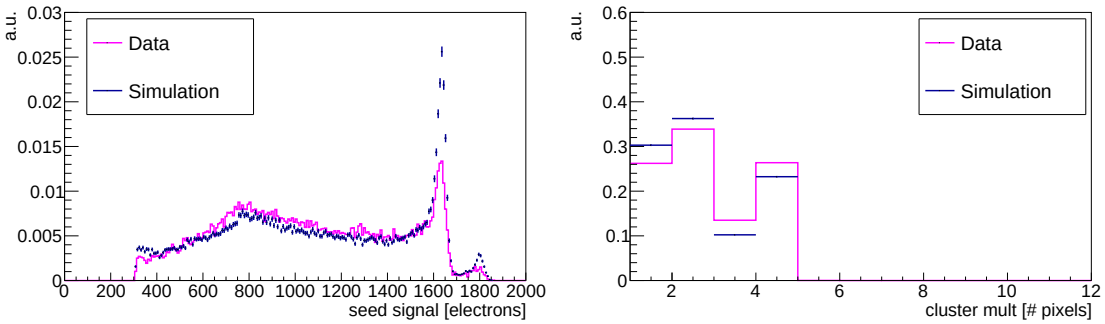

(a) Seed signal **(b)** Cluster size

Figure 6.8: Preliminary simulation: seed signal and cluster size distributions - Seed signal and cluster size distributions compared to the data. $d_{epi} = 18$ µm, $V_{BB} = -3$ V, 28×28 µm^2 pitch.

up to 700 e$^-$, in terms of clusters with size ≤ 2, therefore reinforcing the overestimated substrate contribution hypothesis (see sec. 2.4.1). Furthermore, the seed signal distribution of clusters with size 1 is not described well around 1400 e$^-$.

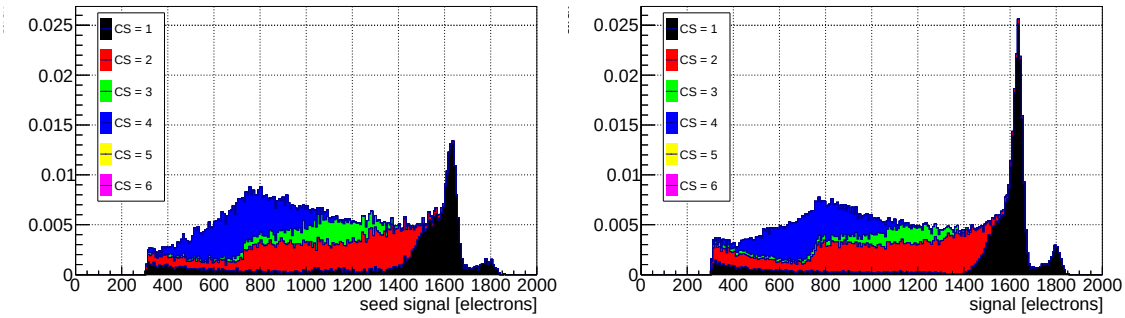

(a) Data **(b)** Simulation

Figure 6.9: Preliminary simulation: seed signal as a function of multiplicity - Simulation (b) compared to data (a). $d_{epi} = 18$ µm, $V_{BB} = -3$ V.

Another important plot to consider is the matrix signal shown in figure 6.10. The overall shape is quite well described by the simulation, but the simulation fails in description of the distribution "tail" towards lower signals. While the excess up to 1000 e$^-$ can be associated with the overestimated contribution from the substrate (which is in line with previous observations), the dip between 1400 and 1600 e$^-$ cannot be attributed to any of the previous hypotheses.

To summarize, there are three observed discrepancies between the simulation and the data:

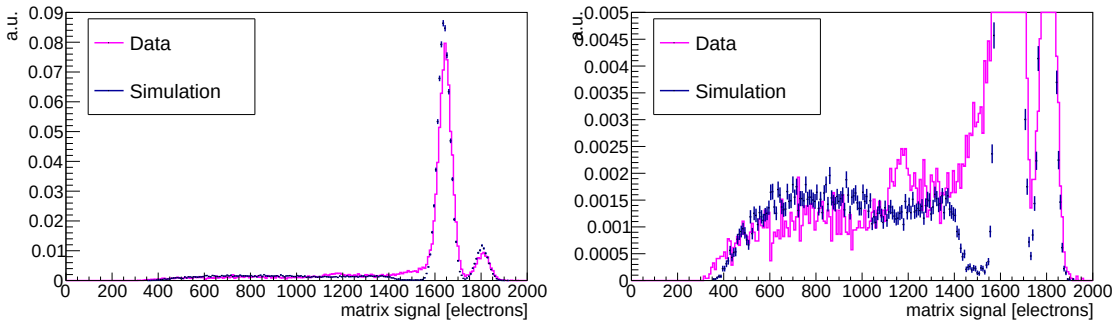

Figure 6.10: Preliminary simulation: matrix signal - The same plot is shown on both sides but on the right the y-axis is zoomed to highlight the events in the distribution tail. $d_{epi} = 18$ µm, $V_{BB} = -3$ V.

1. The "dip" in the matrix signal distribution between 1400 and 1600 e^- (see fig. 6.10).
2. The excess at the lower edge of the seed (see fig. 6.16a and 6.9) and the matrix signal (see fig. 6.10) distributions.
3. The overestimated number of events in the calibration peak (see fig. 6.8).

The following three hypotheses explain these discrepancies, as will be demonstrated in the next section.

1. The epitaxial–substrate interface is not a strictly reflective barrier for the electrons in the epitaxial layer.
2. The carrier lifetime in the substrate is overestimated.
3. The electric field is too strong or too extended.

6.2.2 Reconsidering initial hypotheses and parameter tuning

6.2.2.1 Electron behaviour at the epitaxial–substrate interface

In section 6.1.3 the behaviour of electrons at the epitaxial-substrate interface was discussed and the initial hypothesis was that electrons should not cross from the epitaxial to the substrate. In section 6.1.4, electric field obtained from a TCAD simulation was shown and it already implied that the barrier is not exactly at the interface. In fact, the field creates a reflective barrier extending over few µm (see fig. 2.11). Therefore, the electrons generated in those few µm can cross into the substrate while those that are deep in the epitaxial layer are not able to reach the substrate i.e. are trapped in the epitaxial layer.

In figure 6.11, the matrix signal distributions simulated with different electron behaviour at the epitaxial–substrate interface are shown. It is evident that the non-reflecting interface produces a result compatible with the experimentally observed matrix signal (see fig. 6.10). Therefore, from here on, the interface between epitaxial and substrate will be considered as transparent i.e. non-reflecting[1].

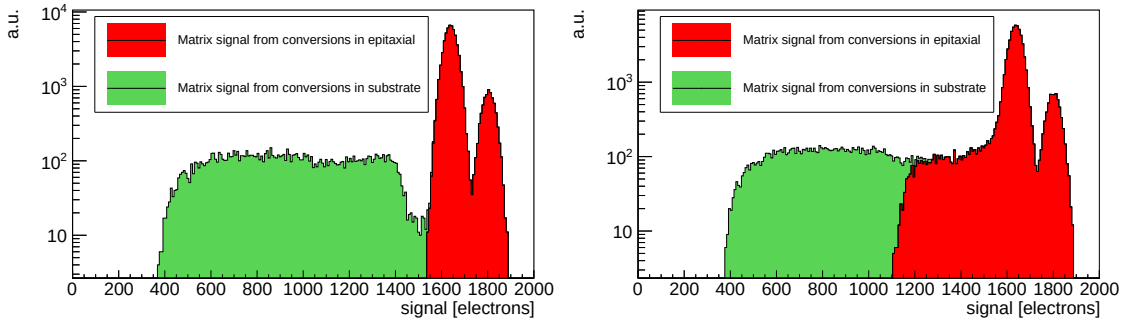

(a) With reflective barrier **(b)** Without reflective barrier

Figure 6.11: Matrix signal distributions for different epitaxial–substrate interface - Contributions from the nominal epitaxial layer and the substrate are marked red and green.

6.2.2.2 Electron lifetime in the substrate

The carrier lifetime in the substrate was set to 50 ns in the initial simulation. This value was calculated (see sec. 2.1.3) based on the nominal value of substrate doping (10^{18} cm^{-3}), which can vary from wafer to wafer (e.g. see fig. 2.11). Therefore, it was expected that this value might have had to be adjusted to obtain matching with the data. The result after adjusting the electron lifetime is shown in figure 6.12, where the electron lifetime in the substrate was set to 15 ns. It can be observed that the substrate contribution is now much better described both in seed and matrix signal distributions. In case of the former, the exception is a structure around 1150 e$^-$ of which the origin still remains unknown[2].

6.2.2.3 Electric field scaling

After adjusting the interface behaviour and substrate contribution, the only remaining major discrepancy is the excess of events in the calibration peak, i.e. a lack of events in charge sharing peak. While in case of 18 µm epitaxial layer thickness (see fig. 6.12) it

[1] N.B. The electric field present in the epitaxial layer still results in electrons having a preferable direction towards the epitaxial layer.

[2] None of the ^{55}Fe emission corresponds to $\sim$ 4 keV (1150 e$^-$) energy deposit in silicon (see sec. 2.2.2.1).

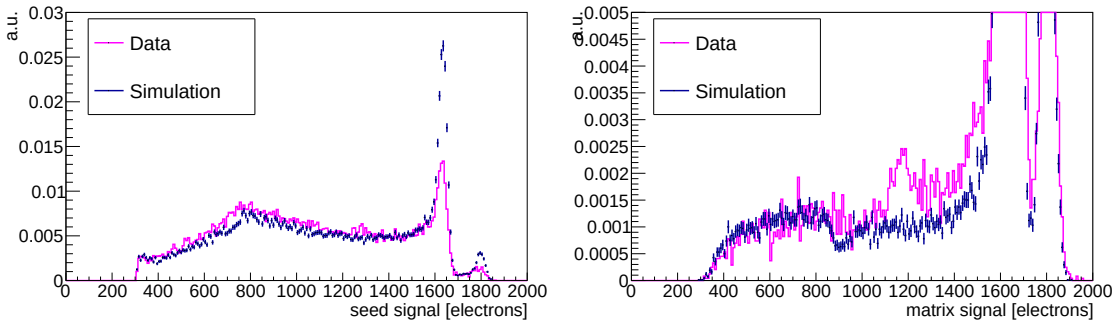

(a) Seed signal **(b)** Matrix signal

Figure 6.12: Seed and matrix signal distributions after electron lifetime in substrate tuning - Seed signal on the left and matrix signal on the right.

doesn't seem drastic, the disagreement between simulation and data is evident for 25 µm epitaxial layer (see fig. 6.13). This behaviour can be well explained by the electric field strength being overestimated. Therefore a free field strength scaling parameter α was introduced, such that $\vec{E}' = \alpha\vec{E}$. The scaling parameters were tuned for each reverse bias voltage and epitaxial layer thickness by comparing the simulation with the seed signal distributions obtained from data.

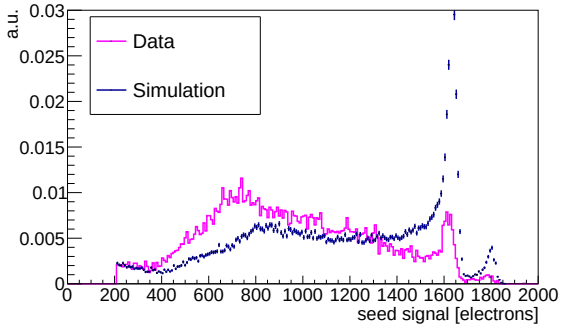

Figure 6.13: Seed signal distribution for 25 µm epitaxial layer - $V_{BB} = -3$ V.

The results after scaling are shown in fig. 6.14. It can be observed that after the scaling the matching between data and simulation is quite good. In the case of the 25 µm epitaxial layer, the simulation still slightly overestimates the distribution around 1500 e^- but this will be addressed in the next section (6.2.3).

Figure 6.15 shows the electric field scaling factor as a function of reverse bias voltage for an epitaxial layer thickness of 18 µm and 25 µm. The dependence of α on both reverse bias and epitaxial thickness is evident.

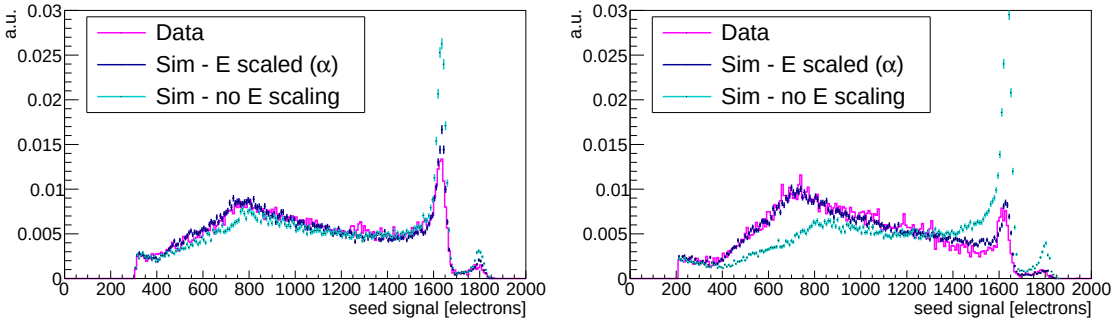

(a) $d_{epi} = 18$ µm, $\alpha = 0.50$ **(b)** $d_{epi} = 25$ µm, $\alpha = 0.28$

Figure 6.14: Seed signal distributions before and after scaling of electric field - Results are shown for 18 µm (a) and 25 µm (b) epitaxial layer. $V_{BB} = -3$ V.

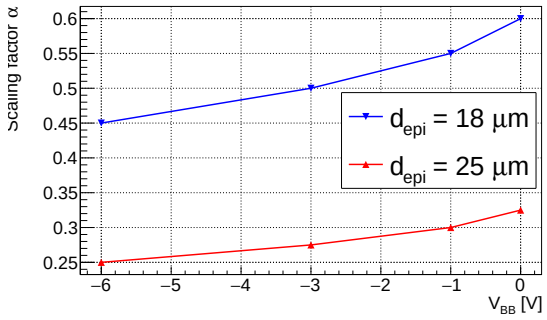

Figure 6.15: Scaling factor α summary - Scaling factor as a function of reverse bias voltage and epitaxial layer thickness.

There are two main candidates that could introduce a discrepancy that would need this kind of correction: electric field and simulation stepping i.e. the way electron drift is modelled in the simulation. Recalling eq. 6.19 and approximating (for the simplicity of the argument) eq. 6.21 with $\vec{v_d} = \mu\vec{E}$, stepping can be expressed as

$$\vec{s_i} = \vec{l_i} + \frac{\Delta l^2}{6D}\mu\vec{E}(\vec{r}, d_{epi}, V_{BB}) = \vec{l_i} + \frac{q}{6k_BT}\Delta l^2\vec{E}(\vec{r}, d_{epi}, V_{BB}). \tag{6.24}$$

where Einstein's relation was used, i.e. k_B is Boltzmann's constant, T the temperature and q the carrier charge (see sec. 2.1.2). Since T is constant, only $\Delta l^2\vec{E}(\vec{r}, d_{epi}, V_{BB})$ is modulating the drift step. From this expression it is clear that scaling factor dependency on V_{BB} can only be associated to the electric field. In fact, the electric field extracted from TCAD is expected not to yield perfect results since the TCAD simulation is 2-D, however the 2-D nature is not expected to result in factor 2 or 4 difference, as it is the case for 18 and 25 µm epitaxial layers. On the other hand, if the doping profile was not estimated

correctly (an there are some indications it might be, see sec. 6.1.4), it could have created a similar effect.

6.2.3 Selection of final results

In this section, only the most notable results from the simulation of the sensor response to ^{55}Fe will be presented; additional plots (for all revere bias voltages and epitaxial layer thicknesses) can be found in appendix A.

6.2.3.1 Results for the 18 µm epitaxial layer and reverse bias of -3 V

Results for $d_{epi} = 18$ µm and $V_{BB} = -3$ V are shown in fig. 6.14a (seed signal), fig. 6.16a (cluster size) and fig. 6.16b (matrix signal). In all three plots a quite good matching between simulation and data can be observed.

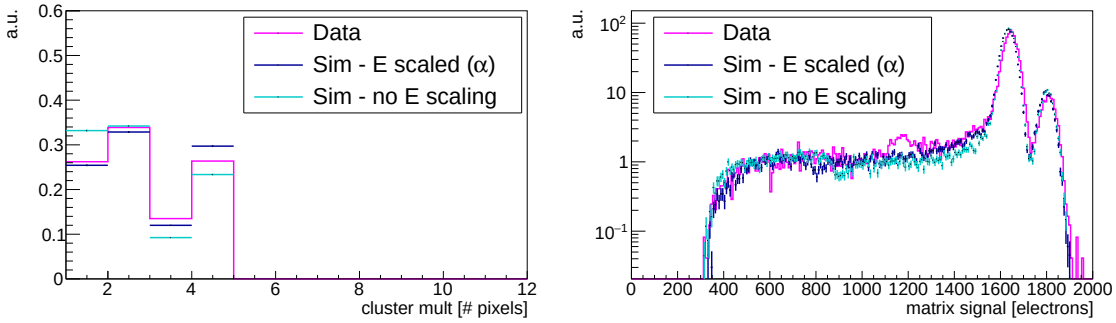

(a) Cluster size distribution **(b)** Matrix signal distribution

Figure 6.16: Cluster size and matrix signal distributions - $d_{epi} = 18$ µm, $V_{BB} = -3$ V, $\alpha = 0.5$.

Figure 6.17 shows measured and simulated seed signal as a function of cluster size (always for 18 µm epitaxial layer and reverse bias of −3 V). This plot is the best example of the level of detail reproduced by the simulation. All of the contributions from different cluster sizes are well described.

6.2.3.2 Results for the 18 µm epitaxial layer and no reverse bias

Results for $d_{epi} = 18$ µm and $V_{BB} = 0$ V are shown in fig. 6.18 (seed signal), fig. 6.19a (cluster size) and fig. 6.19b (matrix signal). In all three plots a quite good matching between simulation and data can be observed. The small shift of the simulated matrix signal

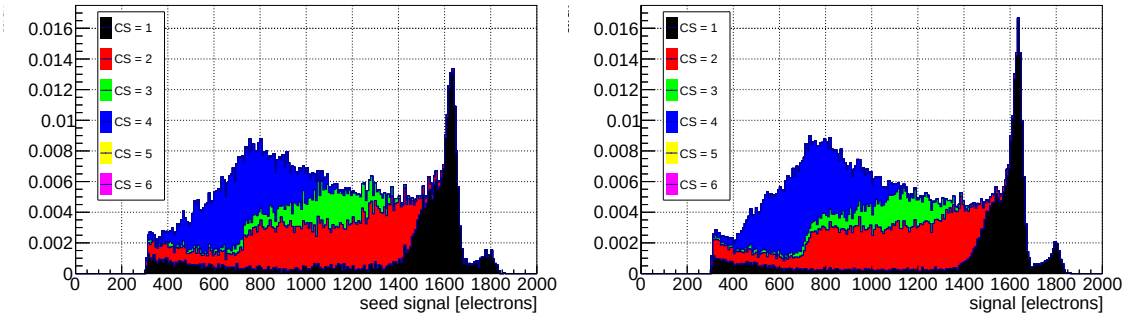

(a) Data **(b)** Simulation

Figure 6.17: Seed signal as function of cluster size - $d_{epi} = 18$ µm, $V_{BB} = -3$ V, $\alpha = 0.5$.

peak position w.r.t. experimental data is within the calibration error (see sections 2.4.1 and 3.1.3).

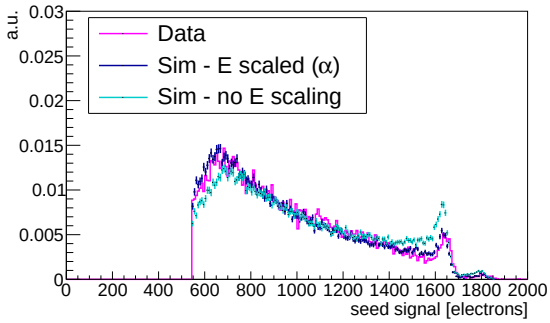

Figure 6.18: Seed signal distribution - $d_{epi} = 18$ µm, $V_{BB} = 0$ V, $\alpha = 0.6$.

6.2.3.3 Results for the 25 µm epitaxial layer and reverse bias of -3 V

Results for $d_{epi} = 25$ µm and $V_{BB} = -3$ V are shown in fig. 6.14b (seed signal), fig. 6.20a (cluster size) and fig. 6.20b (matrix signal). Again, in all three plots a quite good matching of simulation and data can be observed. There is a small discrepancy between 1400 and 1600 e^- but it is more prominent in figure 6.21, which shows seed signal as a function of cluster size compared to data. The events in this range originate from the conversions close to the collection diode i.e. a region which was expected not to reproduce perfectly the data since the field was extracted as 2-D from TCAD and then converted to 3-D (see sec. 6.1.4).

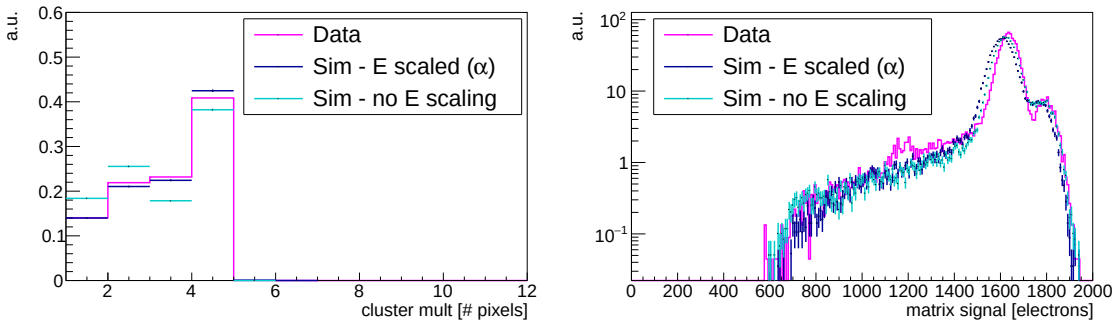

(a) Cluster size distribution **(b)** Matrix signal distribution

Figure 6.19: Cluster size and matrix signal distributions - $d_{epi} = 18$ µm, $V_{BB} = -3$ V, $\alpha = 0.5$.

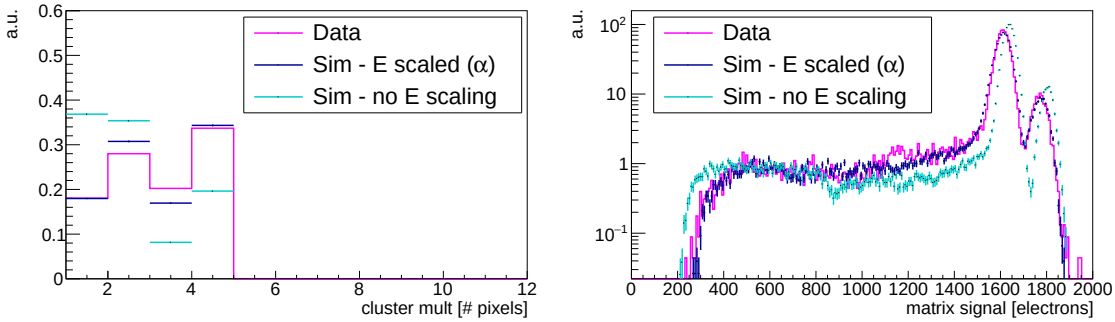

(a) Cluster size distribution **(b)** Matrix signal distribution

Figure 6.20: Cluster size and matrix signal distributions - $d_{epi} = 25$ µm, $V_{BB} = -3$ V, $\alpha = 0.28$.

6.3 Simulation of response of analogue sensors to MIPs

The measurement of the sensor response to minimum ionising particles is a key element in sensor characterisation since it provides information on the detector performance in a typical operational situation (see sec. 2.4). Although it is important to demonstrate the simulation capability in this context, it is less challenging and informative than reproducing ^{55}Fe spectra since the charge is deposited in both substrate and epitaxial layer and therefore the contributions from different regions are less distinct. One particularly interesting point is to study the substrate contribution to the total collected charge (see sec. 6.3.1).

Again, the INVESTIGATOR was chosen as the reference sensor. The same simulation parameters as in the ^{55}Fe simulation were used, i.e. there are no free parameters in the

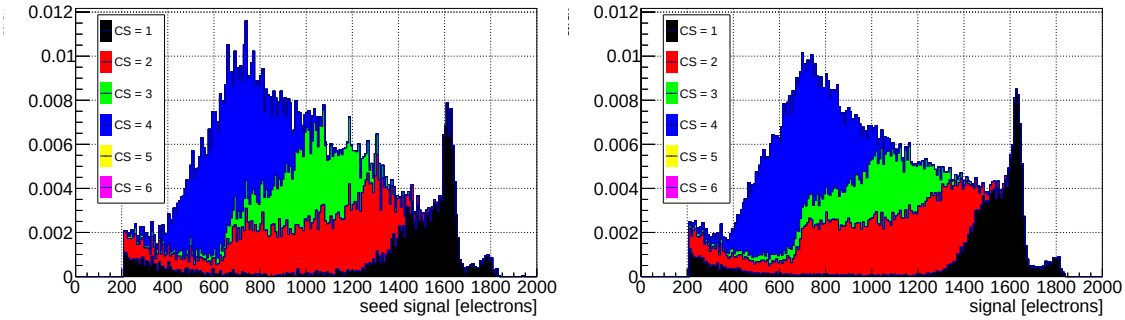

(a) Data **(b)** Simulation

Figure 6.21: Seed signal as function of cluster size - $d_{epi} = 25$ µm, $V_{BB} = -3$ V, $\alpha = 0.28$.

simulation of MIPs. In particular, the same electric field scaling factors (sec. 6.2.2.3) and output voltage to charge calibration (sec. 3.1.3) were used.

6.3.1 Considerations on substrate contribution

A MIP traversing the detector deposits charge all along its track, that is in the entire sensor volume, but not all parts of the sensor volume are equally sensitive. That is, while most of the charge generated in the epitaxial layer[1] gets collected, only a fraction of charge from the substrate does. To optimise the computation time, it was decided to simulate charge deposit only in those regions which contribute with more than 1% to the total collected charge. In order to determine this region, the following analysis was performed.

Figure 6.22 shows the average fraction of collected charge as a function of z-position[2] at which the charge was generated. The average is calculated over a number of events uniformly distributed over the pixel area. The interesting thing to note is that not even all of the charge generated in the epitaxial layer is collected. This is a consequence of the given electric field, i.e. the electron behaviour at the epitaxial–substrate interface. The part of the epitaxial layer ($0 < z < 5$ µm) that is less than 100% efficient in collecting the deposited charge corresponds approximately to the transitional region of the doping profile shown in figure 2.11 and already discussed in section 6.1.4. It is also worth noting that approximately the fraction that is lost from the nominal epitaxial layer is collected from the substrate, so the net gain is not large.

[1] Referring here to the charge generated in the nominal epitaxial layer. For more details see sec. 6.2.2.1.

[2] The coordinate system is defined in sec. 6.1.3. As quick reminder $z < 0$ is the substrate and $z > 0$ is the epitaxial layer.

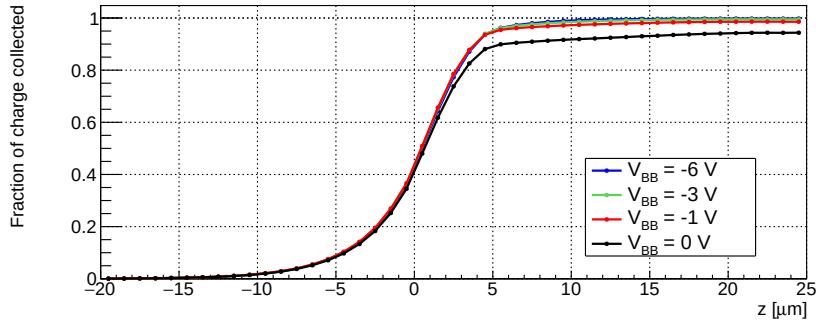

Figure 6.22: Collected fraction of charge as a function of charge creation point - Averaged over pixel area. Blue line is with electric field scaled ($\alpha = 0.5$), red line without scaling. $d_{epi} = 25$ µm.

A more quantitative graph is shown in figure 6.23. It shows, for an orthogonally incident MIP, the average fraction of total charge collected up to a certain sensor depth as a function of the depth. Essentially, it is the integral of the function shown in fig. 6.22 from d_{epi} to z ($d_z = d_{epi} - z$), normalised to unity. From this plot the z-range from which 99% of charge is collected is determined ($z \approx -5$ µm), i.e. the extent of the region in which charge deposit needs to be simulated such that less than 1% of charge is not accounted for.

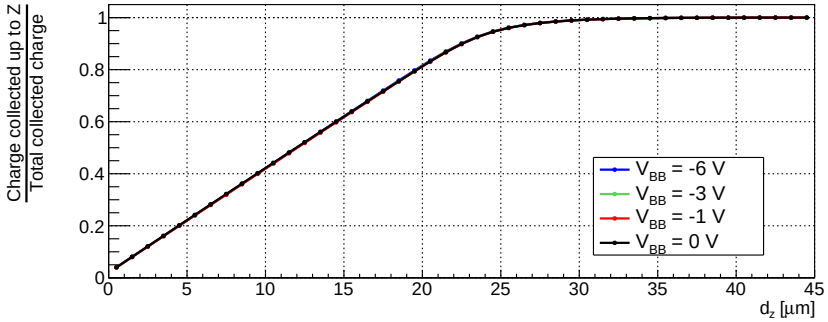

Figure 6.23: Fraction of deposited charge collected up to certain depth as a function of the depth - Averaged over pixel area. $d_{epi} = 25$ µm.

6.3.2 Analysis and results

In this section only results for epitaxial layer thickness of 25 µm and reverse bias voltage of -3 V will be presented as other epitaxial layer thicknesses and bias voltages (available in appendix A) do not show any significant deviation from trends or implications discussed here.

Figure 6.24 shows the seed signal, matrix signal, cluster size and centre of mass distributions (see sec. 2.4). The discrepancies between data and simulation in all of these plots are almost negligible. The centre of mass distribution plot was introduced as it provides information on reconstruction of particle impinging point and in case of MIPs it is better benchmark than seed and matrix signal distributions.

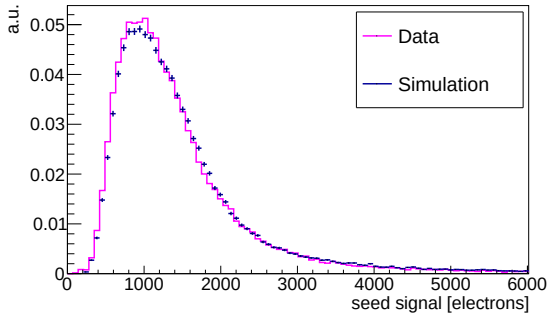

(a) Seed signal distribution

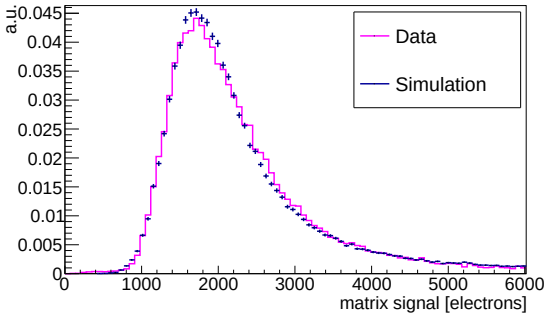

(b) Matrix signal distribution

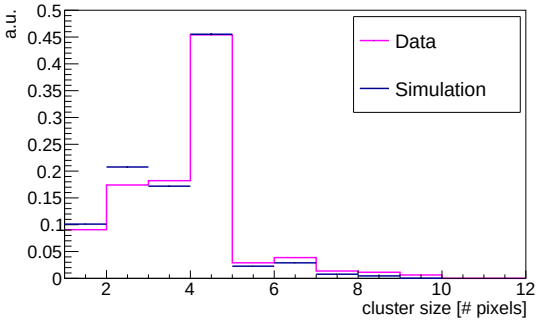

(c) Cluster size distribution

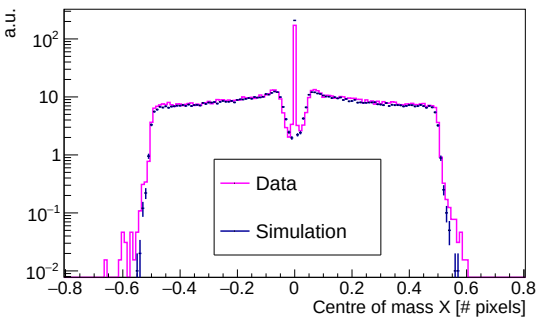

(d) Centre of mass distribution

Figure 6.24: MIP simulation results - $d_{epi} = 25$ µm, $V_{BB} = -3$ V, $\alpha = 0.28$.

Figure 6.25 shows the detection efficiency[1] and average cluster size as a function of charge threshold. There is an increasing difference between the simulated and measured detection efficiency as the threshold increases, but the difference remains smaller than 2% even as the efficiency gets as low as 65%. Furthermore, the simulated detection efficiency closely follows the trend of the measured detection efficiency and drops bellow 99%[2] ap-

[1] Detection efficiency here is defined as

$$\text{Detection efficiency} = \frac{\text{Number of events with seed signal above threshold}}{\text{Total number of triggered events}}$$

since the tracking information for the test-beam this data was taken from (see ch. 3.2.2) was not available.

[2] Value of 99% is taken as a reference value because of the ITS upgrade requirements, see table 1.3.

proximately at the same threshold value. More evident is the offset in average cluster size which starts at 0.3 pixels at the lowest threshold but quickly decreases to less then 0.1 pixels as the threshold increases, which is a less than 10% difference.

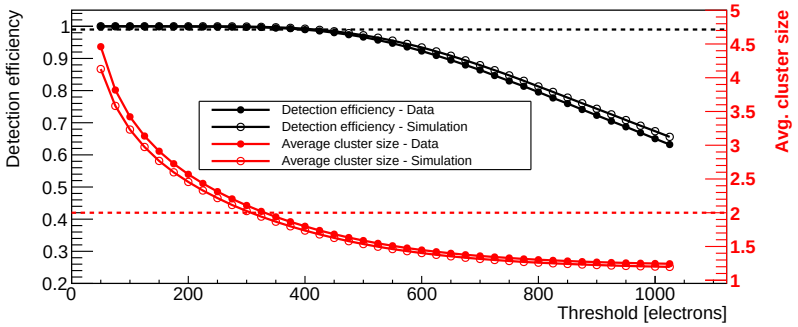

Figure 6.25: MIP simulation results - Detection efficiency and average cluster size as a function of threshold. $d_{epi} = 25$ µm, $V_{BB} = -3$ V, $\alpha = 0.28$

6.4 Simulation of response of binary sensors to MIPs

Studying the response of sensors with analogue output is particularly interesting from an academic point of view and useful as simulation benchmark. However, in large scale HEP experiments, MAPS are intended to be employed with binary readout, so it is important to demonstrate that results obtained with those sensors can also be successfully reproduced.

The simulated sensor in this case is the ALPIDE[1], the MAPS developed for the ALICE ITS upgrade. ALPIDE and INVESTIGATOR[2] have in common the 25 µm epitaxial layer and the pixel collection diode geometry. The main difference concerning the sensitive volume between ALPIDE and INVESTIGATOR is the pixel size; in case of the former it is 28×28 µm^2 and in case of the latter 29.24×26.88 µm^2, which is a difference of about 0.6 µm on each pixel side. In the ALPIDE, there is also a much larger portion of n-well implants (PMOS transistors) because of the more complex in-pixel circuitry. They are, however, shielded by deep p-wells, so their influence on the charge collection process is rather limited. Eventually, these differences were considered negligible and the same electric field extracted from TCAD for the INVESTIGATOR was used. Of course, the field has to be extended along the x-axis, which is done according to the same procedure and arguments followed while extending the field to pixels corners (see sec. 6.1.4), and

[1]The results presented in chapter 4 are used for comparison in this section.
[2]When referring to the INVESTIGATOR, the MM75 is implied (see ch. 3).

shrunk along y-axis, which is done by cutting the last 0.6 µm on each side of pixel electric field. The digitisation was done by applying a fixed charge threshold to all pixels. These were the only modifications w.r.t. the analogue sensor MIP simulation; electric field scaling (see sec. 6.2.2.3) and other parameters were not changed.

6.4.1 Detection efficiency and spatial resolution

In case of sensors with binary output, the seed and matrix signal distributions are unavailable, so detection efficiency, cluster size and spatial resolution plotted as function of threshold were chosen as benchmark plots[1], shown in fig. 6.26. The discrepancy between the measurement and the simulation is evident. However, it can be noted that the simulation reproduces the same pattern but shifted toward higher thresholds. In fact, it can be observed that given any of the variables (detection efficiency, cluster size or spatial resolution), the simulated threshold is approximately 60% higher than the measured threshold for the same variable value. For example, consider the point where the detection efficiency drops bellow 99%[2]; in case of the measured detection efficiency it happens around 260 e^- while in the simulation around 425 e^-. At 260 e^- the measured cluster size and spatial resolution are around 1.7 µm and 5.5 µm, respectively. The same values are obtained in simulation at a threshold of 425 e^-. Therefore, it seems reasonable to try to scale (recalibrate) the measured threshold by a factor of $\frac{425}{260} \approx 1.63$, as shown in figure 6.27, and then try to understand this discrepancy.

After the threshold scaling, very good matching can be observed between measurement and simulation. There is still some remaining discrepancy of the efficiency at higher thresholds, however up to 1000 e^- the discrepancy is still below 10%. The simulated cluster size and spatial resolution are within 10% of the measured (and threshold scaled) values for all the thresholds.

6.4.1.1 Discussion on ALPIDE threshold scaling

The matching between simulation and data obtained after the threshold scaling, in contrast to the results before scaling, indicates that there is an issue with the threshold but doesn't really say whether the threshold is not simulated correctly, the ALPIDE threshold is miscalibrated, or both.

[1] Distributions and observables in this analysis are introduced and discussed in section 2.4.2.
[2] This point is taken since it is minimum allowed efficiency for the ITS upgrade. See table 1.3.

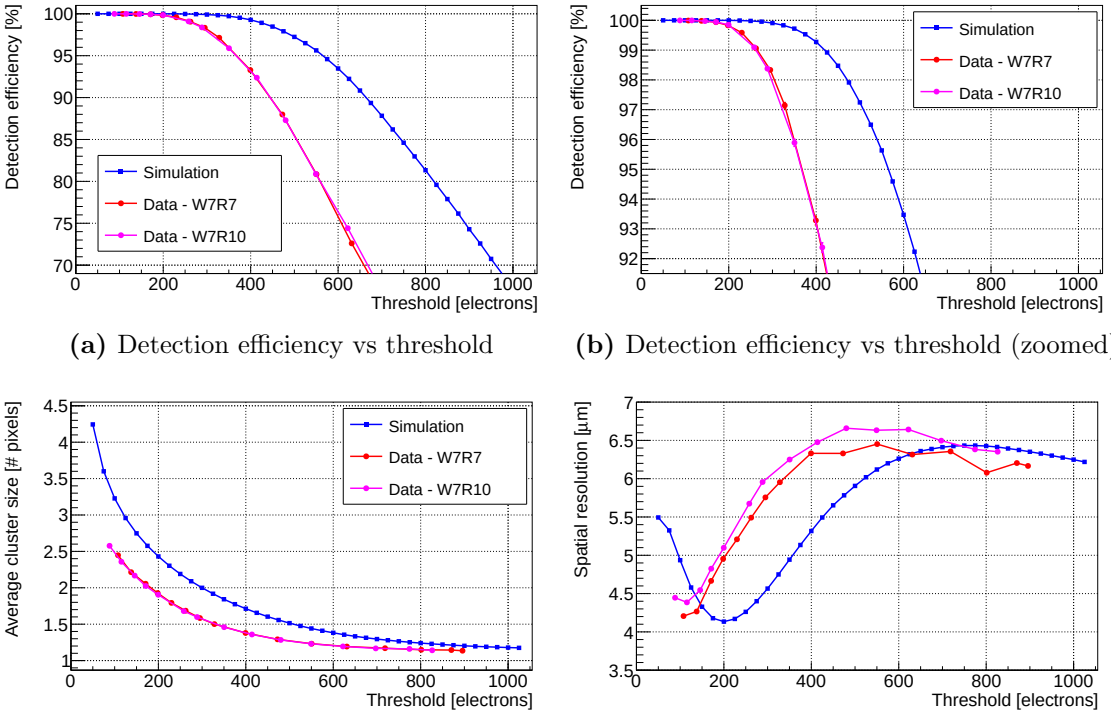

(a) Detection efficiency vs threshold

(b) Detection efficiency vs threshold (zoomed)

(c) Average cluster size vs threshold

(d) Spatial resolution vs threshold

Figure 6.26: ALPIDE simulation results - Detection efficiency, cluster size and spatial resolution as a function of threshold. Performance of two sensors (magenta and red) compared to the simulation (blue). $V_{BB} = -3$ V.

A strong evidence that in the simulation the threshold is correctly modelled is given by the INVESTIGATOR results shown in section 6.3.2, where no threshold adjustments were required to obtain excellent matching. Furthermore, the only difference[1] between binary and analogue sensors in the simulation, that is related to the threshold is the digitisation. In the simulation, when converting the collected charge to a binary signal, the same threshold was applied to all pixels, while in case of the ALPIDE the threshold varies from pixel to pixel[2] (fixed-pattern noise, see sec. 4.2.1). The distribution of ALPIDE thresholds (see sec. 4.2.1) is slightly asymmetric, and this asymmetry is more prominent at lower average threshold. However, while this asymmetry can explain smaller deviations like an increasing detection efficiency difference at higher thresholds (see fig. 6.27), it is insufficient to explain a 60% higher threshold.

[1] The differences are discussed at the beginning of section 6.4.
[2] When plotting ALPIDE threshold it is actually average threshold.

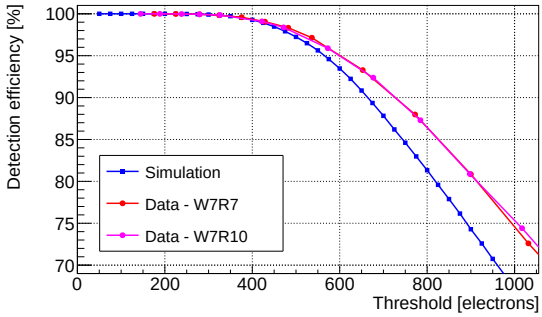

(a) Detection efficiency vs threshold

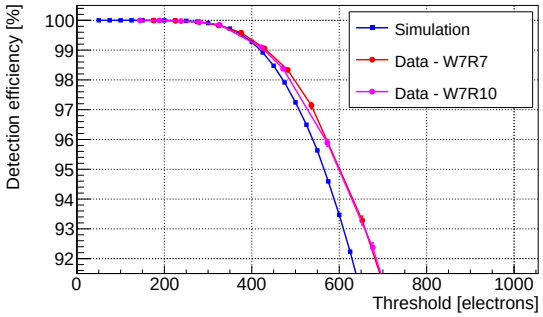

(b) Detection efficiency vs threshold (zoomed)

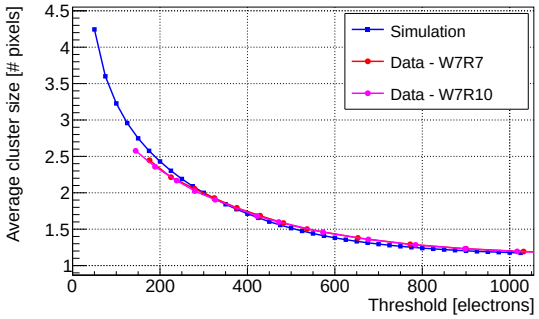

(c) Average cluster size vs threshold

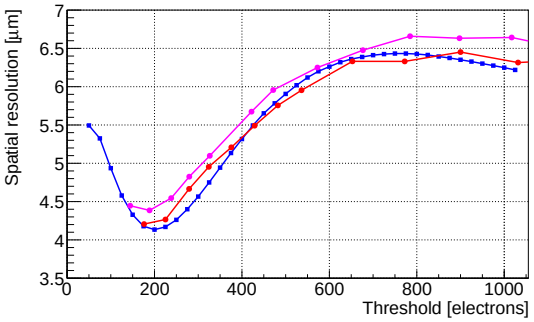

(d) Spatial resolution vs threshold

Figure 6.27: ALPIDE simulation results - Detection efficiency, cluster size and spatial resolution as a function of threshold. Performance of two sensors with scaled threshold (magenta and red) compared to the simulation (blue). $V_{BB} = -3$ V.

The remaining explanation is that the ALPIDE threshold is not calibrated correctly. The ALPIDE calibration procedure and potential sources of calibration error are discussed in section 4.2.1. Already the ALPIDE detection efficiency as a function of threshold in fig. 6.26 showed that the threshold value at which the detection efficiency drops below 100% is lower than expected, considering the INVESTIGATOR results in fig. 6.25. Furthermore, already by looking at seed and matrix signal distribution measured with the INVESTIGATOR (see fig. 6.24), a much better performance would be expected than that exhibited by the ALPIDE (see fig. 6.26).

In conclusion, there is no definite confirmation that the ALPIDE threshold calibration is wrong, but all the evidence points in that direction. For the rest of this chapter, a scaled ALPIDE threshold will be used[1], and it will be shown that all other ALPIDE simulation results describe the data with a scaled threshold quite well. Thus, adding more evidence

[1]The same as calculated in section 6.4.1 - 1.63.

supporting the hypothesis of a miscalibrated charge threshold.

6.4.2 Cluster size and shape distributions

Reproducing cluster size and shape[1] distributions precisely is particularly important for the simulation of the ALICE experiment since, for data reduction purposes, the cluster topologies will be Huffman coded [23]. Therefore, knowing the frequencies of the various cluster topologies is important for efficient coding.

Figure 6.28 shows a comparison of simulated and measured cluster size distributions at different (scaled) thresholds. At lower threshold the frequency of larger clusters is slightly overestimated while at the higher threshold the occurrence of single pixel clusters is overestimated. However, this was expected from the difference in the simulated and the measured cluster size as a function of threshold, shown in fig. 6.27. Nevertheless, the simulated cluster size distribution closely matches the measured distribution in the entire simulated (measured) range[2].

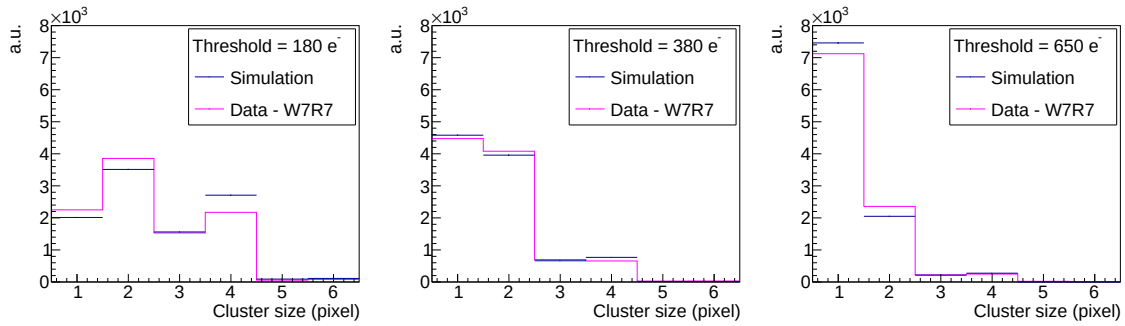

(a) Threshold = 180 e⁻ **(b)** Threshold = 380 e⁻ **(c)** Threshold = 650 e⁻

Figure 6.28: ALPIDE cluster size - Simulated and measured cluster size distributions at different thresholds. $V_{BB} = -3$ V

Figure 6.29 shows comparison of simulated and measured cluster shape distributions at different (scaled) thresholds. The situation is similar as for the cluster size; single pixel clusters are slightly underestimated at lower thresholds and overestimated at higher thresholds, but the simulated cluster shape distribution closely matches the measured distribution in the entire simulated (measured) threshold range.

[1] See sec. 2.4.

[2] Cluster size and shape distribution at other threshold values can be found in appendix A.

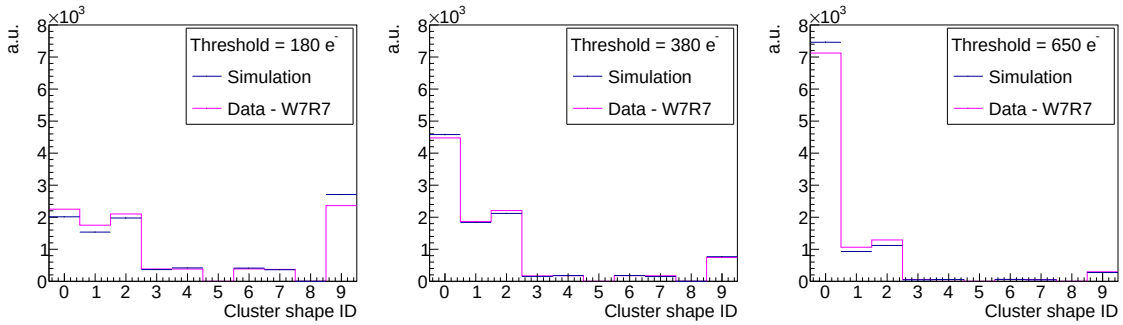

(a) Threshold = 180 e$^-$ **(b)** Threshold = 380 e$^-$ **(c)** Threshold = 650 e$^-$

Figure 6.29: ALPIDE cluster shape - Simulated and measured cluster shape distributions at different thresholds. $V_{BB} = -3$ V

6.4.3 Cluster size and shape vs. track impinging point

A very good simulation benchmark is the analysis of the cluster size and shape as a function of the particle impinging point on the sensor surface[1]. Although this analysis is immediately available in case of the simulation, it is a rather demanding measurement. The test-beam telescope is required to have a very high resolution, preferably at least an order of magnitude smaller than the pixel size, and high statistics are required. Therefore, the measurement results in this analysis are subject to higher uncertainty, which can explain possible discrepancies between simulation and data. To account for the beam telescope resolution, the simulated impinging point was convoluted with a Gaussian distribution[2]

The average cluster size as a function of particle impinging point inside a pixel is shown in fig. 6.30. An excellent agreement between the simulation and the data is achieved.

The impinging point (inside a pixel) for clusters with shape ID 1[3] is shown in fig. 6.31. The small differences between data and simulation can be attributed to a non-perfect alignment of the beam telescope planes, causing a small shift of simulation w.r.t. data.

6.5 Simulation of charge collection time

So far, only the integrated charge has been discussed, but the *fast tool* also offers the possibility to study the time-resolved charge collection, i.e. the charge collection time.

[1] Orthogonally incident minimum ionising particles.

[2] The standard deviation was set to 2.8 µm in both x and y direction [91]. This value was estimated from a beam telescope simulation. See sec. 2.4.2.

[3] Plots for other shape IDs can found in appendix A.

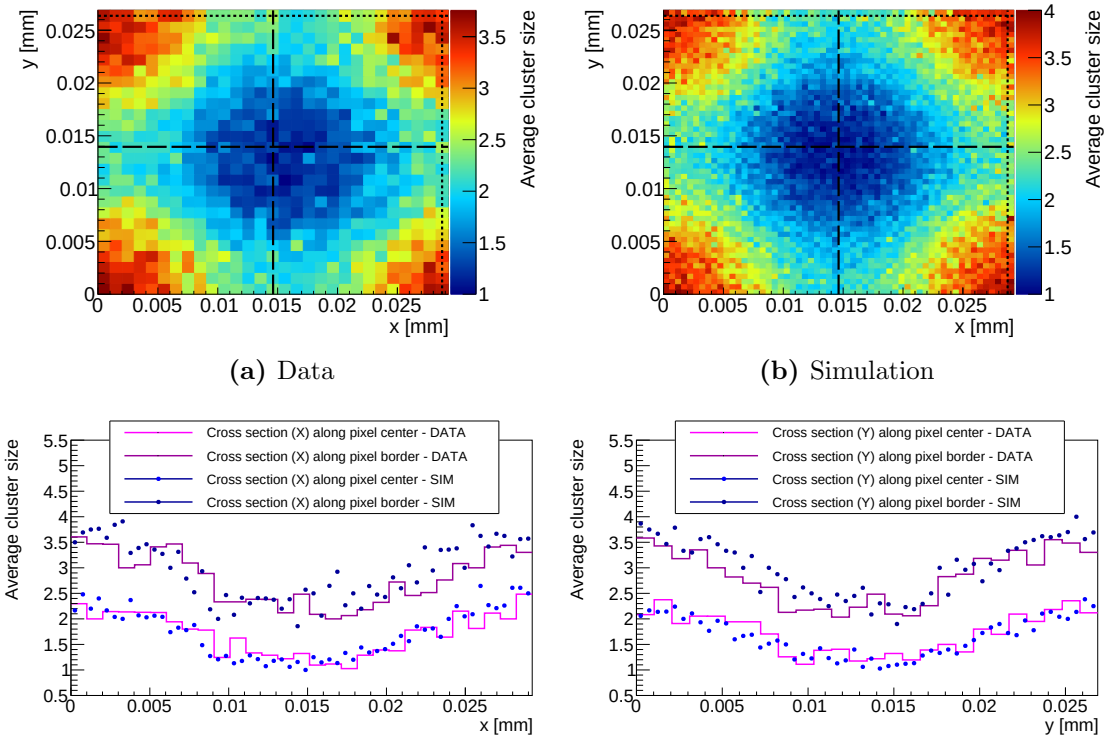

(a) Data **(b)** Simulation

(c) Cross sections along x-axis **(d)** Cross sections along y-axis

Figure 6.30: Average cluster size vs. impinging point - Simulated and measured average cluster size as a function of particle impinging point inside a pixel. The black lines in (a) and (b) indicate cross sections plotted in (c) and (d). The dashed and dotted line represents the cross sections along the pixel centre and border, respectively.

Before presenting the detailed results, the simulation output will be checked against the reference data, which was measured using the INVESTIGATOR chip[1] and an ^{55}Fe source, but in a different experimental setup.

6.5.1 Comparison with analogue sensor ^{55}Fe measurements

Since the time resolution of the INVROS[2] is insufficient for the purposes of the charge collection time measurement, the method described in [92] was adopted to measure the reference data. A differential probe connected to a fast oscilloscope was attached to an output channel of the INVESTIGATOR chip i.e. only a single pixel was measured. The triggering and data acquisition were both given by the oscilloscope. An example of a

[1] MM75, 25 µm epitaxial layer, see ch. 3.
[2] INVESTIGATOR Readout System, see ch. 3.

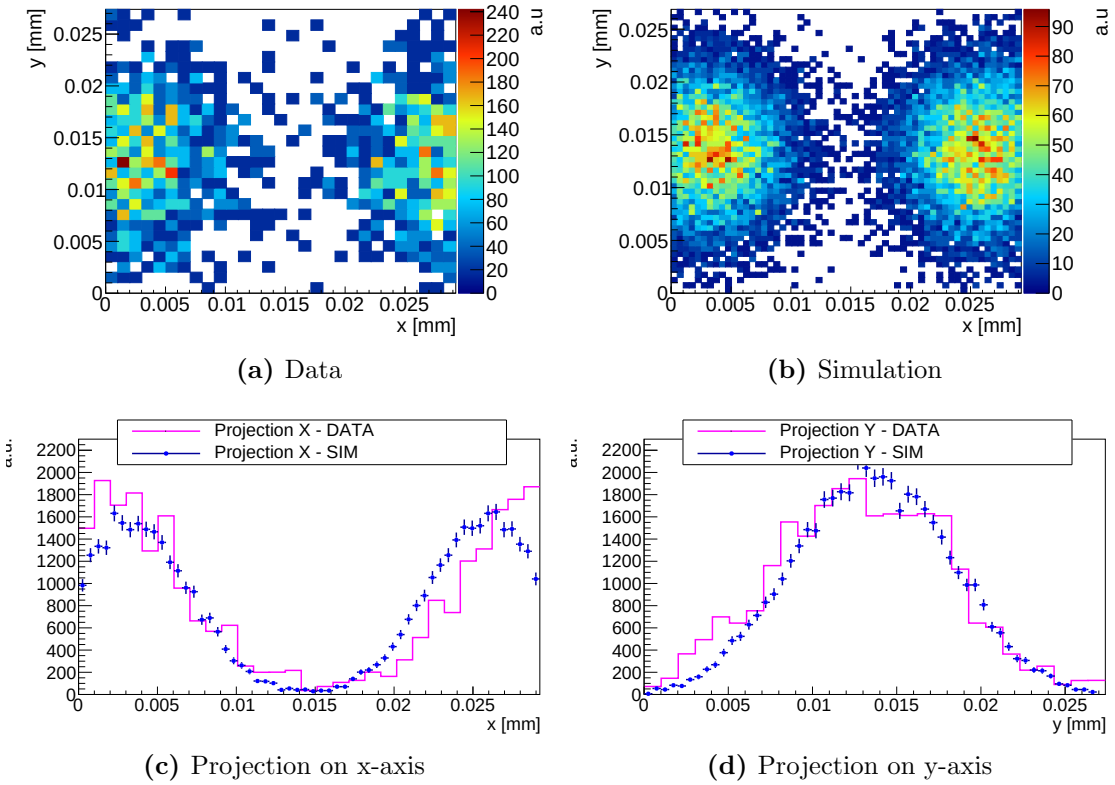

(a) Data **(b)** Simulation

(c) Projection on x-axis **(d)** Projection on y-axis

Figure 6.31: Impinging point for clusters with shape ID=1 - Simulated and measured particle impinging point (inside a pixel) for clusters with shape ID=1.

measured waveform is shown in figure 6.32. The waveform for each event was interpolated with the following function with four free parameters

$$f(t) = \begin{cases} c & t \leq t_0 \\ c - \Delta \left[1 - \exp\left(\frac{-(t-t_0)}{\tau}\right)\right] & t > t_0 \end{cases} \tag{6.25}$$

where c is the baseline prior to charge collection, Δ is the pixel signal, t_0 is the instant at which first charge carrier was collected, and τ is the charge collection time parameter[1]. Since the response of only a single pixel was measured, the standard ^{55}Fe analysis methods and observables do not apply, and the analysis is limited to only two parameters, Δ and τ, representing the collected charge and charge collection time, respectively.

[1] Actually, the data is much better described by a function based on the incomplete gamma function (see e.q. B.5), mainly because of the INVESTIGATOR impulse response function (see appendix B). However, the parameters of the interpolation function used here have proven to be better in characterising the collection time, as parameters α and β of the e.q. B.5 resulted highly correlated and therefore difficult to interpret as a collection time. Furthermore, e.q. 6.25 was used to retain the comparability of the results with [92].

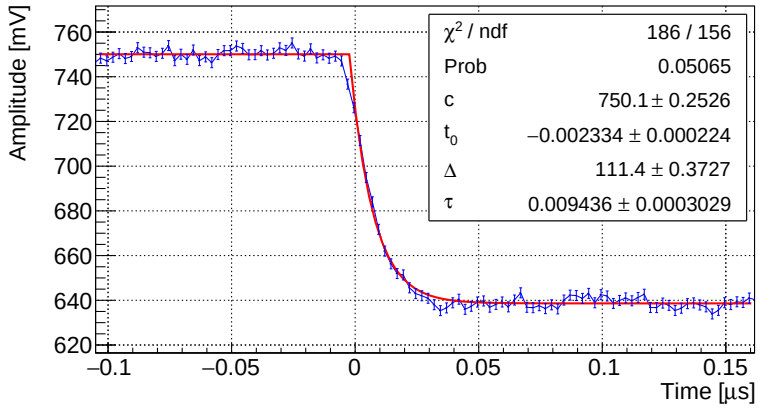

Figure 6.32: Example pixel waveform in the charge collection time measurement - The red curve represents the fit function.

In order to reproduce the said waveforms, the simulation algorithm has to be slightly extended. Considering the algorithm for ^{55}Fe simulation, described in sec. 6.1.5.2, the step 4 is modified so the number of electrons collected by each of the pixels at every step is stored. Furthermore, the simulation response has to be convoluted with the INVESTIGATOR impulse response function and then integrated (see appendix B). The convolution is given by

$$w_i = \sum_{j=0}^{j=i} n^j_{e,coll} \cdot f(t_i - t_j) \tag{6.26}$$

where t_i is the time elapsed at i-th step, $n^j_{e,coll}$ is the number of electrons collected at step j, and $f(t)$ is the impulse response function (see eq. B.7). The sum limits are truncated because the $f(t)$ is defined only in $t \in \langle 0, \infty \rangle$ i.e. is zero for $t \leq 0$. In accordance with eq. B.2 the waveform is calculated as

$$W_i = \sum_{j=0}^{j=i} w_j. \tag{6.27}$$

The simulated waveforms are then interpolated with eq. 6.25 and the rest of the analysis is identical to the one of the measurement.

The measured[1] and simulated charge collection time (τ in eq. 6.25) is plotted against the collected charge i.e. the pixel signal (Δ in eq. 6.25) in figure 6.33 for three reverse bias voltages and an epitaxial layer thickness of 25 µm. It can be observed that the collection

[1] MM75, see ch. 3.

time is shorter for events with higher signal, which is reasonable considering that the events with higher signal are given by photons converted closer to the collection diode. Furthermore, for events with charge sharing, the collection time decreases with increasing reverse bias voltage. This too is expected since the electric field strength increases with reverse bias voltage, resulting in stronger drift and therefore shorter charge collection time. The minimum measured charge collection time is given by the INVESTIGATOR impulse response function (see app. B), and corresponds to ~ 10 ns. This is why the events converted in the high field region (with the highest signal) are fixed at 10 ns instead of having a collection time close to zero. The measurement results are well reproduced in the simulation.

Figures 6.34a, 6.34c, and 6.34e show measured and simulated pixel signal (collected charge) for three reverse bias voltages and epitaxial layer thickness of 25 µm. This plot allows for a more quantitative comparison of simulation and data. A good matching of simulation and data can be observed for all reverse bias voltages.

Figure 6.34b, 6.34d, and 6.34f show measured and simulated charge collection time τ for three reverse bias voltages and epitaxial layer thickness of 25 µm. It can be observed that the high end of spectrum is well described, while there is a discrepancy at $\tau \sim 12$ ns. Considering fig. 6.33, the events in the discrepant region can be associated to photons converting close to the depleted region. In sec. 6.2.3.3, it has already been noted that this region is not well modelled in the simulation.

6.5.2 Results

Now that a reasonable matching with the sensor response has been confirmed, the simulation can be exploited to study the charge collection time via variables that are otherwise not directly observable.

Two new variables are defined to represent the charge collection time; *seed pixel* t_{90} and *matrix* t_{90}. The seed pixel t_{90} is the time for a seed pixel to collect 90% of the relative charge[1]. The matrix t_{90} is the time in which a 5×5 pixel matrix collects 90% of the total charge.

A number of electrons was propagated from starting points uniformly distributed all

[1]Relative charge refers to the fraction of total charge collected by the seed pixel. $t_{90} \sim 2.3\tau$.

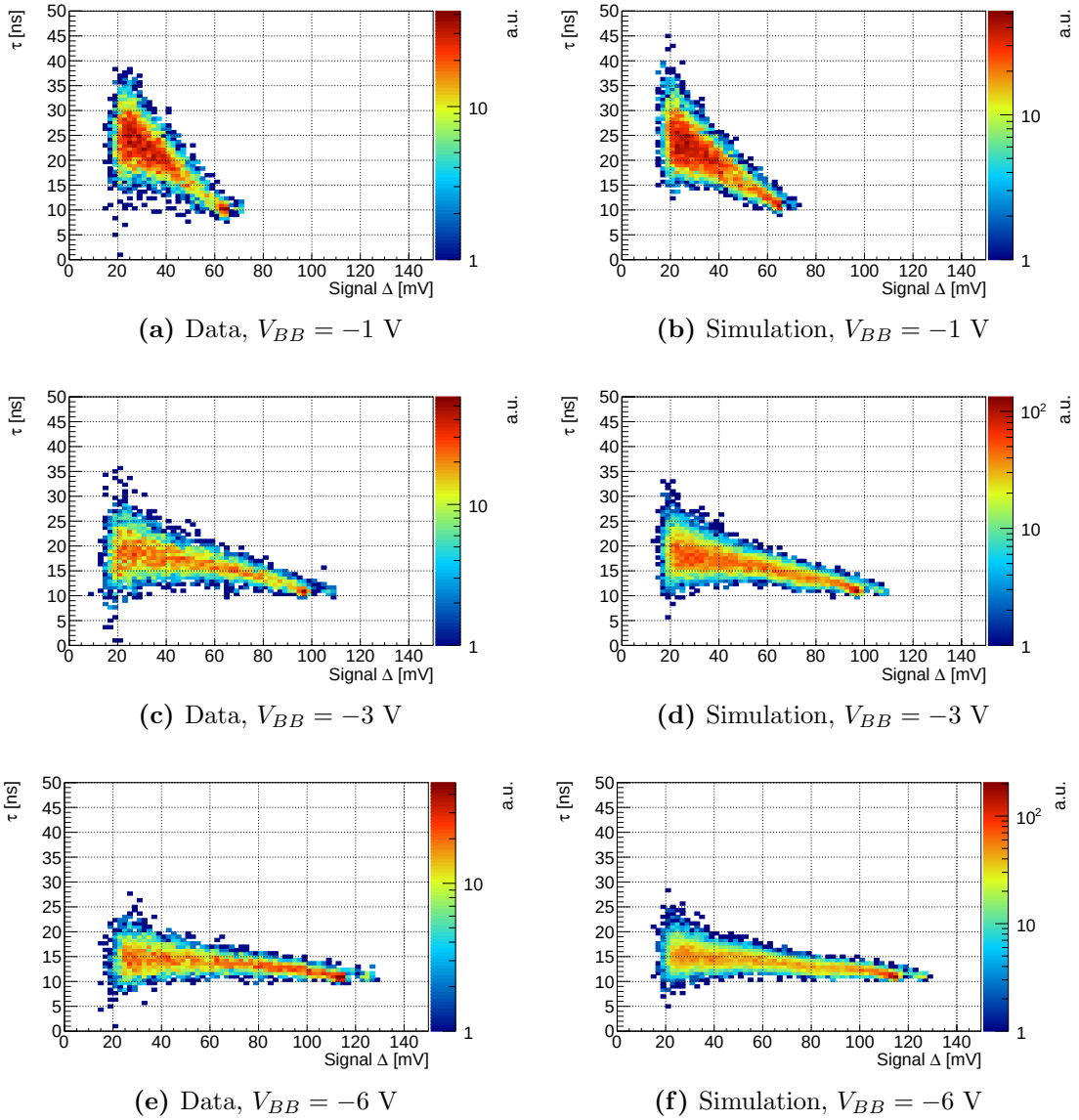

(a) Data, $V_{BB} = -1$ V

(b) Simulation, $V_{BB} = -1$ V

(c) Data, $V_{BB} = -3$ V

(d) Simulation, $V_{BB} = -3$ V

(e) Data, $V_{BB} = -6$ V

(f) Simulation, $V_{BB} = -6$ V

Figure 6.33: Charge collection time vs signal amplitude - Measured and simulated charge collection time plotted against collected charge i.e. pixel signal. $d_{epi} = 25$ µm

over the sensor volume[1]. The resulting distributions of the seed pixel t_{90} and matrix t_{90} for each of the starting points at different reverse bias voltages and epitaxial layer thicknesses are shown in figure 6.35. All distributions are characterised by two peaks; a narrow peak at 0 ns and a wide peak shifting with the reverse bias voltage and epitaxial layer thickness.

[1]Similar to ^{55}Fe algorithm (see sec 6.1.5.2) but the starting points are uniformly distributed along z-axis.

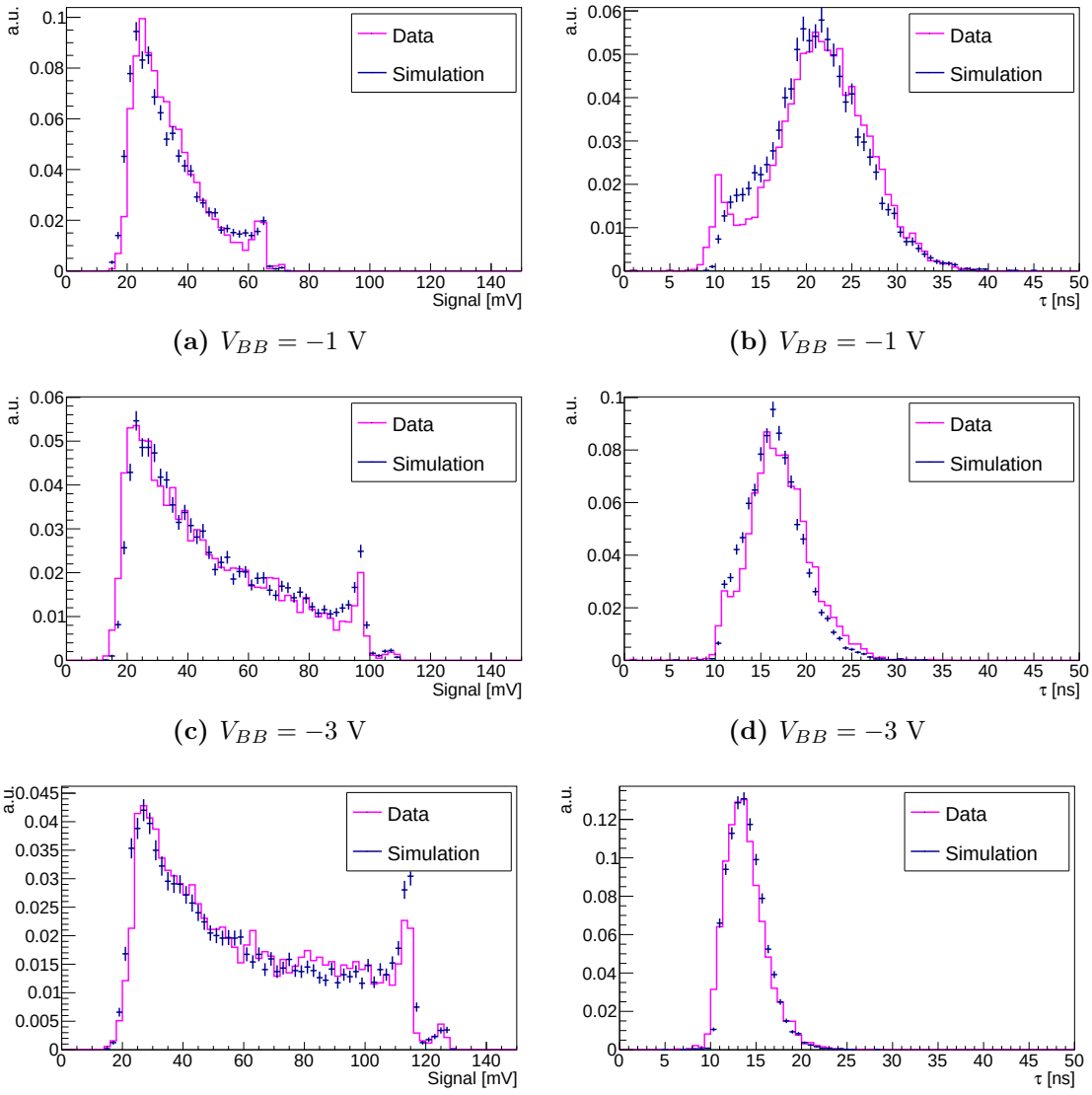

(a) $V_{BB} = -1$ V **(b)** $V_{BB} = -1$ V

(c) $V_{BB} = -3$ V **(d)** $V_{BB} = -3$ V

(e) $V_{BB} = -6$ V **(f)** $V_{BB} = -6$ V

Figure 6.34: Pixel signal (collected charge) and charge collection time (τ) - Measured and simulated distributions of collected charge i.e. pixel signal and charge collection time (τ). $d_{epi} = 25$ µm

The former is given by events originating in the high electric field region and therefore collected almost immediately. The latter is constituted by events originating from the low-field epitaxial layer and the substrate.

Figure 6.35 is summarised in a graph showing average seed pixel and matrix t_{90} as a function of reverse bias voltage. The decreasing difference between the 18 µm and

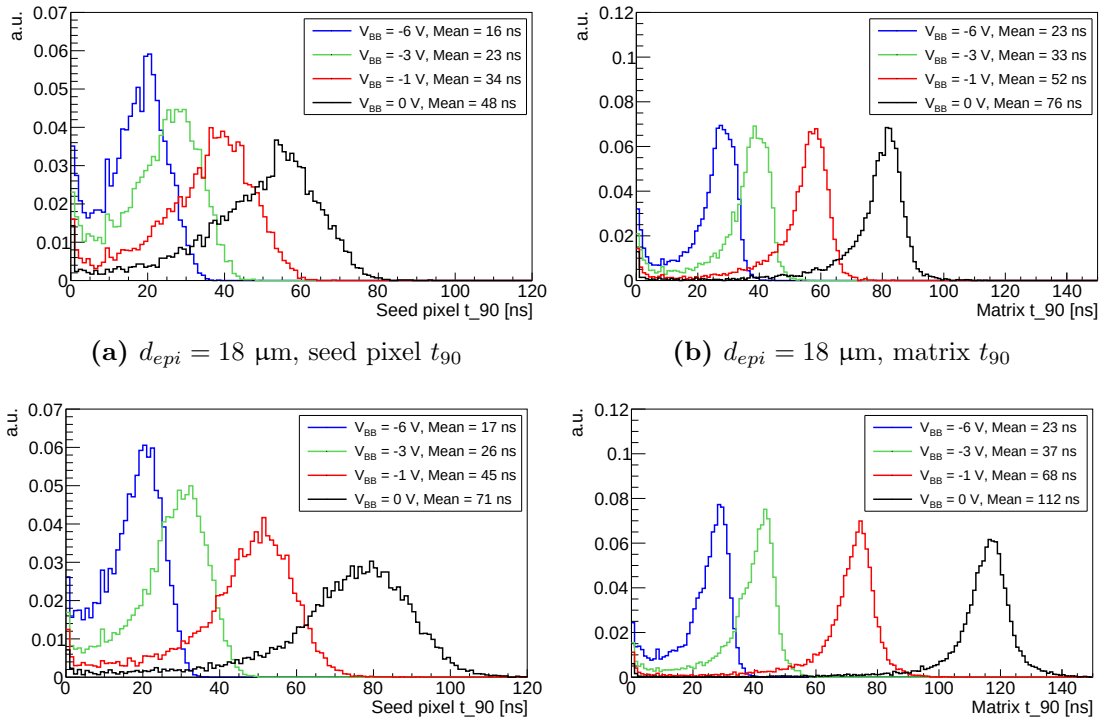

(a) $d_{epi} = 18$ µm, seed pixel t_{90}

(b) $d_{epi} = 18$ µm, matrix t_{90}

(c) $d_{epi} = 25$ µm, seed pixel t_{90}

(d) $d_{epi} = 25$ µm, matrix pixel t_{90}

Figure 6.35: Charge collection time distributions - Seed pixel t_{90} and matrix t_{90} distributions at different reverse bias voltages and epitaxial layer thicknesses.

25 µm epitaxial layer with increasing reverse bias voltage suggests that at high reverse bias voltages, the drift becomes the prevalent charge transport process.

6.6 Summary

The simulation model presented in this chapter can quantitatively reproduce the response of MAPS (e.g. seed signal and cluster size distributions, charge collection time, etc) to different radiation sources with only a few of inputs and one free parameter. The inputs include sensor noise and electron lifetime in the substrate while the free parameter is the electric field scaling factor which was introduced to compensate for the observed differences in the ^{55}Fe spectra. It is suspected that the discrepancy originates from the electric field extracted from a TCAD simulation, requiring additional TCAD simulations to confirm. Apart from reproducing excellent matching with data, the model also has some predictive capabilities; after comparing the simulation to the ALPIDE data, a strong indication of a

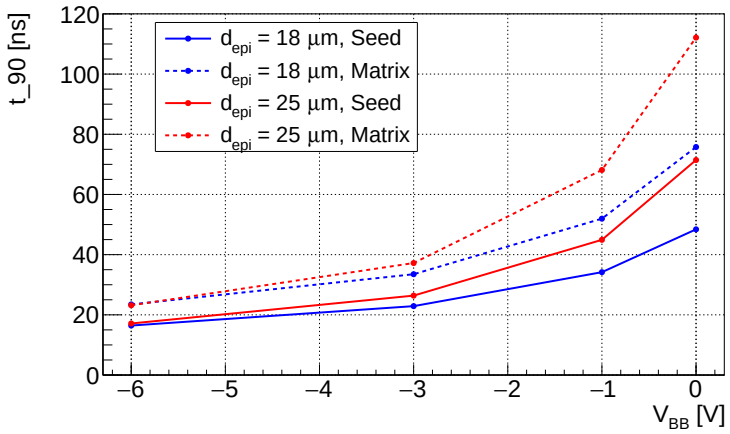

Figure 6.36: Charge collection time summary - Mean seed pixel t_{90} and matrix t_{90} at different reverse bias voltages and epitaxial layer thicknesses.

miscalibration of the ALPIDE threshold was discovered.

The simulation is designed both as a tool to study charge collection process and principles of operation of MAPS, and as a *fast tool* for integrating the response of MAPS into the simulation environment of experiments. The results discussed in this chapter were obtained with the simulation parameters (e.g. step size) optimised for precision so the performance on the standard PC was 500 ms per particle. However, this performance can be immediately improved by at least an order of magnitude just by optimising the parameters for speed. Even faster computation times can be achieved by using the "summable digits" approach (an option already implemented in the *fast tool* code).

7

Summary

The upgrade of the ALICE vertex detector, the Inner Tracking System (ITS), is scheduled to be installed during the next long shutdown period (2019-2020) of the CERN Large Hadron Collider (LHC). The current ITS will be replaced by seven concentric layers of Monolithic Active Pixel Sensors (MAPS) with total active surface of $\sim$10 m^2, thus making ALICE the first LHC experiment implementing MAPS detector technology on a large scale.

The ALPIDE chip, based on TowerJazz 180 nm CMOS Imaging Process, has been developed for this purpose. A particular process feature, the deep p-well, is exploited so the full CMOS logic can be implemented over the active sensor area without impinging on the deposited charge collection. The sensors are produced on wafers with a high resistivity epitaxial layer on top of the substrate, with a total thickness amounting to only 50 µm.

In the present work the characteristics of MAPS were studied through the extensive measurements of the various sensor prototypes developed for the ITS upgrade, including the finals sensor ALPIDE. These measurements were complemented by developing a new *fast tool* in order to simulate the MAPS response to various radiation sources.

An analogue sensor prototype, INVESTIGATOR, was used to study the influence of the design and operational parameters on the pixel performance. The Q/C ratio was studied as a function of the reverse bias voltage of the collection diode, observing it is greatly improved at higher reverse bias voltages not only due to the decrease of the input capacitance but also because of increasing the amount of charge collected by seed pixels. Sensors with different epitaxial layer thicknesses were tested. In particular, considering the pixel geometry similar to the one implemented in the ALPIDE, a better performance was observed for a thicker epitaxial layer. However, no clear improvement was achieved for thicknesses higher than 25 µm. The collection diode geometry (size and spacing from

the surrounding p-well) has a major impact on the sensor performance, though the choice of the exact values is rather empirical and compromises between the collected charge and the input capacitance. The n-well size of 2 µm and 3 µm spacing has shown the best results for the epitaxial layer thickness of 25 µm and 28 µm pixel pitch (the size most similar to that implemented in the final chip).

The ALPIDE in-pixel front-end circuitry features amplification, shaping, and discrimination, whose correct operation was tested and verified in various prototypes. Using an infrared laser beam, the front-end pulse duration was measured in the first full-scale prototype pALPIDE-1, which lead to optimisations of the front-end circuitry and consequently the reduction of the pulse length. The main reason for the fake-hit rate in the ALPIDE prototypes was suspected to be the random telegraph noise originating at the front-end input transistor. Therefore, the pALPIDE-3 was produced in two flavours, differing only in the size of the input transistor. The presented measurements have shown that increasing the input transistor size lowers the fake-hit rate by orders of magnitude.

The upgrade of the ITS presents two different sets of requirements for sensors of the inner and of the outer layers due to the significantly different track density, radiation level, and active detector surface. It has been demonstrated that the final ALPIDE chip fulfils the stringent requirements in both cases. The detection efficiency is higher than 99%, fake hit probability is orders of magnitude lower than the required 10^{-6} pixel^{-1}event^{-1} and spatial resolution within the required 5 µm. This performance is maintained even after an irradiation up to 800 krad and 1.7×10^{13} 1 MeV n_{eq}/cm^2, which is above what is expected during the detector lifetime.

Given the different requirements and constructions challenges, the new ITS is divided in Inner and Outer Barrel, consisting of three and four layers, respectively. The layers are azimuthally segmented in mechanically independent elements named staves. An ALICE ITS Inner Barrel stave, composed of 9 ALPIDE chips was tested in the Pb–Pb collision environment of the NA61/SHINE experiment. The integration was successful and no issues with the readout or chips were encountered. Hit multiplicities up to 30 hit/cm^2 were measured which is the expected maximum hit density at the first layer of the upgraded ITS. The measured chip performance in a stave is comparable with the performance of chips in the laboratory and the test-beam; the detection efficiency is higher than 99% and fake-hit rate is significantly lower than 10^{-6} pixel^{-1}event^{-1}. The spatial resolution was not calculated but the residuals of 7-8 µm are comparable to single-chip results.

While the successful operation of the final sensor for the ITS upgrade has been confirmed, the charge collection process in MAPS had yet to be fully characterised. For this purpose, a new fast simulation tool has been developed. The basic concept of the *fast tool* is a first principles MC simulation, using electric fields extracted from a TCAD simulation to model the charge carrier drift. The INVESTIGATOR (analogue output) and ALPIDE (digital output) chips have been simulated and an excellent agreement between data and simulation has been achieved, both for ^{55}Fe X-rays and minimum ionizing particles.

The *fast tool* uses requires only one free parameter i.e. the electric field scaling factor which was introduced to compensate for the observed differences in the ^{55}Fe spectra. It is suspected that the discrepancy originates from the electric field extracted from the TCAD simulation. Once this free parameter is tuned, the simulation is capable of reproducing both transient and integrated sensor response to all radiations. In particular, the time-resolved simulation was used to study the charge collection time for different epitaxial layer thicknesses and reverse bias voltages.

Apart from reproducing excellent matching with data, the model also has some predictive capabilities; after comparing the simulation to the ALPIDE data, a strong indication of a miscalibration of the ALPIDE threshold was discovered. Furthermore, the *fast tool* has also been designed for integrating the response of MAPS into the Monte Carlo simulation environment of experiments. and is currently being implemented in the ALICE O^2 framework for the simulation of the entire ITS.

Appendix A

Additional simulation plots

A.1 Simulation of response of analogue sensors to ^{55}Fe X-rays

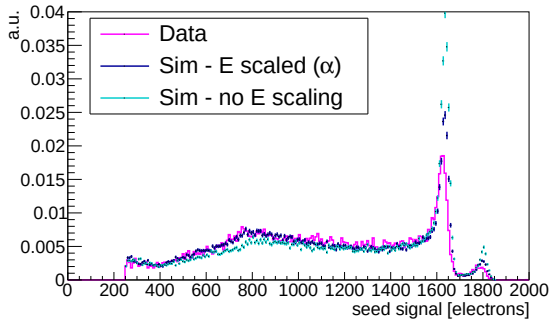

(a) Seed signal distribution

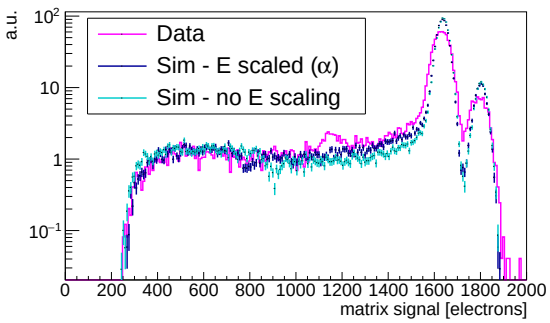

(b) Matrix signal distribution

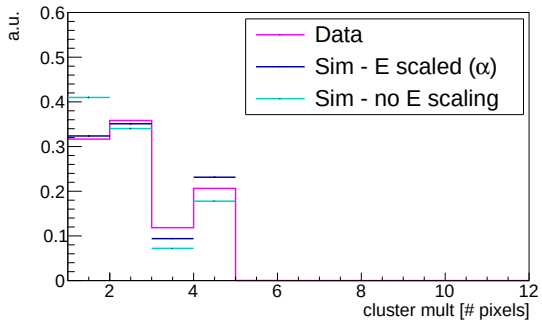

(c) Cluster size distribution

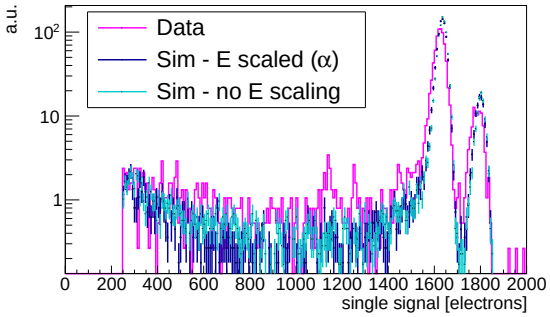

(d) Single pixel cluster signal distribution

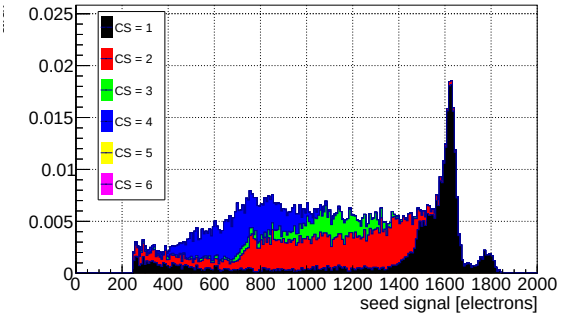

(e) Seed signal vs cluster size - Data

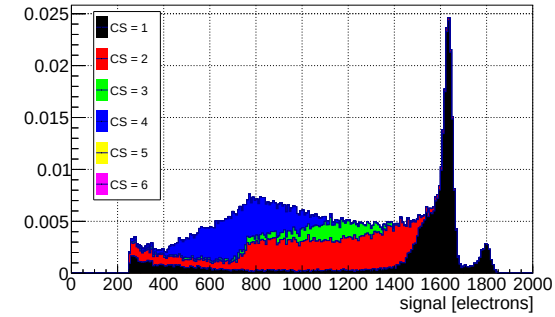

(f) Seed signal vs cluster size - Simulation

Figure A.1: Simulation of response of analogue sensors to X-rays - $d_{epi} = 18$ µm, $V_{BB} = -6$ V, $\alpha = 0.45$.

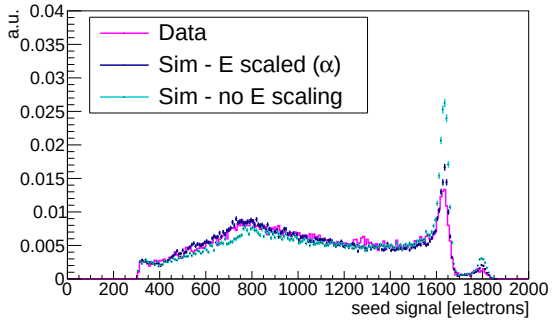

(a) Seed signal distribution

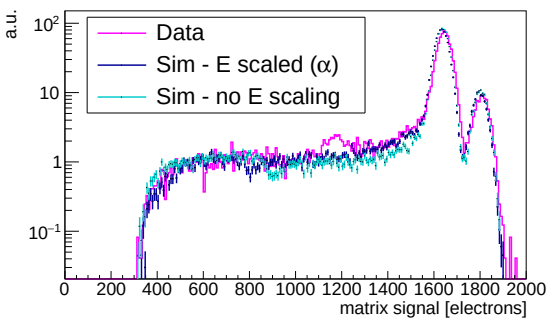

(b) Matrix signal distribution

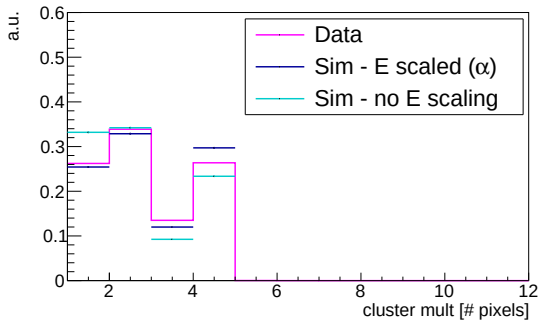

(c) Cluster size distribution

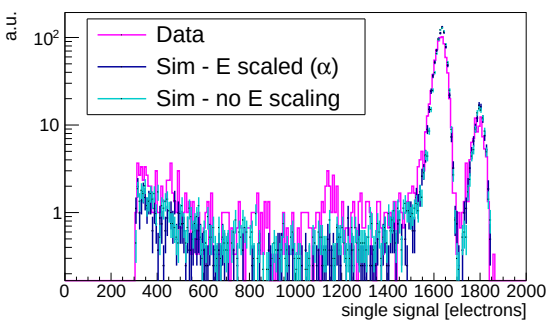

(d) Single pixel cluster signal distribution

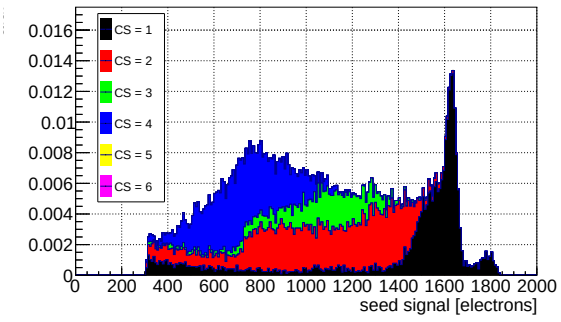

(e) Seed signal vs cluster size - Data

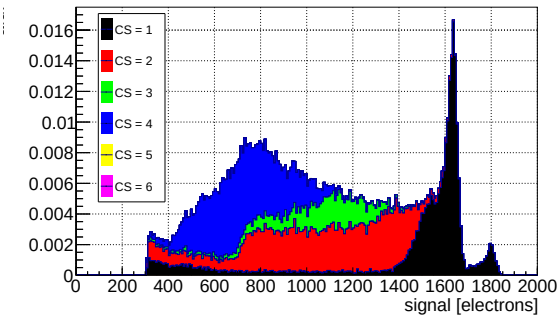

(f) Seed signal vs cluster size - Simulation

Figure A.2: Simulation of response of analogue sensors to X-rays - $d_{epi} = 18$ µm, $V_{BB} = -3$ V, $\alpha = 0.5$.

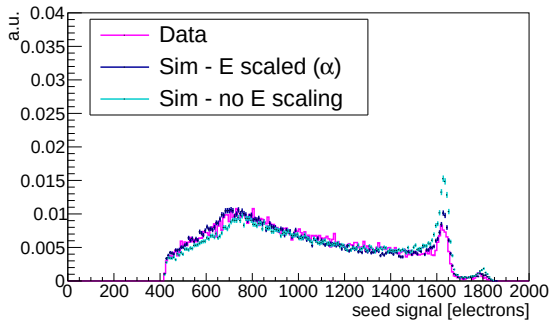

(a) Seed signal distribution

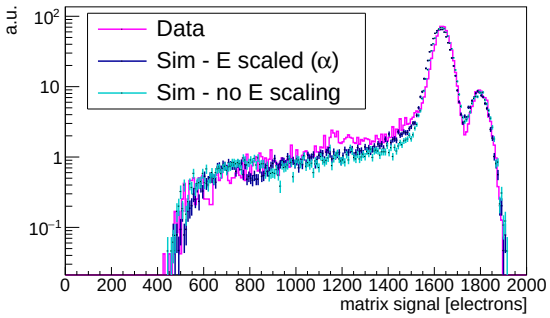

(b) Matrix signal distribution

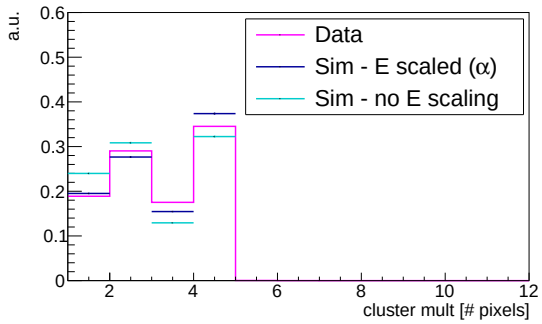

(c) Cluster size distribution

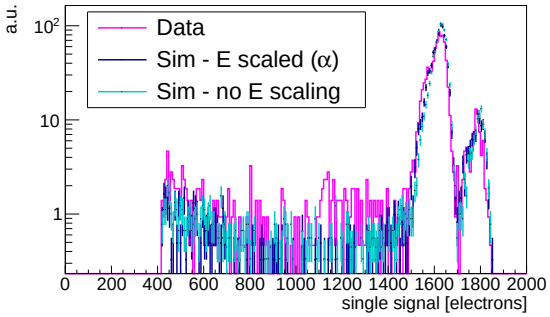

(d) Single pixel cluster signal distribution

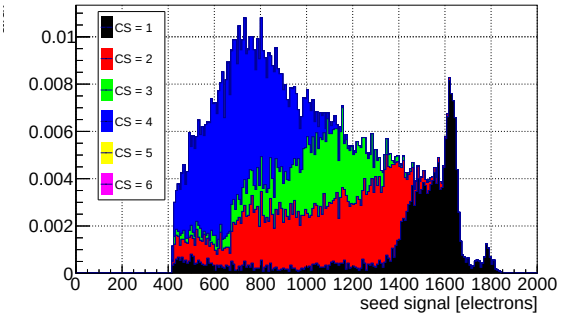

(e) Seed signal vs cluster size - Data

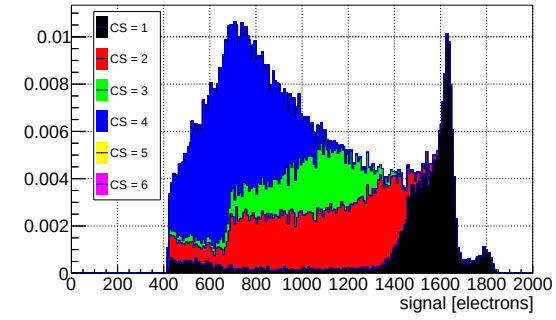

(f) Seed signal vs cluster size - Simulation

Figure A.3: Simulation of response of analogue sensors to X-rays - $d_{epi} = 18$ µm, $V_{BB} = -1$ V, $\alpha = 0.55$.

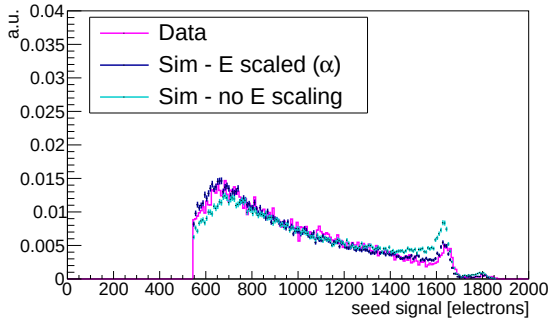

(a) Seed signal distribution

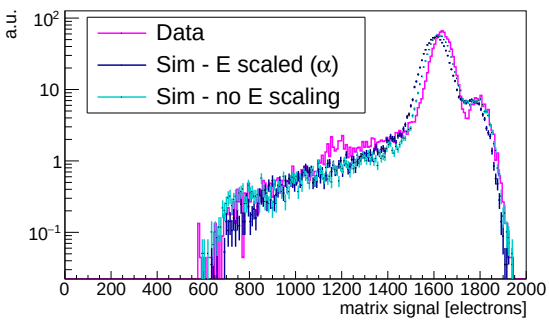

(b) Matrix signal distribution

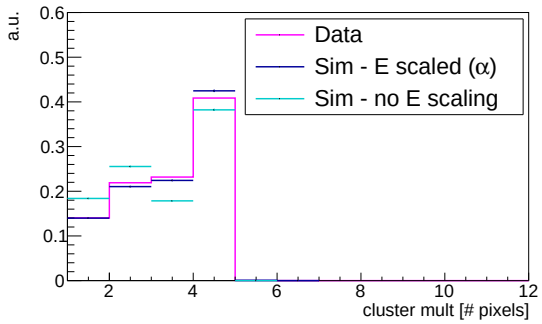

(c) Cluster size distribution

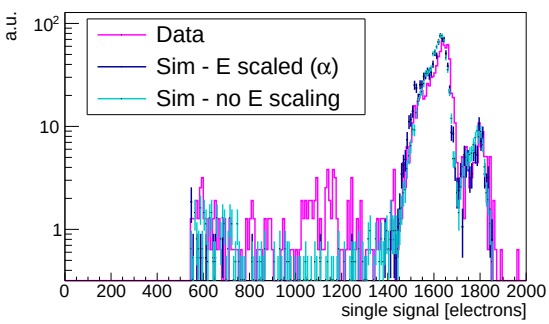

(d) Single pixel cluster signal distribution

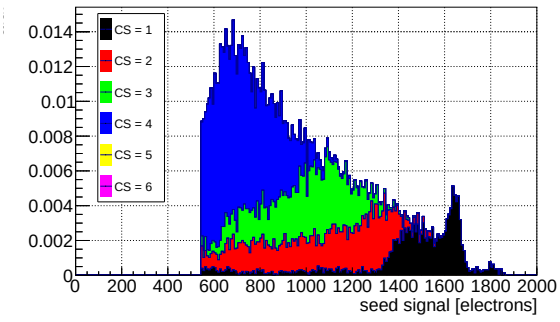

(e) Seed signal vs cluster size - Data

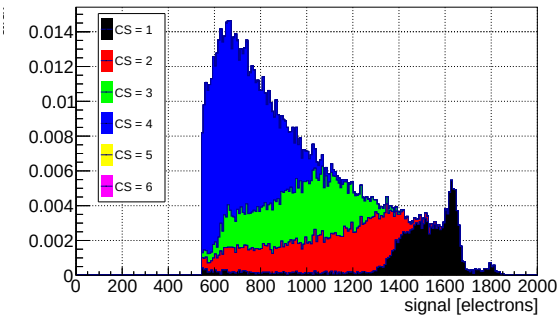

(f) Seed signal vs cluster size - Simulation

Figure A.4: Simulation of response of analogue sensors to X-rays - $d_{epi} = 18$ µm, $V_{BB} = 0$ V, $\alpha = 0.6$.

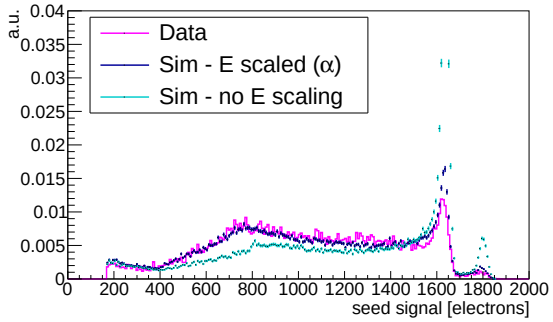

(a) Seed signal distribution

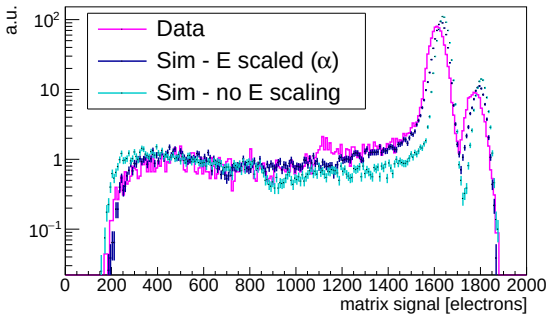

(b) Matrix signal distribution

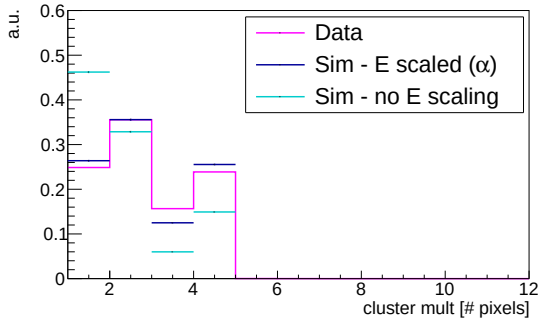

(c) Cluster size distribution

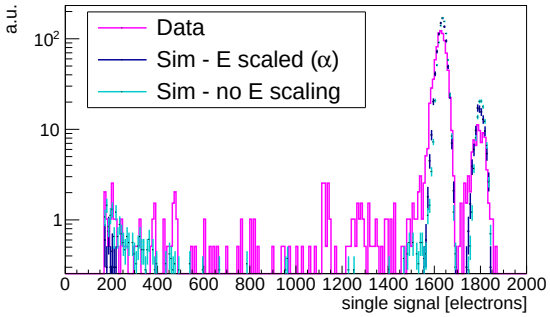

(d) Single pixel cluster signal distribution

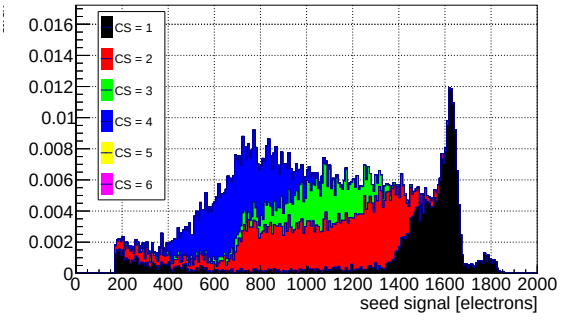

(e) Seed signal vs cluster size - Data

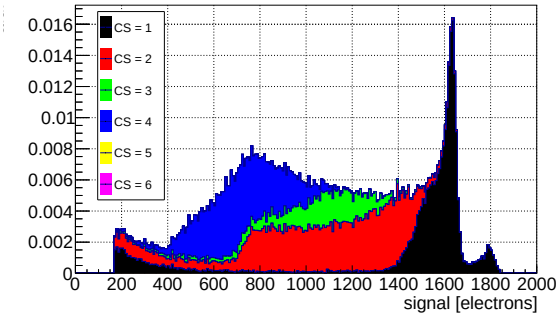

(f) Seed signal vs cluster size - Simulation

Figure A.5: Simulation of response of analogue sensors to X-rays - $d_{epi} = 25$ µm, $V_{BB} = -6$ V, $\alpha = 0.25$.

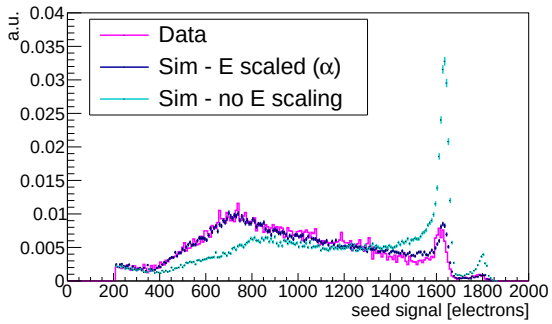

(a) Seed signal distribution

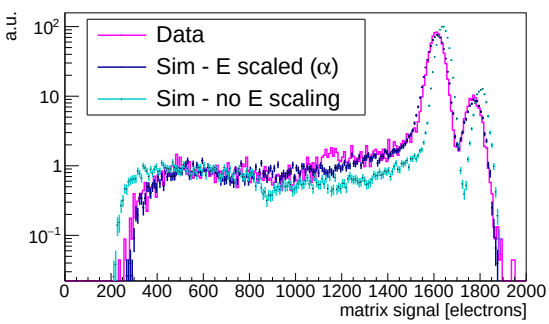

(b) Matrix signal distribution

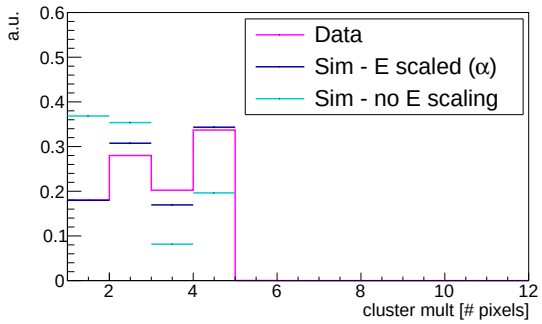

(c) Cluster size distribution

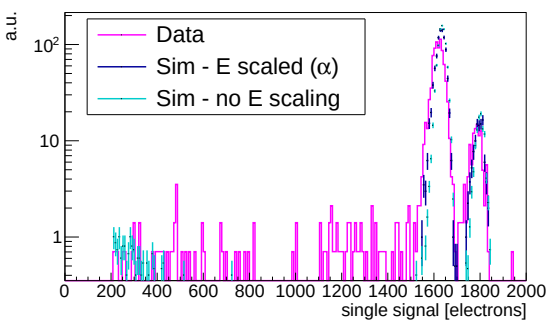

(d) Single pixel cluster signal distribution

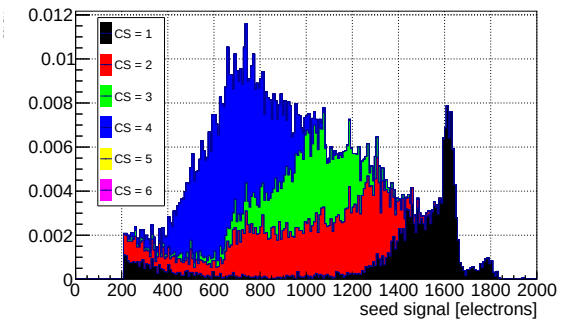

(e) Seed signal vs cluster size - Data

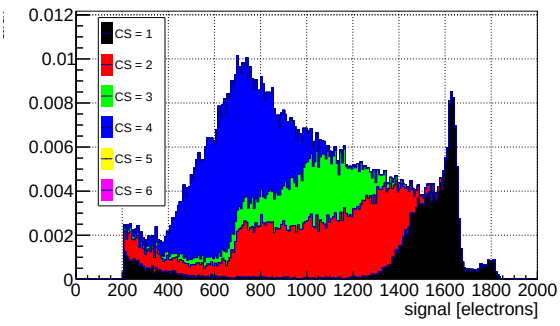

(f) Seed signal vs cluster size - Simulation

Figure A.6: Simulation of response of analogue sensors to X-rays - $d_{epi} = 25$ µm, $V_{BB} = -3$ V, $\alpha = 0.28$.

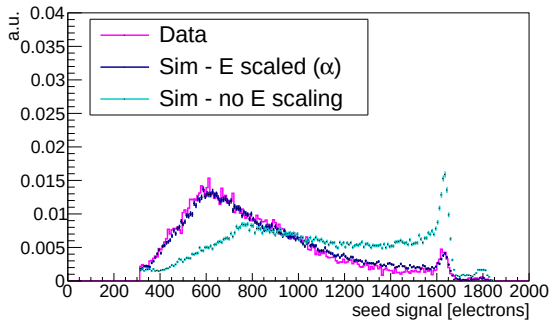

(a) Seed signal distribution

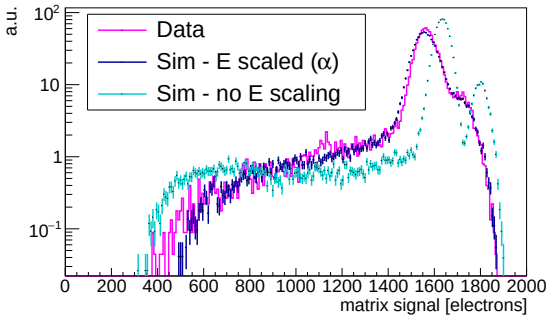

(b) Matrix signal distribution

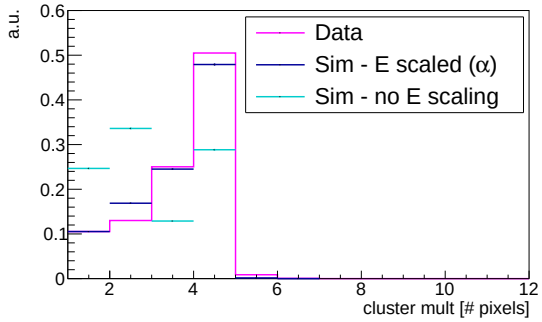

(c) Cluster size distribution

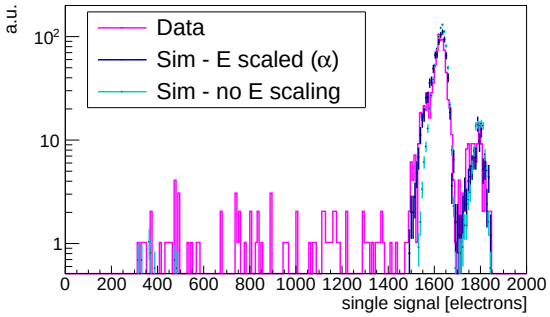

(d) Single pixel cluster signal distribution

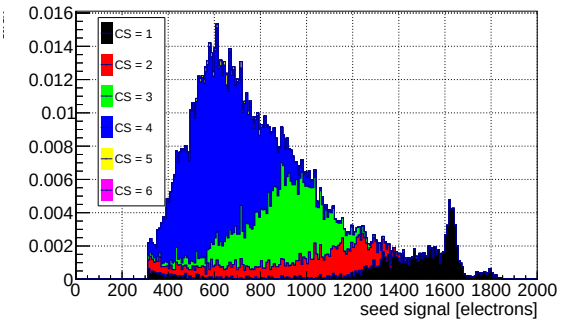

(e) Seed signal vs cluster size - Data

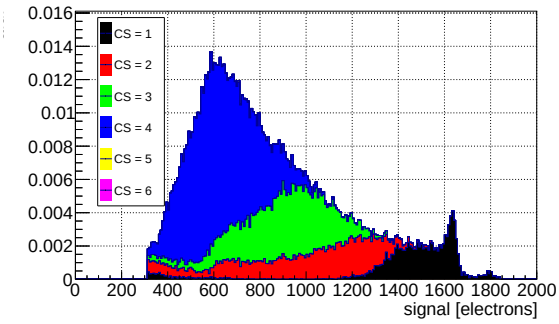

(f) Seed signal vs cluster size - Simulation

Figure A.7: Simulation of response of analogue sensors to X-rays - $d_{epi} = 25$ µm, $V_{BB} = -1$ V, $\alpha = 0.3$.

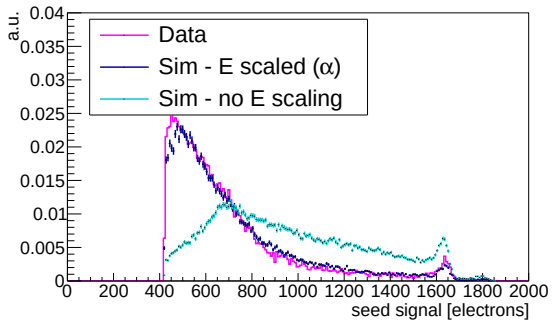

(a) Seed signal distribution

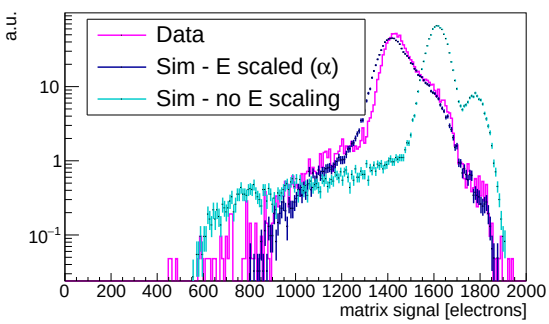

(b) Matrix signal distribution

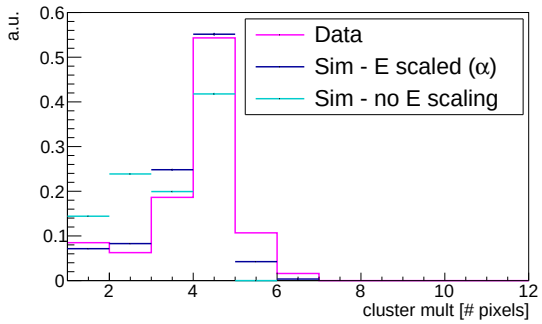

(c) Cluster size distribution

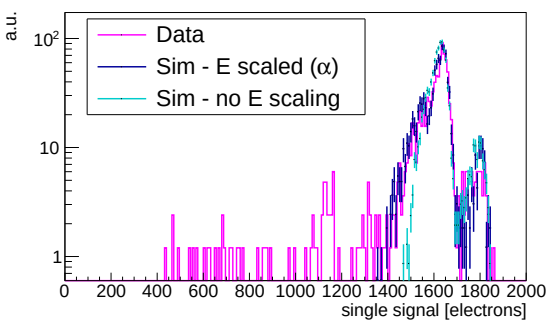

(d) Single pixel cluster signal distribution

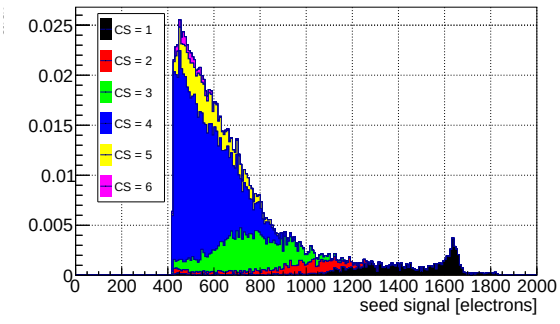

(e) Seed signal vs cluster size - Data

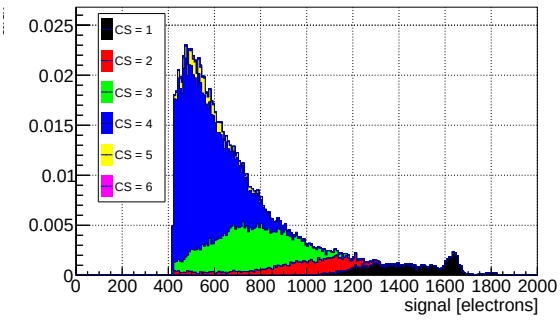

(f) Seed signal vs cluster size - Simulation

Figure A.8: Simulation of response of analogue sensors to X-rays - $d_{epi} = 25$ µm, $V_{BB} = 0$ V, $\alpha = 0.33$.

A.2 Simulation of response of analogue sensors to MIPs

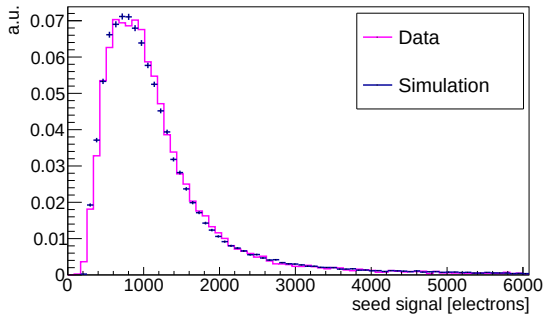

(a) Seed signal distribution

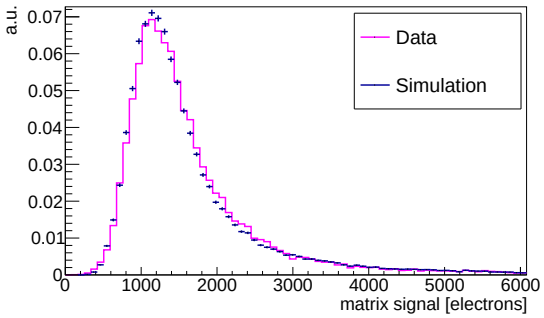

(b) Matrix signal distribution

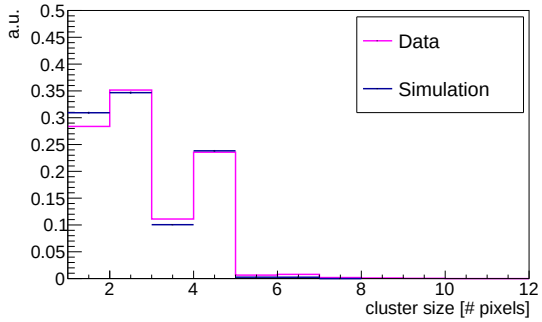

(c) Cluster size distribution

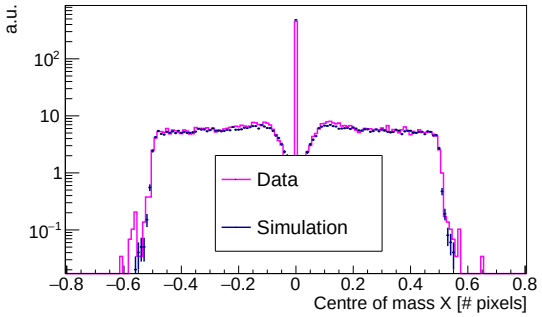

(d) Centre of mass distribution

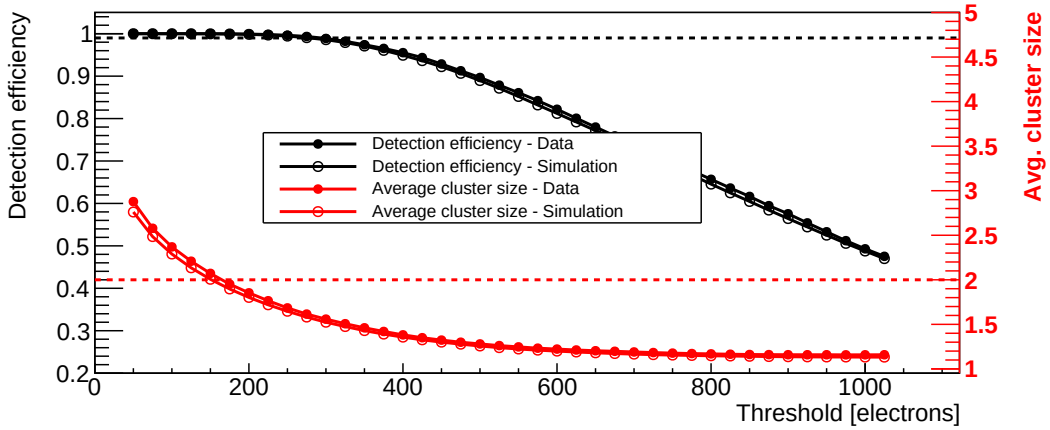

(e) Seed signal vs cluster size - Data

Figure A.9: Simulation of response of analogue sensors to MIPs - $d_{epi} = 18$ µm, $V_{BB} = -6$ V, $\alpha = 0.45$.

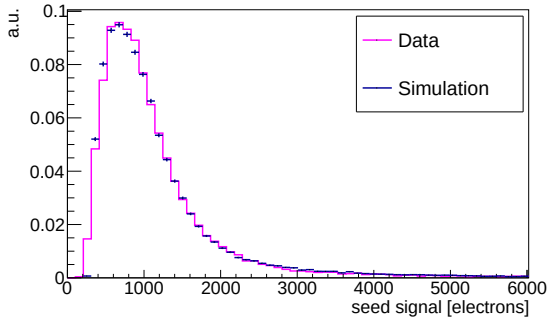

(a) Seed signal distribution

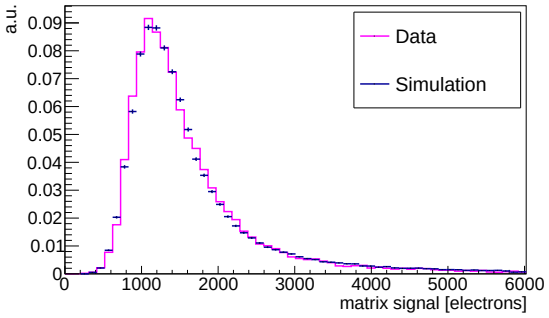

(b) Matrix signal distribution

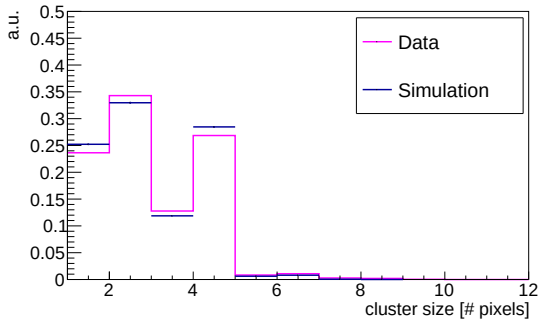

(c) Cluster size distribution

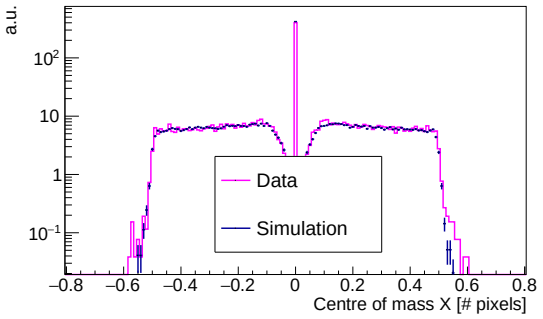

(d) Centre of mass distribution

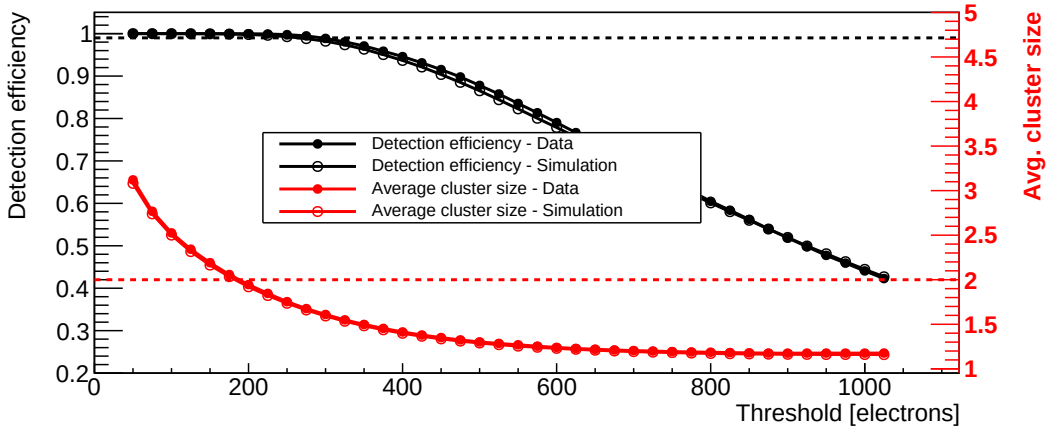

(e) Seed signal vs cluster size - Data

Figure A.10: Simulation of response of analogue sensors to MIPs - $d_{epi} = 18$ µm, $V_{BB} = -3$ V, $\alpha = 0.5$.

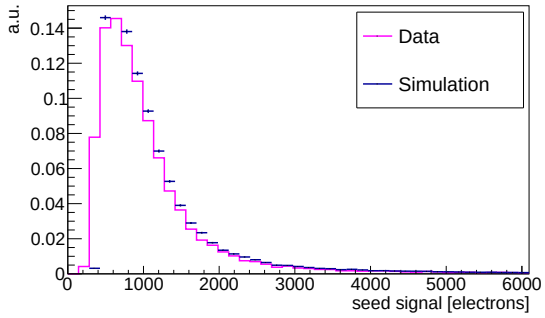

(a) Seed signal distribution

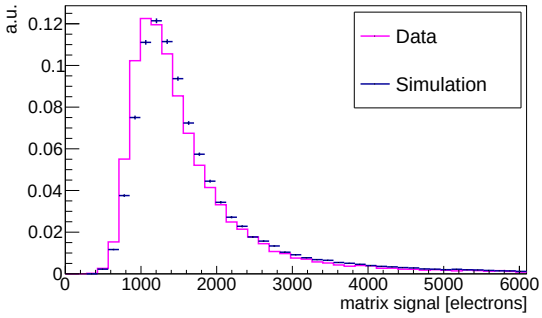

(b) Matrix signal distribution

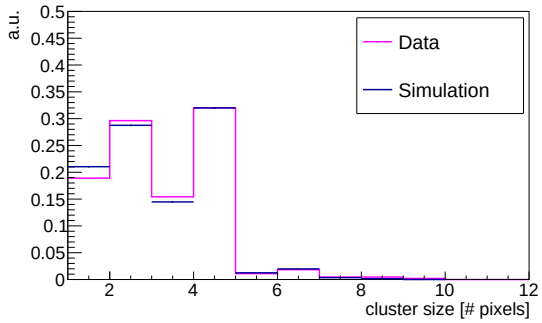

(c) Cluster size distribution

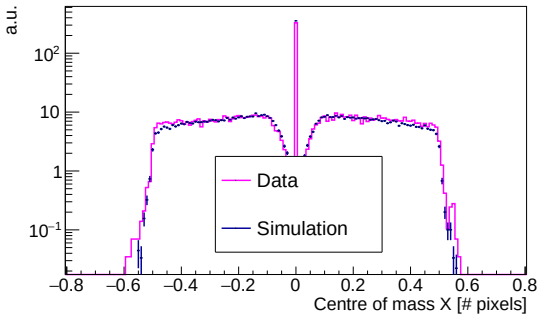

(d) Centre of mass distribution

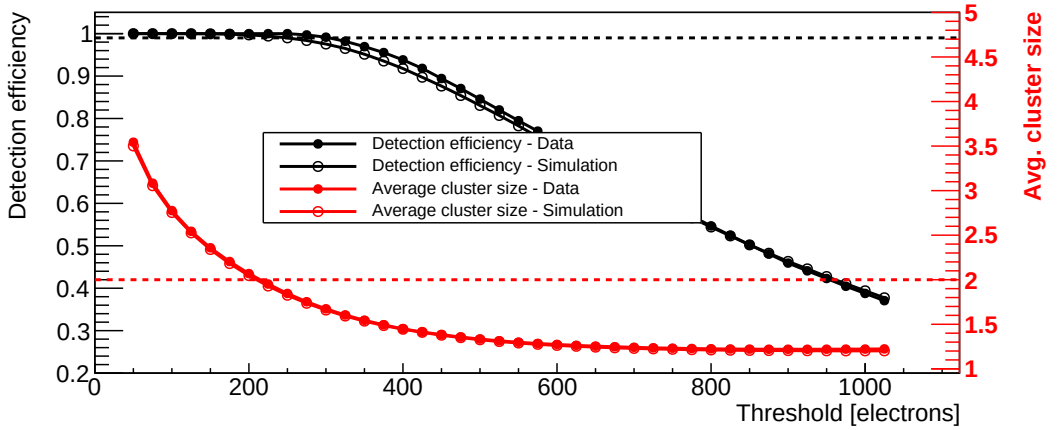

(e) Seed signal vs cluster size - Data

Figure A.11: Simulation of response of analogue sensors to MIPs - $d_{epi} = 18$ µm, $V_{BB} = -1$ V, $\alpha = 0.55$.

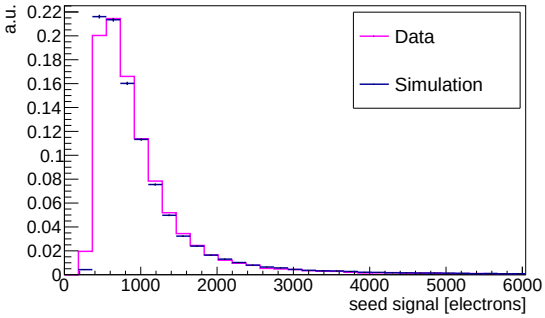

(a) Seed signal distribution

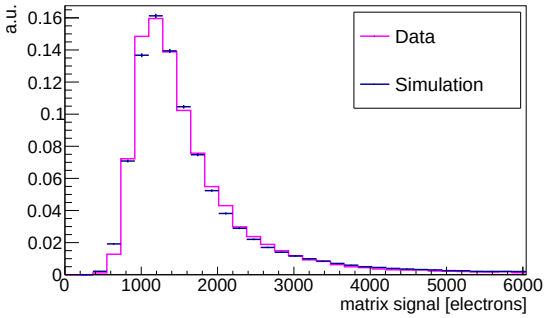

(b) Matrix signal distribution

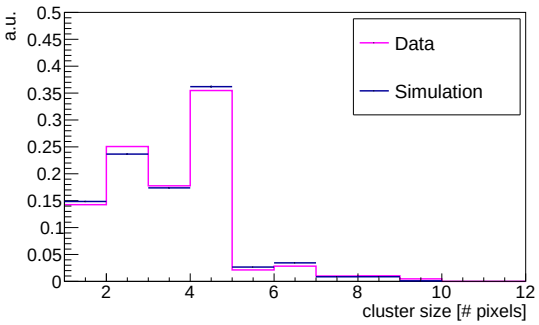

(c) Cluster size distribution

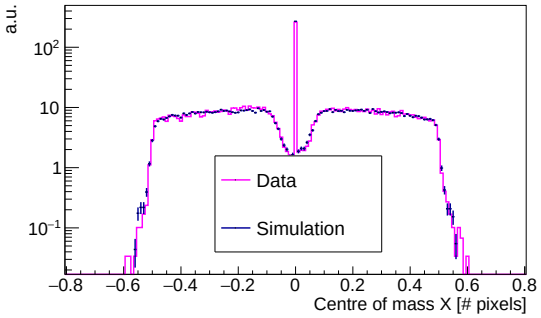

(d) Centre of mass distribution

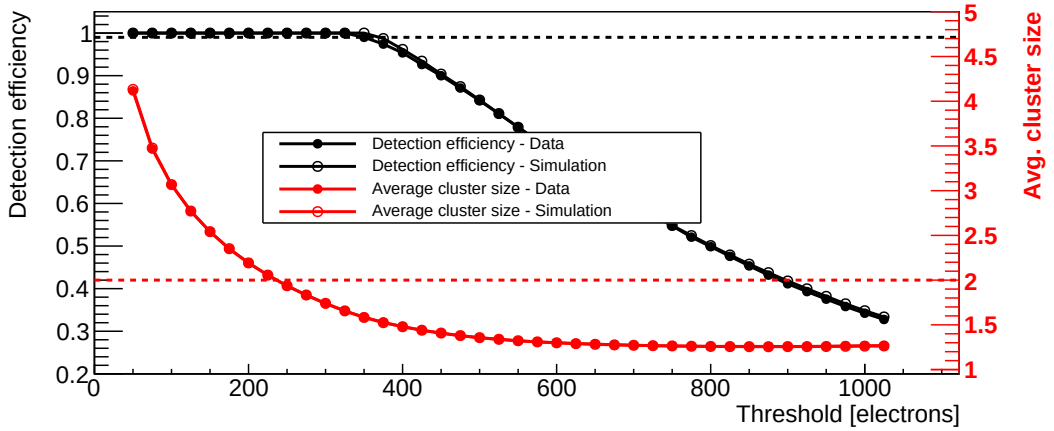

(e) Seed signal vs cluster size - Data

Figure A.12: Simulation of response of analogue sensors to MIPs - $d_{epi} = 18$ µm, $V_{BB} = 0$ V, $\alpha = 0.6$.

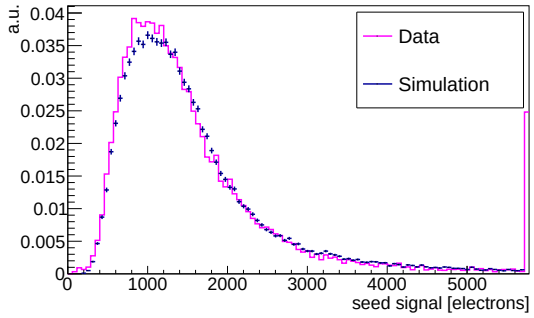

(a) Seed signal distribution

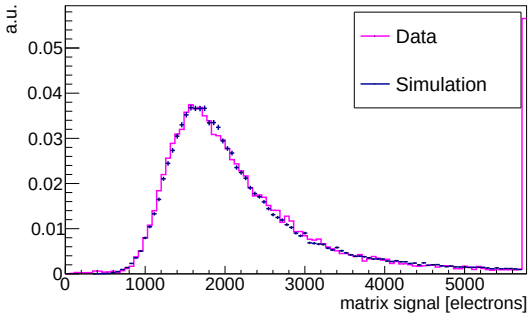

(b) Matrix signal distribution

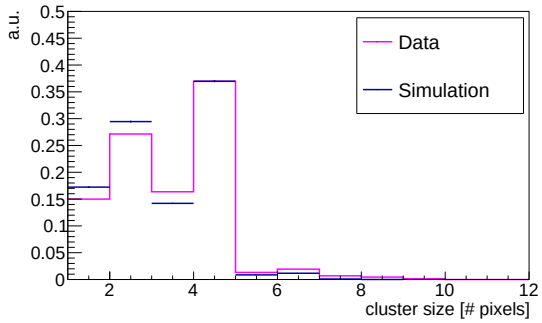

(c) Cluster size distribution

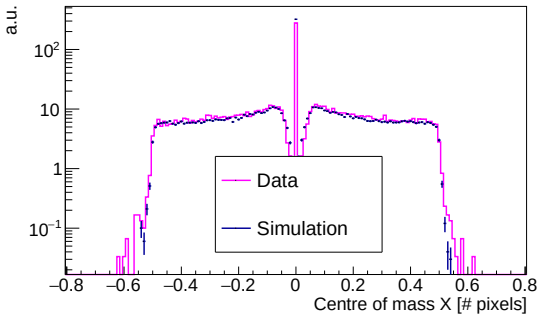

(d) Centre of mass distribution

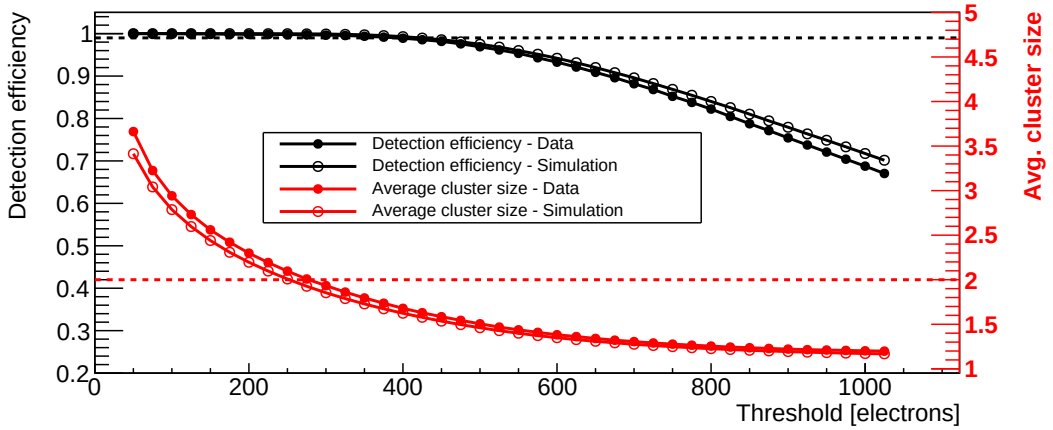

(e) Seed signal vs cluster size - Data

Figure A.13: Simulation of response of analogue sensors to MIPs - $d_{epi} = 25$ µm, $V_{BB} = -6$ V, $\alpha = 0.3$.

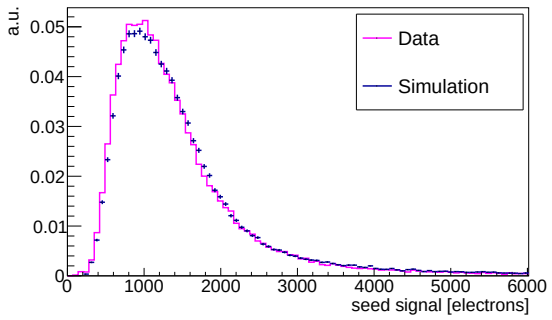

(a) Seed signal distribution

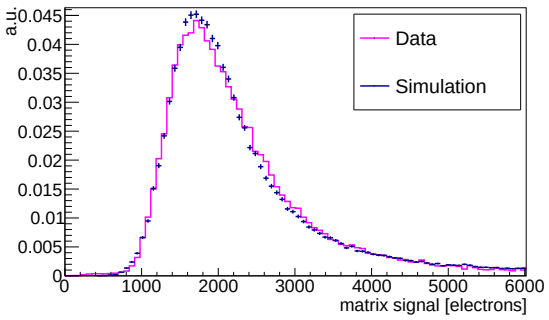

(b) Matrix signal distribution

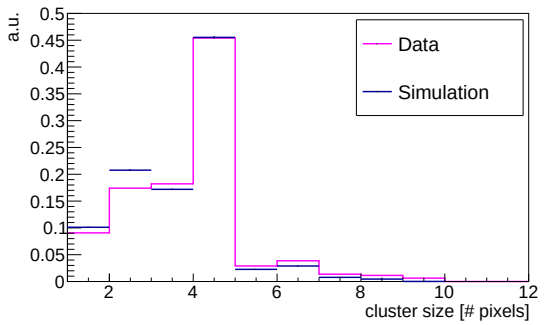

(c) Cluster size distribution

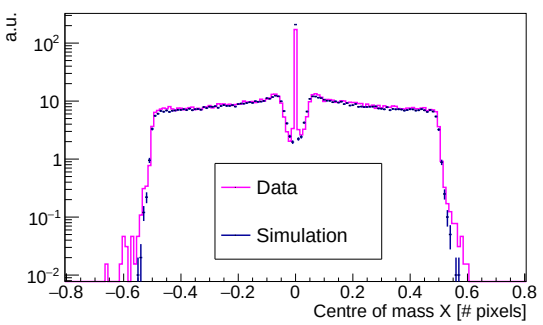

(d) Centre of mass distribution

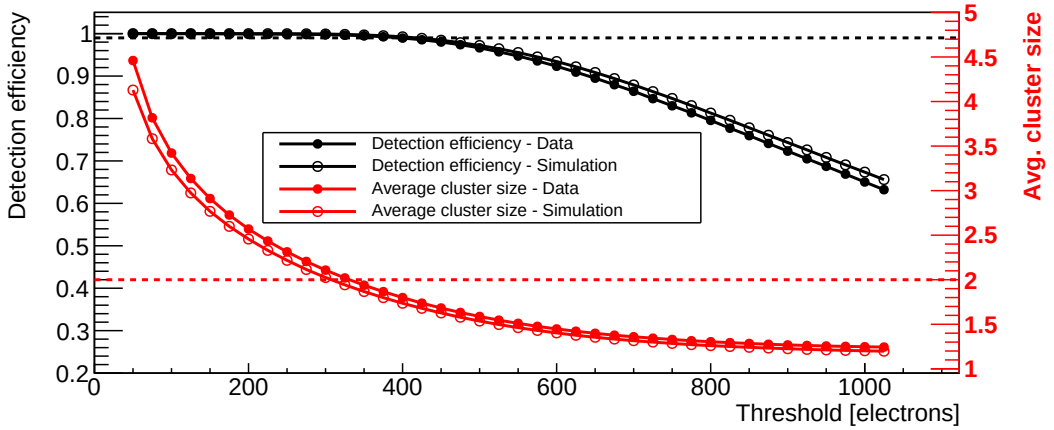

(e) Seed signal vs cluster size - Data

Figure A.14: Simulation of response of analogue sensors to MIPs - $d_{epi} = 25$ µm, $V_{BB} = -3$ V, $\alpha = 0.28$.

A.3 Simulation of response of binary sensors to MIPs

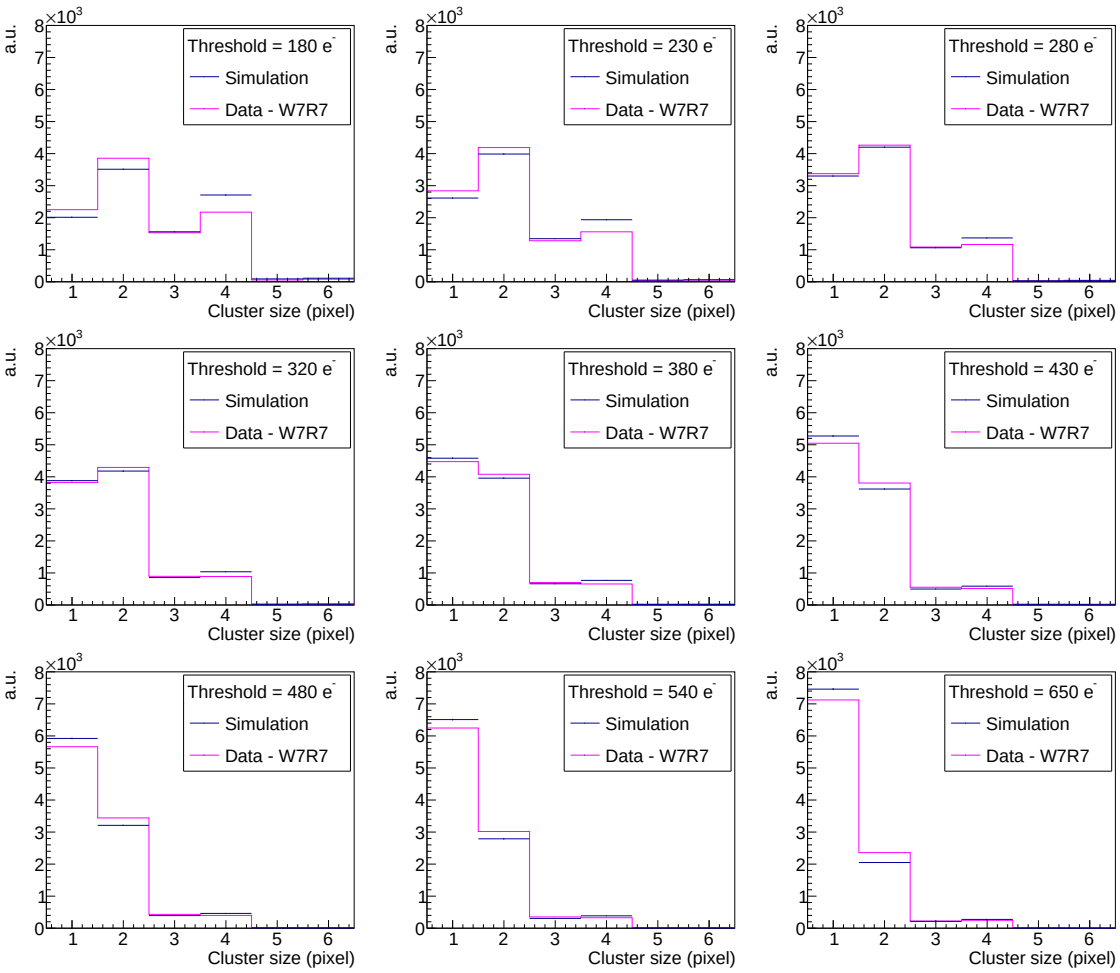

Figure A.15: Simulation of response of binary sensors to MIPs - Simulated and measured ALPIDE cluster size distributions at different thresholds. $V_{BB} = -3$ V

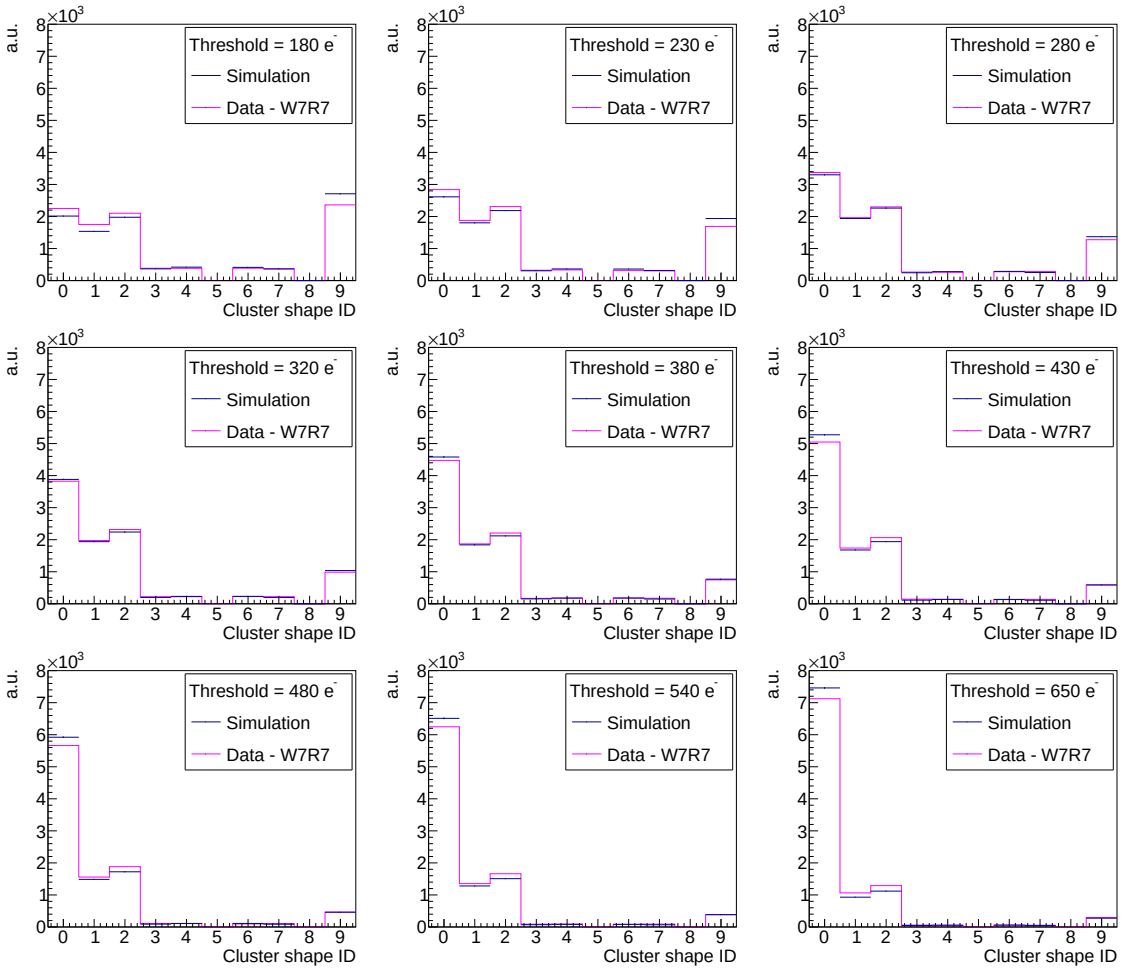

Figure A.16: Simulation of response of binary sensors to MIPs - Simulated and measured ALPIDE cluster shape distributions at different thresholds. $V_{BB} = -3$ V

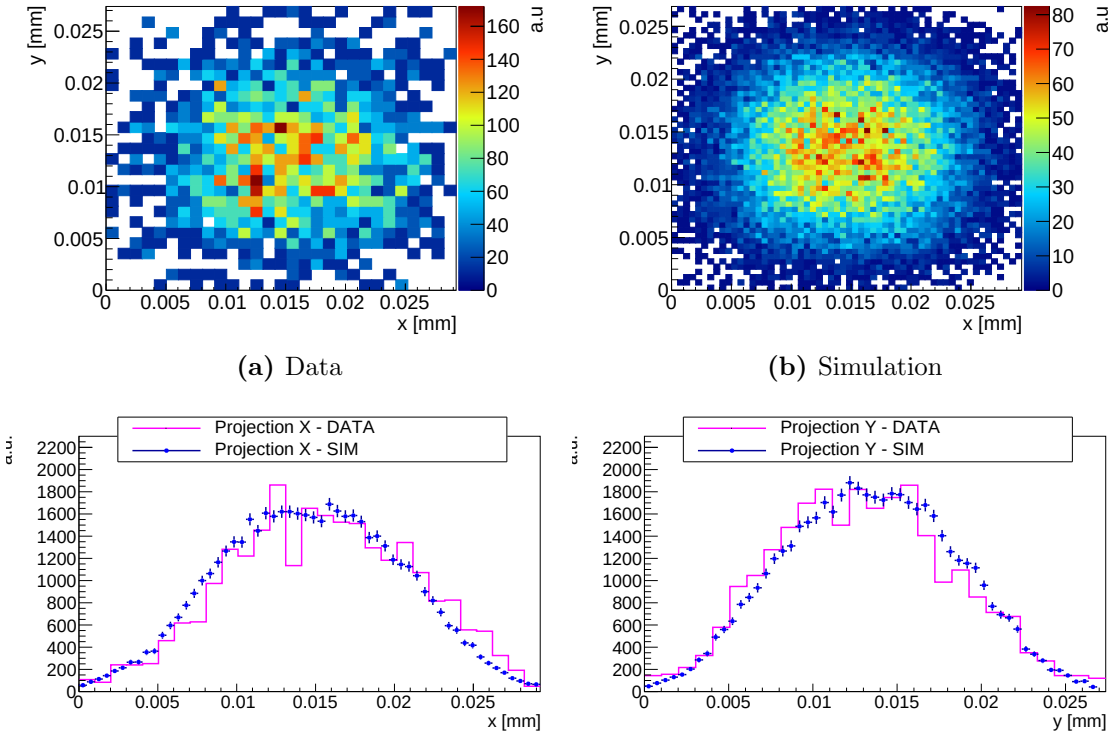

(a) Data

(b) Simulation

(c) Projection on x-axis

(d) Projection on y-axis

Figure A.17: Simulation of response of binary sensors to MIPs - Simulated and measured particle impinging point (inside a pixel) for ALPIDE clusters with shape ID=0.

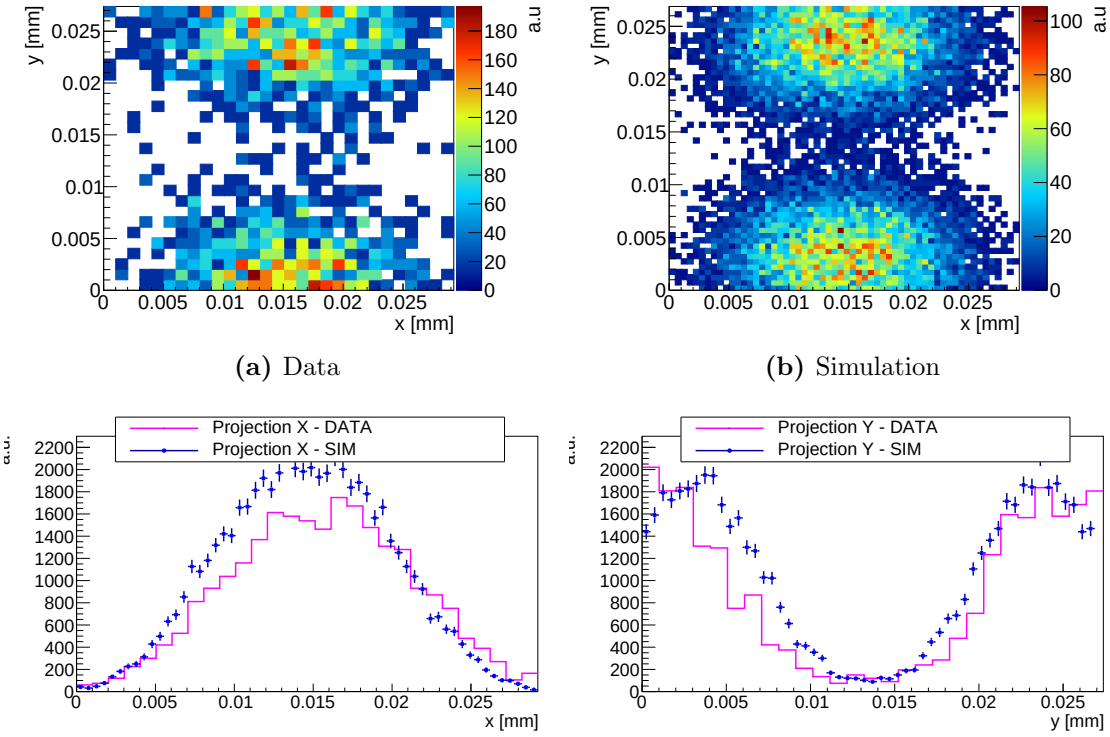

(a) Data

(b) Simulation

(c) Projection on x-axis

(d) Projection on y-axis

Figure A.18: Simulation of response of binary sensors to MIPs - Simulated and measured particle impinging point (inside a pixel) for ALPIDE clusters with shape ID=2.

Appendix B

INVESTIGATOR impulse response function

In case of the charge collection measurements (see sec. 6.5) it was necessary to determine the impulse response function (IRF) of the INVESTIGATOR chip in order to de-convolute the signal given by the charge collection from the response of the INVESTIGATOR readout circuitry (see fig. 3.2). Rephrasing the problem mathematically, the measured charge collected at time t is given by

$$w(t) = (n_{e,coll} * f)(t) = \int_{-\infty}^{+\infty} n_{e,coll}(\tau) f(\tau - t) d\tau \tag{B.1}$$

where $n_{e,coll}(t)$ is number of electrons collected at instant t and $f(t)$ is the impulse response function of the readout circuitry. In fact, since the collected charge is integrated by the sensing node, the output signal can be written as

$$W(t) = \int_{-\infty}^{t} w(\tau) d\tau. \tag{B.2}$$

One way to determine the $f(t)$ is by sending a brief input signal i.e. an impulse (hence the name impulse response function), such as instantaneous charge collection $n_{e,coll}(t) = \delta(t)$. The eq. B.1 then becomes

$$w(t) = \int_{-\infty}^{+\infty} \delta(\tau) f(\tau - t) d\tau = f(t), \tag{B.3}$$

and the measured signal

$$W(t) = \int_{-\infty}^{t} f(\tau) d\tau. \tag{B.4}$$

Therefore, $f(t)$ can be determined as $dW(t)/dt$ for events with instantaneous charge collection i.e. with $n_{e,coll}(t) = \delta(t)$.

The photoelectrons collected from the depleted region directly underneath the collection diode can be assumed as events with instantaneous charge collection, given the high electric field present in that region. Following the same reasoning as for the seed signal distribution in sec. 2.4.1, two peaks at the high end of the spectrum in figure 6.34e can be identified as 5.9 keV and 6.5 keV photons emitted by the ^{55}Fe source. That is, the charge deposited by events in the two peaks is assumed to be collected instantaneously. The corresponding waveforms were selected and fitted with a function based on the incomplete gamma function (see fig. B.1). The fit function was determined empirically and is given by the following expression

$$F(t) = \begin{cases} c & t \leq t_0 \\ c - \Delta \cdot \gamma(\alpha, \frac{t-t_0}{\beta}) & t > t_0 \end{cases} \tag{B.5}$$

where α, β, c, Δ, and t_0 are fit parameters, and $\gamma(t; k, \theta)$ is the lower incomplete gamma function.

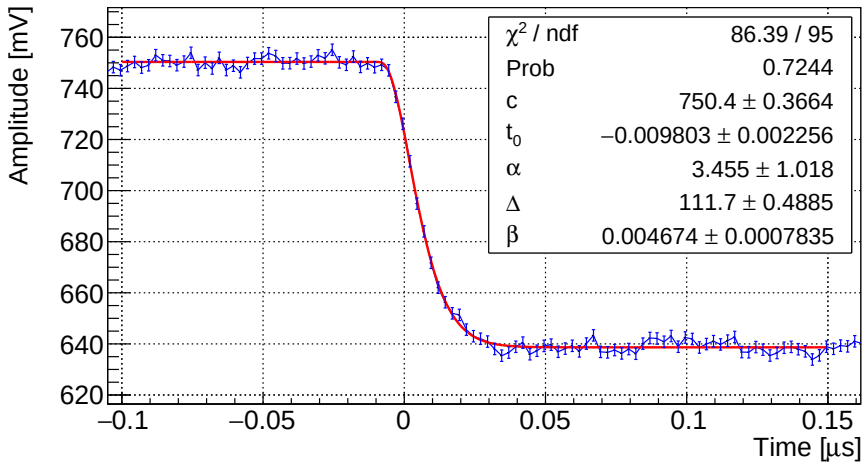

Figure B.1: Example of a selected waveform - The waveform is fitted with the incomplete gamma function (red curve).

Combining eq. B.4 and eq. B.5 yields

$$f(t) = \Delta \cdot t^{\alpha-1} e^{-\frac{t-t_0}{\beta}}. \tag{B.6}$$

Renormalising to unity and setting $t_0 = 0$, eq. B.6 can be rewritten as

$$f(t) = \frac{\beta^\alpha}{\Gamma(\alpha)} t^{\alpha-1} e^{-t/\beta}. \tag{B.7}$$

Therefore, the only relevant fit parameters are α and β. Figure B.2 shows the distributions of those two parameters resulting from the fit of the waveforms of the events converted in the depleted region with the function from eq B.5. The $f(t)$ parameters α and β are set to the mean values of the respective distributions.

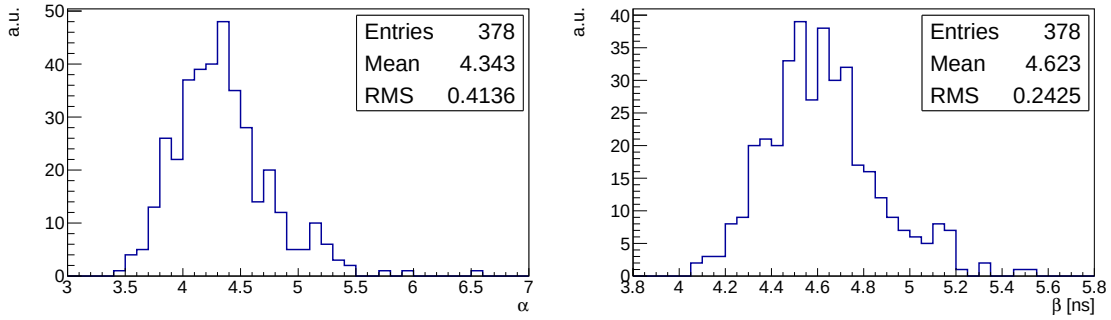

(a) Parameter α **(b)** Parameter β

Figure B.2: Distributions of waveform fit parameters - The mean values of the distributions are used as the IRF parameters.

Appendix C

Laser calibration

C.1 Measurement of the laser beam profile

The laser beam profile measurement setup scheme is shown in figure C.1. The beam profiler[1] is fixed on a X-Y micro-positioning stage while the laser beam focuser is fixed perpendicularly to the sensitive surface, on the Z stage[2]. The setup is enclosed in a light-tight box. The laser beam focuser is connected to the laser driver outside the box via an optical fibre. The laser driver requires a positive input signal (between 1 and 2.5 V) in order to produce laser beam with a proportional optical power (up to 2 mW). The pulse, generated by an external pulse generator and sent to the laser driver, was a 100 ns long trapezoidal signal with 4 ns rise and fall edges, and frequency of 150 kHz.

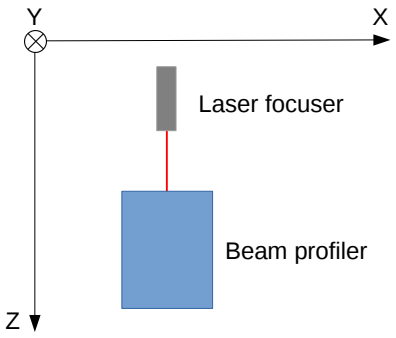

Figure C.1: Beam profiling setup scheme - The beam profiler is fixed on a X-Y micro-positioning stage while the laser beam focuser is fixed perpendicularly to the sensitive surface, on the Z stage.

[1] Ophir-Spiricon NanoScan2 Ge/3.5/1.8 [93].
[2] Zaber T-LSM200A (X and Y stages) and T-LSM100A (Z stage).

In order to determine the minimum spot size, the beam profile was measured[1] at various distances between the beam focuser and the profiler. Figure C.2 shows the spot size (beam width) Γ as a function of position (z) of the laser beam focuser (a higher z means a smaller distance to the beam profiler, see fig. C.1). The variation of the spot size for a Gaussian beam propagating in free space as a function of the distance from its source is given by [95]:

$$w(z) = w_0 \sqrt{1 + \left(\frac{z}{z_R}\right)^2} \tag{C.1}$$

where w_0 is the minimum beam size and z_R is the Rayleigh length[2] that is the distance at which the spot size doubles. Therefore the data were fitted with the following function:

$$\Gamma(z) = \Gamma_0 \sqrt{1 + \left(\frac{z - D_0}{D_R}\right)^2} \tag{C.2}$$

where Γ_0 is the minimum beam size, the D_R provides an estimate of the Rayleigh length, and D_0 is beam focuser position at which the beam size is the smallest. The fit results, reported in fig. C.2, show that the $\Gamma_0 \approx 15$ µm.

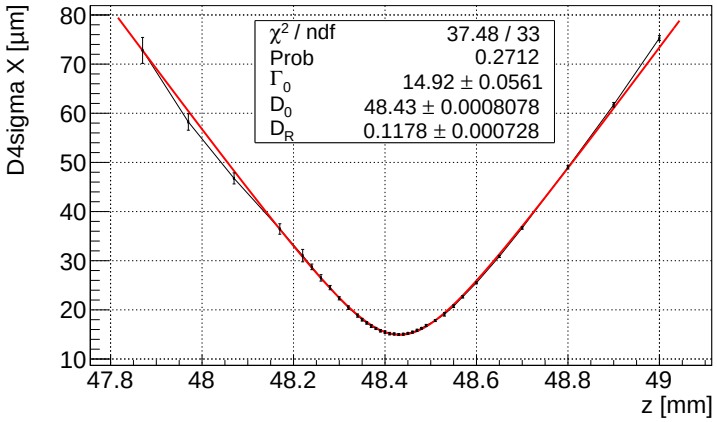

Figure C.2: Beam size as a function of focuser position - Spot size (beam width) Γ as a function of position (z) of the laser beam focuser. Fit parameter Γ_0 is the minimum beam size, the D_R provides an estimate of the Rayleigh length, and D_0 is beam focuser position at which the beam size is the smallest.

[1] ISO Standard 11146 $D_{4\sigma}$ beam width computation method was used [94].
[2] Rayleigh length is the parameter related to the beam divergence.

C.2 Focusing the laser beam on the ALPIDE sensor

The following procedure was adopted in order to obtain the laser beam focused on the ALPIDE chip surface (using the same setup described in sec. 4.3.1):

1. The laser beam focuser is positioned 12.0 ± 0.5 mm (working distance) above the sensor surface, so the laser beam is reasonably well focused (see fig. C.2).

2. The laser beam is moved in 4 µm steps over a 36×36 µm^2 surface. At each position, 100 laser pulses are recorded and the average cluster size is calculated (see fig. C.3a). The laser beam preliminary position (x and y) is selected in correspondence to the maximum measured average cluster size.[1].

3. The beam focuser is moved in 50 µm steps, in range of ± 1 mm around the nominal position above the sensor surface (see step 1). Again, at each position, 100 laser pulses are recorded and the average cluster size is calculated (see fig. C.3b). The laser beam preliminary position (z) is selected in correspondence to the maximum measured average cluster size[2].

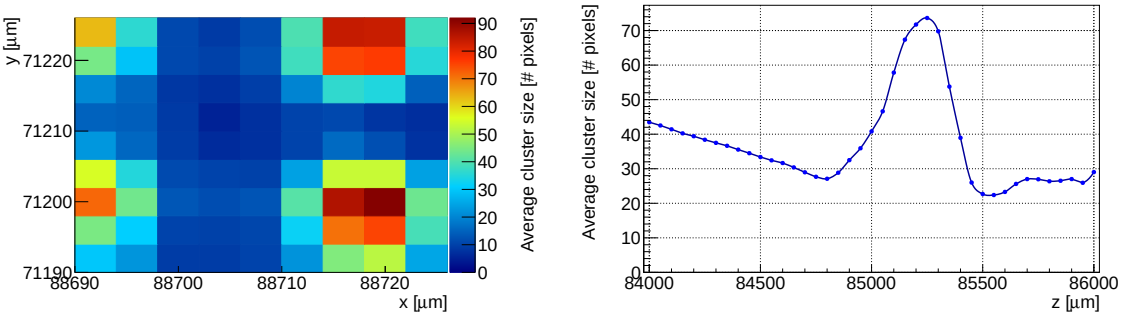

(a) Average cluster size as a function of laser focuser x, y position.

(b) Average cluster size as a function of laser focuser z position.

Figure C.3: Preliminary positioning and focusing - At first, laser beam is moved in large steps to roughly determine the position of the pixel collection diode and then to focus the laser beam on the chip surface.

[1] Only the collection diode of an ALPIDE pixel is not covered by the metal layers, therefore it is expected that the maximum energy deposit occurs when a fouced laser beam is positioned over the collection diode. Moreover, if the laser beam were unfocused, the average cluster size would be expected to vary minimaly with the focuser position.

[2] Since the laser beam is centered on a pixel diode i.e. an opening in the metal layer, reducing the spot size decreases the fraction of the beam reflected by the metallisations.

4. Step 2 is repeated with a step size of 1 µm and a surface equivalent to the pixel size (see fig C.4a).

5. Step 3 is repeated with a step size of 5 µm and range of ±500 µm around the previously determined z-position (see fig C.4b).

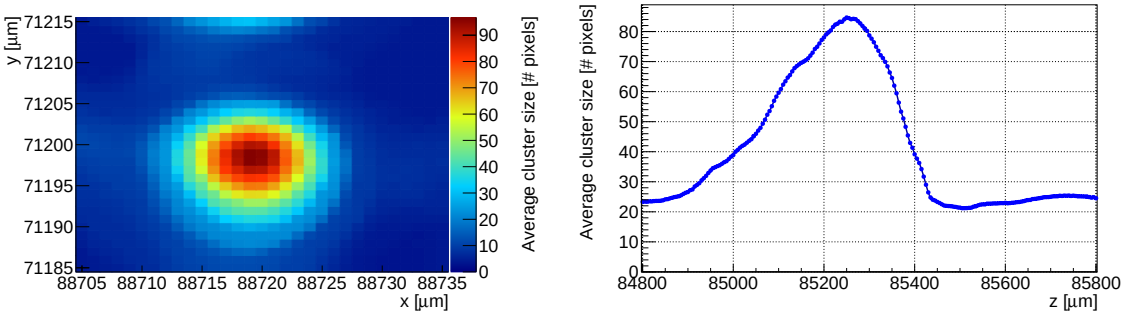

(a) Average cluster size as a function of laser focuser x, y position.

(b) Average cluster size as a function of laser focuser z position.

Figure C.4: Definitive positioning and focusing - After the laser beam focuser has been roughly positioned, the it is moved in small steps to precisely determine the position of the pixel collection diode and the working distance.

The precision (±1 µm in x and y, and ±5 µm in z) and repeatability of this procedure are considered sufficient for the purpose of the measurements discussed in sec. 4.3.1.

C.3 Linearity of laser response

In order to measure the linearity of the laser driver response to the input signal amplitude, the laser driver was connected via optical fibre to an optical/electrical (O/E) converter[1]. The input signal, generated by an external pulse generator, was a 10 ns long trapezoidal signal with 4 ns rise and fall edges. The input signal amplitude was varied from 1 V to 2 V in 0.5 V steps. The optical-electrical converter was coupled with an oscilloscope in order to measure the amplitude and integral of the output signal. The output signal is proportional to input optical power and therefore the integral is proportional to deposited charge. Figure C.5 shows integrated O/E converter output signal as a function of the amplitude of the laser drive input signal.

[1] TTI TIA-950

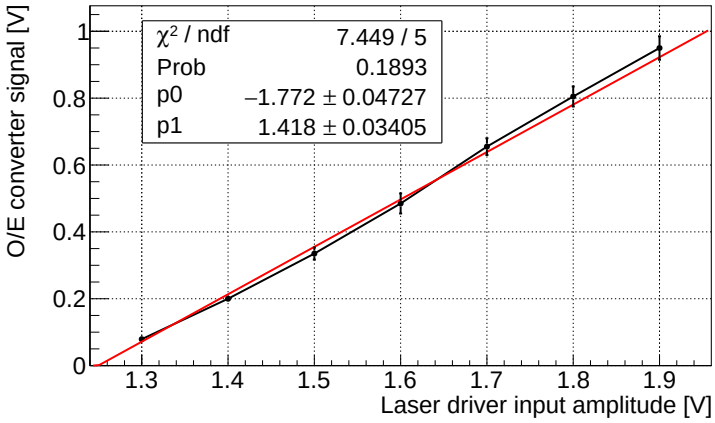

Figure C.5: O/E converter response vs laser driver input amplitude - The red line is a fit with a linear function.

Cluster size as a function of laser power

During the pulse length measurement of pALPIDE-1 (see sec. 4.3.1), it was observed that also the average cluster size scales linearly with laser power, shown in fig. C.6. This implies that for highly ionising particles, the deposited energy could be inferred by measuring the cluster size.

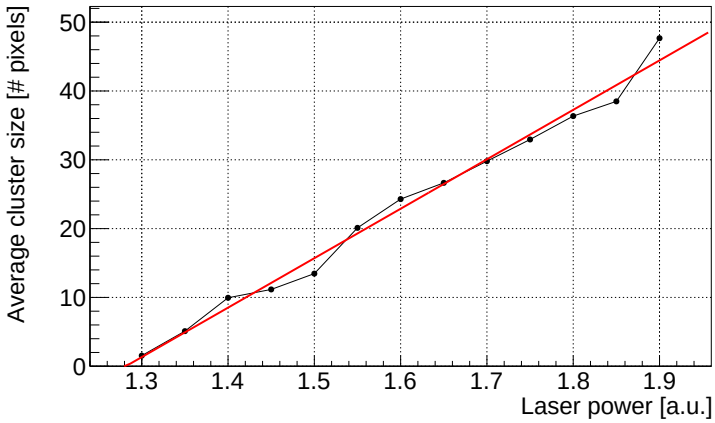

Figure C.6: Average clusters size vs laser power - Average cluster size as a function of laser power. Red line is a linear interpolation.

Acronyms

ALICE	A Large Ion Collider Experiment
ALPIDE	ALICE Pixel Detector
CCE	Charge Collection Efficiency
CMOS	Complementary Metal Oxide Semiconductor
DAC	Digital-to-Analogue Converter
DUT	Device Under Test
FHR	Fake-Hit Rate
FPN	Fixed Pattern Noise
IB	Inner Barrel
ITS	Inner Tracking System
LHC	Large Hadron Collider
LS2	Long Shutdown 2
MAPS	Monolithic Active Pixel Sensor
MIP	Minimum Ionising Particle
MM	Mini Matrix
MPV	Most Probable Value
NIEL	Non-Ionising Energy Loss
OB	Outer Barrel
QGP	Quark-Gluon Plasma
RMS	Root Mean Square
RTN	Random Telegraph Noise
SNR	Signal-to-Noise Ratio
SRP	Spreading Resistance Profiling
TCAD	Technology Computer-Aided Design
TID	Total Ionising Dose
VD	Vertex Detector

References

[1] The ALICE Collaboration. **The ALICE experiment at the CERN LHC**. *Journal of Instrumentation*, **3**(08):S08002, 2008.

[2] Harris and Muller. **The Search for the quark-gluon plasma**. *Ann. Rev. Nucl. Part. Sci.*, **46**, 1996.

[3] Van Hove L. **Two problems concerning hot hadronic matter and high energy collisions (Equilibrium formation, plasma deflagration)**. *Zeitschrift für Physik C Particles and Fields*, **21**(1), 1983.

[4] Rafelski and Müller. **Strangeness Production in the Quark-Gluon Plasma**. *Phys. Rev. Lett.*, **48**, 1982.

[5] The ALICE Collaboration. **Multi-strange baryon production at mid-rapidity in Pb-Pb collisions at $\sqrt{s_{NN}}$ = 2.76 TeV**. *Phys. Lett.*, **B728**, 2014. [Erratum: Phys. Lett.B734,409(2014)].

[6] Matsui and Satz. **J/ψ Suppression by Quark-Gluon Plasma Formation**. *Phys. Lett.*, **B178**, 1986.

[7] Kanaya and Satz. **Correlation and screening in finite-temperature SU(2) gauge theory**. *Phys. Rev. D*, **34**, 1986.

[8] The ALICE collaboration. **Direct photon production in Pb–Pb collisions at**. *Phys. Let. B*, **754**, 2016.

[9] Bjorken J. D. **Energy Loss of Energetic Partons in Quark - Gluon Plasma: Possible Extinction of High p(t) Jets in Hadron - Hadron Collisions**. 1982.

[10] The ALICE Collaboration. **Suppression of high transverse momentum D mesons in central Pb-Pb collisions at $\sqrt{s_{NN}} = 2.76$ TeV**. *JHEP*, **09**, 2012.

[11] The ALICE Collaboration. **Suppression of Charged Particle Production at Large Transverse Momentum in Central Pb-Pb Collisions at $\sqrt{s_{NN}} =$ 2.76 TeV**. *Phys. Lett.*, **B696**, 2011.

[12] The ALICE Collaboration. **Centrality Dependence of Charged Particle Production at Large Transverse Momentum in Pb–Pb Collisions at $\sqrt{s_{\mathrm{NN}}} =$** 2.76 **TeV**. *Phys. Lett.*, **B720**, 2013.

[13] R Snellings. **Elliptic Flow: A Brief Review**. *New J. Phys.*, **13**, 2011.

[14] The ALICE Collaboration. **Elliptic flow of identified hadrons in Pb-Pb collisions at $\sqrt{s_{\mathrm{NN}}} = 2.76$ TeV**. *JHEP*, **06**, 2015.

[15] Bertsch, Gong, and Tohyama. **Pion interferometry in ultrarelativistic heavy-ion collisions**. *Phys. Rev. C*, **37**, 1988.

[16] Muller and Nagle. **Results from the relativistic heavy ion collider**. *Ann. Rev. Nucl. Part. Sci.*, **56**, 2006.

[17] Apollinari, Béjar Alonso, Brüning, Lamont, and Rossi. *High-Luminosity Large Hadron Collider (HL-LHC): Preliminary Design Report.* CERN Yellow Reports: Monographs. CERN, 2015.

[18] The ALICE Collaboration. **Technical Design Report for the Upgrade of the ALICE Inner Tracking System**. Technical Report CERN-LHCC-2013-024. ALICE-TDR-017, CERN, 2013.

[19] The ALICE Collaboration. **Upgrade of the ALICE Time Projection Chamber**. Technical Report CERN-LHCC-2013-020. ALICE-TDR-016, CERN, 2013.

[20] The ALICE Collaboration. **Technical Design Report for the Muon Forward Tracker**. Technical Report CERN-LHCC-2015-001. ALICE-TDR-018, CERN, 2015.

[21] Nakamura et al. (Particle Data Group). **Review of Particle Physics**. *J. Phys. G*, **37**, 2010.

[22] The ALICE Collaboration. **Upgrade of the ALICE Readout & Trigger System**. Technical Report CERN-LHCC-2013-019. ALICE-TDR-015, CERN, 2013.

[23] Buncic et al. **Technical Design Report for the Upgrade of the Online-Offline Computing System**. Technical Report CERN-LHCC-2015-006. ALICE-TDR-019, CERN, 2015.

[24] The ALICE Collaboration. **ALICE: Physics Performance Report, Volume I**. *Journal of Physics G: Nuclear and Particle Physics*, **30**(11), 2004.

[25] The ALICE Collaboration. **Measurement of charm production at central rapidity in proton-proton collisions at $\sqrt{s} = 7$ TeV**. *JHEP*, 2012.

[26] Spieler H. *Semiconductor Detector Systems*. Oxford University Press, 2005.

[27] Schambach et al. **A MAPS Based Micro-Vertex Detector for the STAR Experiment**. *Physics Procedia*, **66**(Supplement C), 2015.

[28] Contin et al. **The MAPS based PXL vertex detector for the STAR experiment**. *JINST*, **10**(03):C03026, 2015.

[29] Sze S.M. *Physics of Semiconductor Devices*. Wiley-Interscience, 2nd edition, 1981.

[30] Leo W. *Techniques for Nuclear and Particle Physics Experiment*. Springer-Verlag, 1987.

[31] Knoll G. *Radiation Detection and Measurement*. John Wiley and Sons, 3rd edition, 1999.

[32] Rossi, Fischer, Rohe, and Wermes. *Pixel Detectors*. Springer-Verlag Berlin Heidelberg, 2006.

[33] Lutz G. *Semiconductor radiation detectors*. Springer, 1st edition, 1999.

[34] Fossum and Lee. **A physical model for the dependence of carrier lifetime on doping density in nondegenerate silicon**. *Solid-State Electronics*, **25**(8), 1982.

[35] Messenger G. C. **A summary review of displacement damage from high energy radiation in silicon semiconductors and semiconductor devices**. *IEEE Transactions on Nuclear Science*, **39**(3), 1992.

[36] Krasel et al. **Measurement of trapping time constants in proton-irradiated silicon pad detectors**. In *2003 IEEE Nuclear Science Symposium*, **1**, 2003.

[37] Pirollo et al. **Radiation damage on p-type silicon detectors**. *Nucl. Instr. Meth. Phys. A*, **426**, 1999.

[38] Kraner, Li, and Posnecker. **Fast Neutron Damage in Silicon Detectors**. *Nucl. Instr. Meth. Phys. A*, **279**, 1989.

[39] Eidelman et al. **Experimental methods and colliders**. *Physics Letters B*, **592**(1), 2004. Review of Particle Physics.

[40] Bichsel H. **Straggling in thin silicon detectors**. *Rev. Mod. Phys.*, **60**, 1998.

[41] Berger et al. **XCOM: Photon Cross Sections Database**, 2010. http://www.nist.gov/pml/data/xcom/index.cfm.

[42] Bé et al. **Table of Radionuclides (Vol. 3 – A = 3 to 244)**. *Monographie BIPM-5*, 2006.

[43] Berger et al. **Stopping-Power and Range Tables for Electrons, Protons, and Helium Ions**, 2005. http://www.nist.gov/pml/data/star/index.cfm.

[44] Thompson et al. *X-Ray Data Booklet.* Lawrence Berkeley National Laboratory, 2009.

[45] Lowe B. G. **Measurements of Fano factors in silicon and germanium in the low-energy X-ray region**. *Nucl. Instr. Meth. Phys. Res. A*, **399**, 1997.

[46] Cavicchioli et al. **Design and characterization of novel monolithic pixel sensors for the ALICE ITS upgrade**. *NIM A*, **765**, 2014.

[47] van Hoorne J. W. *Study and Development of a novel Silicon Pixel Detector for the Upgrade of the ALICE Inner Tracking System.* PhD thesis, Technische Universität Wien, 2008.

[48] Reidt F. *Studies for the ALICE Inner Tracking System Upgrade*. PhD thesis, Heidelberg, 2016.

[49] TowerJazz. **http://www.jazzsemi.com/**.

[50] Glunz et al. **Minority carrier lifetime degradation in boron-doped Czochralski silicon**. *Journal of Applied Physics*, **90**(5), 2001.

[51] Šuljić M. *Characterisation of Monolithic Active Pixel Sensors for the upgrade of the ALICE Inner Tracking System detector*. Master's thesis, Università degli studi di Trieste, 2014.

[52] Perrey H. **EUDAQ and EUTelescope: Software Frameworks for Test Beam Data Acquisition and Analysis**. In *PoS TIPP2014*, 2014.

[53] Kőfaragó M. *To be published*. PhD thesis, Universiteit Utrecht, 2017.

[54] Ullrich and Xu. **Treatment of Errors in Efficiency Calculations**. *ArXiv Physics e-prints*, 2007.

[55] Gao and Rousset. *INVESTIGATOR0 Manual*, December 2013.

[56] Collu A. *Development and characterisation of Monolithic Active Pixel Sensor prototypes for the upgrade of the ALICE Inner Tracking System*. PhD thesis, Università degli studi di Cagliari, 2015.

[57] Mylroie-Smith et al. **First tests of CHERWELL, a Monolithic Active Pixel Sensor: A CMOS Image Sensor (CIS) using 180nm technology**. *NIM A*, **731**, 2013. PIXEL 2012.

[58] Mager M. **ALPIDE, the Monolithic Active Pixel Sensor for the ALICE ITS upgrade**. *NIM A*, **824**, 2016. Frontier Detectors for Frontier Physics: Proceedings of the 13th Pisa Meeting on Advanced Detectors.

[59] Aglieri Rinella G. **The ALPIDE pixel sensor chip for the upgrade of the ALICE Inner Tracking System**. *NIM A*, **845**, 2017. Proceedings of the Vienna Conference on Instrumentation 2016.

[60] Šuljić M. **ALPIDE: the Monolithic Active Pixel Sensor for the ALICE ITS upgrade**. *JINST*, **11**(11):C11025, 2016.

[61] Snoeys W. **CMOS monolithic active pixel sensors for high energy physics**. *NIM A*, **765**, 2014. Proceedings of HSTD-9 2013.

[62] Yang et al. **Low-power priority Address-Encoder and Reset-Decoder data-driven readout for Monolithic Active Pixel Sensors for tracker system**. *NIM A*, **785**, 2015.

[63] ALICE ITS ALPIDE development team. *ALPIDE Operations Manual*, July 2016.

[64] Kim D. **Front end optimization for the monolithic active pixel sensor of the ALICE Inner Tracking System upgrade**. *JINST*, **11**(02):C02042, 2016.

[65] Deveaux et al. **Random Telegraph Signal in Monolithic Active Pixel Sensors**. In *2008 IEEE Nuclear Science Symposium Conference Record*, 2008.

[66] Hung et al. **Random telegraph noise of deep-submicrometer MOSFETs**. *IEEE Electron Device Letters*, **11**(2), 1990.

[67] P. Martin-Gonthier and P. Magnan. **RTS noise impact in CMOS image sensors readout circuit**. In *2009 16th IEEE International Conference on Electronics, Circuits and Systems - (ICECS 2009)*, 2009.

[68] Dash and Newman. **Intrinsic Optical Absorption in Single-Crystal Germanium and Silicon at 77K and 300K**. *Phys. Rev.*, **99**, 1955.

[69] Wagner et al. **Characterization of Silicon Microstrip Detectors Using an Infrared Laser System**. *Nucl. Instr. Meth. A*, **423**, 1999.

[70] Shaheen et al. **Characterization and quality control of silicon microstrip detectors with an infrared diode laser system**. *Nucl. Instr. Meth. A*, **352**, 1995.

[71] Bassi G. *Studio della risposta di un rivelatore monolitico a pixel di silicio alla radiazione alfa proveniente da una sorgente di Am-241*. Bachelor's thesis, Università degli studi di Trieste, 2016.

[72] Doering et al. **Noise performance and ionizing radiation tolerance of CMOS Monolithic Active Pixel Sensors using the 0.18 μm CMOS process**. *Journal of Instrumentation*, **9**(05):C05051, 2014.

[73] Gazdzicki M. **Ion Program of NA61/SHINE at the CERN SPS**. *J. Phys.*, **G36**, 2009. In proceedings of SQM 2008.

[74] Ali and Staszel. **NA61/SHINE experiment upgrade with vertex detector for open charm measurements**. *Journal of Physics: Conference Series*, **509**(1):012083, 2014.

[75] Feofilov G. **NA61/SHINE vertex detector for open charm measurements**. *Journal of Physics: Conference Series*, **668**(1):012012, 2016.

[76] NA61/SHINE Collaboration. **Report from the NA61/SHINE experiment at the CERN SPS**. Technical Report CERN-SPSC-2017-038 (SPSC-SR-221), CERN, 2017. To be published.

[77] Deveaux M. **The Small Acceptance Vertex Detector of NA61/SHINE**. In *SQM2017*, 2017. To be published.

[78] de Robertis G. **MOSAIC board: a modular system for readout and testing of particle physics detectors and their related electronics.** In proceedings of MPGD 2015 & RD51 Collaboration meeting, October 2015.

[79] Wyszyński O. **Trigger system of the NA61/SHINE experiment at the CERN SPS**. In *2014 19th IEEE-NPSS Real Time Conference*, 2014.

[80] Kaptur E. A. Private communication, February 2017.

[81] Staszel P. Private communication, January-March 2017.

[82] James F. and Winkler M. *MINUIT User's Guide*. CERN, 2004.

[83] Ratti et al. **Modeling Charge Loss in CMOS MAPS Exposed to Non-Ionizing Radiation**. *IEEE Transactions on Nuclear Science*, **60**(4), 2013.

[84] Einstein A. **Über die von der molekularkinetischen Theorie der Wärme geforderte Bewegung von in ruhenden Flüssigkeiten suspendierten Teilchen**. *Annalen der Physik*, **322**(8):549–560, 1905.

[85] Canali et al. **Electron and Hole Drift Velocity Measurements in Silicon and Their Empirical Relation to Electric Field and Temperature**. *IEEE Transactions on Electron Devices*, 1975.

[86] Deptcuh G. *New Generation of Monolithic Active Pixel Sensors for Charged Particle Detection*. PhD thesis, Université Louis Pasteur, 2002.

[87] Munker M. Private communication, March-May 2017.

[88] Airaksinen V.-M. **Chapter Fifteen - Introduction to Measuring {MEMS}**. In *Handbook of Silicon Based {MEMS} Materials and Technologies*. William Andrew Publishing, 2010.

[89] Airaksinen V.-M. **Chapter 7 Epitaxial layer characterization and metrology**. In *Silicon Epitaxy*, **72** of *Semiconductors and Semimetals*. Elsevier, 2001.

[90] Drowley C.I. **1 - Application of Materials Characterization Techniques to Silicon Epitaxial Growth**. In *Characterization in Silicon Processing*. Newnes, 1993.

[91] Felix R. Private communication, May 2017.

[92] van Hoorne et al. **The investigator – an efficient tool to optmize design parameters of a CMOS pixel sensor**. presentation at the NSS/MIC 2016 conference, 2017.

[93] Ophir Optronics Solutions. **http://www.ophiropt.com/**.

[94] Ophir-Spiricon, 3050 N 300 W, N. Logan, Utah 84341. *Nanoscan v2 Installation and Operation Manual*, April 2014.

[95] Svelto O. *Principles of Lasers*. Springer, 5th edition, 1998.

Acknowledgements

First and foremost I would like to express my gratitude to my supervisor Paolo Camerini for his guidance and help during my research and writing of this thesis. Second, I would like to thank Luciano Musa and Stefano Piano for making it possible for me to carry out an important part of my research within the ALICE ITS upgrade characterisation team at CERN. I am grateful to Marek Gazdzicki and Pawel Staszel who provided me with the opportunity perform measurements in the NA61 experiment.

Special thanks go to Jacobus W. van Hoorne for all the fruitful discussions, critical assessment of my work, *mentoring* and, most of all, creative and inspirational conversations. I am grateful to Paolo Martinengo for all the support with the measurements at the NA61 experiment and the test-beam facilities. I would like to thank Michael Deveaux for a late night conversation in the NA61 control room that encouraged me to continue working on the MAPS simulation, and also for agreeing to be a referee of this thesis. I am thankful to Magdalena Munker for providing me with the electric field maps, a crucial ingredient for the simulation.

I would also like to thank, in no particular order, to the following people with whom I have been collaborating during the past three years; Felix Reidt, Walter Snoeys, Thanushan Kugathasan, Magnus Mager, Markus Keil, Hyeonjoong Kim, Hartmut Hillemanns, Krzysztof Sielewicz, Rinaldo Rui and Grazia Luparello.

Finally, I would like to express my deepest gratitude to my family and friends for their support, especially to Dajana who endured me in the final months of writing of this thesis.